

GL-TR-89-0264

AD-A222 695

AN ASSESSMENT OF THE APPLICATION OF *IN SITU* ION-DENSITY DATA  
FROM DMSP TO MODELING OF TRANSIONOSPHERIC SCINTILLATION

James A. Secan  
Lee A. Reinleitner  
Northwest Research Associates, Inc.  
P.O. Box 3027  
Bellevue, Washington 98009

15 September 1989

Scientific Report No. 3

Approved for public release; distribution unlimited

Prepared for:


GEOPHYSICS LABORATORY  
AIR FORCE SYSTEMS COMMAND  
UNITED STATES AIR FORCE  
HANSOM AFB, MASSACHUSETTS 01731-5000

DTIC  
ELECTE  
JUN 13 1990  
S B D

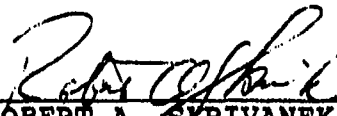
90 06 12 046

"This technical report has been reviewed and is approved for publication"

  
EDWARD J. WEBER  
Contract Manager

  
WILLIAM K. VICKERY  
Branch Chief

FOR THE COMMANDER

  
ROBERT A. SKRIVANEK  
Division Director

This report has been reviewed by the ESD Public Affairs Office (PA) and is releasable to the National Technical Information Service (NTIS).

Qualified requestors may obtain additional copies from Defense Technical Information Center. All others should apply to the National Technical Information Service.

If your address has changed, or if you wish to be removed from the mailing list, or if the addressee is no longer employed by your organization, please notify GL/IMA Hanscom AFB, MA 01731. This will assist us in maintaining a current mailing list.

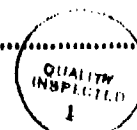
Do not return copies of this report unless contractual obligations or notice on a specific document requires that it be returned.

## REPORT DOCUMENTATION PAGE

1a. REPORT SECURITY CLASSIFICATION Unclassified			1b. RESTRICTIVE MARKINGS	
2a. SECURITY CLASSIFICATION AUTHORITY			3. DISTRIBUTION / AVAILABILITY OF REPORT Approved for public release. Distribution unlimited.	
2b. DECLASSIFICATION / DOWNGRADING SCHEDULE				
4. PERFORMING ORGANIZATION REPORT NUMBER(S) NWAR-CR-89-R047			5. MONITORING ORGANIZATION REPORT NUMBER(S) GL-TR-89-0264	
6a. NAME OF PERFORMING ORGANIZATION Northwest Research Associates, Inc.		6b. OFFICE SYMBOL (If applicable) CR		7a. NAME OF MONITORING ORGANIZATION Geophysics Laboratory
6c. ADDRESS (City, State, and ZIP Code) P.O. Box 3027 Bellevue, WA 98009			7b. ADDRESS (City, State, and ZIP Code) Hanscom AFB, MA 01731	
8a. NAME OF FUNDING / SPONSORING ORGANIZATION		8b. OFFICE SYMBOL (If applicable)		9. PROCUREMENT INSTRUMENT IDENTIFICATION NUMBER F19628-86-C-0195
8c. ADDRESS (City, State, and ZIP Code)			10. SOURCE OF FUNDING NUMBERS	
			PROGRAM ELEMENT NO. 62101F	PROJECT NO. 4643
			TASK NO. 09	WORK UNIT ACCESSION NO. AI
11. TITLE (Include Security Classification) An Assessment of the Application of <i>In situ</i> Ion-density data from DMSP to modeling of Transionospheric Scintillation				
12. PERSONAL AUTHOR(S) Secan, James A., Lee A. Reinleitner				
13a. TYPE OF REPORT Scientific No. 3		13b. TIME COVERED FROM 88 Sep 15 to 89 Sep 14		14. DATE OF REPORT (Year, Month, Day) 89 Sep 15
15. PAGE COUNT 112				
16. SUPPLEMENTARY NOTATION				
17. COSATI CODES			18. SUBJECT TERMS (Continue on reverse if necessary and identify by block number)	
FIELD	GROUP	SUB-GROUP		
04	0		→ Ionosphere, Ionospheric Scintillation, Radiowave Scintillation, Defense Meteorology Satellite Program, (DMSP)	
20	14		→ Scintillation	
19. ABSTRACT (Continue on reverse if necessary and identify by block number) Modern military communication, navigation, and surveillance systems depend on reliable, noise-free transionospheric radio-frequency channels. They can be severely impacted by small-scale electron-density irregularities in the ionosphere, which cause both phase and amplitude scintillation. Basic tools used in planning and mitigation schemes are climatological in nature and thus may greatly over- and under-estimate the effects of scintillation in a given scenario. This report describes the second year of an investigation into the feasibility of using <i>in-situ</i> observations of the ionosphere from the USAF DMSP satellite to calculate estimates of irregularity parameters that could be used to update scintillation models in near real-time. Estimates for the level of intensity and phase scintillation on a transionospheric UHF radio link are calculated from DMSP Scintillation Meter (SM) data and compared to the levels actually observed. The intensity scintillation levels predicted and observed compare quite well, but the comparison with the phase scintillation data was complicated by low-frequency phase noise on the UHF radio link. Results are presented from analysis of DMSP SSIES data collected near Kwajalein Island in conjunction with a propagation-effects experiment. Preliminary conclusions from the assessment study are (1) the DMSP SM data can be used to make quantitative estimates of the level of scintillation at auroral latitudes, and (2) it may be possible to use the data as a qualitative indicator of scintillation-activity levels at equatorial latitudes. <i>Key words:</i>				
20. DISTRIBUTION / AVAILABILITY OF ABSTRACT <input type="checkbox"/> UNCLASSIFIED/UNLIMITED <input type="checkbox"/> SAME AS RPT. <input type="checkbox"/> DTIC USERS			21. ABSTRACT SECURITY CLASSIFICATION Unclassified	
22a. NAME OF RESPONSIBLE INDIVIDUAL ward Weber			22b. TELEPHONE (Include Area Code) GL/LIS	

# TABLE OF CONTENTS

	<u>Page</u>
1. Introduction.....	1
2. Background.....	2
3. Analysis of SSIES/AIO/EISCAT Campaign Data.....	5
3.1 Data Description .....	5
3.2 Data Processing .....	10
3.2.1 SSIES SM Data .....	10
3.2.2 AIO-AFSAT Scintillation Data .....	14
3.3 Data Comparisons.....	14
3.3.1 Intensity Scintillation .....	14
3.3.2 Phase Scintillation .....	16
3.4 Discussion of Results .....	30
4. SSIES Observations of Equatorial Irregularities .....	32
4.1 Nighttime Equatorial F-Region Scintillation - A Micro-Review.....	32
4.1.1 Equatorial Plume Structures .....	32
4.1.2 Equatorial Bottomside Sinusoidal Irregularities .....	33
4.1.3 Topside Studies of Equatorial Irregularities .....	34
4.2 PEAK Campaign Description .....	34
4.3 Data Description .....	35
4.3.1 DMSP SSIES Data.....	35
4.3.2 FLTSAT S <sub>4</sub> Data .....	49
4.3.3 HiLat/Polar Bear S <sub>4</sub> Data.....	56
4.4 Discussion of Results .....	56
5. Conclusion .....	64
References.....	65
Appendix. Plots of SSIES PEAK Campaign Data .....	A-1



For	<input checked="" type="checkbox"/>
I	<input type="checkbox"/>
d	<input type="checkbox"/>
on	
on/	
ty Codes	
and/or	
Special	

Dist  
A-1

## LIST OF FIGURES

Figure	Caption	Page
1	Negative of imagery from the DMSP F8 satellite OLS sensor for Rev 2862 on 8 Jan 88. The numbered points identify 300km field-line "footprints" of the DMSP satellite at 30-second intervals. The dot labeled "AIO" indicates the location of the AIO aircraft at 18:39 GMT, and the arrow points to the 300km ionospheric penetration point (IPP) of the AIO-AFSAT radio link.	6
2	Imagery from the AIO all-sky photometer taken at 18:37:12, 18:39:30, and 18:41:30 GMT on 8 Jan 88. The upper images are at a wavelength of 6300 Å, and the lower images are at 4278 Å. The locations of the DMSP footprints and the AIO-AFSAT IPP shown in Figure 1 are plotted on the 6300 Å image taken at 18:39:30 GMT. The coordinate-grid overlay is geographic latitude and longitude.	7
3	Total ion density data from the DMSP Scintillation Meter (SM) instrument from DMSP Rev 2862 on 8 Jan 88. The times labeled 1-7 correspond to the locations indicated in Figures 1 and 2 as DMSP footprint locations. The time marked with a $\lambda_1$ indicates the time at which the DMSP footprint was at the same apex latitude ( $\lambda_1$ ) at the same time as the AIO-AFSAT IPP.	8
4	The density data from Figure 3 detrended by removing the output from a 6-pole, low-pass Butterworth filter with a cutoff frequency of 0.0469 Hz.	8
5	Signal intensity data from the AIO-AFSAT VHF radio link from 8 Jan 88. The data have been detrended using the same procedure as that used in detrending the density data in Figure 4 except with a 0.01 Hz cutoff frequency.	9
6	Signal phase data from the AIO-AFSAT VHF radio link from 8 Jan 88. The data have been detrended as described in Figure 5.	9

7	Experiment geometry for the 8 Jan 88 pass. The squares indicate the location of the 300km field-line footprint (FLP) of the DMSP satellite at 3-second intervals, and the circles indicate the location of the 300km ionospheric penetration point (IPP) of the AIO-AFSAT link at one-minute intervals. The DMSP FLP and AIO-AFSAT IPP are at the same latitude at the same time at 18:38:49. The coordinates of this plot are modified apex latitude and apex longitude.	11
8	Total ion density from the DMSP SM instrument for the time interval defined in Figure 7. The tic marks along the abscissa correspond to the 3-second locations indicated in Figure 7.	12
9	Data from Figure 8 detrended as described in Figure 4.	12
10	Comparison of $S_4$ calculated from the AIO-AFSAT intensity record shown in Figure 5 (solid line) to $S_4$ calculated from the SSIES $C_k L$ estimates for two irregularity models (17:2 wings - squares; 20:1 rods - diamonds) and from the WBMOD model (crosses). The two AIO-AFSAT points labeled "retune" included retune-discontinuities, and the point labeled "focus" contained a strong focus. The $S_4$ values for these three points are unreliable.	15
11	Comparison of $\sigma_\phi$ calculated from the AIO-AFSAT phase record shown in Figure 6 (solid line) to $\sigma_\phi$ calculated from the SSIES $C_k L$ estimates for two irregularity models (17:2 wings - squares; 20:1 rods - diamonds) and from the WBMOD model (crosses).	15
12	Power density spectrum (PDS) of phase, detrended by end-matching and removing the residual mean, for a 4096-point data sample (204.8 seconds) centered at 67160 seconds. The dotted line is a linear fit to $\log(\text{PDS})$ and $\log(f)$ over the range 0.015 Hz to 0.092 Hz, and the dashed line is a linear fit over the range 0.1 to 1.0 Hz.	18
13	AIO-AFSAT phase record detrended with a 0.05 Hz cutoff frequency.	19
14	AIO-AFSAT phase record detrended with a 0.075 Hz cutoff frequency.	19
15	Comparison of $\sigma_\phi$ calculated from the AIO-AFSAT phase record shown in Figure 14 (solid line) to $\sigma_\phi$ calculated from the SSIES $C_k L$ estimates for two irregularity models (17:2 wings - squares; 20:1 rods - diamonds) and from the WBMOD model (crosses).	20

- 16      Power density spectra from (a) SM density data centered at 67120 (left ordinate scale) and (b) the AIO-AFSAT phase data (0.01 Hz detrend) centered at 66960 (right ordinate scale). The SM PDS has been shifted in log-frequency by -1.76 to compensate for the different effective scan velocities of the SM and AIO-AFSAT data sets. The short vertical bars indicate a potentially-common feature in the two spectra (see text). The horizontal solid bar indicates the value for T derived from the AIO-AFSAT phase spectrum (0.1 to 1.0 Hz fit), and the horizontal dotted line indicates a value for T derived from the SM density data using a 265 m/s effective scan velocity. 23
- 17      Power density spectra from (a) SM density data centered at 67125 (left ordinate scale) and (b) the AIO-AFSAT phase data (0.01 Hz detrend) centered at 67060 (right ordinate scale). The SM PDS has been shifted in log-frequency by -1.57 to compensate for the different effective scan velocities of the SM and AIO-AFSAT data sets. The short vertical bars indicate a potentially common feature in the two spectra (see text). The horizontal solid bar indicates the value for T derived from the AIO-AFSAT phase spectrum (0.1 to 1.0 Hz fit), and the horizontal dotted line indicates a value for T derived from the SM density data using a 265 m/s effective scan velocity. 24
- 18      Power density spectra from (a) SM density data centered at 67130 (left ordinate scale) and (b) the AIO-AFSAT phase data (0.01 Hz detrend) centered at 67160 (right ordinate scale). The SM PDS has been shifted in log-frequency by -1.34 to compensate for the different effective scan velocities of the SM and AIO-AFSAT data sets. The short vertical bars indicate a potentially common feature in the two spectra (see text). The horizontal solid bar indicates the value for T derived from the AIO-AFSAT phase spectrum (0.1 to 1.0 Hz fit), and the horizontal dotted line indicates a value for T derived from the SM density data using a 265 m/s effective scan velocity. 25
- 19      Power density spectra from (a) SM density data centered at 67135 (left ordinate scale) and (b) the AIO-AFSAT phase data (0.01 Hz detrend) centered at 67260 (right ordinate scale). The SM PDS has been shifted in log-frequency by -1.45 to compensate for the different effective scan velocities of the SM and AIO-AFSAT data sets. The short vertical bars indicate a potentially common feature in the two spectra (see text). The horizontal solid bar indicates the value for T derived from the AIO-AFSAT phase spectrum (0.1 to 1.0 Hz fit), and the horizontal dotted line indicates a value for T derived from the SM density data using a 265 m/s effective scan velocity. 26

20	Power density spectra from (a) SM density data centered at 67140 (left ordinate scale) and (b) the AIO-AFSAT phase data (0.01 Hz detrend) centered at 67360 (right ordinate scale). The SM PDS has been shifted in log-frequency by -1.35 to compensate for the different effective scan velocities of the SM and AIO-AFSAT data sets. The short vertical bars indicate a potentially common feature in the two spectra (see text). The horizontal solid bar indicates the value for T derived from the AIO-AFSAT phase spectrum (0.1 to 1.0 Hz fit), and the horizontal dotted line indicates a value for T derived from the SM density data using a 265 m/s effective scan velocity.	27
21	Average phase and <i>in-situ</i> power density spectra constructed from the spectra in Figures 18-20. The vertical lines indicate the location of features described in the text. The <i>in-situ</i> spectrum has been shifted to align the marked features in the two spectra, which implies an effective scan velocity in the phase data of 265 m/s.	29
22a	Total ion density measured by the Scintillation Meter (SM) sensor on DMSP F8 near Kwajalein Atoll on 24 August 1988. The y-axis is ion density ranging from 0.0 to $2.0 \times 10^5$ ; and the x-axis labels are GMT for Greenwich Mean Time (HH:MM:SS), APXLAT for (modified) apex latitude, and APXLON for apex longitude.	36
22b	Total ion density measured by the SM sensor on DMSP F9 near Kwajalein Atoll on 24 August 1988. The axis ranges and labels are as in Figure 1a.	37
23a	Total ion density measured by the SM sensor on DMSP F8 near Kwajalein Atoll on 31 August 1988. The axis ranges and labels are as in Figure 1a.	38
23b	Total ion density measured by the SM sensor on DMSP F9 near Kwajalein Atoll on 31 August 1988. The axis ranges and labels are as in Figure 1a.	39
24a	Total ion density measured by the SM sensor on DMSP F8 near Kwajalein Atoll on 13 August 1988. The axis ranges and labels are as in Figure 1a.	40
24b	Total ion density measured by the SM sensor on DMSP F9 near Kwajalein Atoll on 13 August 1988. The axis ranges and labels are as in Figure 1a.	41

25a	Total ion density measured by the SM sensor on DMSP F8 near Kwajalein Atoll on 28 August 1988. The axis ranges and labels are as in Figure 1a.	42
25b	Total ion density measured by the SM sensor on DMSP F9 near Kwajalein Atoll on 28 August 1988. The axis ranges and labels are as in Figure 1a.	43
26a	Total ion density measured by the SM sensor on DMSP F8 near Kwajalein Atoll on 4 August 1988. The axis ranges and labels are as in Figure 1a.	44
26b	Total ion density measured by the SM sensor on DMSP F9 near Kwajalein Atoll on 4 August 1988. The axis ranges and labels are as in Figure 1a.	45
27a	Total ion density measured by the SM sensor on DMSP F8 near Kwajalein Atoll on 12 August 1988. The axis ranges and labels are as in Figure 1a.	46
27b	Total ion density measured by the SM sensor on DMSP F9 near Kwajalein Atoll on 12 August 1988. The axis ranges and labels are as in Figure 1a.	47
28	The maximum density observed on DMSP F8 passes in the east (top plot), center (middle plot), and west (bottom plot) sectors for August 1988. The x's indicate that the corresponding F9 pass in that same sector showed an irregularity structure.	50
29	The maximum density observed (outside of irregularity structures) on DMSP F9 passes in the east (top plot), center (middle plot), and west (bottom plot) sectors for August 1988. The x's indicate that an irregularity structure was seen in that pass.	51
30	VHF (250MHz) intensity scintillation ( $S_4$ index) observed on a Kwajalein-FLTSAT satellite communications link during August 1988. The 8 and 9 marks indicate times of DMSP F8 and F9 center passes, circled 9 marks indicate center F9 passes with irregularity structures, B marks indicate east or west F9 passes with irregularity structures, and the heavy vertical lines at 0710 GMT and 1030 GMT indicate times at which an F8 or F9 pass is overhead at Kwajalein.	52

31	Plots of (a) 10.7cm solar radio flux (solid line) and the daily $A_p$ planetary magnetic index (bars); (b) the average maximum ion density observed in the three DMSP passes near Kwajalein for F8 (solid line) and F9 (dotted line); and (c) the number of hours that $S_4$ was greater than 0.5 on the FLTSAT link (solid line) and the F9 passes on which irregularity structures were observed (x's; E - East, C - Center, W - West) for August 1988.	55
32	UHF intensity scintillation ( $S_4$ index) observed on the HiLat and Polar BEAR beacons by the ROVER receiver located on Kwajalein Atoll (+s) and the F9 passes on which irregularity structures were observed (x's; E - East, C - Center, W - West) for August 1988. The dashed line indicates theoretical saturation ( $S_4 = 1.0$ ), and the dotted line the effective noise floor of the observations.	57
33	L-band intensity scintillation ( $S_4$ index) observed on the HiLat and Polar BEAR beacons by the ROVER receiver located on Kwajalein Atoll (plotted as in Figure 31).	57
34	Density distribution of DMSP passes with irregularity structures (right of dividing line) and without (left of line) for six DMSP data sets. The horizontal shaded bands represent the ion density thresholds for March and September. [After Young <i>et. al.</i> , 1984.]	59
35	The density distribution of passes with irregularity structures (right of dividing line) and without (left) for the August 1988 data sets. Plot (a) uses the maximum ion density in the F9 pass in which the structure is found, and plot (b) uses the maximum ion density in the F8 pass made earlier in the day in the same sector (east, center, west) as the F9 pass. The dotted line indicates the September threshold from Young, <i>et. al.</i> .	59
36a	Density distribution plots for the east, center, and west F9 passes showing the number of hours that $S_4$ on the FLTSAT link exceeded 0.5 (in tenths of hours; i.e., 55 is 5.5 hours) for the day on which the pass occurred. The dashed line indicates the September threshold from Young <i>et. al.</i> .	62
36b	Density distribution plots for the east, center, and west F9 passes showing the day (in August) on which the pass occurred. The dashed line indicates the September threshold from Young <i>et. al.</i> .	63

## LIST OF TABLES

Table	Caption	Page
1	Results of SSIES SM $C_L$ calculations.	13
2	Phase scintillation parameters from the SM and AIO-AFSAT data sets (100s detrend; 17:2 wings).	16
3	Phase scintillation parameters from the SM and AIO-AFSAT data sets (13-1/3s detrend; 17:2 wings).	20
4	Phase scintillation parameters from the SM and AIO-AFSAT data sets (13-1/3s detrend; 17:2 wings; $v_e$ from T).	22
5	Phase scintillation parameters from the SM and AIO-AFSAT data sets (13-1/3s detrend; 17:2 wings; $v_e$ from $\sigma_\phi$ ).	22
6	Phase scintillation parameters from the SM and AIO-AFSAT data sets (13-1/3s detrend; 17:2 wings; $v_e$ from PDS).	28

## PREFACE

This report describes the work completed during the third year of a multi-year investigation into the feasibility of using *in-situ* observations of the ionosphere from the DMSP SSIES sensors to calculate parameters that characterize ionospheric scintillation effects. Work during this year focused on detailed analysis of data collected during the first day of the SSIES/AIO/AFSAT/EISCAT coordinated data-collection campaign described in the annual report from the second year of the project<sup>(1)</sup> and on analysis of SSIES data collected from both the DMSP F8 and F9 satellites in conjunction with a propagation experiment (PEAK: Propagation Effects Assessment - Kwajalein) conducted under the auspices of the Defense Nuclear Agency (DNA). The results of both analyses are presented in this report.

This work is part of a larger effort with an overall objective of providing the USAF Air Weather Service with the capability of observing ionospheric scintillations, and the plasma density irregularities that cause the scintillations, in near real-time and updating models of ionospheric scintillation with these observations.

## AKNOWLEDGEMENTS

A number of individuals and organizations made data available for this study, which were essential to successful completion of the project. Dr. Fred Rich (GL/PHG) provided the DMSP F8 and F9 data for the month of August 1988; Robert Livingston (SRII) provided the intensity and phase data from the AIO-AFSAT VHF link; Roland Tsunoda (SRII) provided the Kwajalein-FLEETSAT VHF S<sub>4</sub> data; and Dr. Ed Fremouw (NWRA) made the HiLat and Polar BEAR data taken during the PEAK campaign available.

## 1. Introduction

Many modern military systems used for communications, command and control, navigation, and surveillance depend on reliable and relatively noise-free transmission of radiowave signals through the earth's ionosphere. Small-scale irregularities in the ionospheric density can cause severe distortion, known as radiowave scintillation, of both the amplitude and phase of these signals. A basic tool used in estimating these effects on systems is a computer program, WBMOD, based on a single-scatter phase-screen propagation model and a number of empirical models of the global morphology of ionospheric density irregularities<sup>[1,2]</sup>. An inherent weakness of WBMOD is that the irregularity models provide median estimates for parameters with large dynamic ranges, which can lead to large under- and over-estimation of the effects of the ionospheric irregularities on a system.

One solution to this problem, at least for near real-time estimates, is to update the WBMOD irregularity models with observations of the various parameters modeled. One proposed source for these observations is from the *in-situ* plasma density monitor to be flown on the Defense Meteorology Satellite Program (DMSP) satellites. Previous studies<sup>[3]</sup> using *in-situ* measurements from the DE-2 satellite have found that there is potential for using the data in this fashion. This study is designed to assess the applicability of this data set to real-time updates of the WBMOD models. There are two primary objectives:

- (1) Develop and refine techniques for generating estimates of parameters that characterize ionospheric scintillation from *in-situ* observations of the ionospheric plasma from the DMSP SSIES sensors.
- (2) Determine if the parameters calculated from the SSIES data can be used to compute the scintillation effects on a transionospheric radiowave signal.

This report describes the results obtained during the third year of the study. The focus during this year was on (1) continuing the analysis of SSIES data from the DMSP F8 satellite for two intervals in January 1988 during which the AFGL Airborne Ionospheric Observatory (AIO), an AFGL VHF-beacon scintillation monitor, and the EISCAT incoherent-scatter radar were making measurements in the vicinity of Tromso, Norway, and (2) analyzing SSIES data from the DMSP F8 and F9 satellites collected in the equatorial region near Kwajalein Island in conjunction with a Defense Nuclear Agency (DNA) propagation experiment.

## 2. Background

The propagation model used in the WBMOD program (based on weak-scatter phase-screen theory<sup>(1,2)</sup>) characterizes the ionospheric electron density irregularities that cause scintillation via eight independent parameters<sup>(4)</sup>:

- (1)  $a$ : The irregularity axial ratio along the direction of the ambient geomagnetic field.
- (2)  $b$ : The irregularity axial ratio perpendicular to the direction of the ambient geomagnetic field.
- (3)  $\delta$ : The angle between sheet-like irregularity structures and geomagnetic L shells.
- (4)  $h_p$ : The height of the equivalent phase screen above the earth's surface.
- (5)  $v_d$ : The *in-situ* irregularity drift velocity.
- (6)  $\alpha_0$ : The outer scale of the irregularity spectrum.
- (7)  $q$ : The slope of a power-law distribution that describes the one-dimensional power-density spectrum (PDS) of the irregularities.
- (8)  $C_k L$ : The height-integrated strength parameter.

The first three parameters ( $a$ ,  $b$ , and  $\delta$ ) and the direction of the ambient geomagnetic field specify the propagation geometry, while the last three ( $\alpha_0$ ,  $q$ , and  $C_k L$ ) specify the spectral characteristics of the irregularities.

It may be possible to obtain estimates for the values of three of these parameters from the DMSP SSIES sensors:  $v_d$  (from the SSIES Ion Drift Meter (DM)), and  $q$  and  $C_k L$  (from the SSIES Ion Scintillation Meter (SM)). In this study, we will focus on the estimation of  $C_k L$  from this data set and consider  $q$  and  $v_d$  only in terms of the effects of uncertainties in these parameters on the estimates of  $C_k L$ . Of the eight parameters,  $C_k L$  varies the most as a function of location and time, and has the most profound effect on the accuracy of estimates of scintillation levels made by the WBMOD model.

In the phase-screen propagation theory used in WBMOD<sup>(4)</sup>, the  $C_k L$  parameter is actually the product of two parameters:  $C_k$ , the three-dimensional spectral "strength" of the electron density irregularities at a scale size of  $1 \text{ km}^3$  (related to the structure constant used in classical turbulence theory); and  $L$ , the thickness of the irregularity layer. The models in WBMOD were obtained from analysis of phase scintillation data from the WIDEBAND and HiLat satellites, which will provide estimates of the height-integrated value of  $C_k L$  rather than independent measures of  $C_k$  and  $L$ . Because of this, the model was developed for  $C_k L$  rather than for  $C_k$  and  $L$  separately.

---

\* The cited reference develops the theory in terms of an earlier definition of the strength parameter,  $C_s$ , which is defined at a scale size of  $2\pi$  meters. It is related to  $C_k$  according to the equation  $C_s = (2\pi/1000)^{q+2} C_k$ .

The calculation of an estimate of the  $C_k L$  parameter from topside *in-situ* ion density observations requires two operations. First, an estimate of  $C_k$  at the satellite altitude is made from a finite-length time series of density measurements. Second, the estimate of  $C_k$  is converted to an estimate of  $C_k L$  in some fashion which will account for both the thickness of the irregularity layer and the variation of  $C_k$ , or  $\langle \Delta N_e^2 \rangle$ , within the layer.

The data set from which the estimates of these parameters are to be obtained will be collected by three instruments in the DMSP SSIES (Special Sensor for Ions, Electrons, and Scintillation) sensor package. This data set will contain the following *in-situ* observations:

(1) High time-resolution (24 samples/sec) measurements of the ion density and measurements of the ion density irregularity PDS at high fluctuation frequencies from the Ion Scintillation Meter (SM)<sup>[5]</sup>.

(2) Measurements of the horizontal and vertical cross-track ion drift velocities from the Ion Drift Meter (DM)<sup>[5]</sup>.

(3) Measurements of the ion and electron temperatures, the densities of  $O^+$  and the dominant light ion ( $H^+$  or  $He^+$ ), and the horizontal ram ion drift velocity from the ion Retarding Potential Analyzer (RPA)<sup>[6]</sup>.

The basic data of this set are the high time-resolution density data from the SM which will be used to generate estimates of the irregularity PDS. The drift-velocity measurements from the DM and RPA will be used in calculating an estimate of  $C_k$  from parameters obtained from the PDS, and the other measurements from the RPA will be used in calculating  $C_k L$  from  $C_k$ .

In the first year of this project, techniques for calculating estimates of  $C_k L$  from the SSIES data set were developed, and parametric studies were conducted to determine the uncertainties in the final  $C_k L$  estimates due to uncertainties in the parameters and procedures used to calculate the estimates. Since the first SSIES sensor package was not flown until mid-1987, these studies were conducted using simulated SM density data sets and phase scintillation data from the Wideband satellite. The results of these studies were reported in Scientific Report 1 for this project<sup>[7]</sup> (herein referred to as Report #1) and will be summarized in this report where pertinent.

The second phase of the project, which focuses on how well these techniques work using data from the DMSP F8 and F9 spacecraft, was begun during the second year of the project. A coordinated, multi-sensor observation campaign was conducted during January 1988 in the vicinity of Tromso, Norway, in order to collect data for this study. The GL Airborne Ionospheric Observatory (AIO) aircraft flew repeated north-south legs along the magnetic meridian at times when the DMSP F8 satellite was passing overhead. Data collected on the AIO included intensity and phase scintillation observations on a VHF link from an AFSAT satellite, auroral images from an all-sky photometer, and ionograms from a digisonde. Ionospheric soundings by the EISCAT incoherent-scatter radar located in Norway also were made aperiodically throughout the observation period. Data were collected for DMSP passes on 8, 9, 15, 16, 17, and 18 January 1988. The procedures used to

process these data and preliminary results from the analysis were reported in Scientific Report #2 for this project<sup>[8]</sup> (herein referred to as Report #2) and will be summarized in this report where pertinent.

During the third year, a complete analysis was made of the data from the 8 January 1988 data set, and SSIES data collected from both DMSP F8 and F9 during a multi-sensor campaign conducted by the Defense Nuclear Agency (DNA) near Kwajalein Island were analyzed to determine the usefulness of these data for scintillation characterization in the equatorial ionosphere. The results of these studies are presented in this report.

A note on coordinate systems: The geomagnetic latitude, longitude, and local time coordinate system used throughout this report is modified apex coordinates<sup>[9]</sup>, a coordinate system derived from apex coordinates proposed by VanZandt *et. al.*<sup>[10]</sup>. This system, which is used in the WBMOD model, was chosen because it is very similar to both invariant and corrected geomagnetic coordinates at high latitudes, and modified apex latitude is very similar to dip latitude in the equatorial region, becoming identical to dip latitude at the dip equator.

### 3. Analysis of SSIES/AIO/EISCAT Campaign Data

In Report #2, we described in detail the coordinated data-collection campaign that was conducted in January 1988 in the vicinity of the EISCAT radar facility located in northern Norway<sup>(8)</sup>. During the past year, we have received the scintillation observations from the AIO-AFSAT VHF link, which allowed us to compare the level of scintillation predicted by analysis of the DMSP F8 SSIES data to the observed scintillation on this link. We have received the data for only a single day (8 Jan 88), but we believe that this was enough to demonstrate that the DMSP SSIES data potentially can be used to monitor the level of scintillation that would be observed on a transionospheric propagation path.

#### 3.1 Data Description

Figures 1 and 2 place the observations used in this analysis in the context of conditions within the auroral zone at the time of the DMSP pass. Figure 1 is the imagery (in negative) taken by the OLS system on the DMSP F8 satellite as it passed over northern Norway. The overlay grid is geographic latitude and longitude, the dots numbered 1 through 7 are points where the DMSP location has been mapped down to 300km altitude along a magnetic field line at 30-second intervals starting at 18:37:30 GMT at Point 1, and the circled dot labeled "AIO" indicates the location of the AIO aircraft at 18:39 GMT, with the small arrow indicating the 300km penetration point of the propagation path to the AFSAT satellite. The images in Figure 2 are from the all-sky photometer on the AIO aircraft. The center 6330 Å image, taken at 18:39:30, is labeled with the DMSP locations as in Figure 1, and the AIO-AFSAT 300km penetration point at 18:39:30 is marked with a large dot.

Figure 3 is a plot of the total ion density data from the SSIES SM sensor for a five-minute period centered on the location identified as Point #4 in Figure 1. The times corresponding to Points #1-7 in Figures 1 and 2 are labeled on Figure 3, as is the time at which the 300km-point of the field line (FLP) passing through the DMSP location was at the same magnetic latitude as the 300km ionospheric penetration point (IPP) of the AIO-AFSAT radio link (labeled  $\lambda_1$ ). Figure 4 shows the same data over the same time interval, detrended using a 6-pole Butterworth low-pass filter with a 3dB cutoff at a frequency of 0.047 Hz (21-1/3 seconds).

The amplitude and phase data from the AIO-AFSAT VHF radio link (provided by R. Livingston, SR11) are shown in Figures 5 and 6, respectively. These data have both been detrended using the same low-pass filter used to detrend the density data, except with a 3dB cutoff frequency of 0.01Hz (100 seconds). The phase data were preprocessed at SR11 to remove artifacts introduced at points where the ground receiver has been retuned to follow frequency jumps in the AFSAT signal, which occur at 168-second intervals. The effects of these retunes can be seen in the intensity record at 67212 and 67380. Small residual phase discontinuities (on the order of 1-2 radians) were found in the preprocessed data, which were removed prior to detrending by shifting the 168-second data segments up or down to

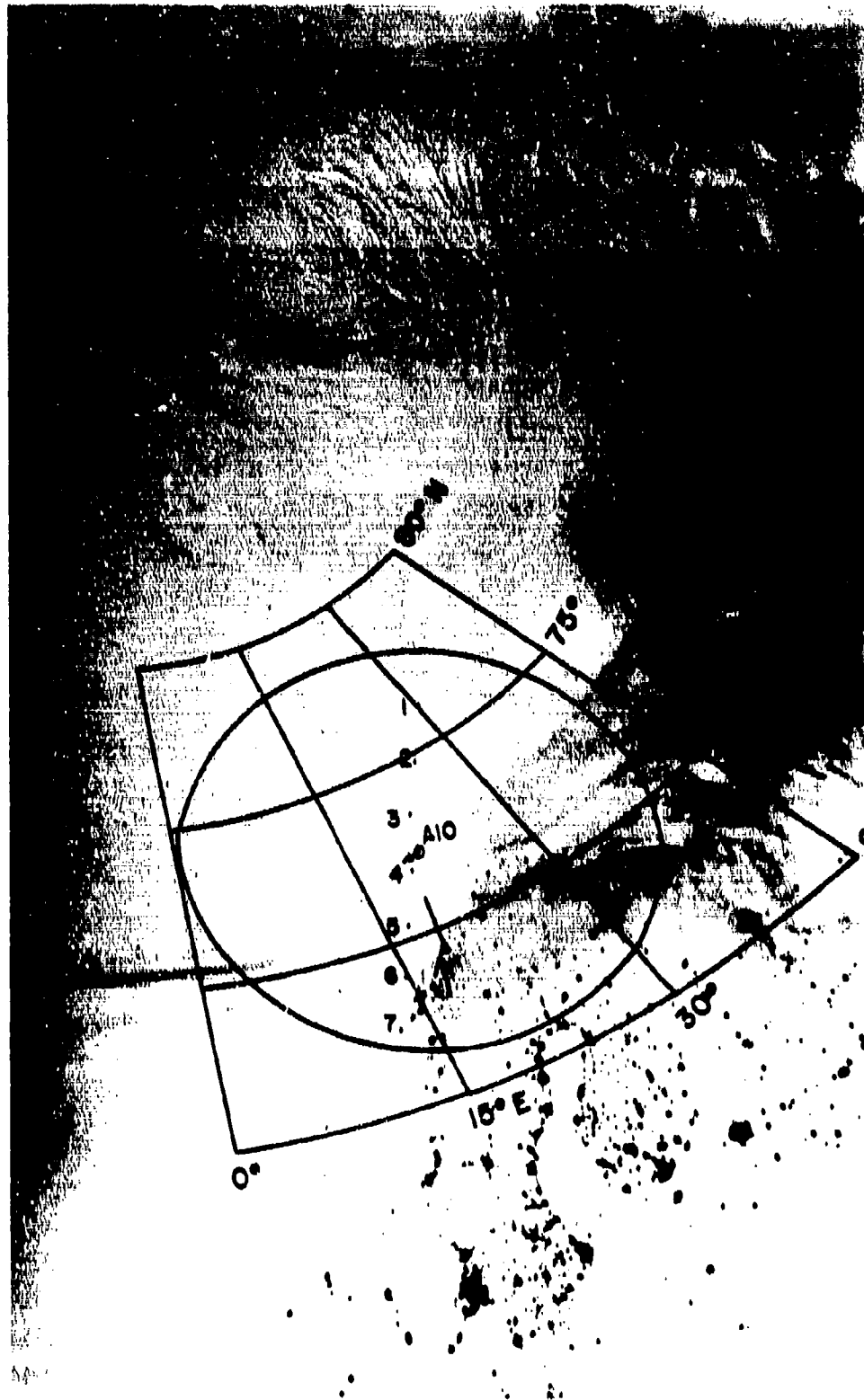


Figure 1. Negative of imagery from the DMSP F8 satellite OLS sensor for Rev 2862 on 8 Jan 88. The numbered points identify 300km field-line "footprints" of the DMSP satellite at 30-second intervals. The dot labeled "AIO" indicates the location of the AIO aircraft at 18:39 GMT, and the arrow points to the 300km ionospheric penetration point (IPP) of the AIO-AFSAT radio link.

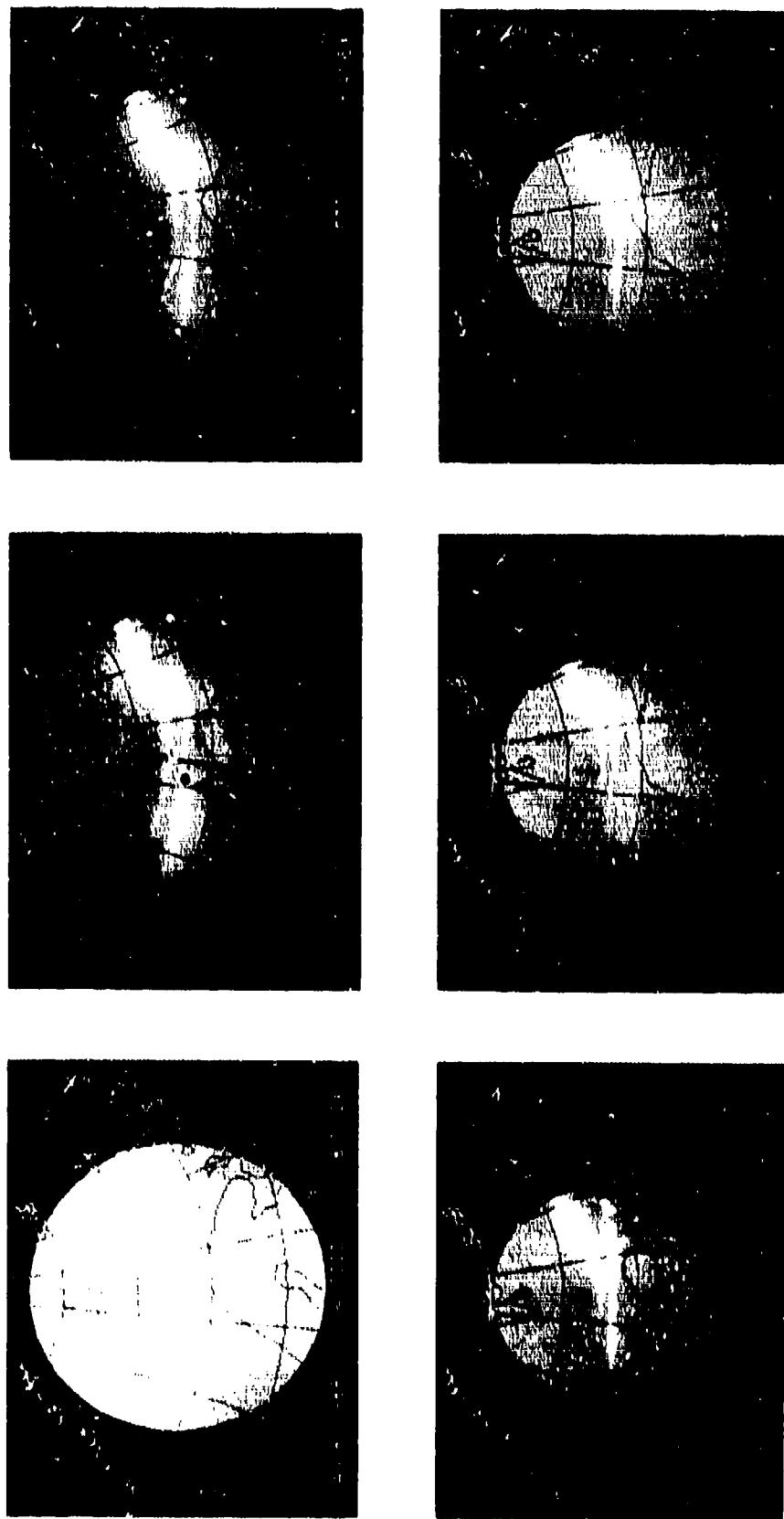


Figure 2. Imagery from the AIO all-sky photometer taken at 18:37:12, 18:39:30, and 18:41:30 GMT on 8 Jan 88. The upper images are at a wavelength of 6300 Å, and the lower images are at 4278 Å. The locations of the DMSP footprints and the AIO-AFSAT IPP shown in Figure 1 are plotted on the 6300 Å image taken at 18:39:30 GMT. The coordinate-grid overlay is geographic latitude and longitude.

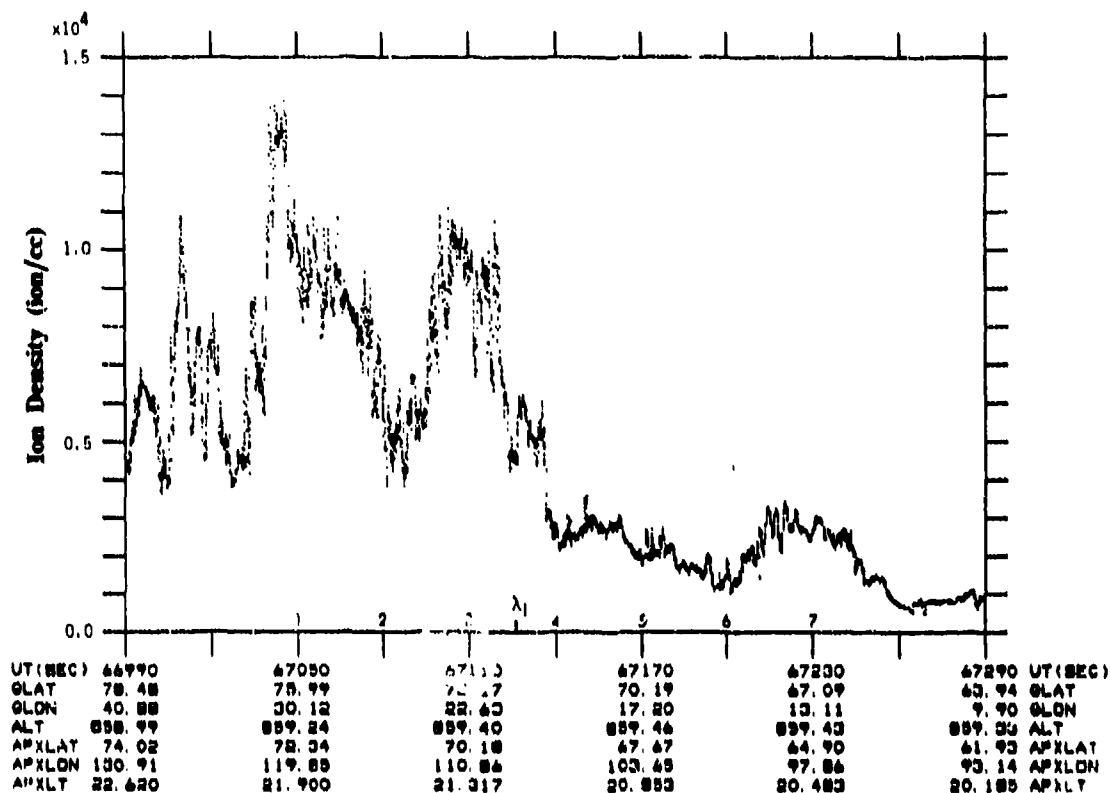


Figure 3. Total ion density data from the DMSP Scintillation Meter (SM) instrument from DMSP Rev 2862 on 8 Jan 88. The times labeled 1-7 correspond to the locations indicated in Figures 1 and 2 as DMSP footprint locations. The time marked with a  $\lambda_1$  indicates the time at which the DMSP footprint was at the same apex latitude ( $\lambda_1$ ) at the same time as the AIO-AFSAT IPP.

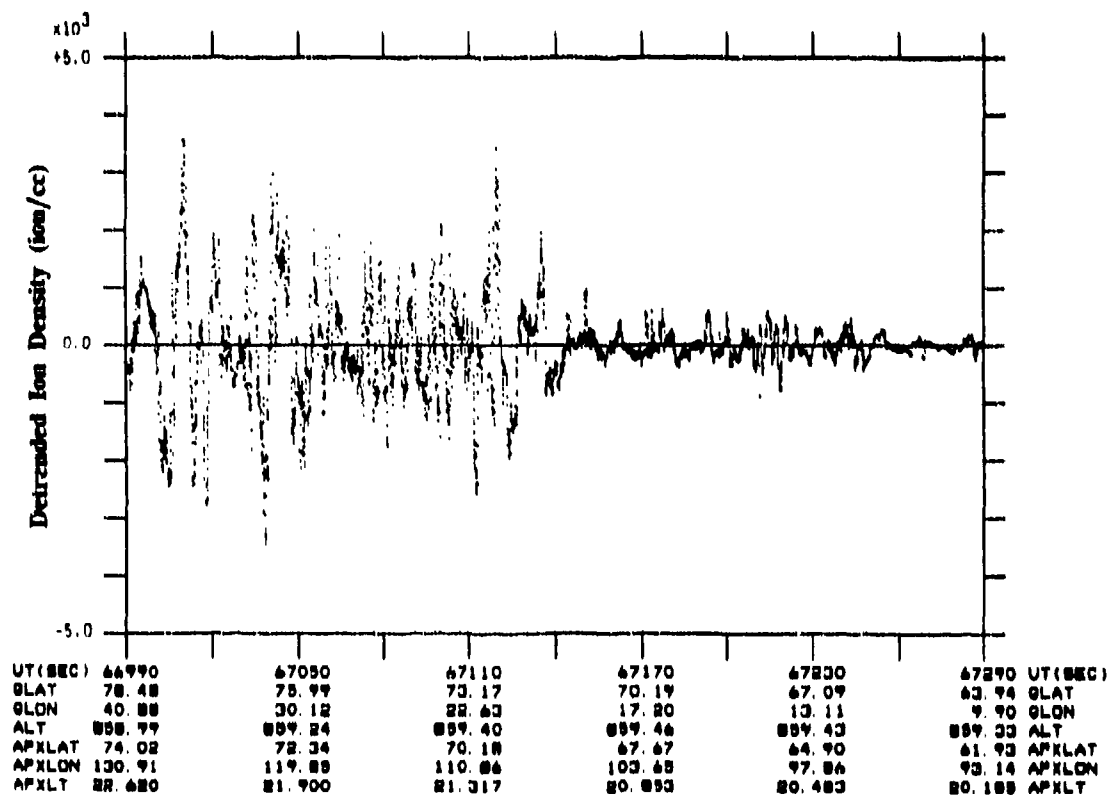


Figure 4. The density data from Figure 3 detrended by removing the output from a 6-pole, low-pass Butterworth filter with a cutoff frequency of 0.0469 Hz.

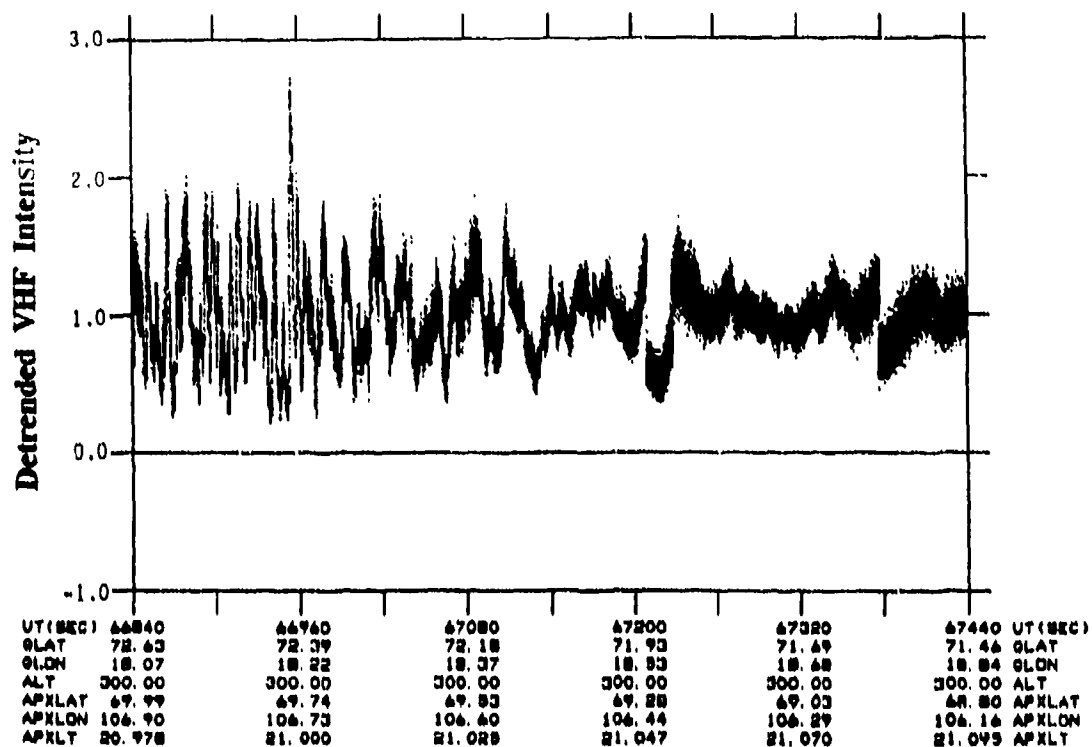


Figure 5. Signal intensity data from the AIO-AFSAT VHF radio link from 8 Jan 88. The data have been detrended using the same procedure as that used in detrending the density data in Figure 4 except with a 0.01 Hz cutoff frequency.

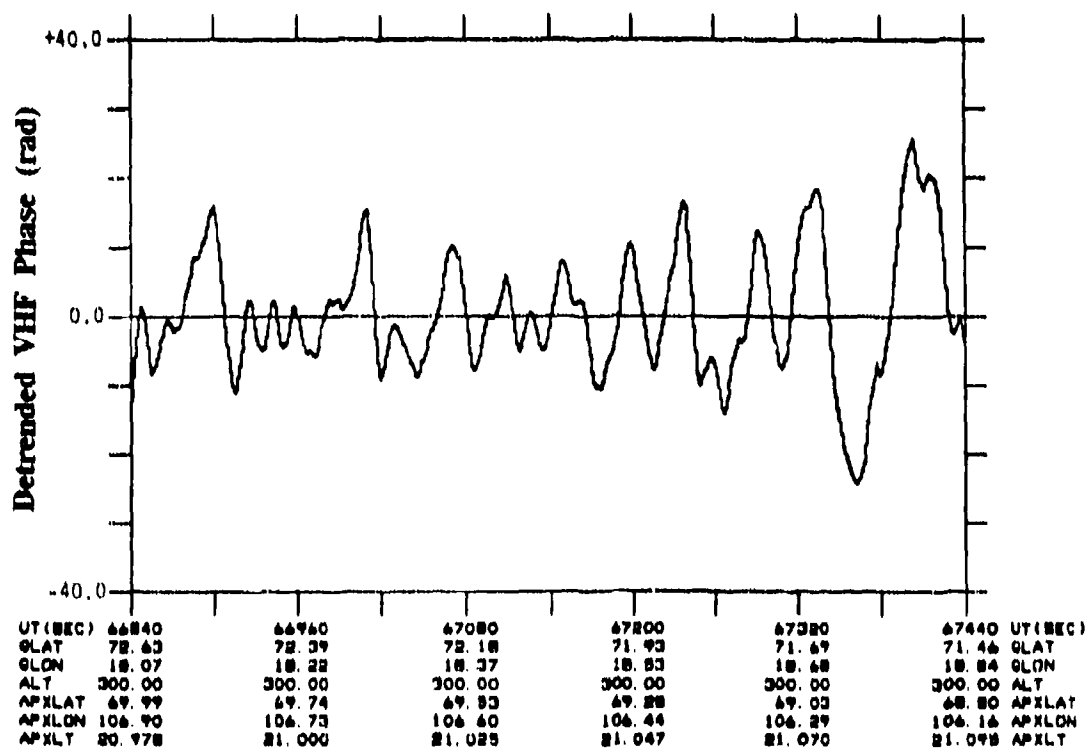


Figure 6. Signal phase data from the AIO-AFSAT VHF radio link from 8 Jan 88. The data have been detrended as described in Figure 5.

remove the discontinuities at the retune boundaries. The data interval shown in these plots covers an entire southbound leg flown by the AIO aircraft and is bounded by a 180° northward-to-southward turn from 18:30 to 18:33 GMT and a 40° turn to the southwest from 18:46 to 18:48 GMT.

The first order of business in attempting to compare the DMSP density data and the AIO-AFSAT propagation data is to determine the time period for comparison. Figure 7 shows the location of the DMSP 300km FLP at 3-second intervals during the time period 18:38:34 to 18:39:04 (squares) and the location of the AIO-AFSAT 300km IPP at one-minute intervals during the time period 18:34:00 to 18:44:00 (circles), plotted in apex coordinates. The DMSP 300km FLP and the AIO-AFSAT 300km IPP cross the same magnetic latitude (67.42°) at 18:39:49 (67129 seconds). Figures 8 and 9 are expanded plots of the SSIES SM density data and the detrended density data from Figures 3 and 4, covering the time period corresponding to the DMSP FLP location plot in Figure 7. The plots of the AIO-AFSAT intensity and phase data in Figures 5 and 6 cover the time period corresponding to the IPP location plot in Figure 7. The following analysis will focus on these data intervals.

### 3.2 Data Processing

#### 3.2.1 SSIES SM Data

The processing procedures used to generate estimates of scintillation parameters from the SSIES SM telemetry data are essentially as described in Report #2. The only changes are in the sample size used to generate the *in-situ* irregularity spectra and in the velocities used to calculate the phase-scintillation parameters. The sample size was decreased from 512 points to 256 points to increase the temporal/spatial resolution of the scintillation estimates. This had no effect on the remainder of the processing, as the range over which the log-log least-squares fit was made to estimate  $T_1$  and  $q$  is above the frequencies affected by decreasing the sample size.

There are three sources of motion in the experiment that must be accounted for: (1) the DMSP satellite orbital motion, (2) the motion of the 300km IPP (due to motion of the AIO aircraft and the AFSAT satellite orbital motion), and (3) the *in-situ* motion of the irregularities (both at the DMSP observation point and at the AIO-AFSAT IPP). Values for the first two are relatively easy to obtain, but the third is not readily available and is the source of most of the uncertainty in generating the phase scintillation parameters. The DMSP satellite velocity was derived directly from the satellite ephemeris, and the velocity of the AIO-AFSAT 300km IPP was calculated from the time rate-of-change of the locations of the IPP. The average velocity for the IPP used in the calculations was 230 m/s south and 140 m/s west in a coordinate system aligned with the geomagnetic field.

# AIO / DMSP Locations - 8 Jan 1988

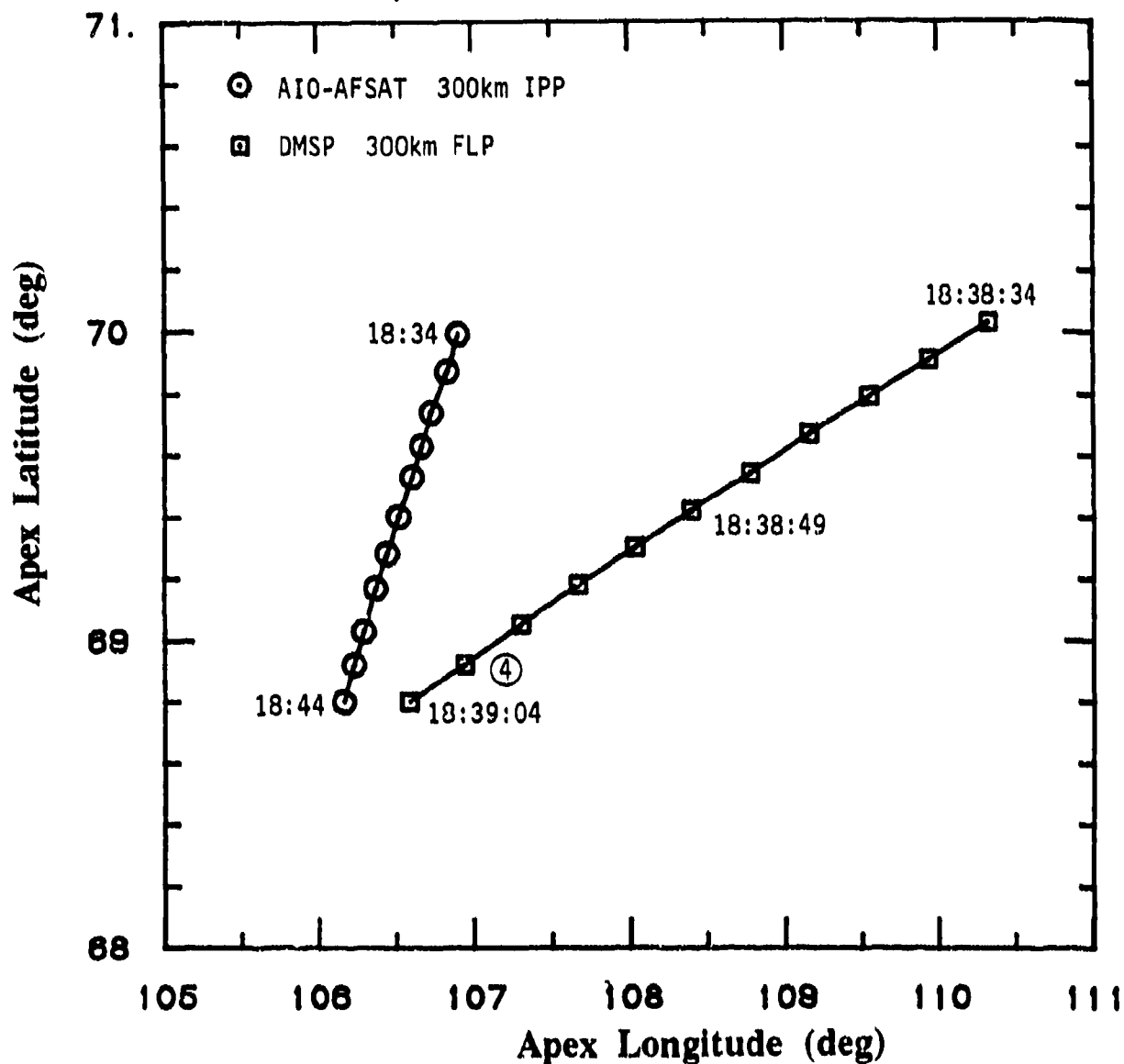


Figure 7. Experiment geometry for the 8 Jan 88 pass. The squares indicate the location of the 300km field-line footprint (FLP) of the DMSP satellite at 3-second intervals, and the circles indicate the location of the 300km ionospheric penetration point (IPP) of the AIO-AFSAT link at one-minute intervals. The DMSP FLP and AIO-AFSAT IPP are at the same latitude at the same time at 18:38:49. The coordinates of this plot are modified apex latitude and apex longitude.

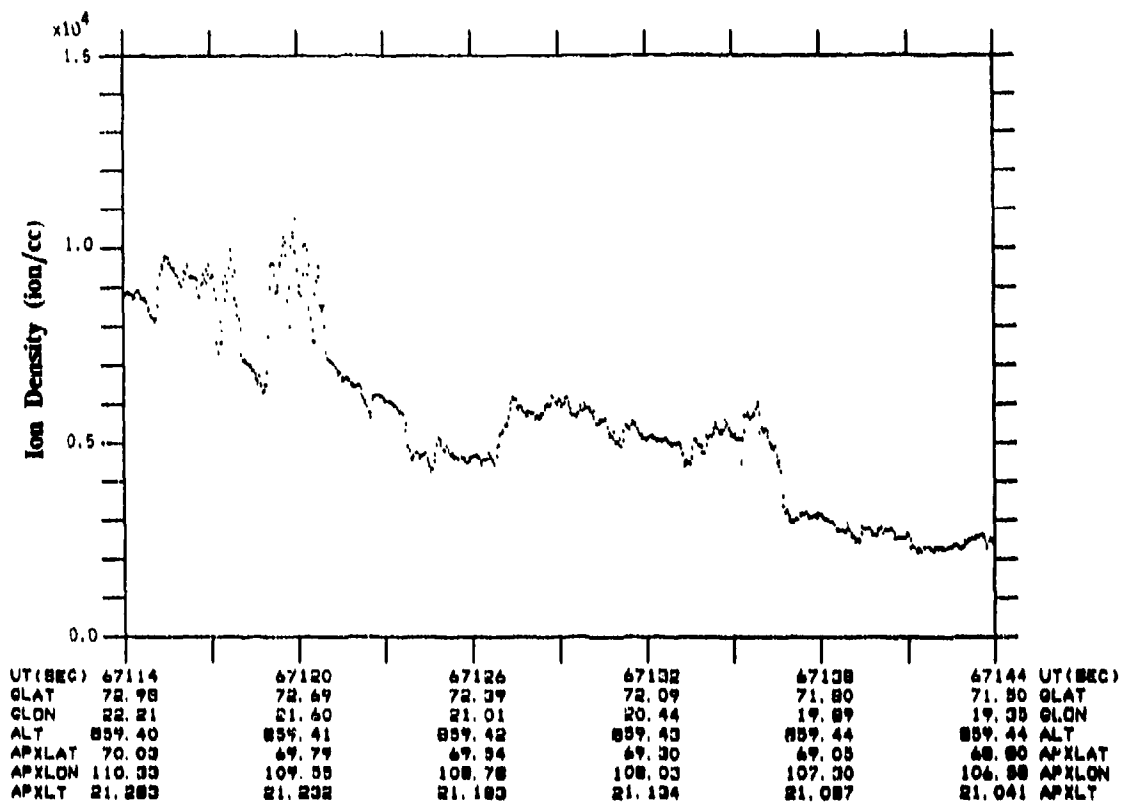


Figure 8. Total ion density from the DMSP SM instrument for the time interval defined in Figure 7. The tic marks along the abscissa correspond to the 3-second locations indicated in Figure 7.

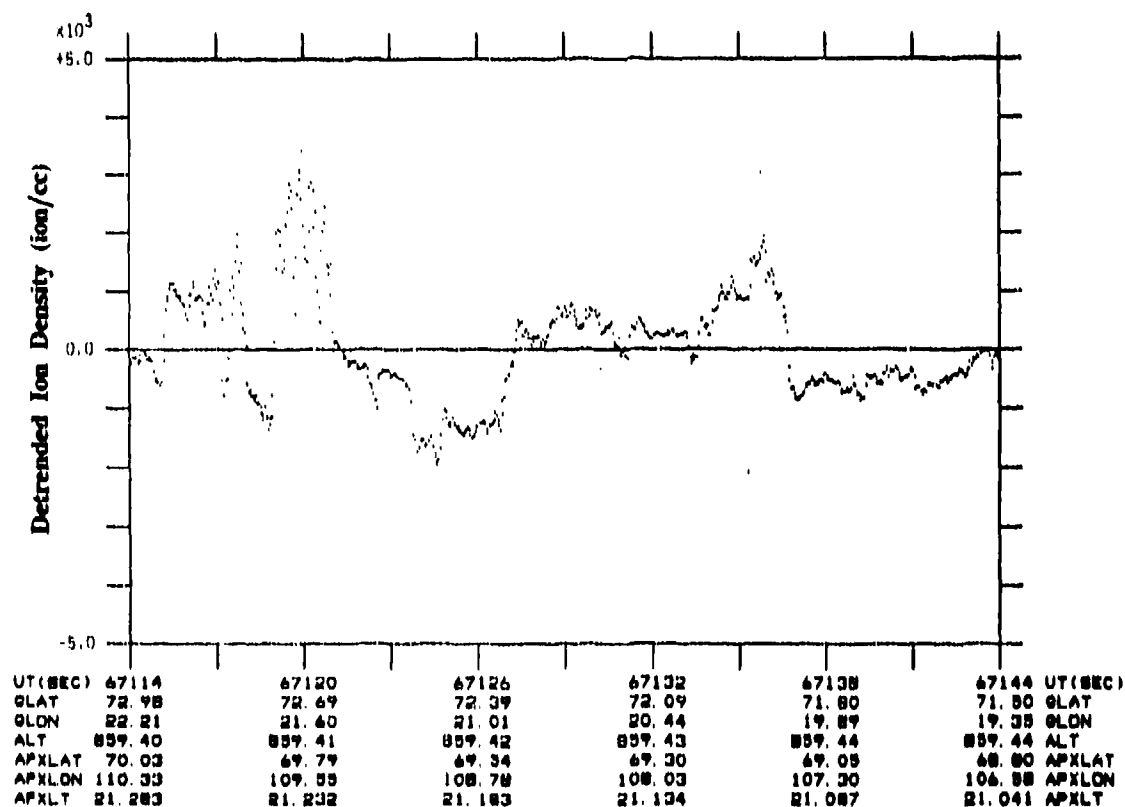


Figure 9. Data from Figure 8 detrended as described in Figure 4.

The velocities are used in calculating  $C_k$  from the  $T_1$  and  $q$  measurements taken from the *in-situ* irregularity spectra (requiring the DMSP velocity and the local *in-situ* velocity) and in calculating  $T$  (the 1Hz intercept of the phase spectrum) from the  $C_k L$  estimate (requiring the AIO-AFSAT IPP velocity and the *in-situ* velocity at the IPP). The orbital velocity of the DMSP satellite and the horizontal cross-track *in-situ* plasma velocity from the SSIES Drift Meter (DM) were used to calculate  $C_k$ . The ram-direction *in-situ* velocity was not available due to failure of the SSIES Retarding Potential Analyzer (RPA), which measures this parameter. The vertical velocity was very small with a large amount of scatter due to low plasma density, so it was set to zero in the calculation. In initial calculations of the phase scintillation parameters presented in Report #2, only the AIO-AFSAT IPP velocity was used (i.e., the *in-situ* velocity at the IPP was set to zero).

Two models were used for the axial ratios ( $a$  and  $b$ ) of the irregularities, parameters that are used to transform the various motions into an effective probe (or scan) velocity through the irregularity field. One model was for simple rod-shaped irregularities elongated along the magnetic field with  $a = 20$  and  $b = 1$ , and the second was taken from the WBMOD irregularity model<sup>(2,11)</sup>, which provided for "wing-shaped" irregularities with  $a = 17$  and  $b = 2$ . Both models were used to generate the  $C_k$  estimates from  $T_1$  and  $q$  and in generating phase scintillation parameters from  $C_k L$ . This provided an effective probe velocity of 7330 (6630) m/s for the DMSP satellite for 20:1 rods (17:2 wings), and an effective scan velocity of 260 (225) m/s for the AIO-AFSAT IPP. Table 1 lists the results of the  $C_k L$  calculation from the SSIES SM data for both the 20:1 rods and 17:2 wings cases. The effective layer thickness ( $L_{eff}$ ) was calculated using the method described in Report #2.

Table 1. Results of SSIES SM  $C_k L$  Calculations.

Time	$q$	$L_{eff}$	20:1 Rods		17:2 Wings	
			$C_k$	$C_k L$	$C_k$	$C_k L$
67115	2.54	$3.28 \times 10^7$	$4.42 \times 10^{24}$	$1.45 \times 10^{32}$	$5.21 \times 10^{24}$	$1.71 \times 10^{32}$
67120	2.07	$3.39 \times 10^7$	$1.14 \times 10^{25}$	$3.78 \times 10^{32}$	$1.24 \times 10^{25}$	$4.21 \times 10^{32}$
67125	2.03	$3.55 \times 10^7$	$2.97 \times 10^{24}$	$1.05 \times 10^{32}$	$3.30 \times 10^{24}$	$1.17 \times 10^{32}$
67130	2.25	$3.71 \times 10^7$	$8.83 \times 10^{23}$	$3.27 \times 10^{31}$	$1.00 \times 10^{24}$	$3.71 \times 10^{31}$
67135	2.16	$3.87 \times 10^7$	$1.32 \times 10^{24}$	$5.11 \times 10^{31}$	$1.48 \times 10^{24}$	$5.74 \times 10^{31}$
67140	2.25	$4.13 \times 10^7$	$8.51 \times 10^{23}$	$3.51 \times 10^{31}$	$9.59 \times 10^{23}$	$3.96 \times 10^{31}$

### 3.2.2 AIO-AFSAT Scintillation Data

The AIO-AFSAT intensity and phase data were detrended using a 6-pole Butterworth low-pass filter with a cutoff at 0.01Hz (100 seconds) and were resampled from the original 100Hz sample rate to 20Hz. The resampling was accomplished by averaging five samples centered on the resample time and was done to shift the spatial/temporal range permitted by a 4096-point FFT to larger scale-sizes/lower frequencies. Estimates of the intensity scintillation parameter ( $S_4$ ) were calculated in the time domain from 50-second data samples selected at 50-second intervals, and estimates of the phase scintillation parameter ( $\sigma_\phi$ ) were calculated in similar fashion from the detrended phase data.

Estimates of the phase spectral slope ( $p$ ) and power at 1Hz ( $T$ ) were calculated using a procedure similar to that used to calculate  $T_1$  and  $q$  from the DMSP SM data. Data samples of 4096 points (204.8 seconds) were selected at 100-second intervals, windowed with a 30% split-bell cosine taper, and the resulting PDS was smoothed with a 5-point binomial-weight smoother. Parameters  $T$  and  $p$  were then obtained from a linear least-squares fit in  $\log(\text{PDS}) - \log(\text{frequency})$  over a specified frequency range. The selection of the range for this fit was based on the desire to fit the AIO-AFSAT data over the same range of scale sizes as in the fits to the SM data. To do this, the range used in the SM data must be multiplied by the ratio of the effective velocity of the AIO-AFSAT IPP to that of the DMSP satellite. This provided an initial fit range of 0.015 to 0.092 Hz. The effective scan velocity,  $v_e$ , used in the initial calculations includes only the scan velocity due to the relative motions of the aircraft and satellite.

### 3.3 Data Comparisons

#### 3.3.1 Intensity Scintillation

Figure 10 shows the comparison between  $S_4$  calculated from the AIO-AFSAT intensity data (solid line) with estimates of  $S_4$  calculated from the  $C_kL$  and  $q$  data from Table 1 for two different irregularity geometries (diamonds for 20:1 rods, squares for 17:2 wings) and calculated from the WBMOD model using only the standard inputs of date, time, SSN, and  $K_p$  (crosses). The points on the AIO-AFSAT curve labeled "retune" indicate  $S_4$  estimates that have been noticeably contaminated by sharp discontinuities in the intensity record at receiver retune times, and the local peak at 18:38:30 labeled "focus" indicates an  $S_4$  estimate that is dominated by a single strong feature that has the signature of a sharp focus rather than that of a scatter effect.

The agreement between the observed  $S_4$  and the estimates calculated from the SSIES observations is excellent, particularly in light of the many assumptions made in generating the SSIES  $S_4$  estimates. The agreement between the SSIES  $S_4$  values generated using the 17:2 WBMOD model value for the irregularity axial ratios is slightly better than

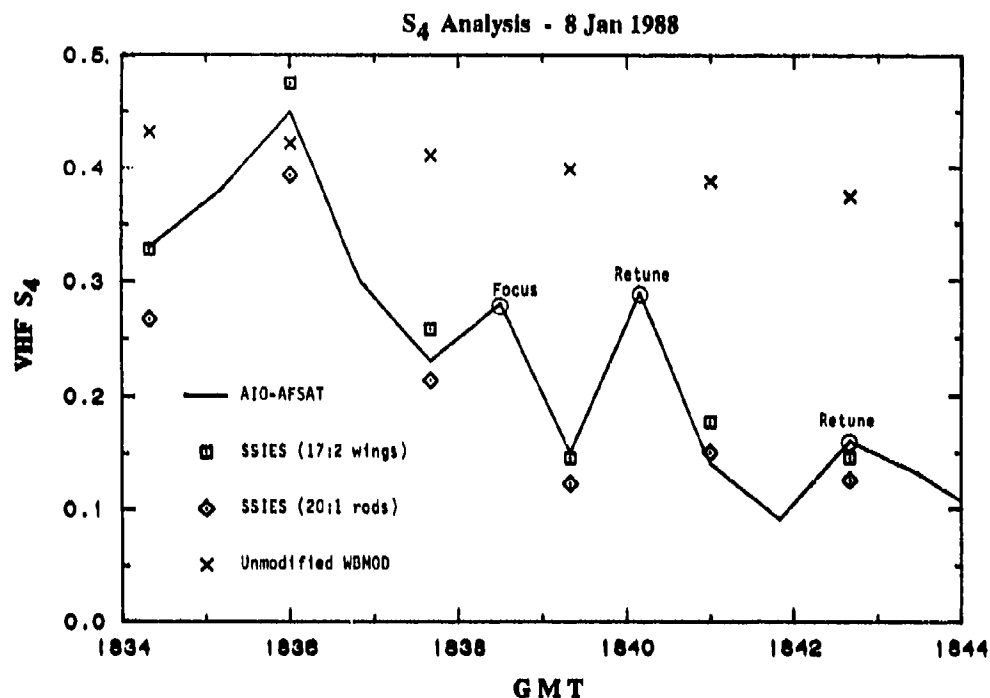


Figure 10. Comparison of  $S_4$  calculated from the AIO-AFSAT intensity record shown in Figure 5 (solid line) to  $S_4$  calculated from the SSIES  $C_k L$  estimates for two irregularity models (17:2 wings - squares; 20:1 rods - diamonds) and from the WBMOD model (crosses). The two AIO-AFSAT points labeled "retune" included retune-discontinuities, and the point labeled "focus" contained a strong focus. The  $S_4$  values for these three points are unreliable.

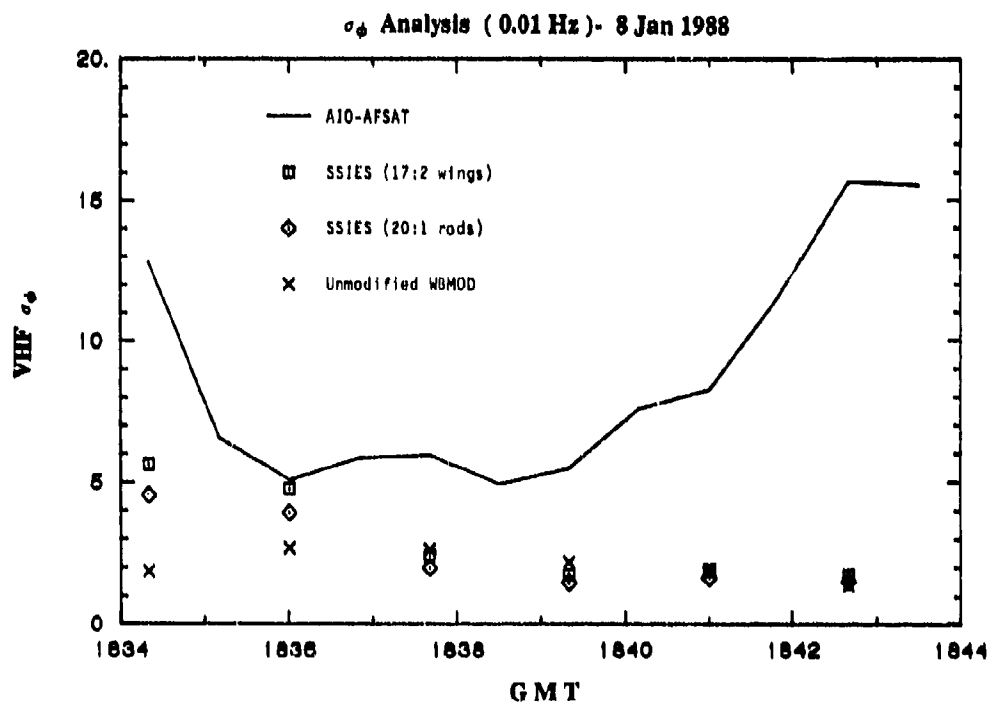


Figure 11. Comparison of  $\sigma_\phi$  calculated from the AIO-AFSAT phase record shown in Figure 6 (solid line) to  $\sigma_\phi$  calculated from the SSIES  $C_k L$  estimates for two irregularity models (17:2 wings - squares; 20:1 rods - diamonds) and from the WBMOD model (crosses).

for the simple 20:1 rods, but only enough to indicate that if one assumes that all other factors are correct, the irregularities tend to be more wing-like in shape than rod-like.

### 3.3.2 Phase Scintillation

After the good match between the estimated and observed  $S_4$  values, the first look at the phase-scintillation results were very disappointing. Figure 11 shows a comparison for the  $\sigma_\phi$  parameter similar to that shown in Figure 10 for  $S_4$ . With the exception of the points at 18:36, all estimates from the SM data are low by more than a factor of 2, and the better agreement at 18:36 is probably more coincidental than real. The agreement between the values for T and p calculated from the SM data and those calculated from the AIO-AFSAT data was no better. Table 2 lists p, T, and  $\sigma_\phi$  calculated from the SM data and derived from the 100-second detrended AIO-AFSAT phase data. It is obvious from this

Table 2. Phase scintillation parameters from the SM and AIO-AFSAT data sets (100s detrend; 17:2 wings).

GMT	p		$v_e$	T		$\sigma_\phi$	
	DMSP	AIO		DMSP	AIO	DMSP	AIO
66960	3.07	6.84	228	$1.72 \times 10^{-3}$	$1.89 \times 10^{-7}$	4.72	5.07
67060	3.03	7.58	227	$4.94 \times 10^{-4}$	$1.15 \times 10^{-8}$	2.36	5.92
67160	3.25	7.07	226	$1.05 \times 10^{-4}$	$6.04 \times 10^{-8}$	1.74	5.46
67260	3.16	6.88	224	$1.84 \times 10^{-4}$	$2.19 \times 10^{-7}$	1.90	8.26
67360	3.25	7.62	223	$1.06 \times 10^{-4}$	$8.99 \times 10^{-9}$	1.74	15.65
			m/s				rad

table that there is something amiss. We were expecting problems due to uncertainty in the velocities, but the results indicate that the velocity should be adjusted in one direction to obtain a better fit to the observed  $\sigma_\phi$  values and in the other direction for a better fit to T. [Note: No comparison is given in Table 2, or in the following tables, between the AIO-AFSAT phase-data set centered at time 66860 and the corresponding DMSP data set as the phase-data set at this time contains severe contamination from aircraft motion at the end of a turn from north to south.]

The clue to this problem is in the large values for the phase spectral slope, p, obtained from the phase data. Data collected over a three-year period from the HiLat and Polar BEAR satellites at Tromso, Norway, indicated that the average value for this slope at the scale sizes of interest here (a few kilometers) should be around 2.75 with a standard deviation of about 0.5. This would place all of the AIO-AFSAT values for p eight to ten

standard deviations above the average, while the estimates from the SM data are just one standard deviation or less above the average.

Figure 12 contains the PDS derived from the AIO-AFSAT phase data sample centered at 67160 seconds (18:39:20 GMT). The dotted line over the AIO-AFSAT PDS shows the fit from which  $T$  and  $p$  were extracted, and the dashed line over the lower portion of this PDS is from a fit over a frequency range of 0.1 to 1.0 Hz. The slope of this second fit is 3.41, much closer to both the  $p$  derived from the *in-situ* data (3.25) and to the average value from the HiLat/Polar BEAR data set. There appears to be a great deal of low-frequency phase noise in the AIO-AFSAT data, starting at about 0.1 Hz (10 seconds).

A second indication that there is contamination in the phase data can be found in qualitative comparison of the intensity and phase records plotted in Figures 5 and 6. With some minor exceptions, there is little correlation between the gross features in these two records. The intensity record shows an initially disturbed propagation environment which gradually transitions to a mostly undisturbed environment. If anything, the phase record shows the opposite.

The source of this noise, if that is indeed what it is, is uncertain. Previous studies<sup>[12]</sup> have found that aircraft motions will introduce phase noise at low frequencies, but at time scales on the order of minutes rather than tens of seconds. In detrending the phase data at progressively shorter detrender cutoff times, we may have identified one potential source. Figure 13 shows the AIO-AFSAT phase data detrended with a cutoff of 0.05 Hz (20 seconds). Again, there is little apparent correlation with the intensity record, but a very suggestive signature has appeared. This record looks very much like a classic "beat" pattern generated by the sum of two signals with slightly differing frequencies. Since the AIO-AFSAT phase data are generated using a local oscillator to synthesize the phase reference, a slight difference between the frequency of the local oscillator and the AFSAT transmitter could result in addition of phase noise from this sort of beat pattern. Such a difference could easily arise from any number of different sources, and could be exacerbated by the automatic frequency shifts in the AFSAT transmissions at 168-second intervals. A possible geophysical source could be scintillation from large-scale features in the auroral E region, which is speculated to cause a steepening of the low-frequency end of phase spectra in data from the various DNA beacon satellites<sup>[13]</sup>. However, the slopes shown in Table 2 are steeper than those reported from the DNA satellites (on the order of 5.0).

After some experimentation with various detrender cutoff frequencies, we decided to use a cutoff of 0.075 Hz ( $13\frac{1}{3}$  seconds) for calculating  $\sigma_\phi$  and to derive  $T$  and  $p$  from a fit to the phase PDS over the frequency range 0.1 to 1.0 Hz. Figure 14 shows the AIO-AFSAT phase for the time period under analysis detrended at 0.075 Hz, and Figure 15 shows the comparison of  $\sigma_\phi$  calculated from the AIO-AFSAT data detrended at 0.075 Hz and that calculated from the SM data and from WBMOD. It is still difficult to correlate qualitatively the phase record in Figure 14 to the intensity record in Figure 3, but the  $\sigma_\phi$  record in Figure 15 is now behaving in roughly similar fashion to the  $S_4$  record in Figure 10.

# Phase Spectrum ( 8 Jan 1988 , 67160 )

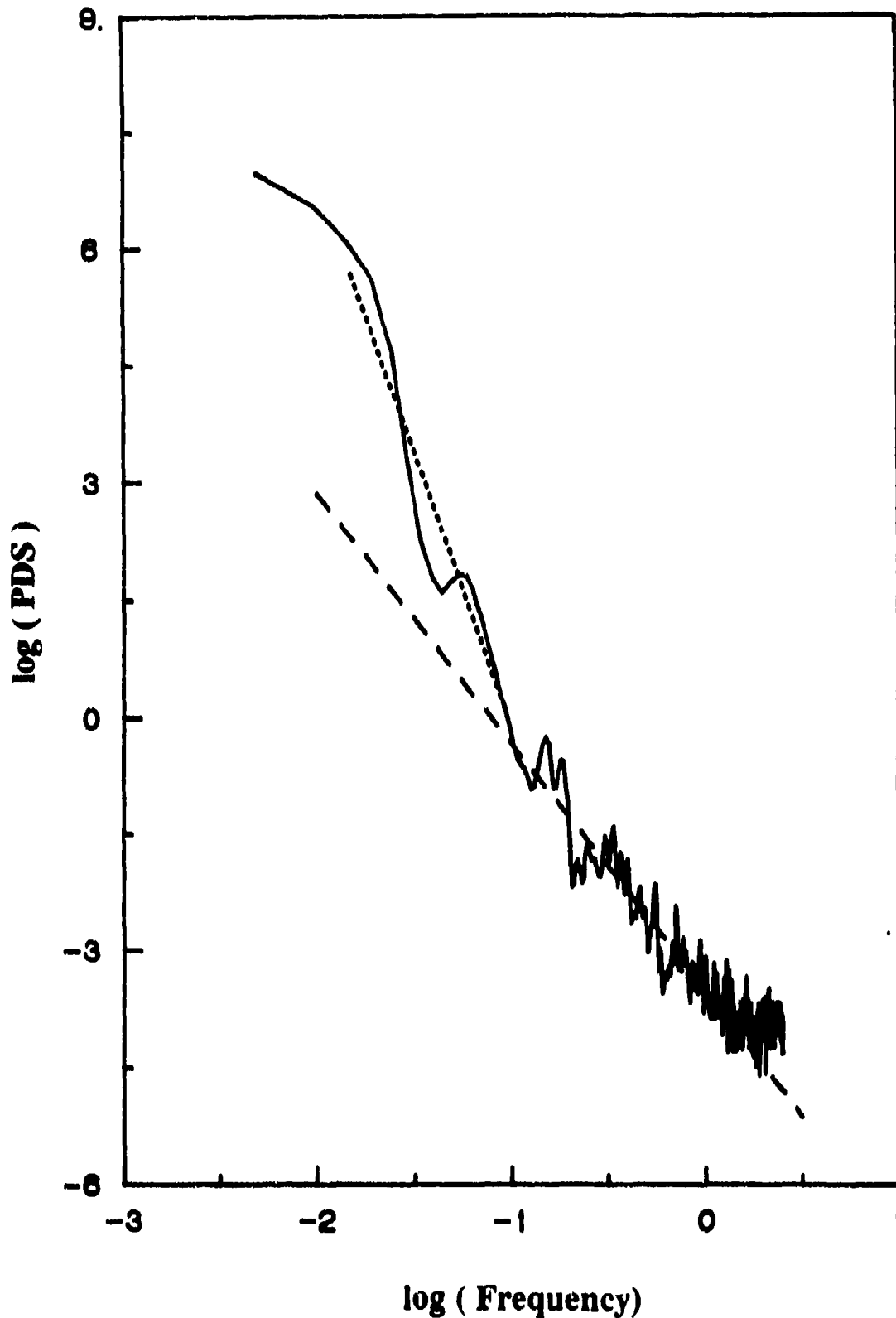


Figure 12. Power density spectrum (PDS) of phase, detrended by end-matching and removing the residual mean, for a 4096-point data sample (204.8 seconds) centered at 67160 seconds. The dotted line is a linear fit to  $\log(PDS)$  and  $\log(f)$  over the range 0.015 Hz to 0.092 Hz, and the dashed line is a linear fit over the range 0.1 to 1.0 Hz.

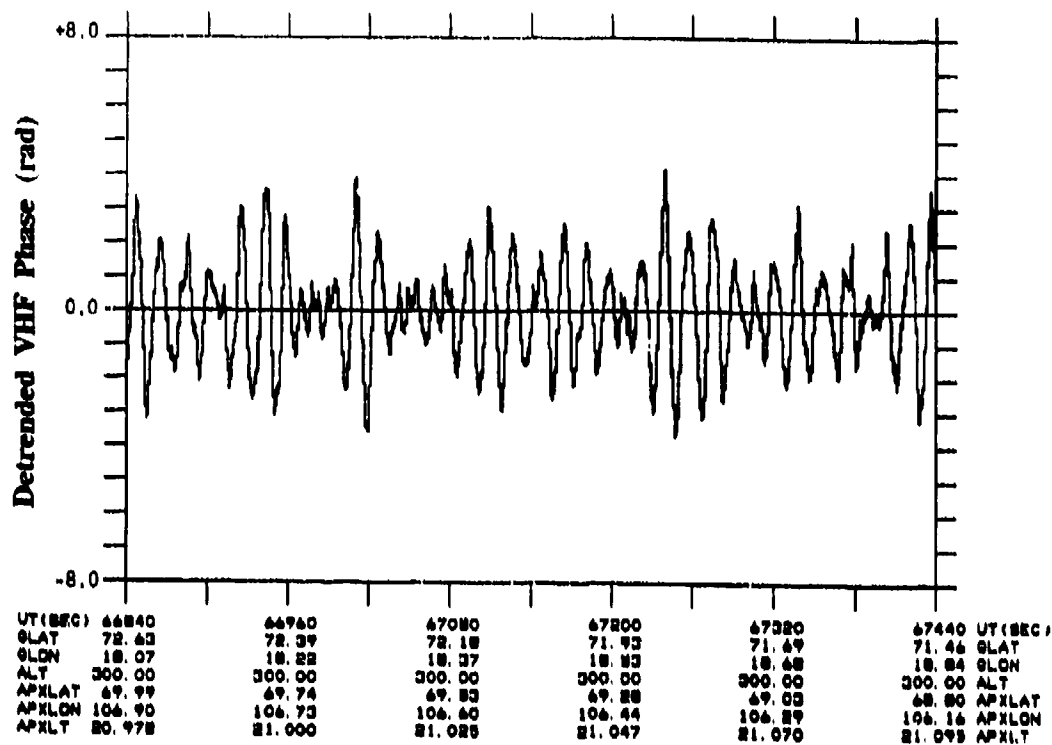


Figure 13. AIO-AFSAT phase record detrended with a 0.05 Hz cutoff frequency.

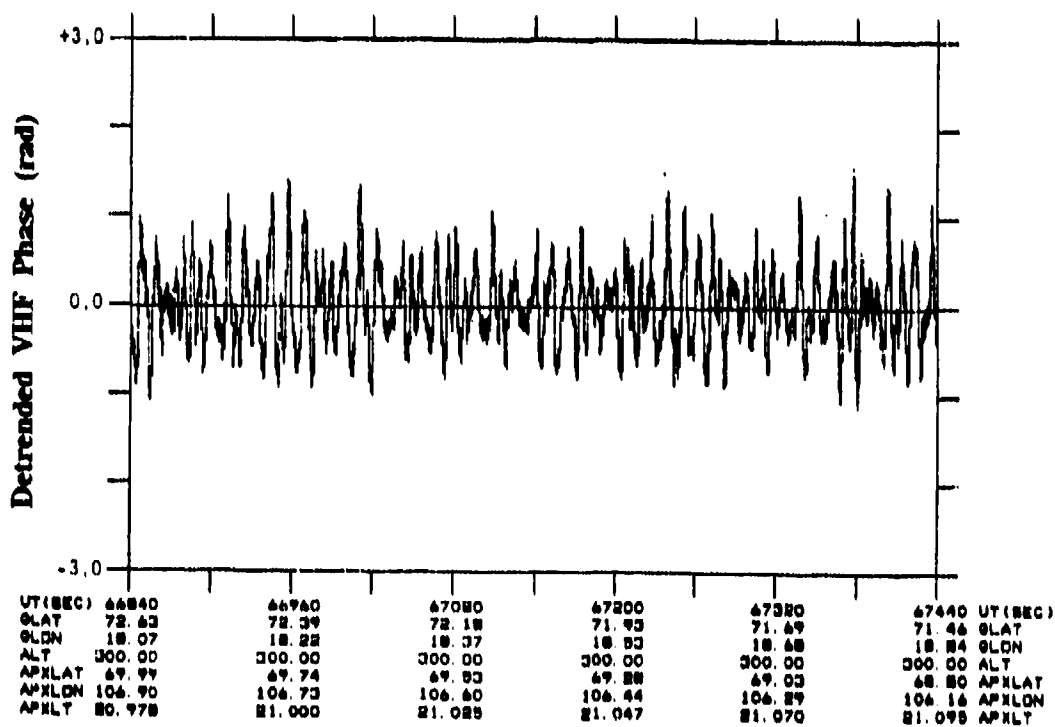


Figure 14. AIO-AFSAT phase record detrended with a 0.075 Hz cutoff frequency.

$\sigma_\phi$  Analysis (0.075 Hz) - 8 Jan 1988

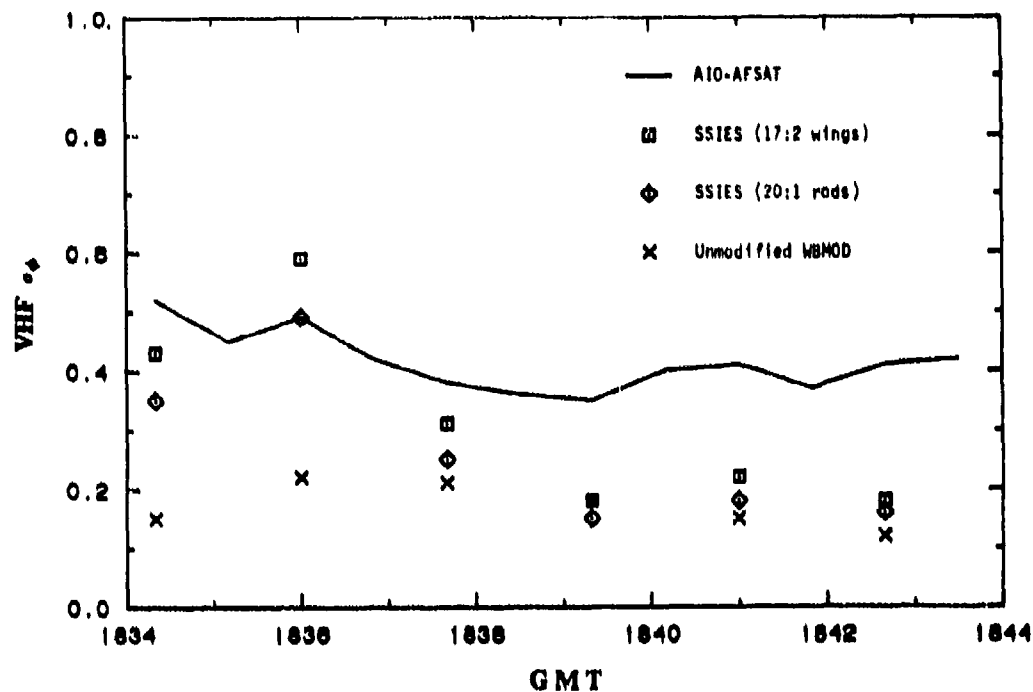


Figure 15. Comparison of  $\sigma_\phi$  calculated from the AIO-AFSAT phase record shown in Figure 14 (solid line) to  $\sigma_\phi$  calculated from the SSIES  $C_{\phi L}$  estimates for two Irregularity models (17:2 wings - squares; 20:1 rods - diamonds) and from the WBMOD model (crosses).

Table 3. Phase scintillation parameters from the SM and AIO-AFSAT data sets (13-1/3s detrend; 17:2 wings).

GMT	p		$v_e$	T		$\sigma_\phi$	
	DMSP	AIO		DMSP	AIO	DMSP	AIO
66960	3.07	3.22	228	$1.72 \times 10^{-3}$	$4.08 \times 10^{-4}$	0.59	0.46
67060	3.03	3.21	227	$4.94 \times 10^{-4}$	$3.03 \times 10^{-4}$	0.31	0.36
67160	3.25	3.41	226	$1.05 \times 10^{-4}$	$2.03 \times 10^{-4}$	0.18	0.36
67260	3.16	3.43	224	$1.84 \times 10^{-4}$	$2.04 \times 10^{-4}$	0.22	0.39
67360	3.25	3.70	223	$1.06 \times 10^{-4}$	$1.97 \times 10^{-4}$	0.18	0.40
			m/s				rad

The match with the  $\sigma_\phi$  values calculated from the SM data is still, however, not nearly as good as that between the two  $S_4$  calculations.

Table 3 presents a comparison of the new results to the calculations from the SM data. While there is still general disagreement between the two data sets, they are in much closer agreement than before, and the AIO-AFSAT results look far more reasonable than those presented in Table 2. In particular, the phase spectral slopes from the AIO-AFSAT data are more in line with both the *in-situ* results and those obtained from the HiLat/Polar BEAR experiments, and (with one exception) the adjustments required to bring the T and  $\sigma_\phi$  values into agreement are now in the same direction.

In all phase calculations to this point, it was assumed that the *in-situ* drift velocity at the AIO-AFSAT IPP was zero. As we have no direct measure of this, we will use this velocity as a free parameter which will allow us to adjust the effective scan velocity,  $v_e$ , to bring the various phase parameters generated from the SM density data into line with those generated from the AIO-AFSAT phase data. This will be done for three measures of the phase scintillation: T,  $\sigma_\phi$ , and the PDS.

The power-law phase-screen equation used to calculate T from  $C_k L$  is

$$T = N(\lambda, q) \sec\theta C_k L v_e^q \quad [1]$$

where  $N(\lambda, q)$  is a normalization function of the wavelength ( $\lambda$ ) and *in-situ* spectral slope ( $q$ ), and  $\theta$  is the angle between the local nadir and the line-of-sight propagation direction at the IPP. If we need to calculate the effective velocity required to adjust a previously calculated T to an observed value for T, Equation [1] can be used to generate the following relationship:

$$v_e' = \left( \frac{T_{obs}}{T_{calc}} \right)^{1/q} v_e \quad [2]$$

Since  $\sigma_\phi$  is proportional to the square-root of T, a similar equation can be generated for this parameter:

$$v_e' = \left( \frac{\sigma_{\phi obs}}{\sigma_{\phi calc}} \right)^{2/q} v_e \quad [3]$$

These equations were used to calculate the effective velocities required to match the T and  $\sigma_\phi$  values obtained from the AIO-AFSAT phase data using the  $C_k L$  estimates from the SM density data. Tables 4 and 5 present the results of these calculations. In both tables, T and

Table 4. Phase scintillation parameters from the SM and AIO-AFSAT data sets (13-1/3s detrend; 17:2 wings;  $v_e$  from T).

GMT	$v_e$	T		$\sigma_\phi$	
		DMSP	AIO	DMSP	AIO
66960	113	$4.08 \times 10^{-4}$	$4.08 \times 10^{-4}$	0.31	0.46
67060	178	$3.03 \times 10^{-4}$	$3.03 \times 10^{-4}$	0.26	0.36
67160	303	$2.03 \times 10^{-4}$	$2.03 \times 10^{-4}$	0.27	0.36
67260	235	$2.04 \times 10^{-4}$	$2.04 \times 10^{-4}$	0.24	0.39
67360	294	$1.97 \times 10^{-4}$	$1.97 \times 10^{-4}$	0.27	0.40
	m/s				rad

Table 5. Phase scintillation parameters from the SM and AIO-AFSAT data sets (13-1/3s detrend; 17:2 wings;  $v_e$  from  $\sigma_\phi$ ).

GMT	$v_e$	T		$\sigma_\phi$	
		DMSP	AIO	DMSP	AIO
66960	179	$9.42 \times 10^{-4}$	$4.08 \times 10^{-4}$	0.46	0.46
67060	263	$5.99 \times 10^{-4}$	$3.03 \times 10^{-4}$	0.36	0.36
67160	418	$3.72 \times 10^{-4}$	$2.03 \times 10^{-4}$	0.36	0.36
67260	381	$5.15 \times 10^{-4}$	$2.04 \times 10^{-4}$	0.39	0.39
67360	453	$4.65 \times 10^{-4}$	$1.97 \times 10^{-4}$	0.40	0.40
	m/s				rad

$\sigma_\phi$  are calculated from the SM  $C_k L$  estimates using the  $v_e$  value generated by either Equation [2] (Table 4) or [3] (Table 5).

The third comparison used to make an estimate of the effective scan velocity is between the *in-situ* density PDS from the SM density data and the phase PDS from the AIO-AFSAT phase data. The effective scan velocity can be used to change the PDS from a function of frequency (temporal variations) to a function of wavelength (spatial variations) by dividing the frequency scale by  $v_e$ . Therefore, the SM *in-situ* PDS can be "shifted" into the frequency domain of the corresponding AIO-AFSAT PDS by multiplying the frequency scale by the ratio of the AIO-AFSAT effective scan velocity to the DMSP effective probe velocity. Figures 16 through 20 show comparisons of the corresponding SM *in-situ* density

# **In-Situ and Phase Spectra - 67120 / 66960**

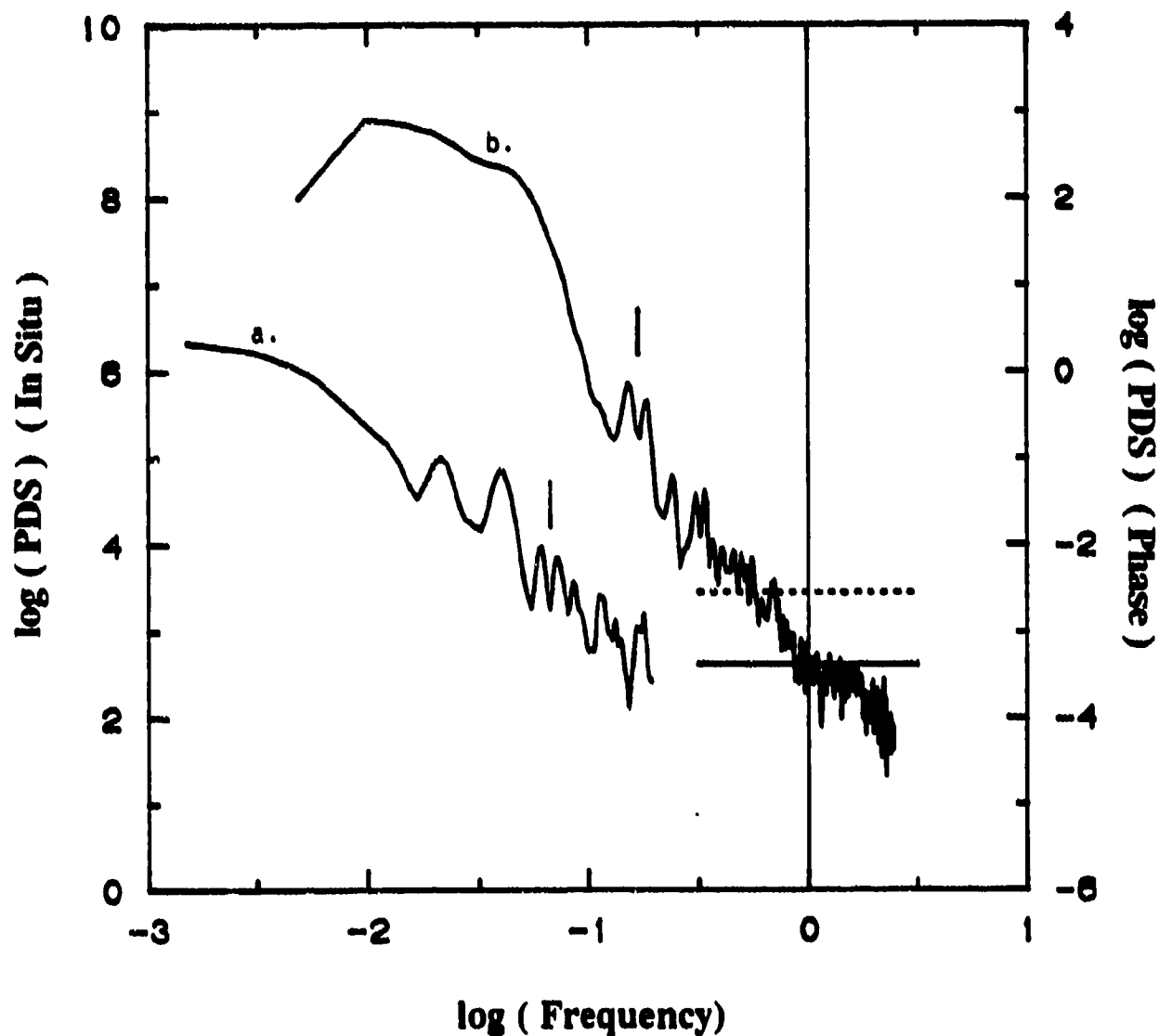


Figure 16. Power density spectra from (a) SM density data centered at 67120 (left ordinate scale) and (b) the AIO-AFSAT phase data (0.01 Hz detrend) centered at 66960 (right ordinate scale). The SM PDS has been shifted in log-frequency by -1.76 to compensate for the different effective scan velocities of the SM and AIO-AFSAT data sets. The short vertical bars indicate a potentially-common feature in the two spectra (see text). The horizontal solid bar indicates the value for T derived from the AIO-AFSAT phase spectrum (0.1 to 1.0 Hz fit), and the horizontal dotted line indicates a value for T derived from the SM density data using a 265 m/s effective scan velocity.

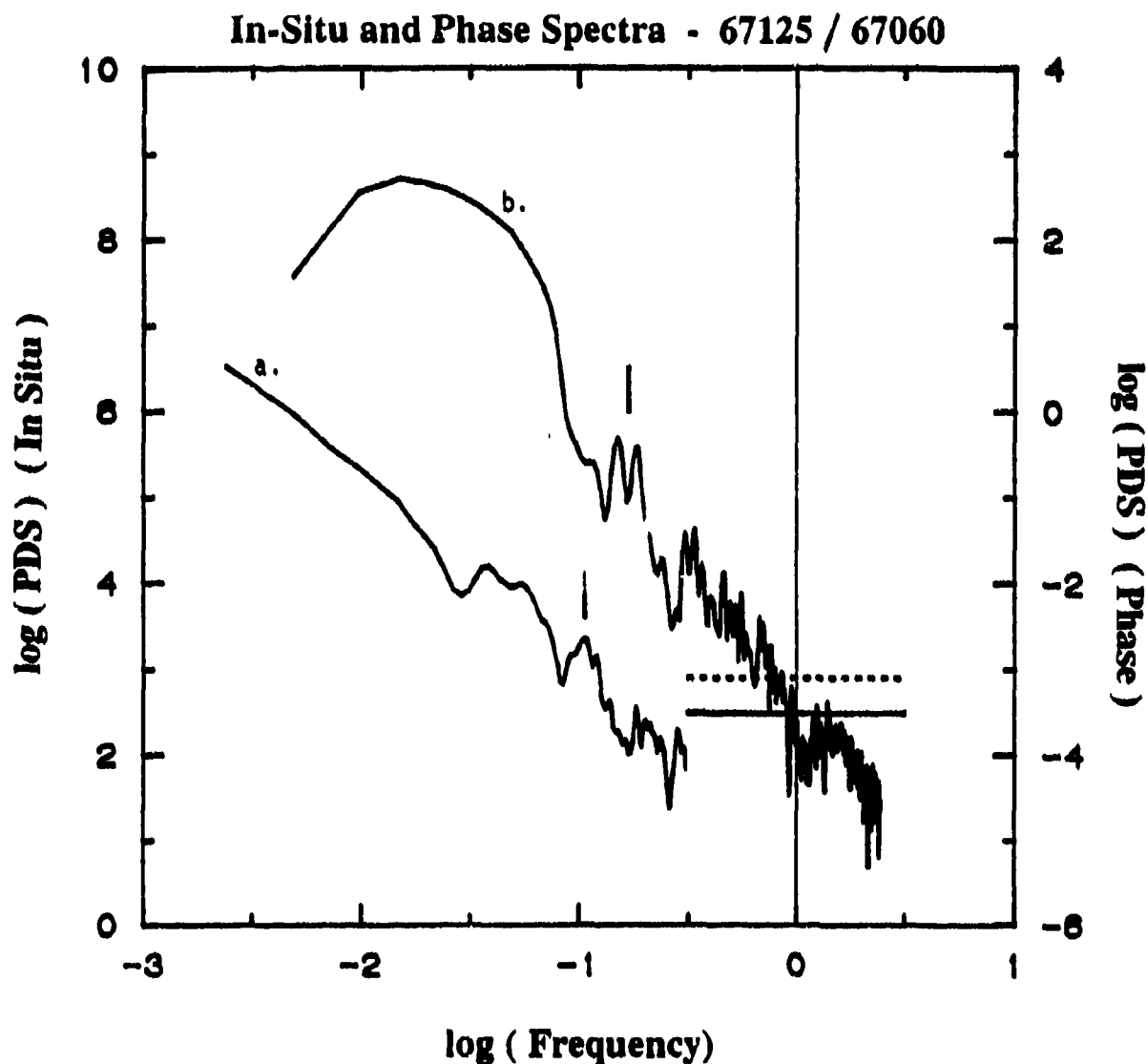


Figure 17. Power density spectra from (a) SM density data centered at 67125 (left ordinate scale) and (b) the AIO-AFSAT phase data (0.01 Hz detrend) centered at 67060 (right ordinate scale). The SM PDS has been shifted in log-frequency by -1.57 to compensate for the different effective scan velocities of the SM and AIO-AFSAT data sets. The short vertical bars indicate a potentially-common feature in the two spectra (see text). The horizontal solid bar indicates the value for T derived from the AIO-AFSAT phase spectrum (0.1 to 1.0 Hz fit), and the horizontal dotted line indicates a value for T derived from the SM density data using a 265 m/s effective scan velocity.

# In-Situ and Phase Spectra - 67130 / 67160

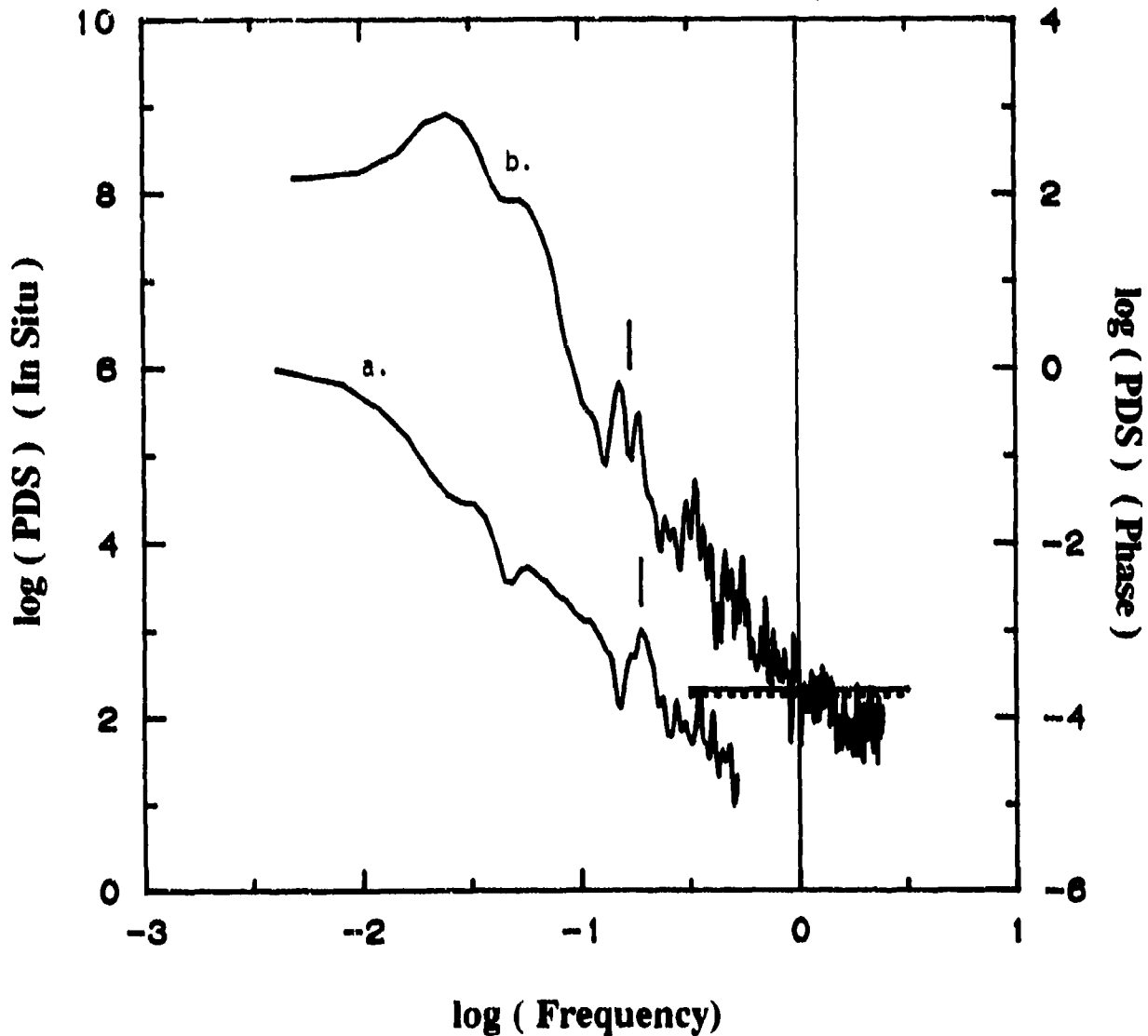


Figure 18. Power density spectra from (a) SM density data centered at 67130 (left ordinate scale) and (b) the AIO-AFSAT phase data (0.01 Hz detrend) centered at 67160 (right ordinate scale). The SM PDS has been shifted in log-frequency by -1.34 to compensate for the different effective scan velocities of the SM and AIO-AFSAT data sets. The short vertical bars indicate a potentially-common feature in the two spectra (see text). The horizontal solid bar indicates the value for T derived from the AIO-AFSAT phase spectrum (0.1 to 1.0 Hz fit), and the horizontal dotted line indicates a value for T derived from the SM density data using a 265 m/s effective scan velocity.

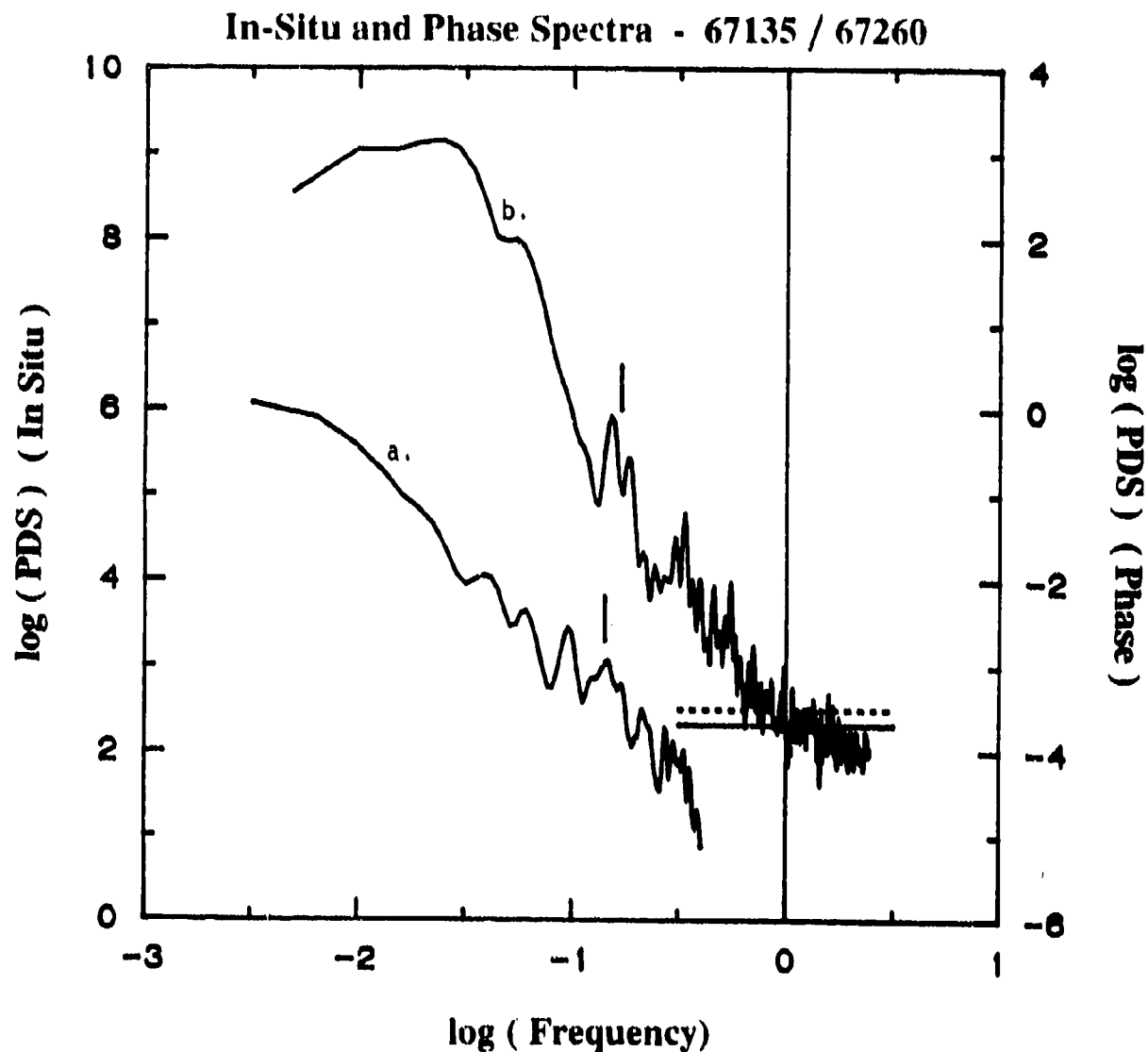


Figure 19. Power density spectra from (a) SM density data centered at 67135 (left ordinate scale) and (b) the AIO-AFSAT phase data (0.01 Hz detrend) centered at 67260 (right ordinate scale). The SM PDS has been shifted in log-frequency by -1.45 to compensate for the different effective scan velocities of the SM and AIO-AFSAT data sets. The short vertical bars indicate a potentially-common feature in the two spectra (see text). The horizontal solid bar indicates the value for 'T' derived from the AIO-AFSAT phase spectrum (0.1 to 1.0 Hz fit), and the horizontal dotted line indicates a value for 'T' derived from the SM density data using a 265 m/s effective scan velocity.

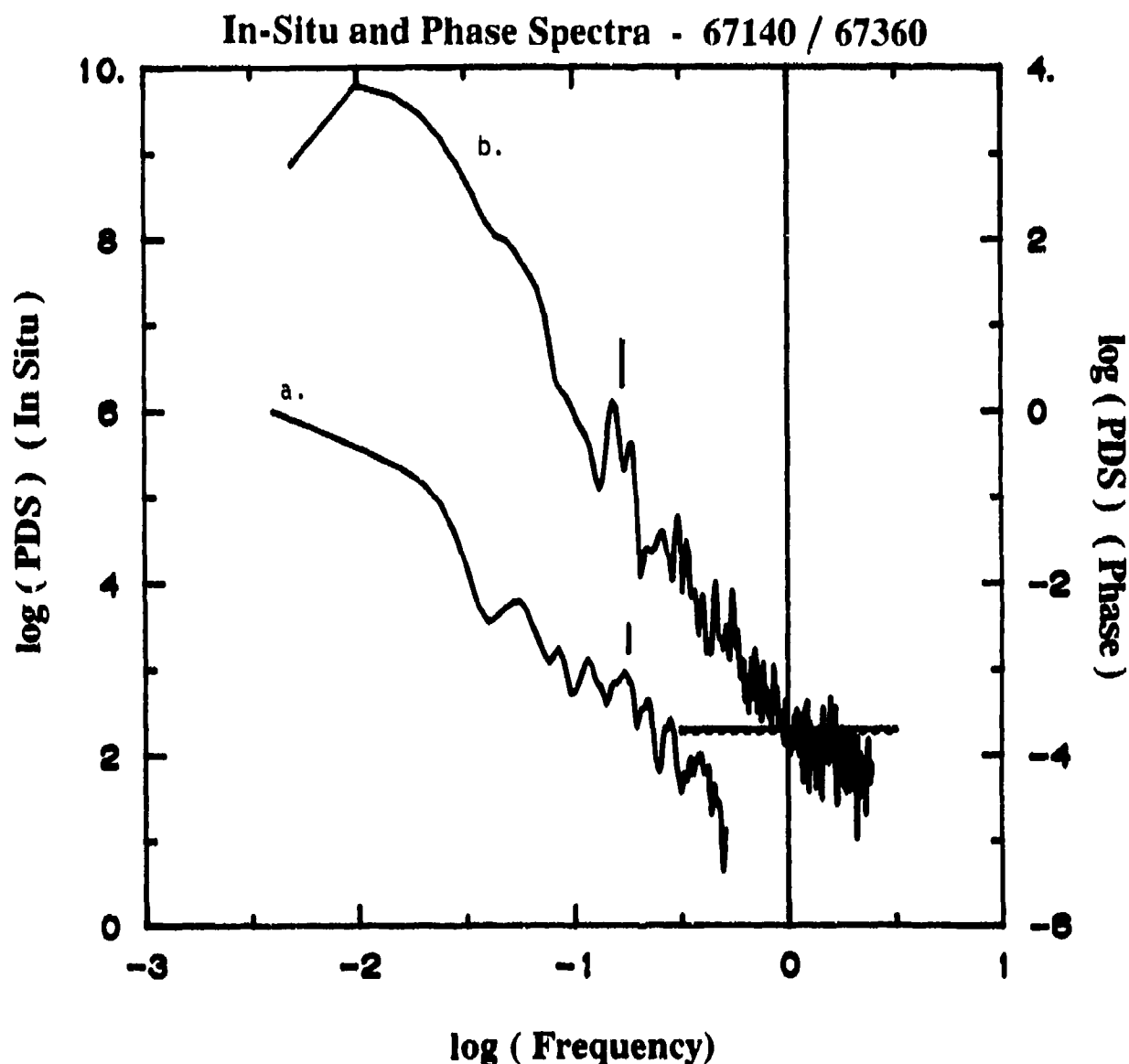


Figure 20. Power density spectra from (a) SM density data centered at 67140 (left ordinate scale) and (b) the AIO-AFSAT phase data (0.01 Hz detrend) centered at 67360 (right ordinate scale). The SM PDS has been shifted in log-frequency by -1.35 to compensate for the different effective scan velocities of the SM and AIO-AFSAT data sets. The short vertical bars indicate a potentially-common feature in the two spectra (see text). The horizontal solid bar indicates the value for  $T$  derived from the AIO-AFSAT phase spectrum (0.1 to 1.0 Hz fit), and the horizontal dotted line indicates a value for  $T$  derived from the SM density data using a 265 m/s effective scan velocity.

PDS, shifted using the effective velocities from Table 4. to the AIO-AFSAT phase PDS. [Note: The low-frequency "roll-off" in the phase PDS in these plots is due to the detrender, which had a cut-off frequency of 0.01Hz.]

In working with these spectra, a pattern of similar features in the *in situ* and phase spectra began to emerge. These features show up most clearly in the spectra in Figure 18, which compares the data sets taken at the intercept latitude/time, and in Figure 21, a plot of the average of the *in situ* and phase spectra from Figures 18-20 in which the *in-situ* spectrum has been shifted to align the similar features in the two spectra, which requires an assumed effective scan velocity of 265 m/s. There are three features marked in this plot: two local minima at  $\log(f)$  of -1.37 (0.043Hz) and -0.90 (0.126Hz), and a local enhancement at  $\log(f)$  of -0.76 (0.174Hz) (a single broad enhancement *in situ* and a pair of narrow enhancements in phase). Using the assumed value for  $v_e$ , these features would be at scale sizes of 6200m, 2100m, and 1500m, respectively. These features can also, to some extent, be found in most of the other spectra as well, most noticeably the enhancement which has been marked in all five of the individual spectra.

The effective velocity required to align these features is fairly close to the  $v_e$  calculated using the T observations for the last three data sets. The horizontal solid and dotted lines on the PDS plots indicate the observed T (solid) and T calculated using 265 m/s for the effective scan velocity (dotted). At least in the last three spectra, the differences between these values for T is within the noise evident in both spectra. The results for T and  $\sigma_\phi$  using  $v_e = 265$  m/s are compared to the observed values in Table 6.

Table 6. Phase scintillation parameters from the SM and AIO-AFSAT data sets (13-1/3s detrend; 17:2 wings;  $v_e$  from PDS).

GMT	$v_e$	T		$\sigma_\phi$	
		DMSP	AIO	DMSP	AIO
66960	265	$2.35 \times 10^{-3}$	$4.08 \times 10^{-4}$	0.69	0.46
67060	265	$6.76 \times 10^{-4}$	$3.03 \times 10^{-4}$	0.36	0.36
67160	265	$1.50 \times 10^{-4}$	$2.03 \times 10^{-4}$	0.22	0.36
67260	265	$2.64 \times 10^{-4}$	$2.04 \times 10^{-4}$	0.26	0.39
67360	265	$1.56 \times 10^{-4}$	$1.97 \times 10^{-4}$	0.22	0.40
	m/s			rad	

The results of this comparison of individual spectral features should be viewed with some caution. While the resulting effective scan velocity obtained is in excellent agreement

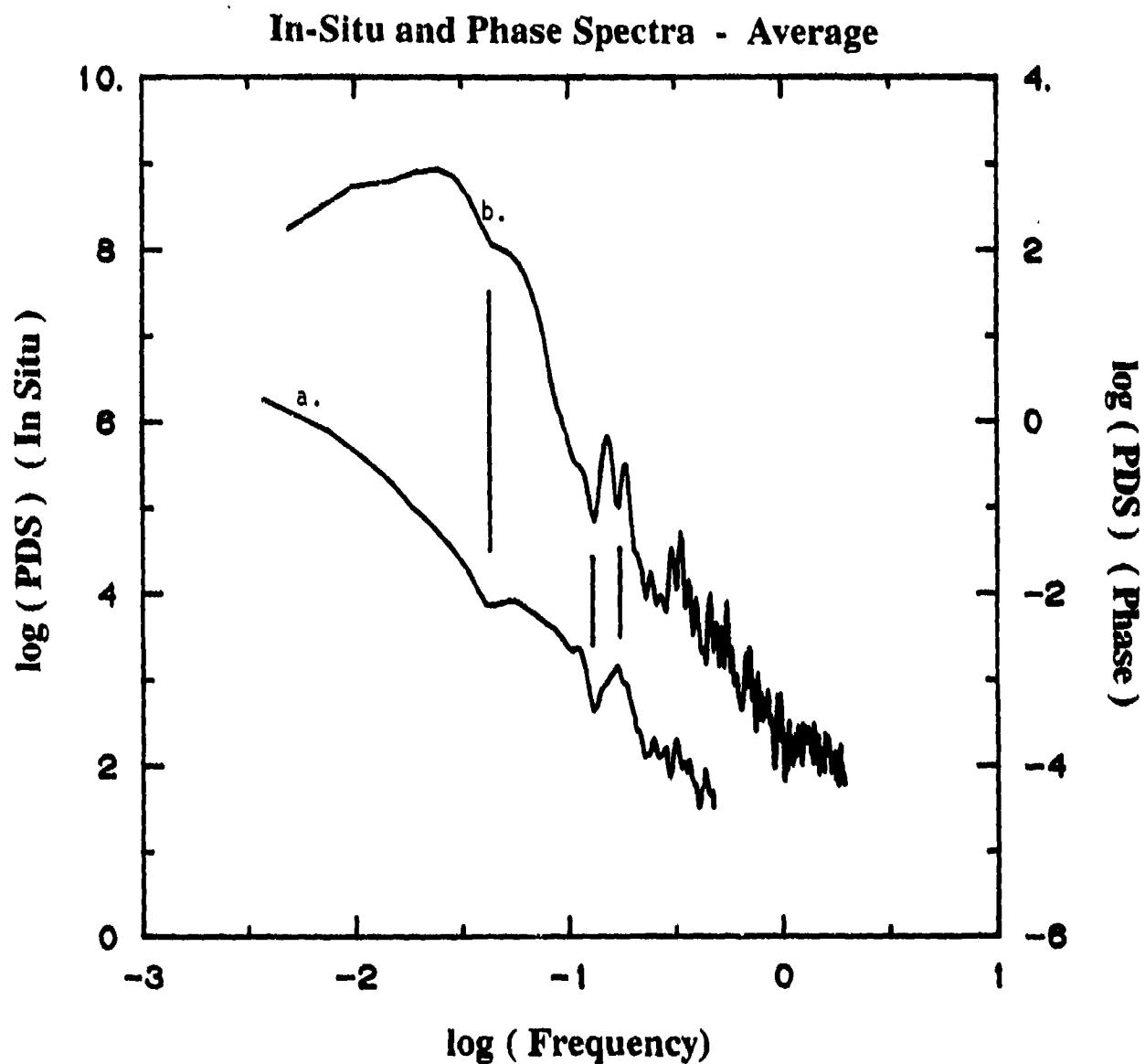


Figure 21. Average phase and *in-situ* power density spectra constructed from the spectra in Figures 18-20. The vertical lines indicate the location of features described in the text. The *in-situ* spectrum has been shifted to align the marked features in the two spectra, which implies an effective scan velocity in the phase data of 265 m/s.

with that obtained from the comparison of the T values, the features used in the analysis are not far removed from the noise in the spectra. In addition, there will be features in the phase spectrum due to propagation effects that have no correspondence, other than coincidence, to features in the *in-situ* spectrum. All of this notwithstanding, these features do appear in nearly all of the spectra reviewed, and the robustness of these features to different ways of processing the data indicate that they are not processing artifacts.

### 3.4 Discussion of Results

The results of the data comparisons for this single event are somewhat mixed. The intensity-scintillation comparisons indicate that, for this data set, analysis of the DMSP SSIES data was able to quantify the level of intensity scintillation encountered on a ray path passing through the section of the ionosphere sampled by the instrument. The results were good enough that, barring luck and coincidence in this single case, they should be borne out in analysis of the remaining five days' data sets. Part of the confidence in this result comes from qualitative comparison of the detrended intensity (Figure 5) and density (Figure 9) data sets. Both show a great deal of small-scale structure at the beginning of the data interval, decreasing steadily through the end of the interval.

The results from the phase-scintillation comparisons are not as clear (nor as positive!) as those from the intensity scintillation, but they at least show some promise. When the discovery was made that the AIO-AFSAT phase data were in some way contaminated by low-frequency noise, the analysis of the phase data was nearly abandoned. The analysis was carried as far as it was due to the discovery of similar features in the spectra generated from the two data sets which appeared at nearly the same scale sizes (see Figure 18). In the discussion that follows, the basic assumption is made that the spectral slope is relatively constant over the frequency range 0.012 to 1.0 Hz, corresponding roughly to a scale-size range of 25 kilometers to 300 meters, which covers the ranges spanned by the fits made to the SM data (25 to 1.5 kilometers) and the AIO-AFSAT data (3 kilometers to 300 meters). This assumption cannot be fully verified with these two data sets, but the slopes of the high-frequency end of the SM spectra, which reach down to scale sizes on the order of 600-700 meters, do not appear to differ drastically from that obtained from the lower-frequency sections. In short, this is not an unjustifiable assumption.

Making this assumption, the following observations can be made from the phase-parameter comparisons:

- a. The effective velocity required to adjust the phase parameters calculated from the SM data to match the corresponding parameters derived from the AIO-AFSAT data ranged from about 115 to 455 m/s and averaged around 280 m/s. The velocities required to match T and  $\sigma_\phi$  increased from the northern end of the data segment to the southern end (which agrees generally with the cross-track velocities obtained from the DMSP DM sensor, which increased from 150 m/s in an anti-sunward sense to 400 m/s in a sunward sense),

while the velocities required to align the spectra appear to be constant across the data interval at 265 m/s.

b. The spectral slopes ( $p$ ) generated from the phase spectra were slightly steeper than those calculated from the *in-situ* spectra ( $q + 1$ ). If a comparison of these slopes is valid, considering the difficulties with the AIO-AFSAT phase data and the different scale-size range fit to obtain the slope from the spectra, this would indicate that there is relatively more power in the low frequency (large-scale) end of the spectrum than at the high-frequency (small-scale) end at the DMSP altitude (roughly 850 km) than there is in the bulk of the irregularity layer (roughly 300-350 km). This relationship between the *in-situ* spectral slope and the phase spectral slope differs from that found in a comparison of DE-2 RPA density data collected in the northern polar cap with VHF phase measurements made using AFSAT signals collected at Thule, Greenland<sup>[3]</sup>. This study found an average phase spectral slope ( $p$ ) of between 2.2 and 2.4, and an average *in-situ* slope ( $q$ ) of 1.9. These values differ from each other by much less than the unity difference called for by weak-scatter phase-screen theory. Moreover, they are both much less than both the phase and *in-situ* values reported here and a value of 2.75 derived from an analysis of over two years of HiLat data collected at Sondre Stromfjord, Greenland. Without knowing exactly the scale-size ranges over which the fits were made to determine the slopes, it is difficult to explain this discrepancy.

c. When the effective velocity is set so that the  $T$  values agree, the  $\sigma_\phi$  values calculated from the phase data is systematically 50-60% higher than that calculated from the density data. Roughly a quarter of this can be accounted for by the difference in  $p$  values described above and residual power in the spectrum at frequencies below the detrender cutoff frequency, but the remainder is still unexplained. This may represent more effects of the low-frequency noise, but it is impossible to tell from this data set.

In summary, the phase-data comparisons give indications that the various phase-parameter estimates made from the SM data ( $p$ ,  $T$ ,  $\sigma_\phi$ , and the phase PDS) are reasonably close to the values observed in the AIO-AFSAT data, but the lack of good measurements of the *in-situ* drift velocity at the AIO-AFSAT IPP and the low-frequency phase noise in the AIO-AFSAT phase data make it impossible to draw firm conclusions. The remaining data from the campaign should be processed to find if the AIO-AFSAT phase data are contaminated in all six data sets, and future campaigns should either find a way to remove or reduce the phase noise in the AIO-AFSAT data or use a phase-coherent transionospheric radio link, such as GPS or Polar BEAR, to provide the phase scintillation data for comparison to the DMSP SM estimates.

## 4. SSIES Observations of Equatorial Irregularities

During the month of August, 1988, the Defense Nuclear Agency (DNA) conducted an extensive multi-sensor data-collection campaign near Kwajalein Island to assess the effects of ionospheric scintillation on radar signal propagation (Propagation Effects Assessment - Kwajalein, or PEAK). This campaign was used as a target of opportunity to conduct an assessment of the potential for using the DMSP SSIES data for characterizing scintillation in the equatorial region. In this section we will present a very brief review of nighttime equatorial F-region scintillation including previous analyses of high-altitude ( $> 800$  km) *in-situ* plasma density observations, followed by a description of the PEAK campaign and the results obtained from analysis of data from the DMSP F8 and F9 SSIES instruments.

### 4.1 Nighttime Equatorial F-Region Scintillation - A Micro-Review

There are two major sources of nighttime scintillation in the equatorial region<sup>[15]</sup>: large three-dimensional plasma-depletion structures known as bubbles<sup>[15]</sup> or plumes<sup>[16,17]</sup> and quasi-periodic plasma-density structures confined in altitude to the bottomside F2-region known as bottomside sinusoidal (BSS) irregularities<sup>[18,19]</sup>. The two sources have different morphologies and different effects on transionospheric propagation - the plume structures can cause quite severe scintillation even at GHz frequencies, while the BSS irregularities will produce moderate levels of scintillation at VHF and lower UHF. Since the BSS irregularities are restricted to the bottomside F region, it will be impossible to observe them directly with an *in-situ* sensor on DMSP. They are included in the discussions that follow as (1) they may be a major limitation to the usefulness of the DMSP SSIES data in characterizing equatorial scintillation levels, (2) they could explain some of the discrepancies found in the analysis of data from the PEAK campaign discussed in later sections of this report, and (3) it may be possible to infer indirectly the presence of BSS irregularities from the spatial/temporal behavior of the background plasma density as observed by the SSIES instruments.

#### 4.1.1 Equatorial Plume Structures

It is generally held<sup>[20]</sup> that the plume structures are the result of plasma depletion "bubbles" that form on the bottomside of the F layer during the post-sunset period when the F layer is lifted in altitude by  $E \times B$  forces, intensify due to the generalized collisional Rayleigh-Taylor (GRT) instability<sup>[21]</sup>, and propagate upwards into the topside F region to altitudes above 1000 km<sup>[22,23]</sup>. Longitudinal cross sections of these structures made by incoherent scatter radars<sup>[16,17]</sup> show them to be wedge-shaped regions tilted toward the west extending from below the F-layer density peak well into the topside ionosphere. The east-west horizontal extent is on the order of 100-200 km, and the structures travel eastwards with velocities on the order of 100-200 m/s. Airglow studies at 6300 Å<sup>[24]</sup> have shown that the plume structures are oriented along magnetic flux tubes, often extending thousands of

kilometers from one end of the flux tube to the other in the opposite hemisphere. The plumes begin to appear within an hour or so of local sunset, and have typically run their course and blended back into the background plasma structure within a few hours after local midnight.

In general, the seasonal occurrence frequency of the plume structures peaks near the equinoxes, occasionally with secondary maxima at one or the other solstices<sup>(14)</sup>. Details of the seasonal variation at a particular station are strongly dependent on the station's longitude sector. This strongly coupled longitudinal/seasonal morphology is quite complicated and is not yet well understood<sup>(14)</sup>. Although the mechanism for the growth of the plumes is almost certainly the nonlinear GRT instability, there are two sources of modulation on the production of plumes that may be controlling the longitudinal-seasonal morphology. The first is the requirement for a "seed" mechanism to provide the initial small perturbation in the bottomside F-region density which then grows into the plume structure via the GRT instability, and the second is a number of mechanisms that can either enhance or inhibit the GRT instability. A commonly mentioned seed mechanism is gravity waves, generated either locally<sup>(25)</sup> or propagating upward from lower in the atmosphere<sup>(26)</sup>, that can interact with the bottomside plasma to produce sinusoidal variations in density. A mixed bag of mechanisms have been proposed which could control the GRT instability once the bubble has formed, including (1) variations in the reversal time of the zonal electric field<sup>(27)</sup>, (2) asymmetry in field-aligned currents generated by the E-region dynamo<sup>(28)</sup>, (3) the transequatorial component of thermospheric neutral winds which can alter the Pedersen conductivity along the field line<sup>(29,30)</sup>, and (4) variations in the longitudinal gradient of the field-line integrated Pedersen conductivity controlled by the solar and magnetic declination angles<sup>(31)</sup>. The interplay and relative importance of these mechanisms in producing the observed longitudinal-seasonal morphology is still an open and active area of investigation.

#### 4.1.2 Equatorial Bottomside Sinusoidal Irregularities

Equatorial bottomside sinusoidal (BSS) irregularities were first observed using *in-situ* data from the AE-C and AE-E satellites<sup>(18,32)</sup> and have been associated with moderate VHF and UHF scintillation extending over periods five to six hours in length<sup>(19)</sup>. Only a few studies have been made of this type of irregularity, so only a little is known of its spatial and temporal morphology. It is a nighttime phenomenon, with the peak in diurnal occurrence-frequency near local midnight and seasonal frequency peaks near the solstices. It is limited in altitude extent to a layer 50 to 100 km in depth along the bottomside of the F-layer peak. The horizontal extent is large, with east-west extents ranging from 1000 km to 7500 km. No values have been given for typical north-south extents, but these irregularities are predominantly found within the dip latitude range of  $-10^\circ$  to  $+10^\circ$ . Onset and decay of scintillation from BSS irregularities has been found to be nearly simultaneous at widely spaced (in longitude) locations, which may indicate that the physical mechanisms controlling the BSS irregularities act over large spatial scales<sup>(19)</sup>. These irregularities appear to be coupled to

frequency-spread F, while the plume/bubble structures are associated with range-spread F[18].

#### 4.1.3 Topside Studies of Equatorial Irregularities

Satellite-based observations of irregularities in the topside equatorial ionosphere have been made for over two decades using both remote sensors, such as topside sounders[23,29], and *in-situ* probes[15,22,33-37]. While numerous studies have been made covering the topside ionosphere from the F2 peak to well over 1000 km, the most germane of these studies to the work described in this report is that conducted by Young *et. al.*[37] using data from the Retarding Potential Analyzer (RPA) on the DMSP F2 and F4 satellites. In their study, which could be considered a direct predecessor of the current project, they showed that an *in-situ* probe on a DMSP satellite in the pre-noon/pre-midnight orbital plane encounters irregularities that probably are the high-altitude sections of equatorial depletion plumes. They found a longitudinal bias in the observations, identified a number of problems with the DMSP orbit for making routine synoptic observations of equatorial scintillation-producing irregularities, and developed a zeroth-order probability model for observing the plume structures from the DMSP satellite. Details of this study, and comparisons of their results to results from the current study, will be presented where appropriate in the following sections.

#### 4.2 PEAK Campaign Description

The purpose of the DNA PEAK campaign, as stated above, was to collect data from a number of ionospheric probes, both remote and *in-situ*, which could be used to characterize plasma density irregularities in the equatorial ionosphere in order to assess the effect of these irregularities on transionospheric radar propagation. The campaign ran during the period 3-31 August 1988, with most of the ground-based instruments located on islands in the Kwajalein Atoll (9°24'N, 167°28'E). Of the various data sets collected, the following have been made available for this study:

- a. SSIES data from both F8 and F9 DMSP satellites for the entire month of August (provided by F. J. Rich, GL/PHG).
- b. Intensity scintillation data ( $S_4$ ) from a UHF link from Kwajalein Island to a FLTSAT satellite located over the equator at 172° E longitude for the period 3-31 August (provided by R. T. Tsunoda, SRII).
- c. Intensity scintillation data ( $S_4$ ) from UHF and L-band links to the HiLat and Polar BEAR satellites obtained at Kwajalein Island with the DNA ROVER receiver for the period 1-29 August (provided by E. J. Fremouw, NWRA).

Although longitudinal-scan maps of the ionosphere similar to those presented in Tsunoda *et. al.*[17] were made periodically throughout the PEAK period using the Altair radar, we

were unable to obtain them in time to include them in this study. We hope to have access to them prior to the completion of this project to aid in interpreting and perhaps understanding some of the discrepancies described later.

### 4.3 Data Description

#### 4.3.1 DMSP SSIES Data

Much of the effort for this project was in processing the SSIES SM data. The plan was to process the SM data from the magnetic latitude range  $+40^\circ$  to  $-40^\circ$  for the pass nearest Kwajalein and the passes prior to and after this pass for each day for the descending (nighttime) passes from both satellites - a total of 186 partial orbits including 3720 minutes of data. These data would then be plotted to form a catalog of ion-density plots for comparison with the other data sets.

With the large volume of data to be processed, it was clearly impossible to employ as much manual intervention in interpreting the data as had been done with the limited data set used in the high-latitude study (a total of 30 minutes of data), as this would have been prohibitively expensive in both computer and manpower resources. The major problem that had to be dealt with in order to process much of the data was that of the floating range flags described in earlier reports (see Appendix B in Report #2). This problem was alleviated by processing several passes from both F8 and F9, extracting the electrometer range data from these passes, and generating an updated look-up table for the electrometer range data for use in processing the SM data. While this did not solve all problems relating to the floating flags, it did reduce the number of these down to an acceptable level. The processing was done using software based on the operational software package used at the US Air Force Global Weather Central for routine processing of the SSIES data<sup>[39]</sup>.

A more serious problem, related to sensor behavior rather than processing difficulties, was that in large segments of several passes the electrometer appeared to "freeze" at a value equal to one of the range flags. This tended to happen when the ionosphere was very smooth and at nearly constant density. A sample of this problem was identified in our last annual report (see Figure B-07, page B-7, in Report #2). The builders of the SM instruments at the University of Texas at Dallas (UTD) are aware of this problem and have corrected all SM instruments not now in orbit, so both this and the floating-flags problem will be corrected on the next SM instrument to be launched.<sup>[39]</sup>

Figures 22 through 27 are samples of the data obtained from this processing. (The entire catalog of 31 days is included in the appendix to this report.) Each figure shows the total ion density plotted against time for each of the six partial orbits (passes) processed for a specific date. Each plot contains 20 minutes of data starting (roughly) at  $+40^\circ$  geomagnetic (modified apex) latitude. The first three plots (a) in each set are from F8 and the last three (b) from F9. The center plot on each page is from the pass nearest (in location)

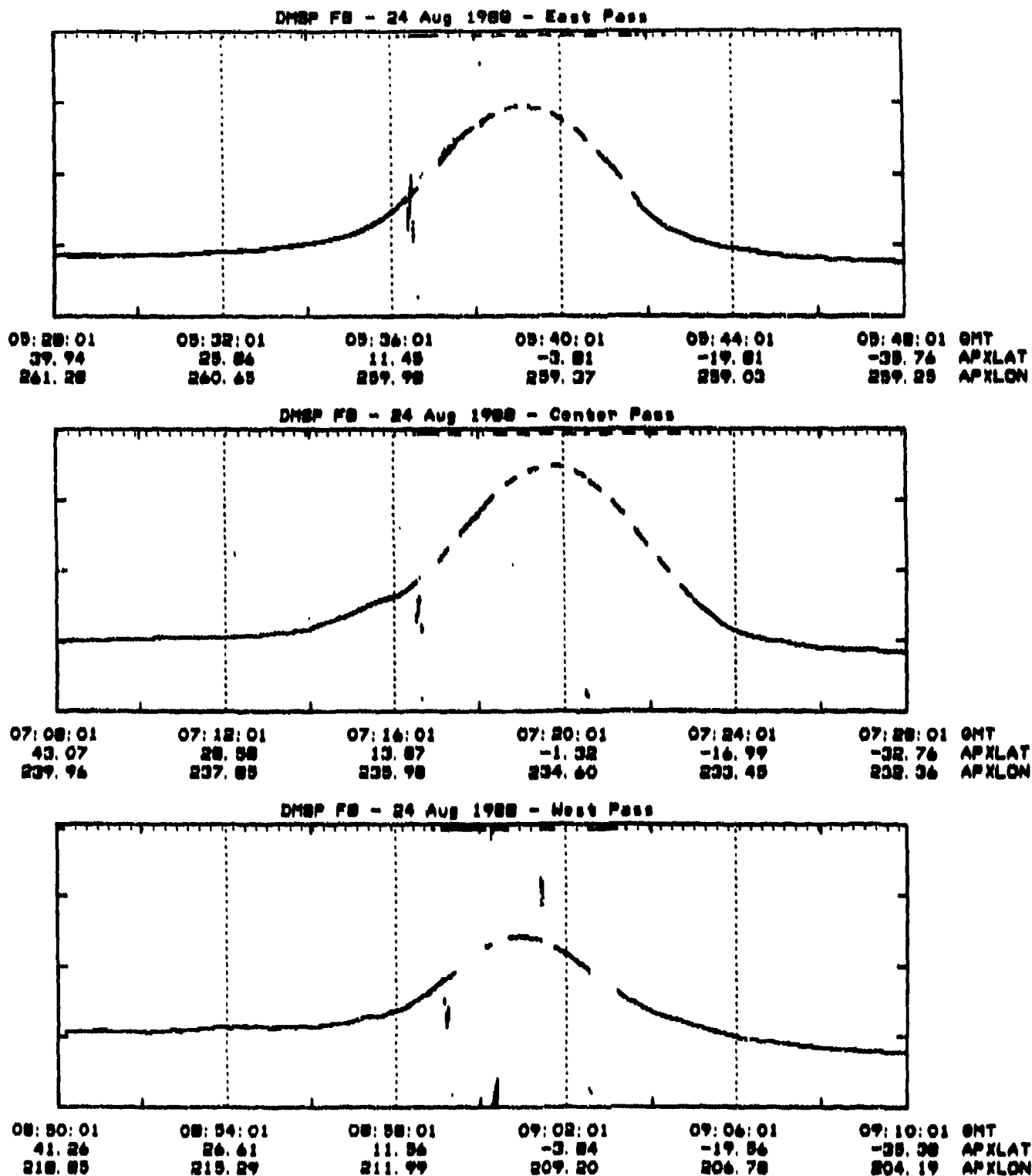
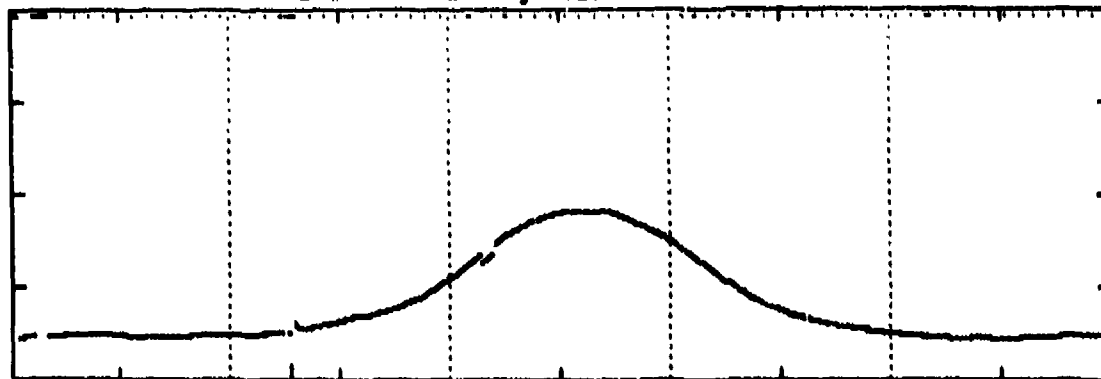


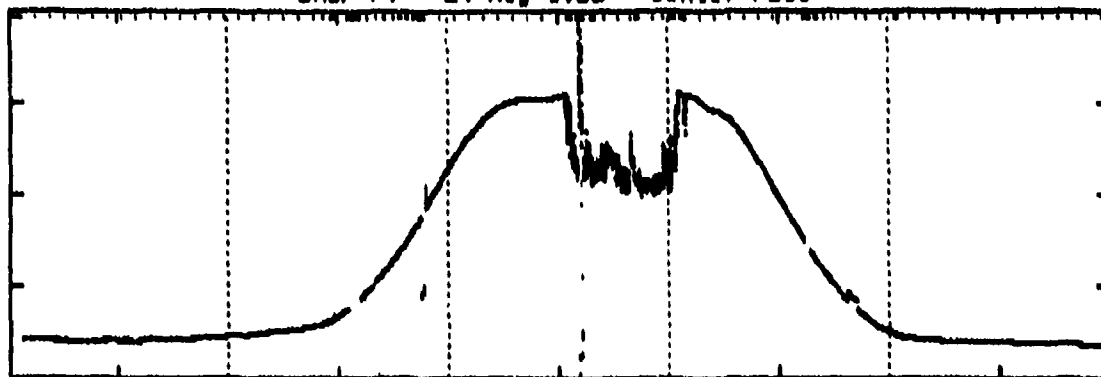
Figure 22a. Total ion density measured by the Scintillation Meter (SM) sensor on DMSP F8 near Kwajalein Atoll on 24 August 1988. The y-axis is ion density ranging from 0.0 to  $2.0 \times 10^5$ ; and the x-axis labels are GMT for Greenwich Mean Time (HH:MM:SS), APXLAT for (modified) apex latitude, and APXLON for apex longitude.

DMSP F9 - 24 Aug 1988 - East Pass



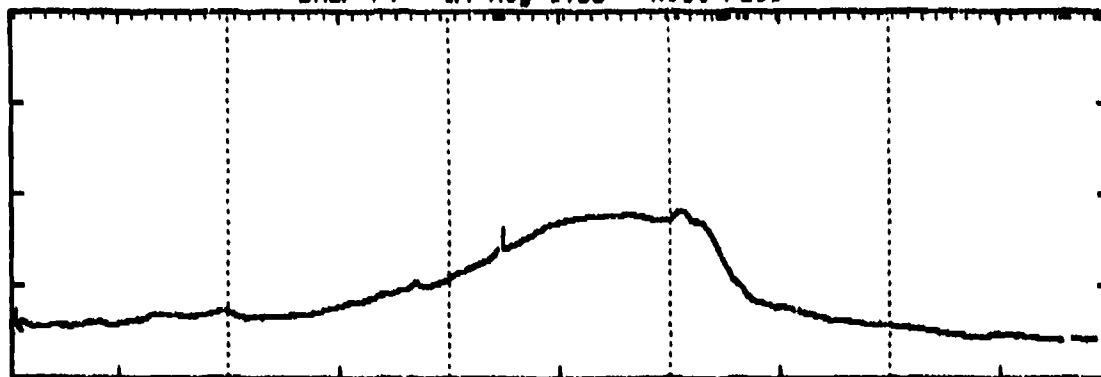
08:24:01	08:28:01	08:32:01	08:36:01	08:40:01	08:44:01	GMT
39.84	25.48	11.16	-4.18	-20.17	-36.07	APXLAT
267.00	266.68	266.17	265.58	265.35	265.86	APXLON

DMSP F9 - 24 Aug 1988 - Center Pass



10:04:01	10:08:01	10:12:01	10:16:01	10:20:01	10:24:01	GMT
40.74	26.36	11.71	-3.58	-19.45	-35.36	APXLAT
244.89	243.20	241.80	240.81	240.00	239.31	APXLON

DMSP F9 - 24 Aug 1988 - West Pass



11:45:01	11:49:01	11:53:01	11:57:01	12:01:01	12:05:01	GMT
40.01	25.26	10.16	-5.26	-20.96	-36.75	APXLAT
224.02	220.85	217.97	215.58	213.49	211.32	APXLON

Figure 22b. Total ion density measured by the SM sensor on DMSP F9 near Kwajalein Atoll on 24 August 1988. The axis ranges and labels are as in Figure 1a.

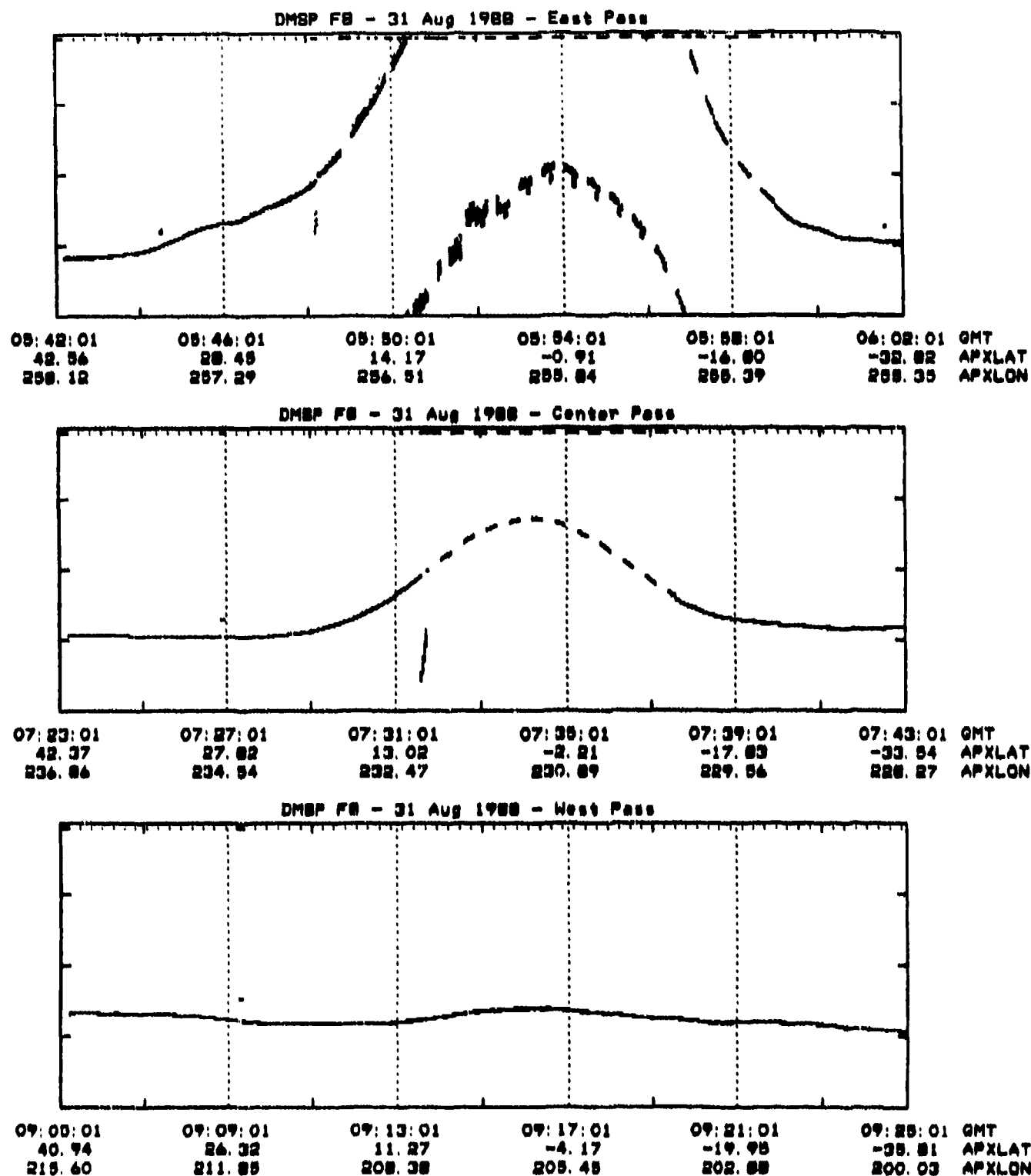


Figure 23a. Total ion density measured by the SM sensor on DMSF F8 near Kwajalein Atoll on 31 August 1988. The axis ranges and labels are as in Figure 1a.

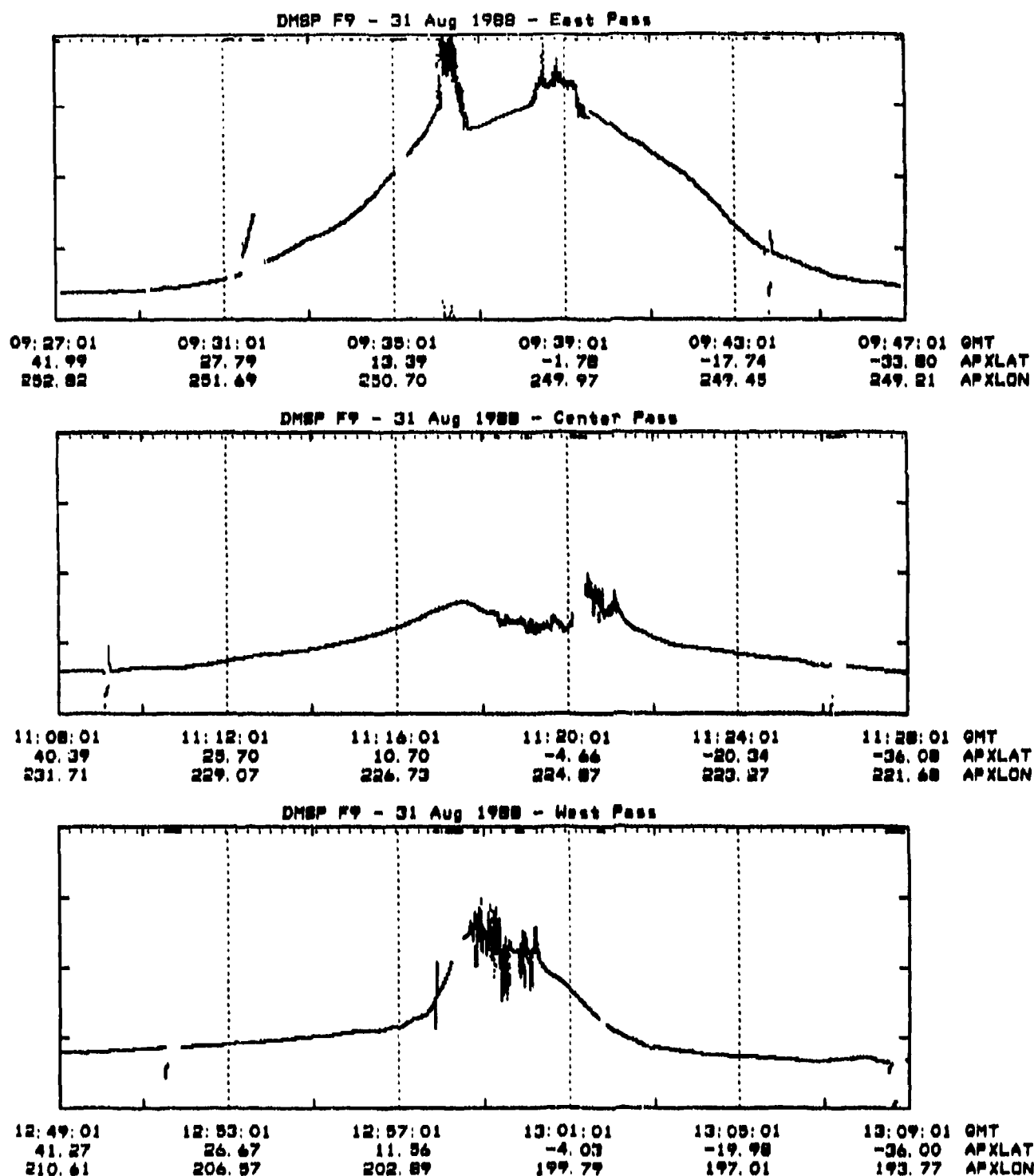


Figure 23b. Total ion density measured by the SM sensor on DMSP F9 near Kwajalein Atoll on 31 August 1988. The axis ranges and labels are as in Figure 1a.

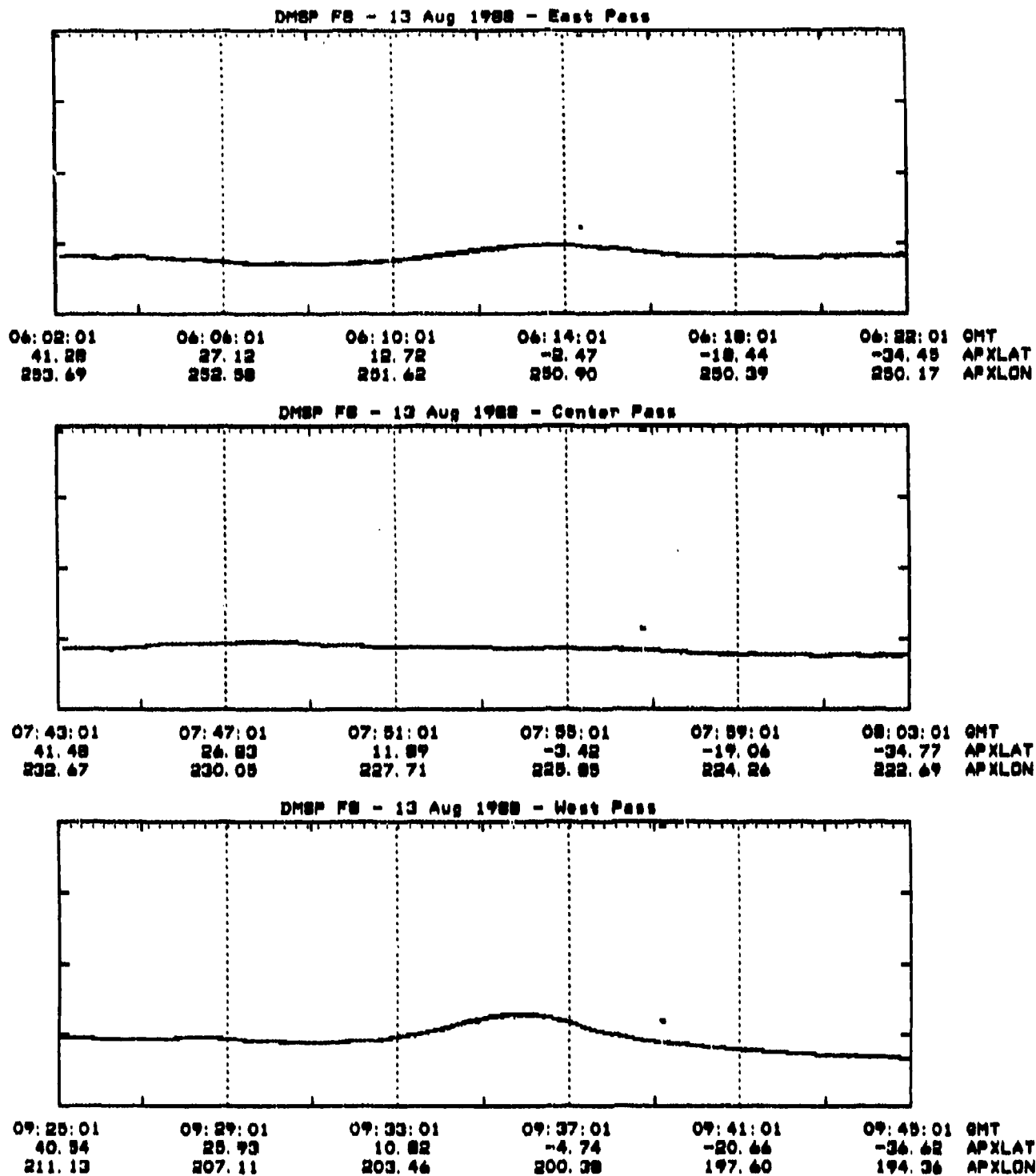
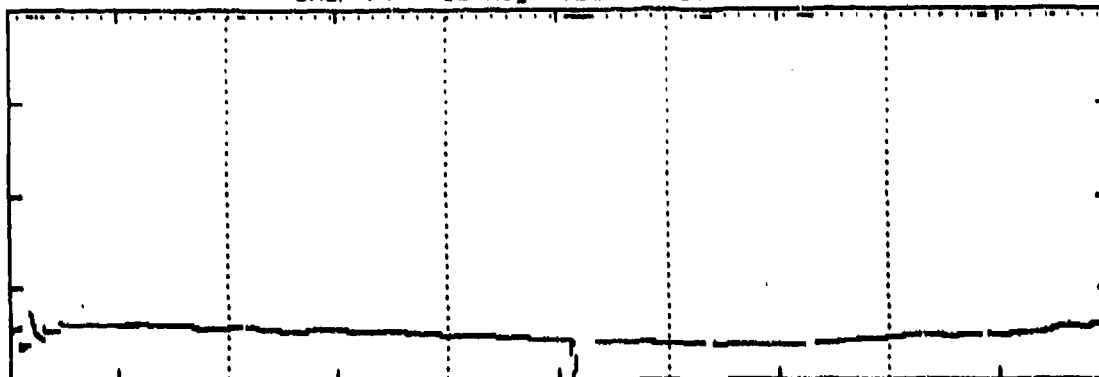


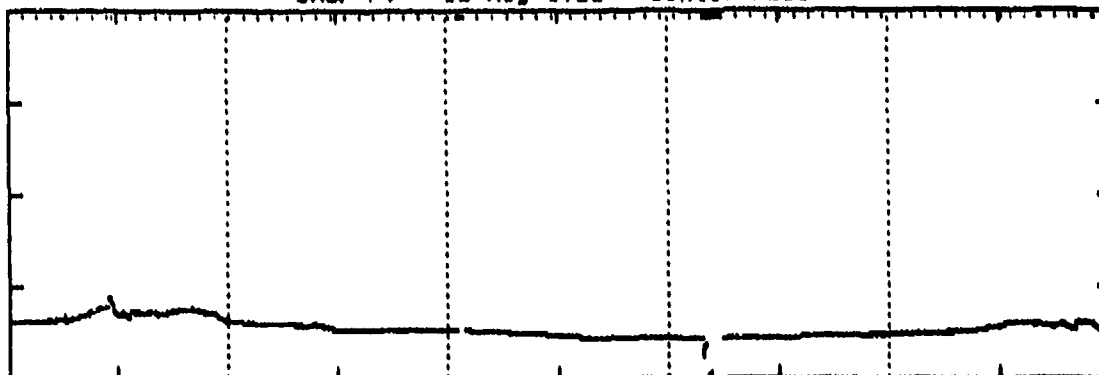
Figure 24a. Total ion density measured by the SM sensor on DMSP F8 near Kwajalein Atoll on 13 August 1988. The axis ranges and labels are as in Figure 1a.

DMSP F9 - 13 Aug 1988 - East Pass



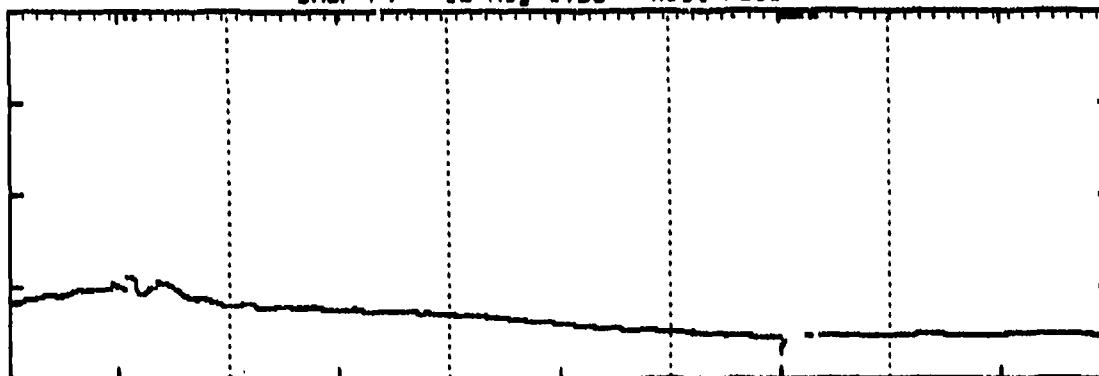
08:38:01	08:42:01	08:46:01	08:50:01	08:54:01	08:58:01	GMT
41.76	27.61	13.21	-1.99	-17.99	-34.01	APXLAT
243.69	243.18	242.62	242.02	241.69	241.97	APXLON

DMSP F9 - 13 Aug 1988 - Center Pass



10:18:01	10:22:01	10:26:01	10:30:01	10:34:01	10:38:01	GMT
42.89	28.40	13.71	-1.51	-17.28	-33.15	APXLAT
242.10	240.18	238.51	237.29	236.31	235.40	APXLON

DMSP F9 - 13 Aug 1988 - West Pass



11:59:01	12:03:01	12:07:01	12:11:01	12:15:01	12:19:01	GMT
42.84	27.85	12.79	-2.62	-18.33	-34.17	APXLAT
221.49	218.12	214.96	212.28	209.99	207.64	APXLON

Figure 24b. Total ion density measured by the SM sensor on DMSP F9 near Kwajalein Atoll on 13 August 1988. The axis ranges and labels are as in Figure 1a.

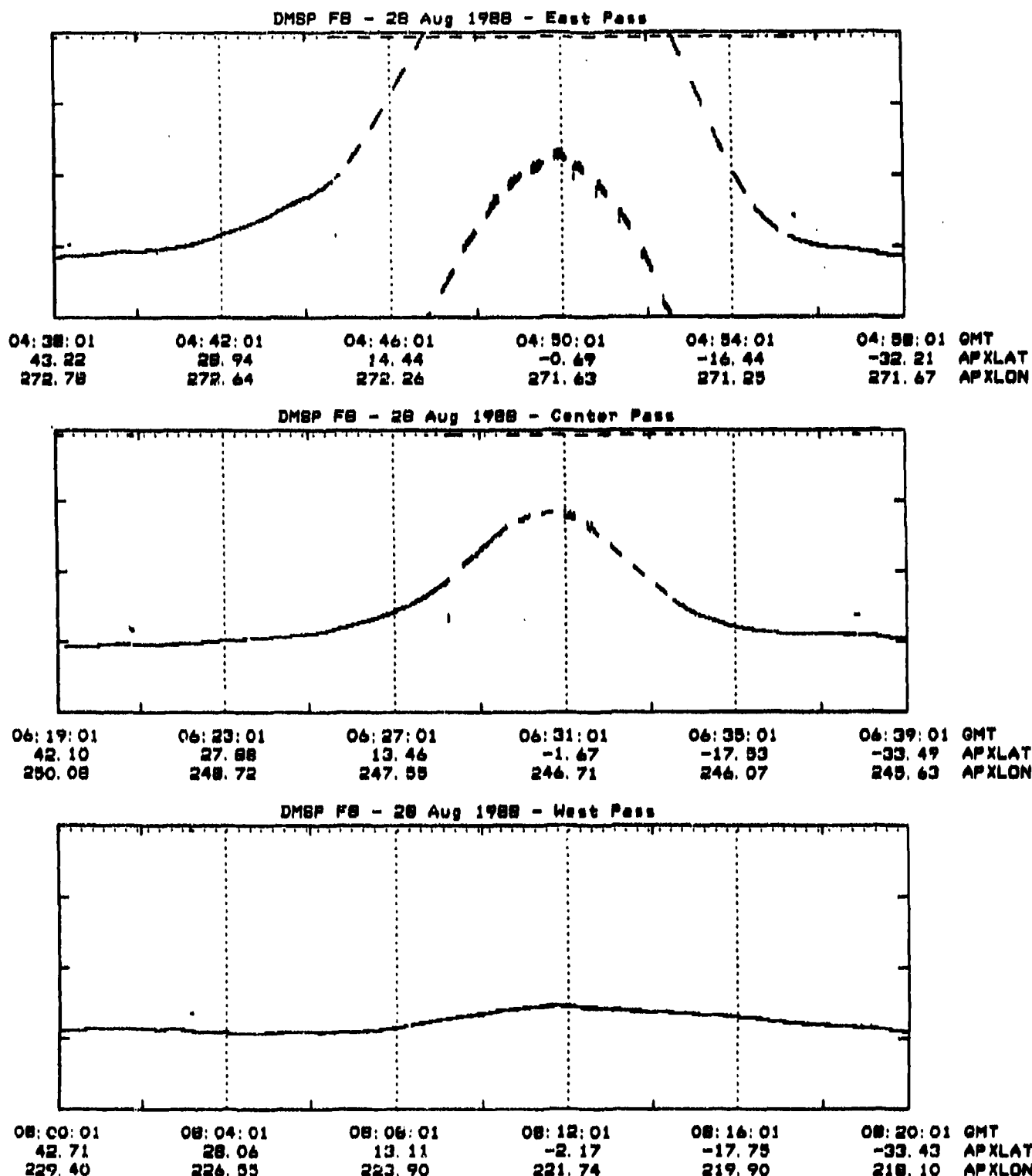
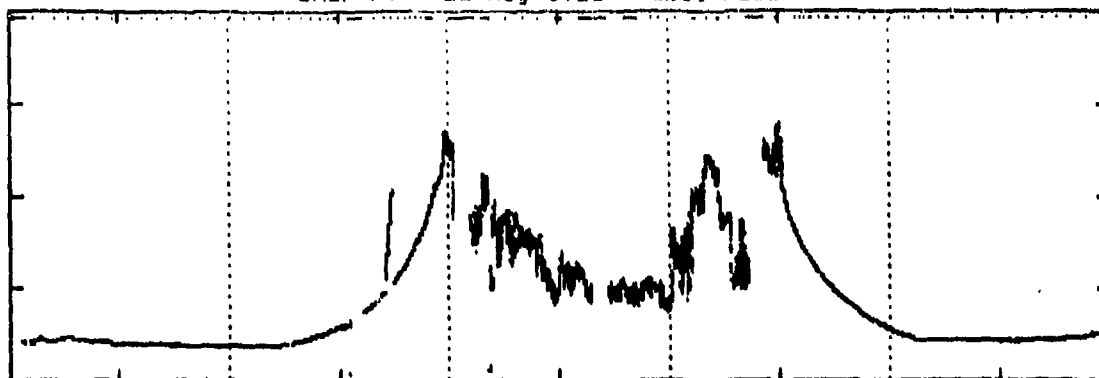


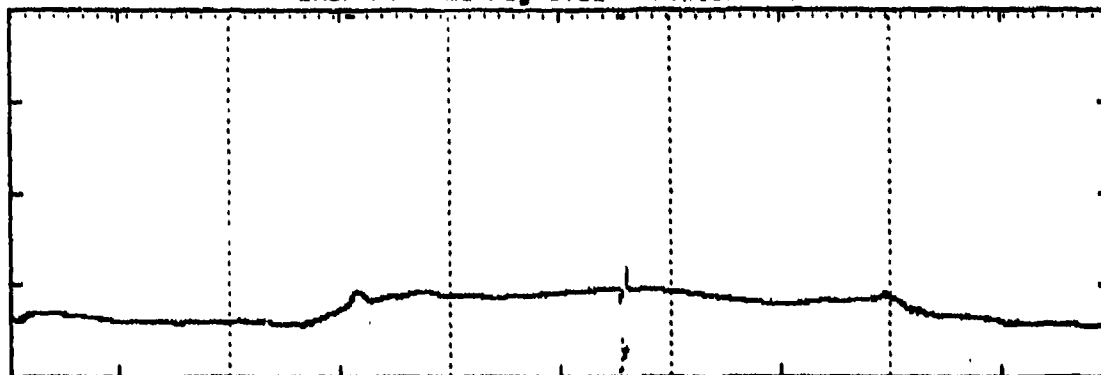
Figure 25a. Total ion density measured by the SM sensor on DMSP F8 near Kwajalein Atoll on 28 August 1988. The axis ranges and labels are as in Figure 1a.

DMSP F9 - 28 Aug 1988 - East Pass



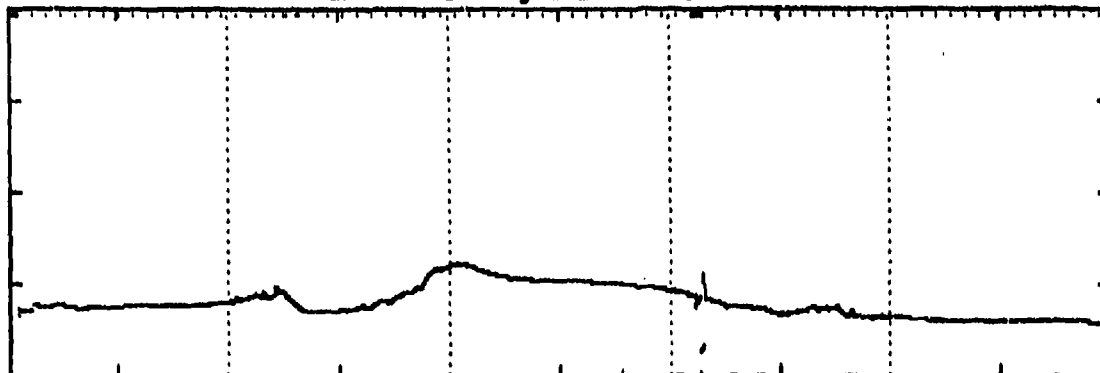
08:46:01	08:50:01	08:54:01	08:58:01	09:02:01	09:06:01	GMT
39.92	25.82	11.37	-3.94	-19.99	-35.99	APXLAT
261.93	261.37	260.75	260.16	259.56	240.17	APXLON

DMSP F9 - 28 Aug 1988 - Center Pass



10:26:01	10:30:01	10:34:01	10:38:01	10:42:01	10:46:01	GMT
41.12	26.62	11.85	-3.45	-19.22	-35.05	APXLAT
240.37	238.34	234.61	235.35	234.29	233.30	APXLON

DMSP F9 - 28 Aug 1988 - West Pass



12:07:01	12:11:01	12:15:01	12:19:01	12:23:01	12:27:01	GMT
40.96	26.26	11.17	-4.27	-20.03	-35.89	APXLAT
219.59	216.11	212.90	210.19	207.84	205.33	APXLON

Figure 25b. Total ion density measured by the SM sensor on DMSP F9 near Kwajalein Atoll on 28 August 1988. The axis ranges and labels are as in Figure 1a.

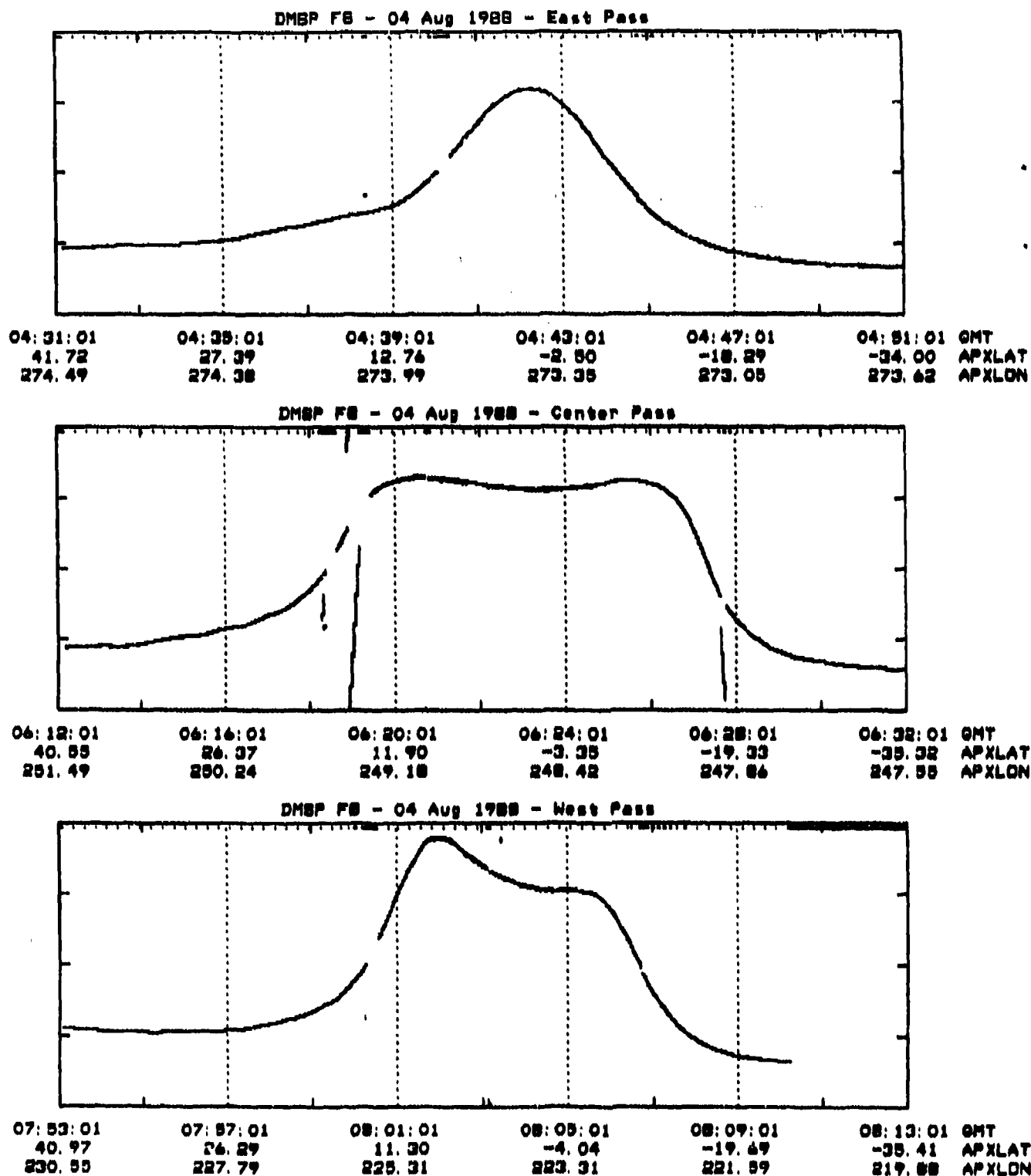


Figure 26a. Total ion density measured by the SM sensor on DMSF F8 near Kwajalein Atoll on 4 August 1988. The axis ranges and labels are as in Figure 1a.

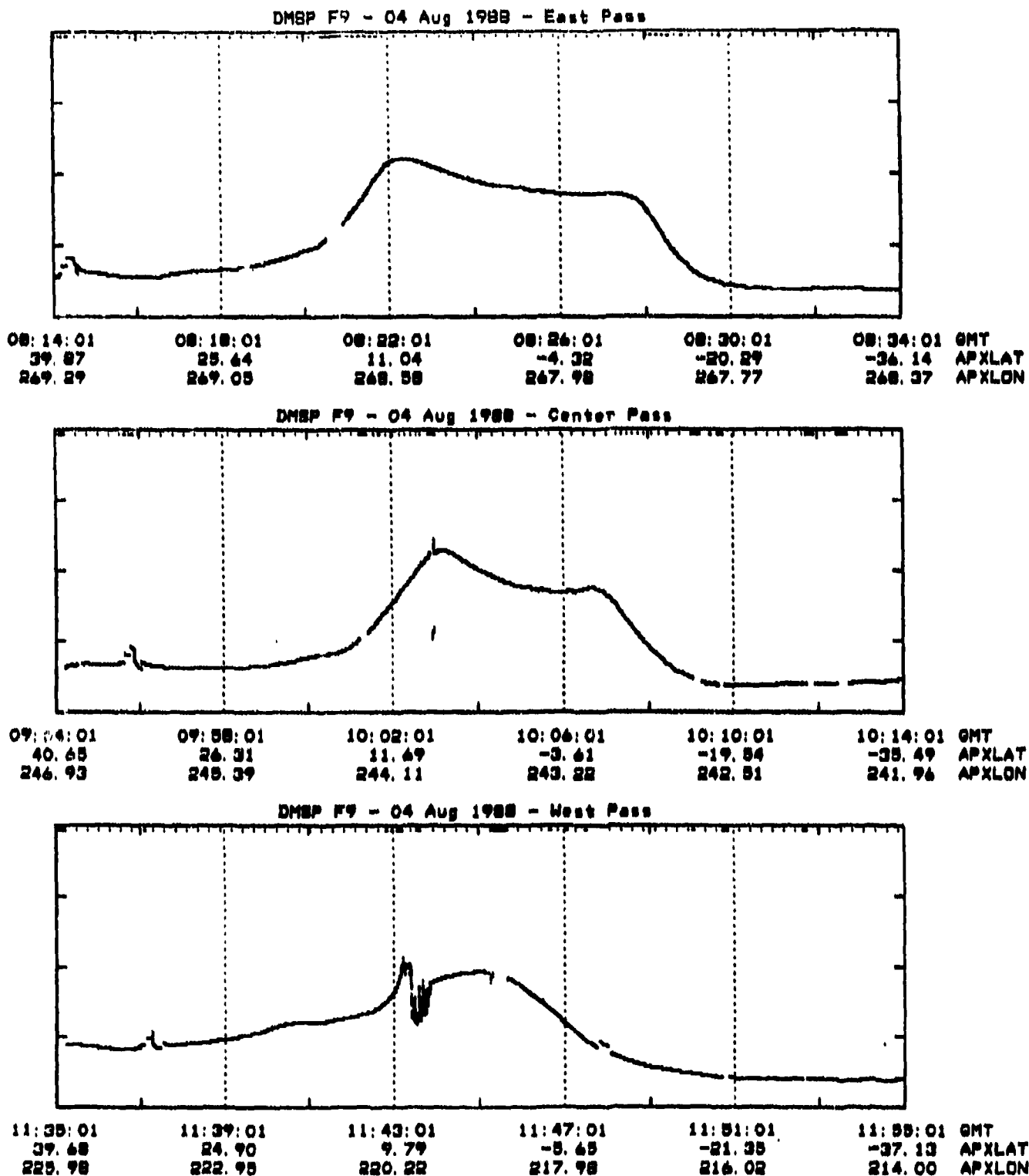


Figure 26b. Total ion density measured by the SM sensor on DMSP F9 near Kwajalein Atoll on 4 August 1988. The axis ranges and labels are as in Figure 1a.

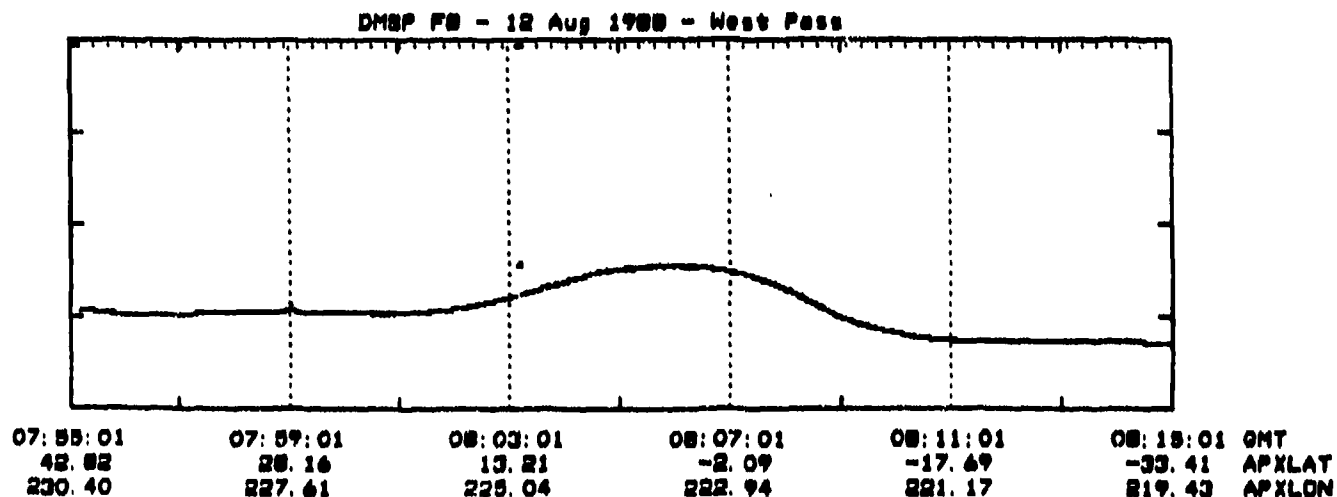
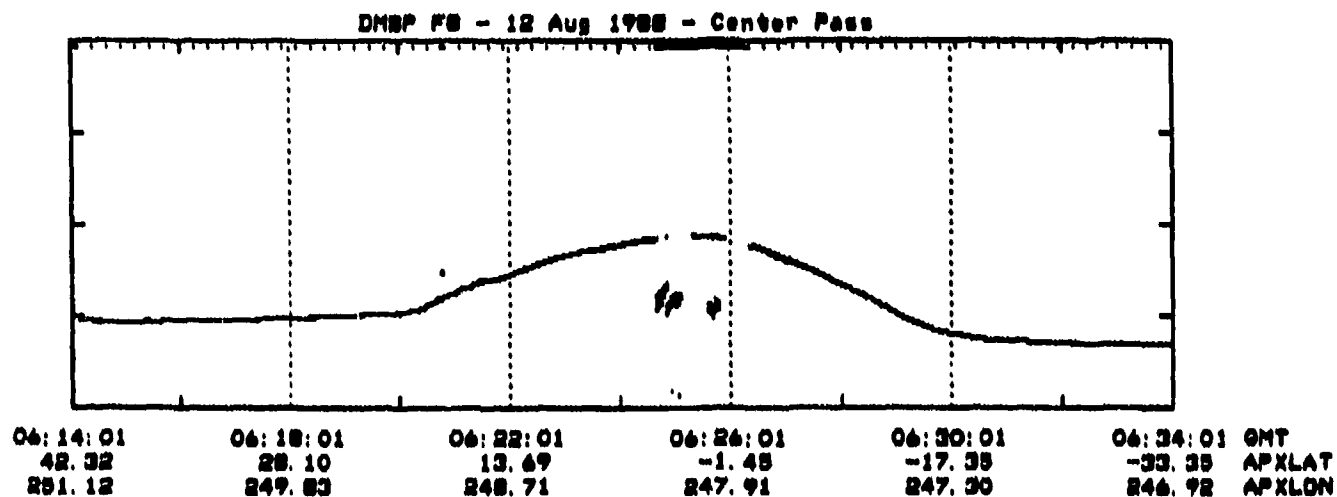
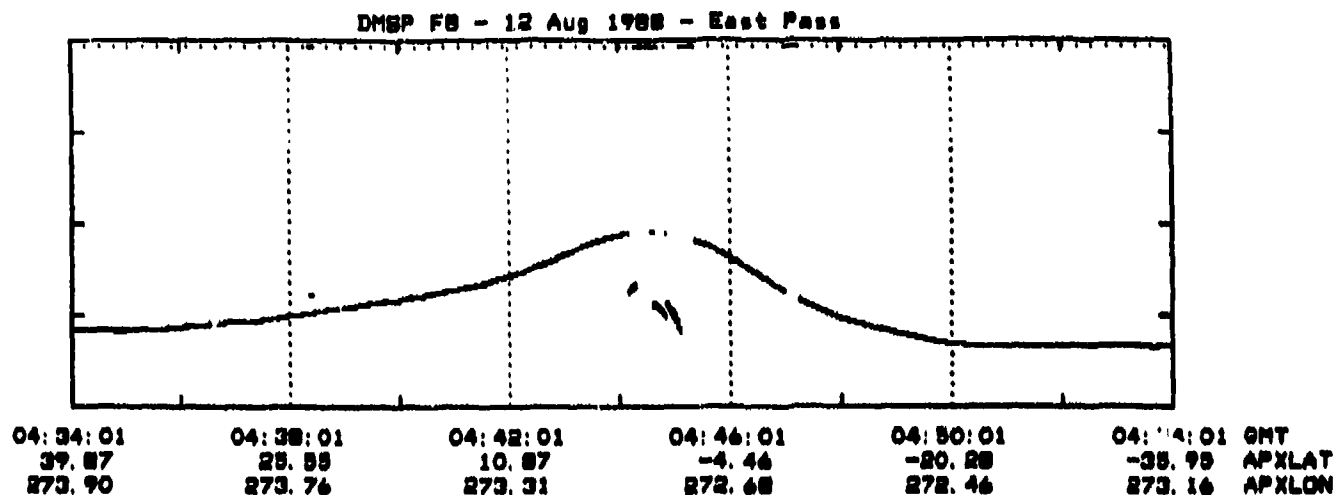


Figure 27a. Total ion density measured by the SM sensor on DMSP F8 near Kwajalein Atoll on 12 August 1988. The axis ranges and labels are as in Figure 1a.

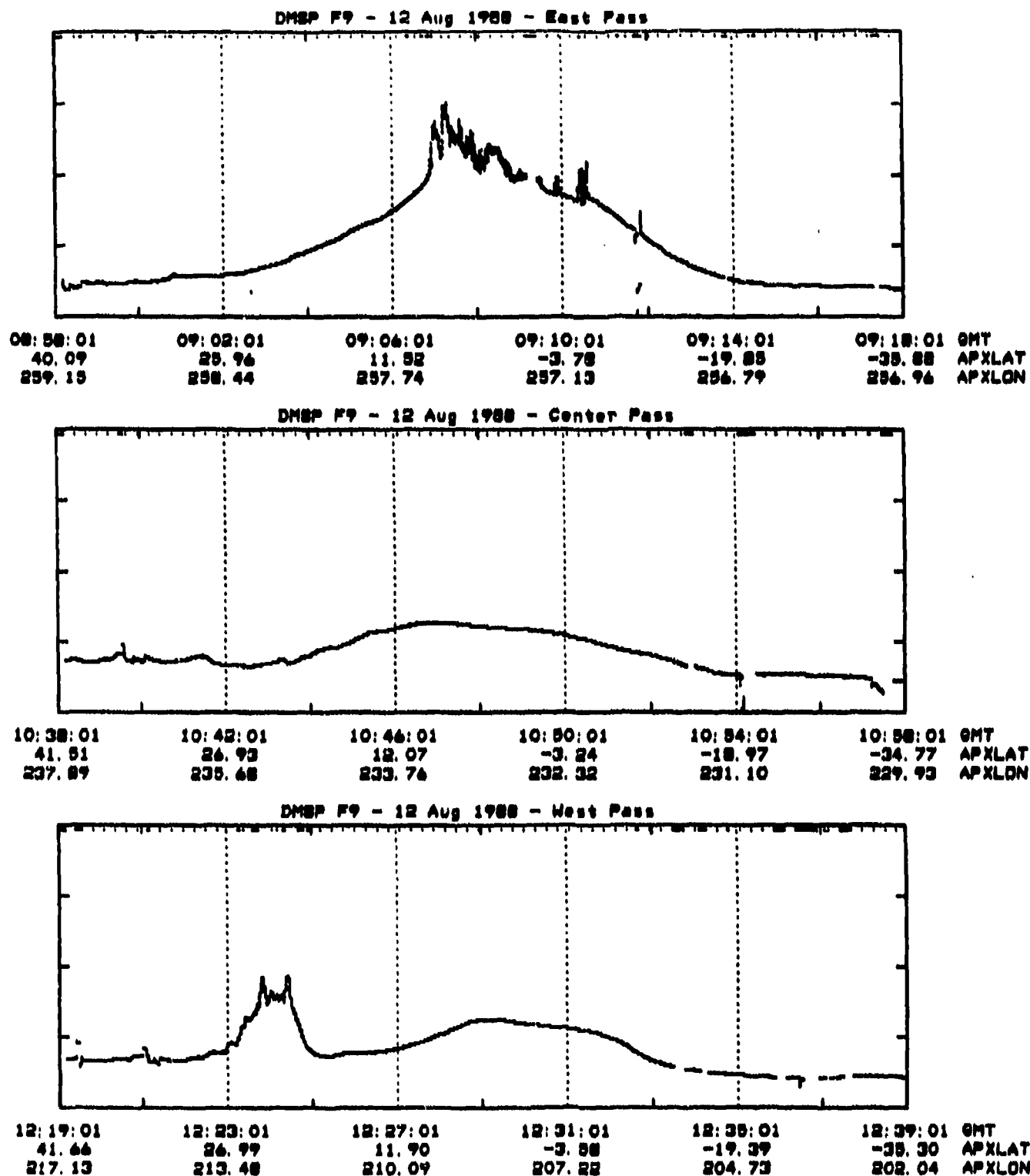


Figure 27b. Total ion density measured by the SM sensor on DMSP F9 near Kwajalein Atoll on 12 August 1988. The axis ranges and labels are as in Figure 1a.

Kwajalein on that day, the top plot is from the prior pass (east of Kwajalein), and the bottom plot is from the following pass (west of Kwajalein). The density scale is the same in all plots, ranging (linearly) from 0.0 to  $2.0 \times 10^5$  ion/cm<sup>3</sup>. (Note: The density plots "wrap-around" if the density is over  $2.0 \times 10^5$ ; i.e., a density of  $3.0 \times 10^5$  is plotted at  $1.0 \times 10^5$ .)

These six days were chosen to illustrate a number of features and behaviors noted in the data set as a whole. The center F9 pass in Figure 22b (24 August) is what could be considered a "classical" plume signature - a smoothly varying density that suddenly drops into a highly structured depletion and just as suddenly returns to a smooth trace. Our expectation when entering this study was that when we encountered a plume, or a patch of irregularities, this is the signature we would see. In fact, this case is one of the few of this type found in the entire data set. Figure 23b (31 August) shows several examples which are more typical of what was observed. All three F9 passes show areas of structured plasma, but only the center one is even remotely like a "classical" plume, and none of the three is very similar to the other two. (Note: The "fuzz" on the density trace in the east pass from F8 is an instrumental artifact of some sort. This effect shows up on several plots. The dashed-line effect in this plot is an example of the "freezing" problem described earlier.) The range of behavior observed in the set is bracketed by the plots in Figures 24 (13 August) and 25 (28 August). The density traces in Figure 24 are featureless save an occasional instrumental anomaly, and the large plume structure in Figure 25b is the largest in both latitudinal extent and in "depth" found in the data set.

The final two sets are included to illustrate other behaviors noted in the full set. We had been expecting, again with some naivete, to see a "double-hump" signature in the ion density centered on the geomagnetic equator and associated with the Appleton anomaly, particularly in the F8 data taken near the sunset terminator. In fact, this type of signature was seen in only 9% of the passes (16 of 186). Figure 26 (4 August) shows the passes from the only day in which a majority of the passes showed this signature. The small structure shown in the west F9 pass near 8° latitude, with a density enhancement adjacent to a more nearly classical depletion signature, is more typical of the irregularity structures seen in this data set than the classical signature shown in Figure 22. Finally, the west F9 plot in Figure 27 (12 August) shows a feature that is, at this time, a puzzle. It does not appear to be an instrumental artifact, and a nearly identical feature appeared in nearly the same location in the west F9 pass on 8 August. Best guesses to date on what they might be are either a large TID-like structure or the result of a very localized piston-like heave of the ionosphere from below, forcing ionization up field lines to regions of lower loss. These two features were not included in this study as irregularity structures, but it would be interesting to find out what they really are.

Once the catalog was completed, a small database was constructed for comparison with the other data sets that contained, for each day, the maximum density in each of the passes exclusive of density in an irregularity structure or in odd features such as that shown in Figure 27, and a flag indicating whether an irregularity structure was found in one of the F9 passes. No irregularity flags were required for the F8 passes, as none of these passes

showed any structure. The variation of the maximum density for the east, center, and west passes for both satellites through the month are shown in Figures 28 and 29. The x's along the abscissa indicate days on which irregularity structures were observed in the F9 data. In the F8 plots, the x's mark days in which the corresponding F9 pass (east, center, or west) showed a structure. (Note the difference in the density scale between the F8 and F9 plots.)

#### 4.3.2 FLTSAT $S_4$ Data

Figure 30 shows the Kwajalein-FLTSAT UHF  $S_4$  data summary plots provided by Roland Tsunoda. The times of the nearest passes from both F8 and F9 are indicated on these plots by an 8 or 9, respectively. A circled "9" indicates that an irregularity structure was observed on that F9 pass. The vertical lines crossing all plots on each page at 0710 GMT and 1030 GMT indicate the times at which the nearest F8 or F9 pass would be overhead at Kwajalein. All F8 (F9) passes to the left of the 0710 GMT (1030 GMT) line are east of Kwajalein, and all passes to the right of the line are west of Kwajalein. The heavy horizontal lines on these plots indicate times at which the Altair radar was being operated as part of the PEAK experiment, and the X's indicate times of questionable data (interference, equipment problems, etc.). The FLTSAT satellite is located on the equator at 172° east longitude, so the ionospheric penetration point is very near to Kwajalein. For the purposes of this study, we will assume that it is at Kwajalein. A daily (or nightly) scintillation "severity index," defined as the number of hours during the observing period that  $S_4$  was above 0.5, was generated for each of the days shown in Figure 28 and added to the database generated from the DMSP SM data. In a recent discussion of these data with Roland Tsunoda, we requested Altair longitude-sweep maps (if available) for the times of the F9 center passes on 8, 18, 19, 24, and 25 August. If such data exist, he will try to send preliminary plots in the next month.

The plots in Figure 31 are taken from the DMSP/FLTSAT database we have generated. The top plot shows the variation of the 10.7 cm solar radio flux (solid line) and the daily  $A_p$  index (bar plot) for the month of August, 1988. As can be seen from the  $A_p$  plot, the entire month was fairly quiet geomagnetically, with only two moderately disturbed periods. The center plot shows the variation of the average of the three maximum ion densities for each day for F8 (solid line) and F9 (dotted line). The bottom plot shows the variation of the number of hours that  $S_4$  on the FLTSAT link was above 0.5 (solid line) and the days and passes on which an irregularity structure was observed in the F9 data (x marks). (The lower part of this last plot is interpreted as follows: an x in the upper position for a given day (such as on 12 August) indicates that a structure was observed on the east pass, an x in the center position (24 August) indicates one in the center pass, and an x in the lower position (9 August) indicates one in the west pass. On 31 August, for instance, all three passes showed structuring.)

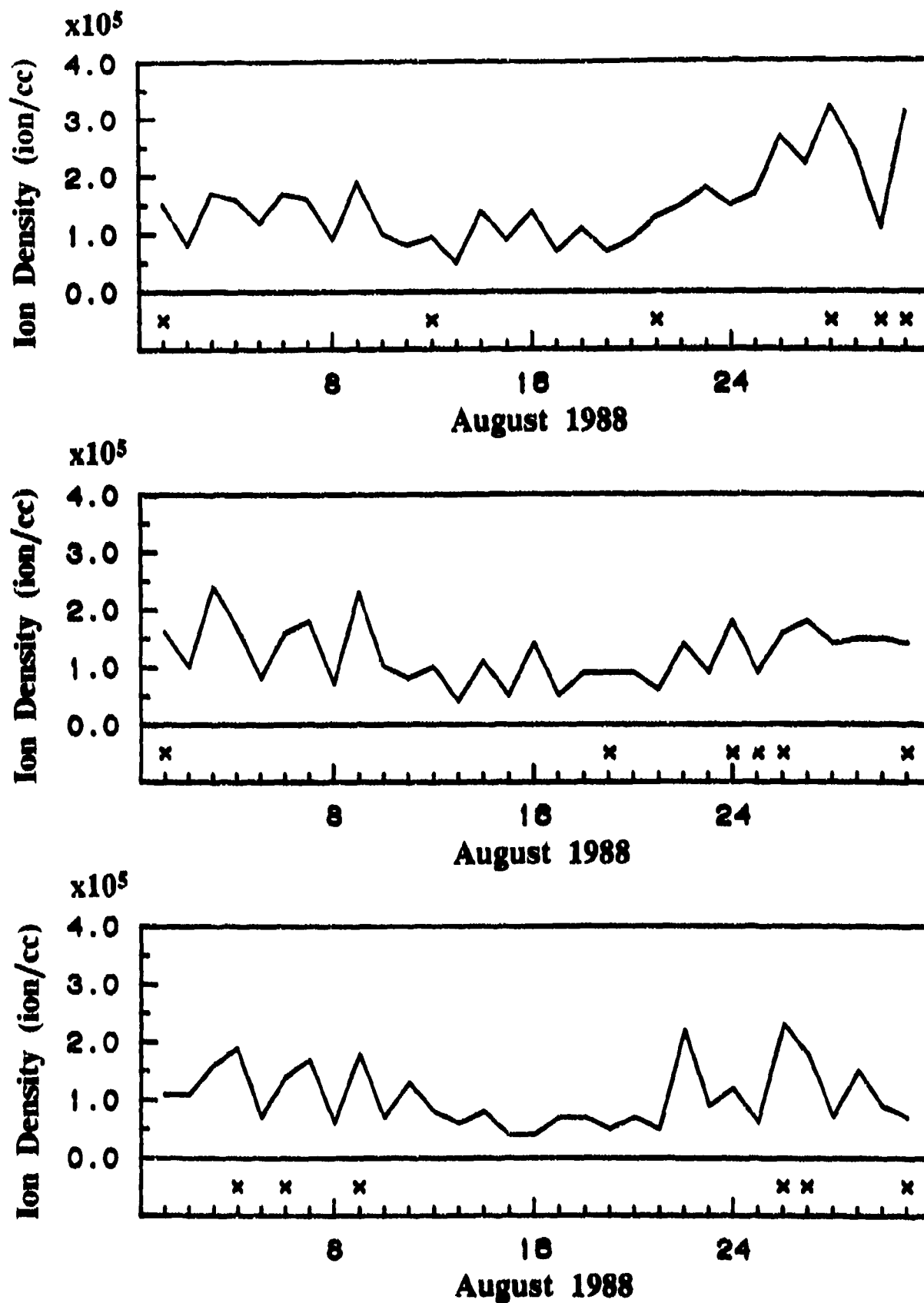


Figure 28. The maximum density observed on DMSP F8 passes in the east (top plot), center (middle plot), and west (bottom plot) sectors for August 1988. The x's indicate that the corresponding F9 pass in that same sector showed an irregularity structure.

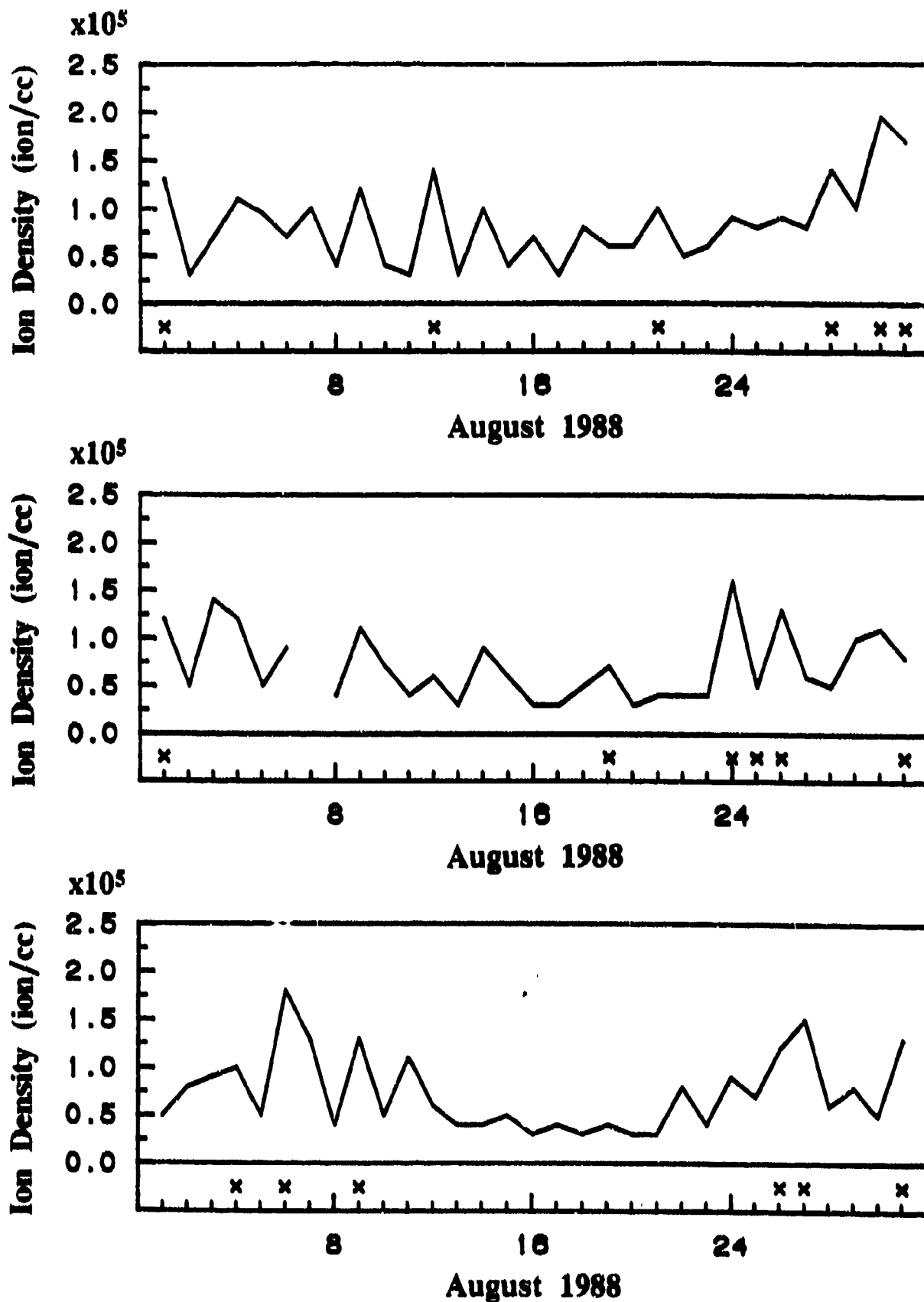


Figure 29. The maximum density observed (outside of irregularity structures) on DMSP F9 passes in the east (top plot), center (middle plot), and west (bottom plot) sectors for August 1988. The x's indicate that an irregularity structure was seen in that pass.

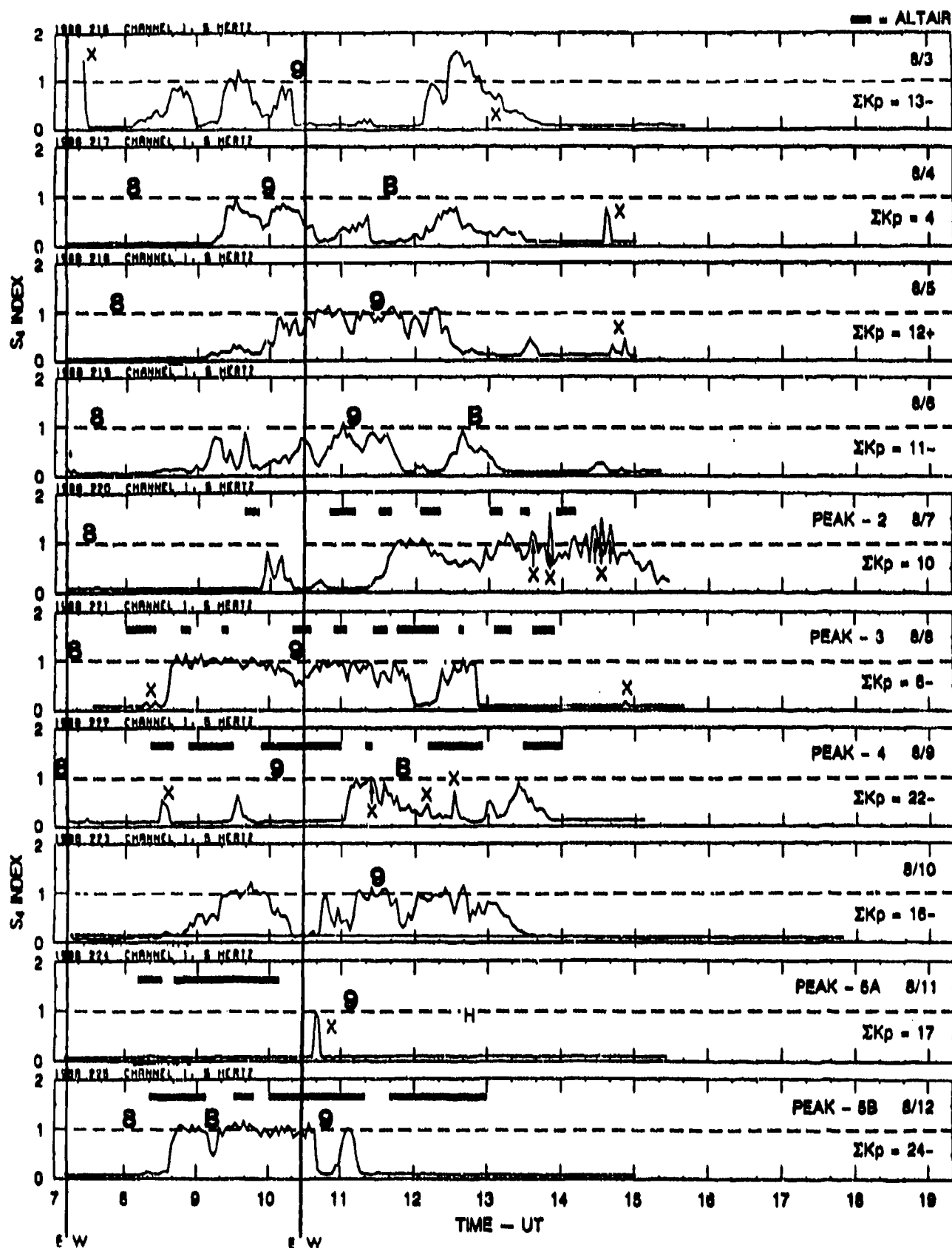


Figure 30. VHF (250 MHz) intensity scintillation ( $S_4$  index) observed on a Kwajalein-FLTSAT satellite communications link during August 1988. The 8 and 9 marks indicate times of DMSP F8 and F9 center passes, circled 9 marks indicate center F9 passes with irregularity structures, B marks indicate east or west F9 passes with irregularity structures, and the heavy vertical lines at 0710 GMT and 1030 GMT indicate times at which an F8 or F9 pass is overhead at Kwajalein.

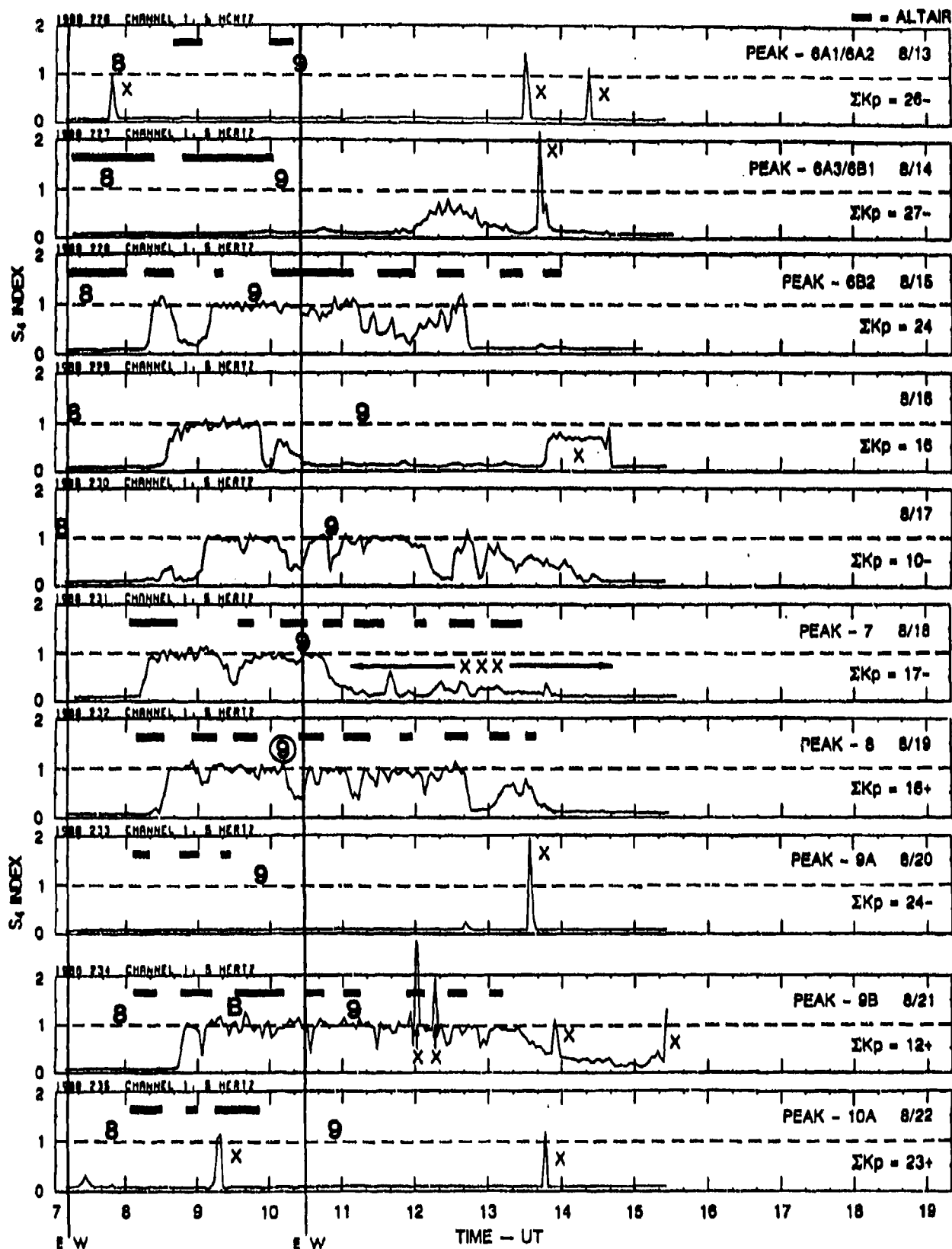


Figure 30. (Continued)

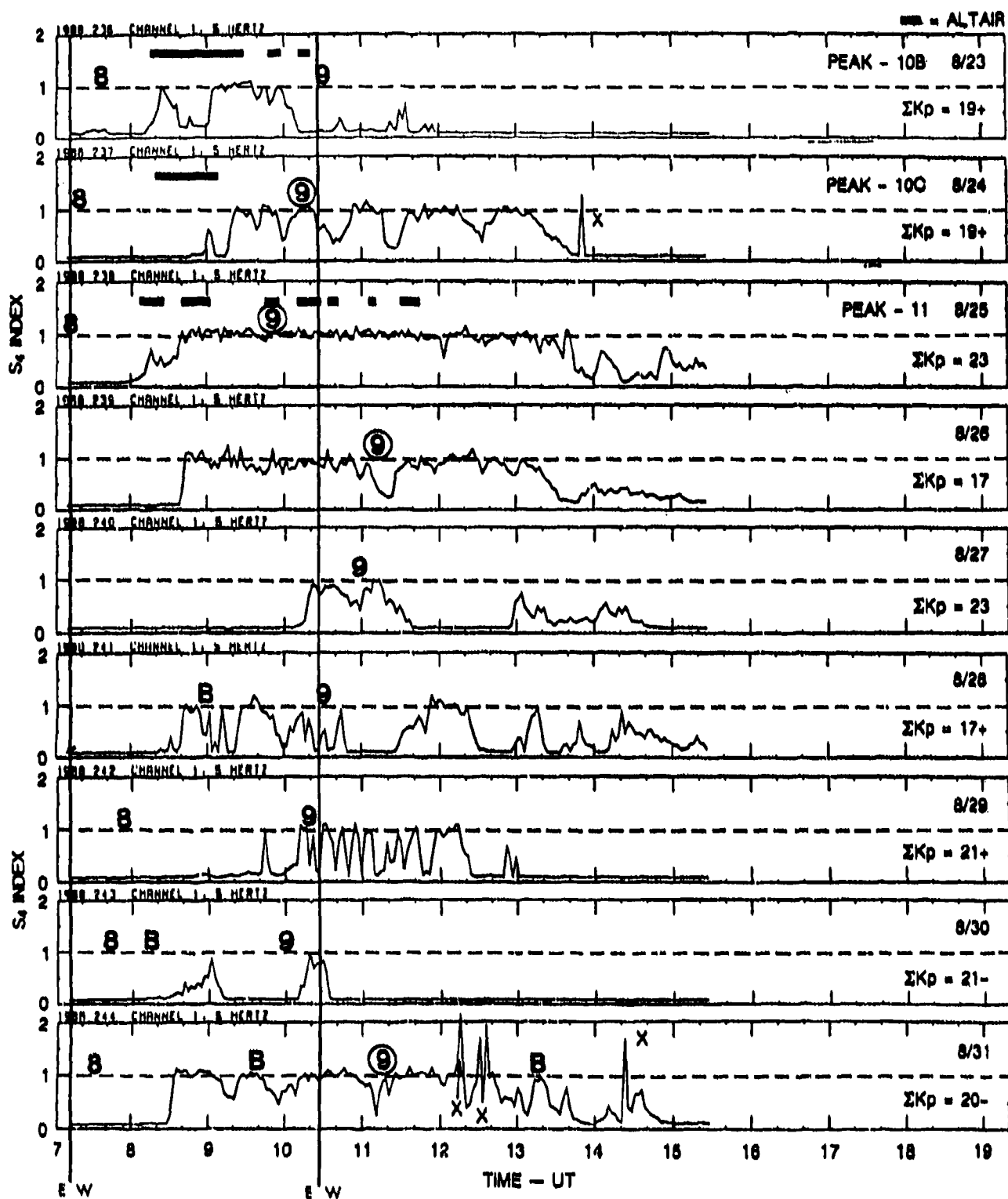


Figure 30. (Concluded)

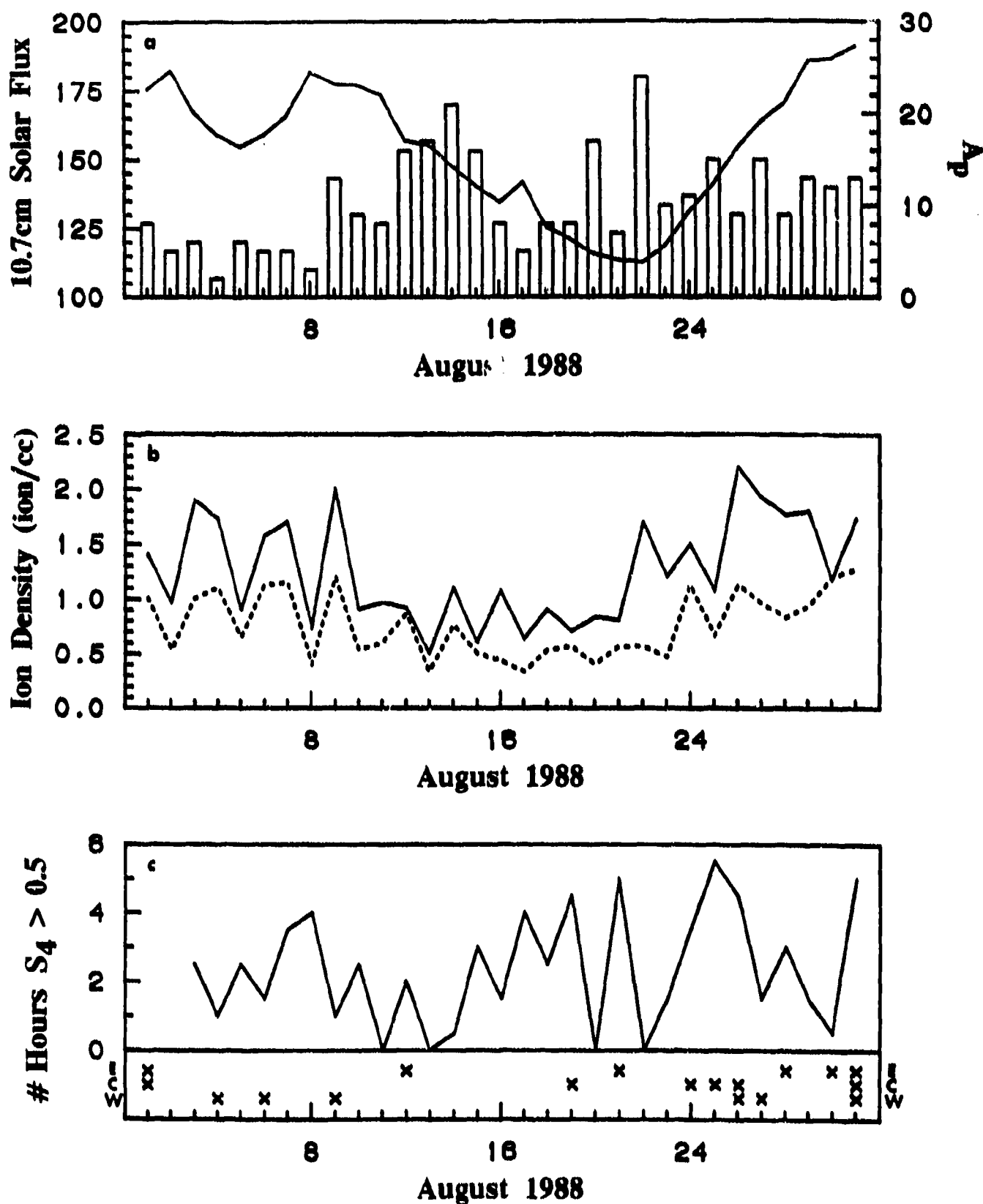


Figure 31. Plots of (a) 10.7cm solar radio flux (solid line) and the daily  $A_p$  planetary magnetic index (bars); (b) the average maximum ion density observed in the three DMSP passes near Kwajalein for F8 (solid line) and F9 (dotted line); and (c) the number of hours that  $S_4$  was greater than 0.5 on the FLT SAT link (solid line) and the F9 passes on which irregularity structures were observed (x's; E - East, C - Center, W - West) for August 1988.

### 4.3.3 HiLat/Polar BEAR $S_4$ Data

The final data set included in this study is a database of UHF (413 MHz) and L-band (1239 MHz) intensity scintillation observations ( $S_4$ ) from HiLat and Polar BEAR passes collected by the ROVER receiver at Kwajalein. This database has 1445  $S_4$  observations from 55 passes taken between 1 and 29 August covering a local time interval of 1800 through 0100. Figures 32 and 33 are scatter plots of the UHF and L-band  $S_4$  values in this database, respectively, plotted against the date. The dotted line at  $S_4 = 0.2$  indicates the estimated noise threshold for this data set (Lansinger, private communication), and the dashed line is at  $S_4 = 1.0$ . As in the lower plot in Figure 31, the dates and passes on which structures were found in the F9 data are identified in the lower section of both plots.

### 4.4 Discussion of Results

It is obvious from the comparisons of the FLTSAT  $S_4$  and ROVER  $S_4$  to the DMSP structure observations (lower plot in Figures 31-33) that *in situ* density observations from a satellite in the nominal DMSP orbit will not provide an unambiguous indication that intense scintillation is occurring in a particular longitudinal sector. There are only two unequivocal statements that can be made from a comparison of the scintillation activity at Kwajalein and the presence (or absence) of irregularity structures in the F9 data: (1) if an irregularity structure is observed in the F9 center pass (5 cases), UHF scintillation at  $S_4$  levels greater than 0.5 were observed at Kwajalein, and (2) if there was no scintillation observed at Kwajalein (4 cases), there were no irregularity structures in any of the three F9 passes for that day. In other words, if an irregularity structure is observed, it is a good indication of intense scintillation activity in that longitude sector, and if no scintillation is being observed on the ground for an entire evening, it is very unlikely that an irregularity structure would be observed by any DMSP pass through that longitude sector. What cannot be said, unfortunately, is that if there are no irregularity structures in the DMSP data then there is no scintillation in that sector. The periods 7-8 and 15-17 August are prime examples of cases where such a statement is completely false: the F9 data showed no evidence of irregularity structures in any of the three passes on these days, but both the FLTSAT and ROVER data sets showed substantial scintillation levels.

These results point up the main difficulty in using the DMSP data for scintillation monitoring in the equatorial region - the satellite must pass through the irregularity structure in order to see it. This is a seemingly simple observation, but one which is complicated by the facts that (1) the plume structures which are thought to be the main source of the equatorial irregularities seen by DMSP are elongated along the magnetic field direction and have a (relatively) limited longitudinal extent, (2) the DMSP orbit is such that it samples only a small longitude range in any given pass, and (3) the DMSP satellite may pass above the irregularities causing the scintillation (either a plume which has not reached 840 km or BSS irregularities). The second point is particularly true in the Kwajalein sector, where the

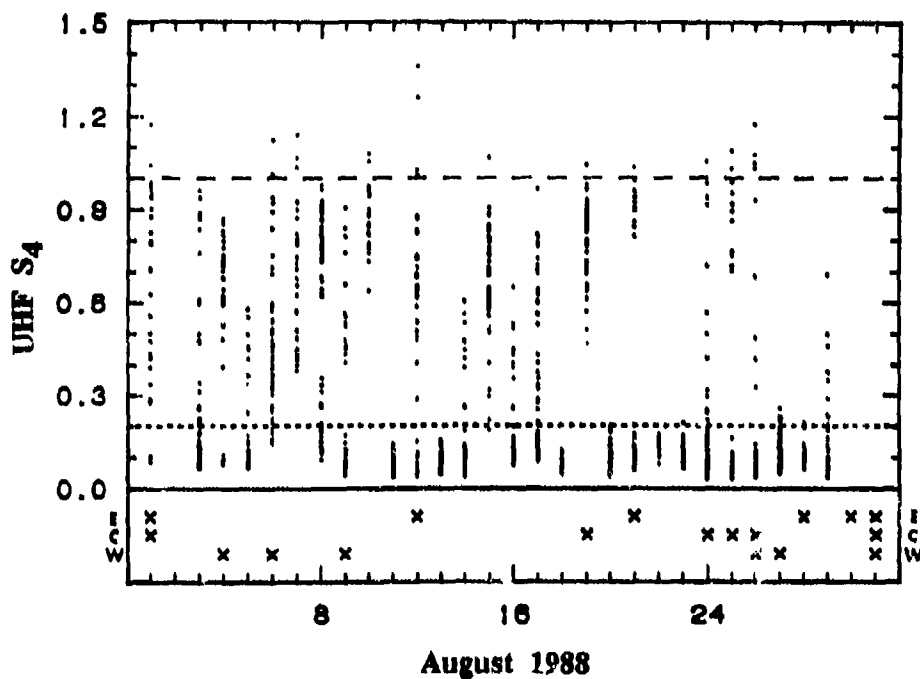


Figure 32. UHF intensity scintillation ( $S_4$  index) observed on the HiLat and Polar BEAR beacons by the ROVER receiver located on Kwajalein Atoll (+s) and the F9 passes on which irregularity structures were observed (x's; E - East, C - Center, W - West) for August 1988. The dashed line indicates theoretical saturation ( $S_4 = 1.0$ ), and the dotted line the effective noise floor of the observations.

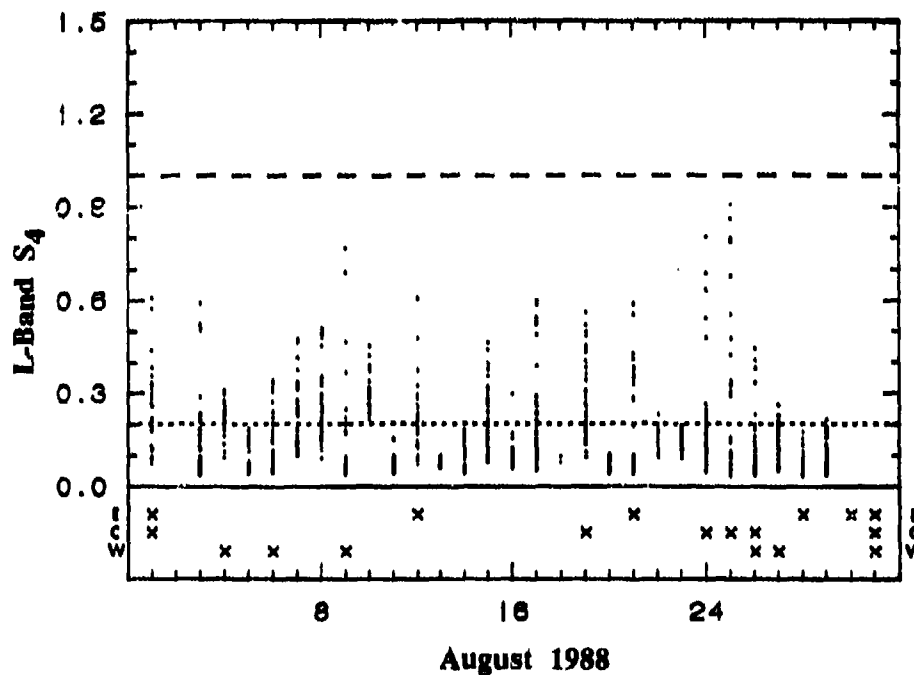


Figure 33. L-band intensity scintillation ( $S_4$  index) observed on the HiLat and Polar BEAR beacons by the ROVER receiver located on Kwajalein Atoll (plotted as in Figure 31).

orbital plane is nearly aligned with the magnetic field direction. Thus, there is a reasonable probability that the satellite could pass between large plume structures and see nothing but a smooth ionosphere on nights when intense scintillation is observed.

This problem was addressed in a study of ion density data from the RPA sensor on the DMSP F2 and F4 satellites by Young *et. al.*<sup>[37]</sup> They developed a two-component model for the probability of observing a plume structure from the DMSP platform. The first component of this model contained all geometry effects (the size and spacing of the plumes and the orientation of the DMSP orbit with respect to the geomagnetic field), and the second component described a density threshold effect observed in their data set. The model assumed that the plumes were randomly (as opposed to uniformly) distributed in longitude and gave the probability of observing a plume structure as

$$P_r = 1 - \left[ \frac{e^{-\mu_o \Lambda}}{1 + \mu_o l} \right] H[N_{1t}(\text{DOY}), N_{1m}] \quad [4]$$

where  $\mu_o$  is the longitudinal plume density;  $l$  is the longitudinal width of the plumes;  $\Lambda$  is the number of degrees of geomagnetic longitude covered by the DMSP orbit between two specified geomagnetic latitudes; and  $H$  is a unit step function, which is zero when the maximum ion density observed in the pass ( $N_{1m}$ ) is less than a threshold value ( $N_{1t}$ , a function of the day of year (DOY)) and one when the observed density is above the threshold. If the plumes are assumed to cover a geomagnetic latitude range of  $20^\circ$  on either side of the dip equator, their analysis of the DMSP observations provided values of 0.11 plumes/deg for  $\mu_o$ ,  $3.4^\circ$  for  $l$ , and values of  $5.6 \times 10^5$  ion/cm<sup>3</sup> and  $1.64 \times 10^5$  ion/cm<sup>3</sup> for  $N_{1t}$  for the spring and autumn equinoxes, respectively. The longitude coverage for the DMSP orbit for the present study varies from just over  $7^\circ$  for the west cases to  $3^\circ$  for the center cases to  $1^\circ$  for the east cases. According to the model, this results in observation probabilities of 66%, 48%, and 35% for the west, center, and east cases, respectively, times the density-threshold step function,  $H$ .

Figure 34, taken from Young *et. al.*<sup>[37]</sup> (their Figure 4), illustrates how they determined the threshold density for the step function. A two-sided ion density distribution function was generated for each of the six data sets in their study, with cases including irregularity structures plotted to the right of the center line and cases without such structures to the left. The two cross-hatched lines indicate the density levels at which the mechanism that creates the irregularity structures (i.e., the plumes) appears to "turn on" in each of the two seasons observed. Figure 35 shows similar plots for the data from the present study. In both plots, each x mark represents a single sector-day case (i.e., center pass on 24 August, west pass on 2 August, etc.). The determination of whether a particular pass is plotted to the right or left of the vertical line is based on whether an irregularity structure was observed in the F9 data for that particular sector-day. In Figure 35a, the maximum density observed in the F9 pass is used to build the distribution; in Figure 35b, the density from the

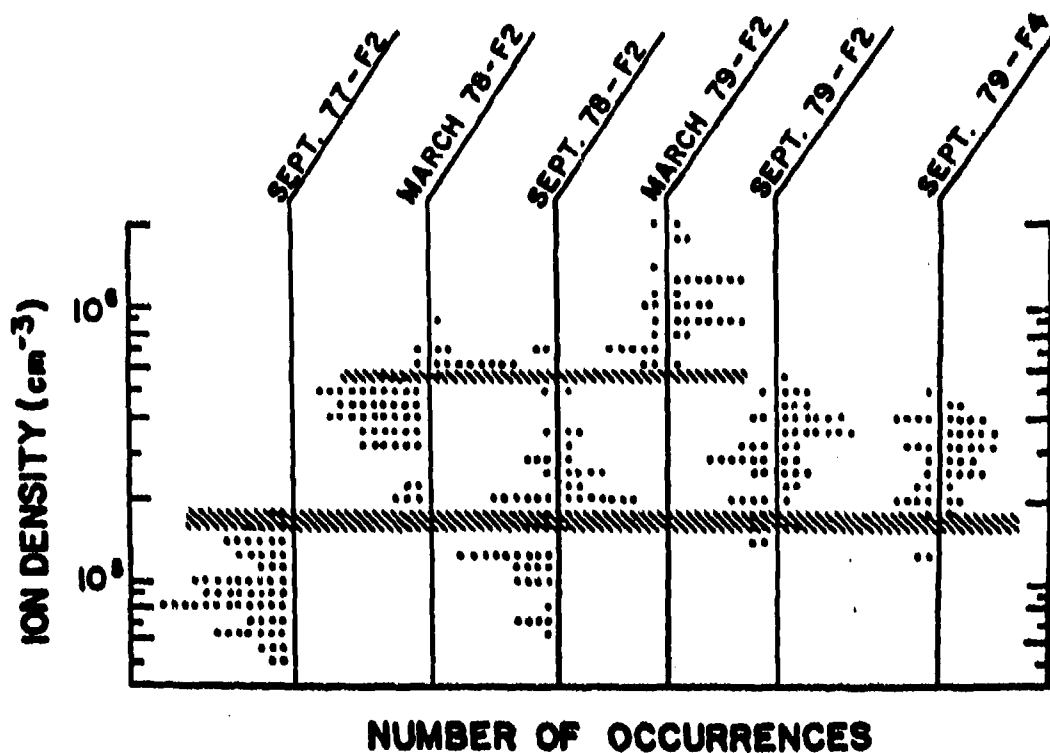


Figure 34. Density distribution of DMSP passes with irregularity structures (right of dividing line) and without (left of line) for six DMSP data sets. The horizontal shaded bands represent the ion density thresholds for March and September. [After Young *et. al.*, 1984.]

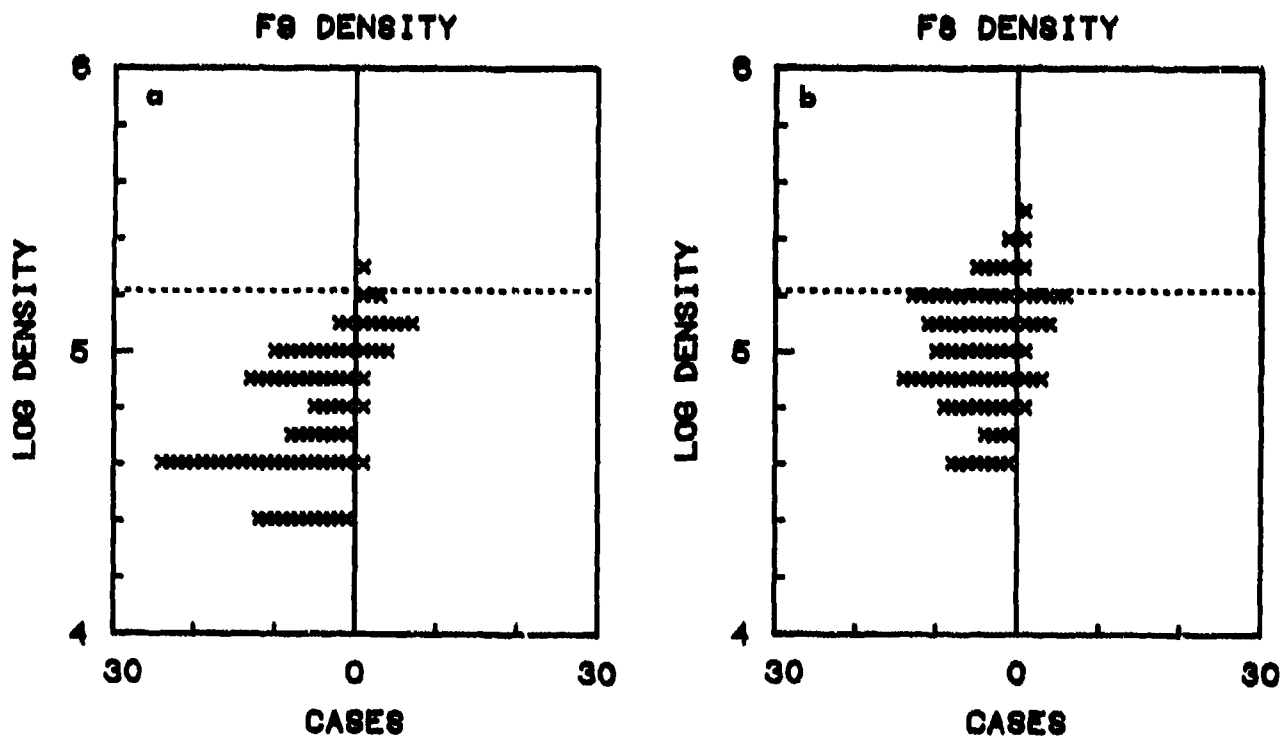


Figure 35. The density distribution of passes with irregularity structures (right of dividing line) and without (left) for the August 1988 data sets. Plot (a) uses the maximum ion density in the F9 pass in which the structure is found, and plot (b) uses the maximum ion density in the F8 pass made earlier in the day in the same sector (east, center, west) as the F9 pass. The dotted line indicates the September threshold from Young, *et. al.* [1984].

F8 pass made in the same sector (east, center, west) as the F9 data used to make the structure/no structure determination is used. The dotted line is the September equinox threshold from Young *et. al.*<sup>[37]</sup> (this line corresponds to the lower threshold limit plotted in Figure 34).

While there is evidence of a threshold effect in Figure 35a, it is at a lower density than reported by Young *et. al.*. While it is not clear where the threshold should be placed, it is at least a factor of two to three lower than that derived in the earlier study. This could be due to problems with the absolute calibrations of the instruments. Young *et. al.* state that their observed densities "exceed some values reported elsewhere," and conclude that they feel that their densities are accurate "within a factor of 2 or better." In the present study to date, we have focused more on the relative changes in the density than on the absolute value of the density, so there are uncertainties in the accuracy of the absolute densities obtained from the SSIES SM sensor. Potential sources of error in the density measurements from the SM sensor are (1) the lack of information about the ion drift velocity in the ram direction due to failure of the RPA sensor, (2) uncertainties in the calibration constants used to convert the telemetry data into densities, (3) a bias due to the sensor not being at zero potential with respect to the surrounding plasma, (4) uncertainties due to plasma flow-dynamics around the satellite, and (5) a non-uniform electrostatic potential pattern in the vicinity of the SM sensor. Since the expected ion drifts are relatively slow in the equatorial region (a few hundred meters/sec), uncertainties due to (1) should be less than 5% or so.

This problem was discussed with R. A. Heelis at UTD<sup>[39]</sup>, who is of the opinion that (5) is a potential source of error in the total ion density measurements, as the SM instrument appears to be measuring only the  $O^+$  ions. In comparisons with density measurements made with the RPA instrument (when it was operational) on the F8 satellite, they found that the total ion density observed by the SM sensor agreed well with that from the RPA when only  $O^+$  was present. When a measurable amount of  $H^+$  was present, the total ion density measured by the SM sensor was less than the sum of the  $O^+$  and  $H^+$  number densities and tended to track the  $O^+$  density. This type of behavior was also seen during the early-orbit checkout of the SSIES instruments on F8<sup>[40]</sup>. A correction for this effect would increase the densities reported by the SM sensor, which would increase any threshold level extracted from Figure 35a. It is difficult to quantify the magnitude of the correction, as it would be a function of the number of  $H^+$  ions present, which in turn is a function of time, location, season, and solar epoch. This issue will need to be addressed after the launch of the next DMSP satellite, when a detailed comparison between the SM and RPA densities can be made.

Figure 35b was generated to see if there would be an observable threshold effect in measurements of the density near local sunset in a particular longitude sector, i.e., in the F8 density observations. As with the F9 density data, there appears to be a threshold effect. It would be premature, however, to attempt to set a threshold value from the present data set for several reasons. First, there are uncertainties in the absolute density measurements;

second, the data set used is not large enough to yield a high level of statistical confidence in any threshold derived from it; third, the data are from a single longitudinal region (central Pacific) which may not be representative of other sectors; and fourth, it is not clear where the threshold should be set. For instance, in Figure 35a should the threshold be set above or below the single structure observation at a log density of 4.6? This feature, located in the center pass on 25 August, is odd (see the appendix), and may be due to an instrument effect<sup>(41)</sup>. (However, this observation was made on a night with nearly 5 hours of saturated intensity scintillation ( $S_4 \approx 1.0$ ) at Kwajalein!)

A second way in which an *in-situ* sensor on a DMSP satellite may not "see" the irregularities that are causing scintillation is that it may be passing above them. There appear to be two situations which may arise: (1) a plume that has not reached 840 km, and (2) BSS irregularities. We hope to be able to address this problem using backscatter data from the Altair radar for several nights, including cases when there was intense scintillation on all of the beacon observations (FLTSAT, HiLat, and Polar BEAR) but no irregularity structures were observed in the F9 data. As mentioned earlier, we hope to obtain the necessary backscatter data prior to the end of the project to address this issue.

Since the overall objective of this study is to assess the potential for characterizing scintillation based on the DMSP observations, Figures 36a and b have been generated to compare the DMSP results to the FLTSAT observations in a form similar to Figure 35. In Figure 36a, the data plotted in Figure 35a have been divided into separate sectors (east, center, west), and the number of hours that  $S_4$  on the FLTSAT link was above 0.5 on the night corresponding to a given pass (in tenths of hours) has been plotted instead of an x mark. The average values listed at the top of each plot in this figure are the average number of hours that  $S_4 > 0.5$  was observed in all structure and non-structure cases. The two cases in each plot shown by \*\* are for the first two days in August, during which the FLTSAT link was not monitored. Figure 36b is similar, but the date of the pass is plotted instead of an x mark.

Two observations may be made from Figure 36a: first, the threshold effect is much clearer in the east and west sectors than in the center sector; and second, the average number of hours with  $S_4 > 0.5$  in the structure cases for the center sector is much larger than that in the non-structure cases, while in the east and west sectors, they are comparable. It is not clear what the first observation is indicating - with such a small data set it may merely be reflecting the "luck of the draw." The second observation, however, may be telling us that, at least in the Pacific sector, passes more than 15° or so from a target transionospheric radio link are of marginal use in determining whether that link will be experiencing scintillation.

Log ( Ion Density ) ( ion/cc )

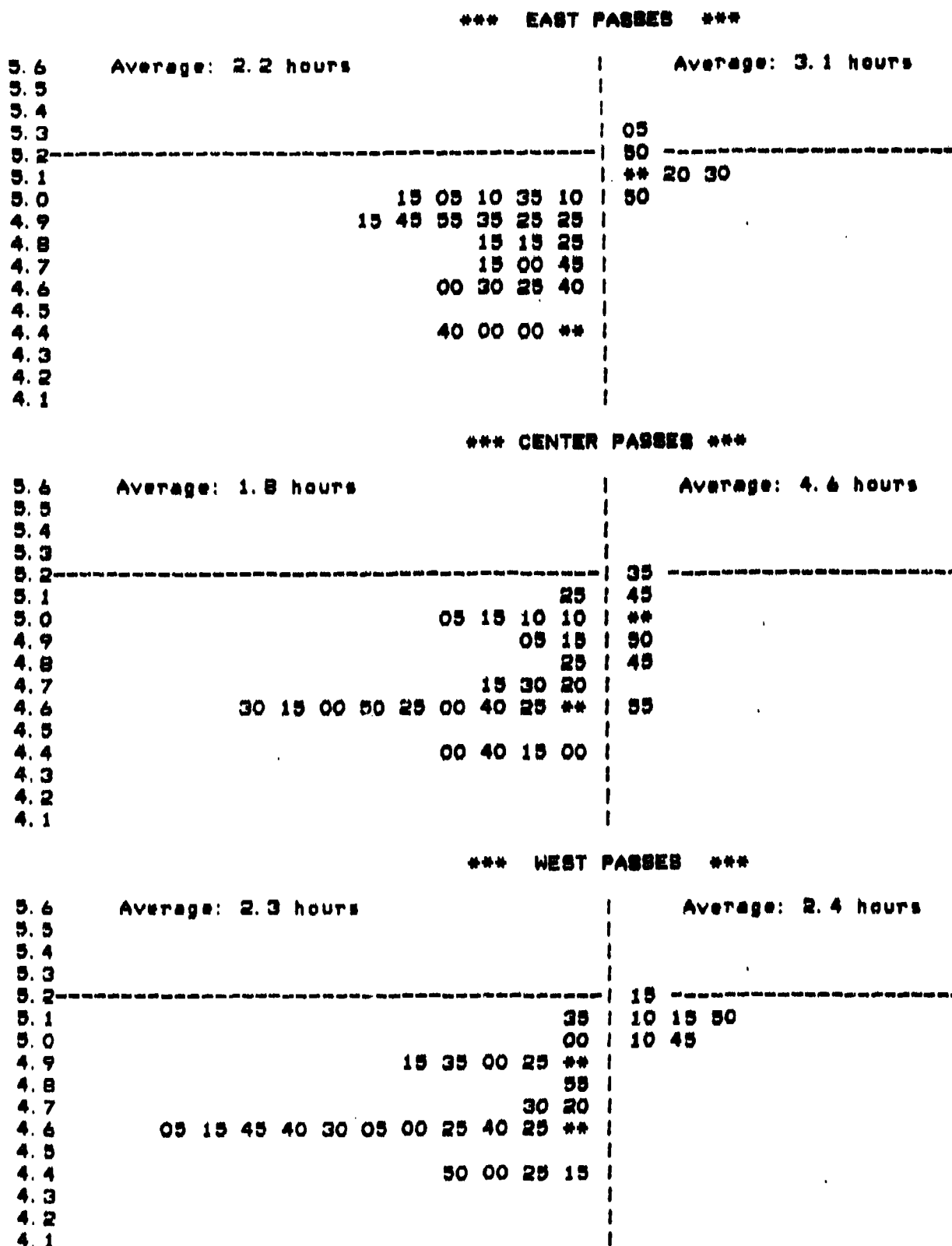
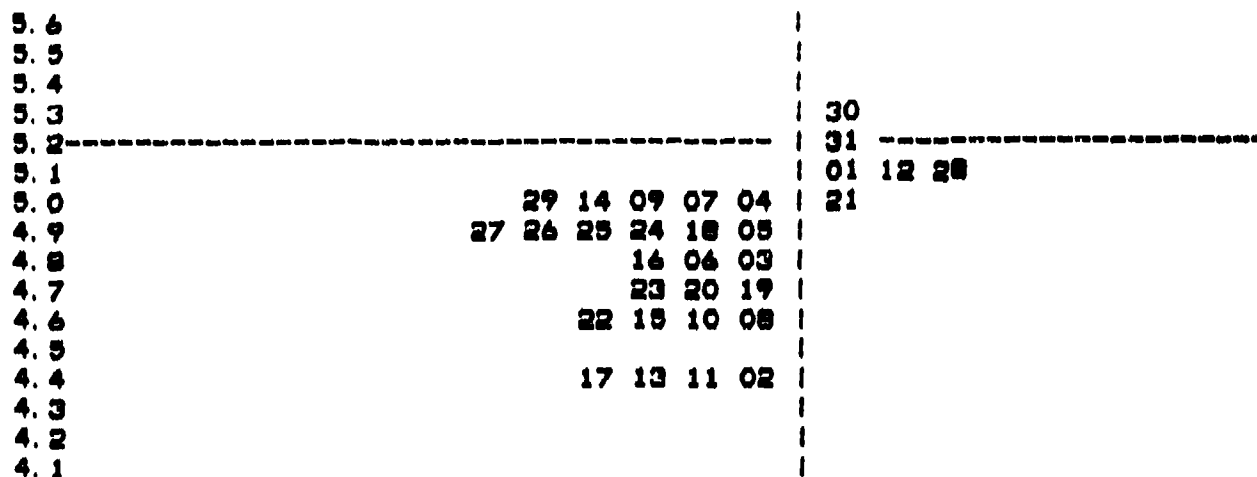
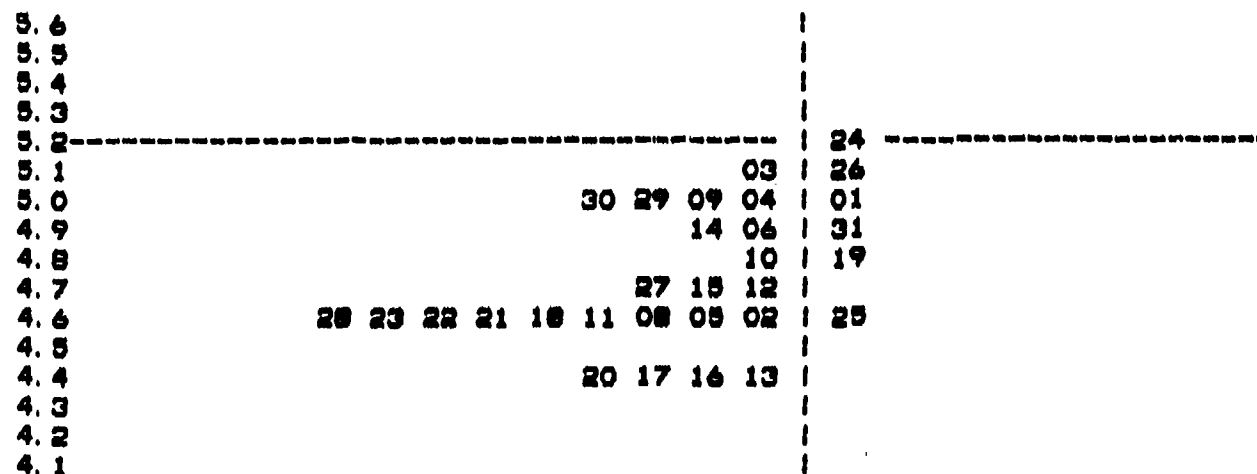


Figure 36a. Density distribution plots for the east, center, and west F9 passes showing the number of hours that  $S_4$  on the FLTSAT link exceeded 0.5 (in tenths of hours; i.e., 55 is 5.5 hours) for the day on which the pass occurred. The dashed line indicates the September threshold from Young *et al.* [1984].

\*\*\* EAST PASSES \*\*\*



\*\*\* CENTER PASSES \*\*\*



\*\*\* WEST PASSES \*\*\*

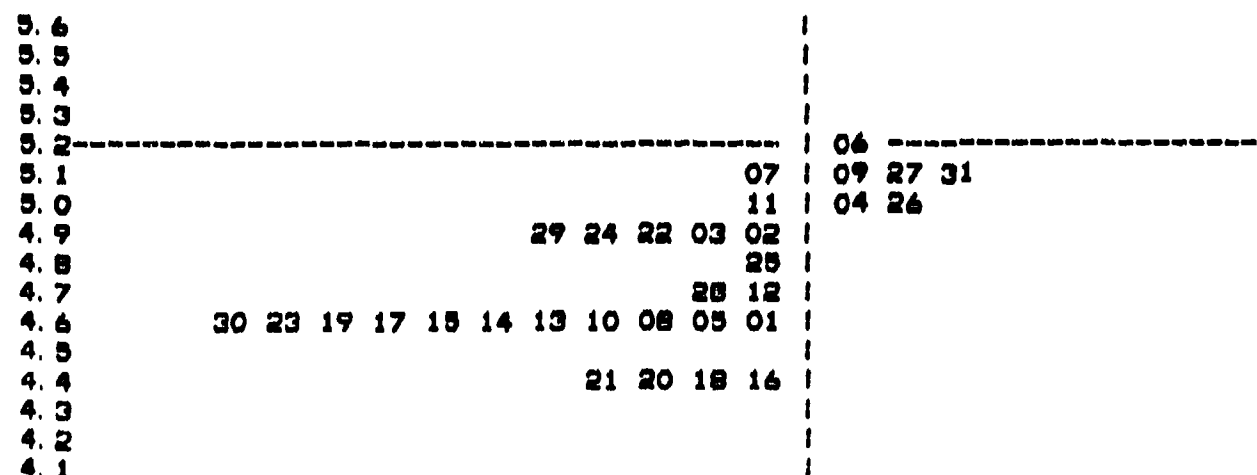


Figure 36b. Density distribution plots for the east, center, and west F9 passes showing the day (in August) on which the pass occurred. The dashed line indicates the September threshold from Young *et al.* (1984).

## 5. Conclusions

During the past year we have (1) completed the analysis of both the *in-situ* (DMSP SSIES) and propagation (AIO-AFSAT) data for one of the near-coincident passes from the January 1988 high-latitude data-collection campaign and (2) conducted an analysis of both *in-situ* (DMSP SSIES) and propagation (FLTSAT, HiLat, and Polar BEAR) data collected near Kwajalein Island during the DNA PEAK campaign. As a result of these analyses, we have reached the following conclusions as to the potential for using the DMSP SSIES data for characterizing scintillation effects:

1. The data show a good potential for use at auroral latitudes. The excellent agreement between the  $S_4$  observed on the AIO-AFSAT link and that generated from the SSIES analysis indicates that the  $C_k L$  estimates calculated from the SM data are fairly accurate. The agreement between the observed phase scintillation parameters and those generated from the SSIES analysis is not as clearly "good" as that between the two estimates of  $S_4$ , but this assessment was difficult to make owing to problems with the AIO-AFSAT phase data and the lack of observations of the *in-situ* drift velocity at the AIO-AFSAT IPP.

2. The excellent agreement between the SSIES and AIO-AFSAT  $S_4$  values was obtained using a model topside distribution, with only the ion density at the satellite altitude as an input, to calculate  $C_k L$  from  $C_k$ .

3. It is not clear exactly how the SSIES data should be used to characterize scintillation in the equatorial region, but it is likely to be more as an indirect indicator of the presence (and possibly the severity) of irregularity plume structures rather than as a direct measure of  $C_k L$ , as at auroral latitudes. The results of our equatorial study were in general agreement with a study made with RPA data from the DMSP F2 and F4 satellites<sup>[36]</sup> which found that (1) an *in-situ* sensor on a satellite in the current DMSP orbit plane will not necessarily pass through plume structures present in the equatorial topside, and (2) there may be a threshold density which can be used to infer the existence of plumes even though they have not been encountered.

It must be emphasized that the primary purpose of this project was to assess the potential for using data from the SSIES sensors to characterize scintillation effects. The results to date indicate that the potential is there, and a larger scale effort should be undertaken to (1) refine and validate the methods developed during this project to calculate  $C_k L$  from the SM data at high latitudes, (2) develop methods for locating the high-latitude scintillation boundary using data from both SSIES and SSJ/4, and (3) develop detailed methods for using the SSIES data to characterize the irregularity environment at equatorial latitudes.

## REFERENCES

- [1] Fremouw, E. J. and Lansinger, J. M., *A Computer Model for High-Latitude Phase Scintillation Based on WIDEBAND Satellite data From Poker Flat*, DNA Report 5685F, Defense Nuclear Agency, Washington, DC, February 1981.
- [2] Secan, J. A., E. J. Fremouw, and R. E. Robins, "A review of recent improvements to the WBMOD ionospheric scintillation model," in *The Effect of the Ionosphere on Communications, Navigation, and Surveillance Systems*, edited by J. Goodman, pp. 607-616, Naval Research Laboratory, Washington, DC, 1987.
- [3] Basu, Su., Basu, S., Weber, E. J., and W. R. Coley, "Case study of polar cap scintillation modeling using DE-2 irregularity measurements at 800 km," in *The Effect of the Ionosphere on Communications, Navigation, and Surveillance Systems*, edited by J. Goodman, pp. 599-606, Naval Research Laboratory, Washington, DC, 1987.
- [4] Rino, C. L., "A power law phase screen model for ionospheric scintillation, 1. Weak scatter," *Radio Sci.*, 14, 1135-1145, 1979.
- [5] Holt, B. J., *Drift Scintillation Meter*, AFGL-TR-84-0103, Air Force Geophysics Laboratory, Hanscom AFB, MA, March 1984. ADA142523.
- [6] Greenspan, M. E., P. B. Anderson, and J. M. Pelagatti, *Characteristics of the Thermal Plasma Monitor (SSIES) for the Defense Meteorological Satellite Program (DMSP) Spacecraft S8 Through S10*, AFGL-TR-86-0227, Air Force Geophysics Laboratory, Hanscom AFB, MA, October 1986. ADA176924.
- [7] Secan, J. A., *An Assessment of the Application of In Situ Ion-Density Data From DMSP to Modeling of Transionospheric Scintillation*, Scientific Report No. 1, AFGL-TR-87-0269, Air Force Geophysics Laboratory, Hanscom AFB, MA, September 1987. ADA188919.
- [8] Secan, J. A. and R. M. Bussey, *An Assessment of the Application of In Situ Ion-Density Data From DMSP to Modeling of Transionospheric Scintillation*, Scientific Report No. 2, AFGL-TR-88-0280, Air Force Geophysics Laboratory, Hanscom AFB, MA, September 1988. ADA202415.
- [9] Secan, J. A., *Use of Apex Coordinate Transformation Tables*, NWRA-CR-87-R020, Northwest Research Associates, Inc., Bellevue, WA, 1987.
- [10] VanZandt, T. E., W. L. Clark, and J. M. Warnick, "Magnetic apex coordinates: a magnetic coordinate system for the ionospheric F2 layer," *J. Geophys. Res.*, 77, 2406-2411, 1972.

- [11] Fremouw, E. J., J. A. Secan, and J. M. Lansinger, *Operation of and Reduction of Data from DNA's "ROVER" Satellite Ground Station, Progress Report No. 2*, DNA Contract DNA001-88-C-0001, Northwest Research Associates, Inc., Bellevue, WA, 1988.
- [12] Livingston, R. C., Private communication, 1989.
- [13] Livingston, R. C., "Morphology of Scintillation in the Vicinity of the Polar-Cap Boundary," presented at HiLat/Polar BEAR Science Team Meeting, 26-27 July 1988, Springfield, VA.
- [14] Basu, Su. and S. Basu, "Equatorial scintillations: advances since ISEA-6," *J. Atmosph. Terr. Phys.*, **47**, 753-768, 1985.
- [15] Hanson, W. B. and S. Sanatani, "Large  $N_i$  gradients below the equatorial F peak," *J. Geophys. Res.*, **78**, 1167-1173, 1973.
- [16] Woodman, R. F. and C. La Hoz, "Radar observations of F region equatorial irregularities," *J. Geophys. Res.*, **81**, 5447-5466, 1976.
- [17] Tsunoda, R. T., R. C. Livingston, J. P. McClure, and W. B. Hanson, "Equatorial plasma bubbles: vertically elongated wedges from the bottomside F layer," *J. Geophys. Res.*, **87**, 9171-9180, 1982.
- [18] Valladares, C. E., W. B. Hanson, J. P. McClure, and B. L. Cragin, "Bottomside sinusoidal irregularities in the equatorial F region," *J. Geophys. Res.*, **88**, 8025-8042, 1983.
- [19] Basu, S., Su. Basu, C. E. Valladares, A. DasGupta, and H. E. Whitney, "Scintillations associated with bottomside sinusoidal irregularities in the equatorial F region," *J. Geophys. Res.*, **91**, 270-276, 1986.
- [20] Kelley, M. C., "Equatorial spread-F: recent results and outstanding problems," *J. Atmosph. Terr. Phys.*, **47**, 745-752, 1985.
- [21] Zalesak, S. T., S. L. Ossakow, and P. K. Chaturvedi, "Nonlinear equatorial spread-F: The effect of neutral winds and background Pedersen conductivity," *J. Geophys. Res.*, **87**, 151-166, 1982.
- [22] Burke, W. J., D. E. Donatelli, R. C. Sagalyn, and M. C. Kelley, "Low density regions observed at high altitudes and their connection with equatorial spread-F," *Planet. Space Sci.*, **27**, 593-599, 1979.

- [23] Benson, R. F., "Remote detection of the maximum altitude of equatorial ionospheric plasma bubbles," in *Effect of the Ionosphere on Radiowave Systems*, edited by J. Goodman, pp. 244-252, Naval Research Laboratory, Washington, DC, 1982.
- [24] Weber, E. J., H. C. Brinton, J. Buchau, and J. G. Moore, "Coordinated airborne and satellite measurements of equatorial plasma depletions," *J. Geophys. Res.*, **87**, 10503-10513, 1982.
- [25] Anderson, D. N., A. D. Richmond, B. B. Balsley, R. G. Roble, M. A. Biondi, and D. P. Sipler, "In-situ generated gravity waves as a possible seeding mechanism for equatorial spread-F," *Geophys. Res. Lett.*, **9**, 789-792, 1982.
- [26] Kelley, M. C., M. F. Larsen, C. LaHoz, and J. P. McClure, "Gravity wave initiation of equatorial spread-F: A case study," *J. Geophys. Res.*, **86**, 9087-9100, 1981.
- [27] Rastogi, R. G., "Seasonal variation of equatorial spread-F in the American and Indian zones," *J. Geophys. Res.*, **85**, 722-725, 1980.
- [28] Muldrew, D. B., "The formation of ducts and spread F and the initiation of bubbles by field-aligned currents," *J. Geophys. Res.*, **85**, 613-625, 1980.
- [29] Maruyama, T. and N. Matuura, "Longitudinal variability of annual changes in activity of equatorial spread F and plasma bubbles," *J. Geophys. Res.*, **89**, 10903-10912, 1984.
- [30] Maruyama, T., "A diagnostic model for equatorial spread F, 1. Model description and application to electric field and neutral wind effects," *J. Geophys. Res.*, **93**, 14611-14622, 1988.
- [31] Tsunoda, R. T., "Control of the seasonal and longitudinal occurrence of equatorial scintillation by the longitudinal gradient in integrated E region Pedersen conductivity," *J. Geophys. Res.*, **90**, 447-456, 1985.
- [32] Cragin, B. L., C. E. Valladares, W. B. Hanson, and J. P. McClure, "Bottomside sinusoidal irregularities in the equatorial F region, 2. cross correlations and spectral analysis," *J. Geophys. Res.*, **90**, 1721-1734, 1985.
- [33] Basu, Su., S. Basu, and B. K. Kahn, "Model of equatorial scintillations from in situ measurements," *Radio Sci.*, **11**, 821-832, 1976.
- [34] Burke, W. J., D. E. Donatelli, and R. C. Sagalyn, "The longitudinal distribution of equatorial spread F plasma bubbles in the topside ionosphere," *J. Geophys. Res.*, **85**, 1335-1340, 1980.

- [35] Basu, Su., S. Basu, J. P. McClure, W. B. Hanson, and H. E. Whitney, "High resolution topside in situ data of electron densities and VHF/GHz scintillations in the equatorial region," *J. Geophys. Res.*, 88, 403-415, 1983.
- [36] Hoegy, W. R., S. A. Curtis, and L. H. Brace, "Electron density irregularities observed on DE-2," in *Effect of the Ionosphere on C3I Systems*, edited by J. Goodman, pp. 463-471, Naval Research Laboratory, Washington, DC, 1984.
- [37] Young, E. R., W. J. Burke, F. J. Rich, and R. C. Sagalyn, "The distribution of topside spread F from in situ measurements by Defense Meteorological Satellite Program: F2 and F4," *J. Geophys. Res.*, 89, 5565-5574, 1984.
- [38] Secan, J. A., and R. M. Bussey, *DMSP SSIES Flight Data Processor System Documentation, Volume III. Program Maintenance Manual*, NWRA-CR-87-R001, Northwest Research Associates, Inc., Bellevue, WA, 1987.
- [39] Heelis, R. A., Private communication, 1989.
- [40] Secan, J. A., and R. M. Bussey, *DMSP SSIES Flight Data Processor System Documentation, Volume Va. Test Analysis Report for Post-Launch Support*, NWRA-CR-87-R001, Northwest Research Associates, Inc., Bellevue, WA, 1987.
- [41] Hanson, W. B., Private communication, 1989.

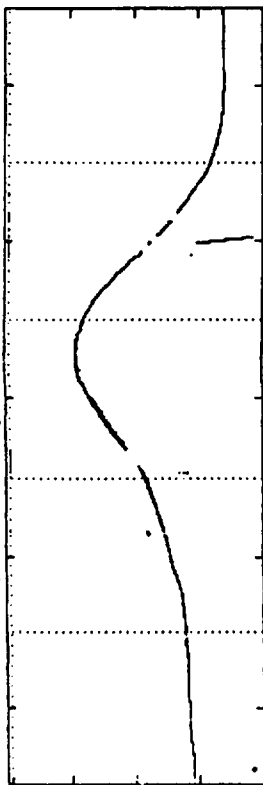
## **Appendix. Plots of SSIES PEAK Campaign Data**

This appendix contains time-series plots of all DMSP F8 and F9 SSIES Scintillation Meter data used in the PEAK campaign analysis described in Section 4. The data from both satellites for each date are plotted on a single page. The three plots on the left side of each page are from DMSP satellite F8, and the three plots on the right side are from F9. The three selected passes from each satellite were centered on Kwajalein's latitude ( $167^{\circ}$  E), with the center plot being the pass nearest to Kwajalein, the top plot the pass just prior to the center plot (east of Kwajalein), and the bottom plot the pass just after the center plot (west of Kwajalein).

The abscissa and ordinate scales are the same on all plots. Time (and satellite location) is plotted along the x-axis, with four minutes between the vertical dotted lines. The start time of the plots was selected to begin the plot near apex latitude  $+40^{\circ}$ . Total ion density is plotted along the y-axis, ranging from 0.0 to  $2.0 \times 10^5$  ion/cm<sup>3</sup>. The data are allowed to "wrap-around" along the y-axis, so that, for example, the data point for an ion density of  $3.0 \times 10^5$  ion/cm<sup>3</sup> is plotted as  $1.0 \times 10^5$  ion/cm<sup>3</sup>.

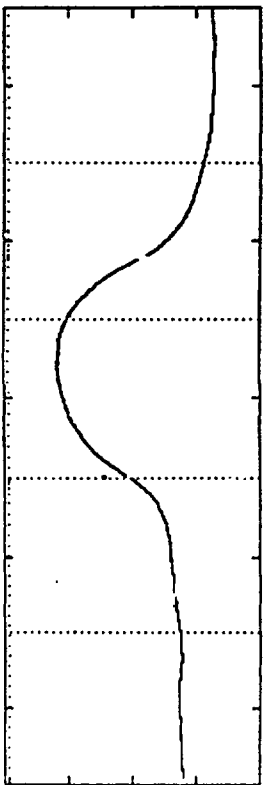
As mentioned in Section 4, these data were processed with no manual intervention to correct for instrument anomalies such as missing data frames or effects of RPA calibration sweeps. Most of the large data gaps are due to the SM instrument "freezing" on an EL-AMP status-flag setting, as described in Section 4.

DNBP F8 - 01 Aug 1988 - East Pass



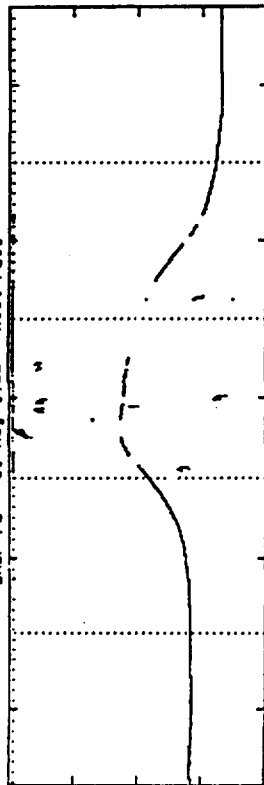
05:08:01	05:12:01	05:16:01	05:20:01	05:24:01	05:28:01 GMT
40.97	26.84	12.41	-2.83	-18.80	-34.73 APILAT
253.79	263.39	264.84	264.22	263.91	264.27 APILON

DNBP F8 - 01 Aug 1988 - Center Pass



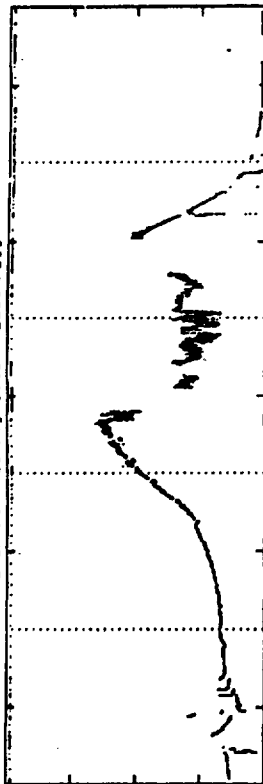
06:49:01	06:53:01	06:57:01	07:01:01	07:05:01	07:09:01 GMT
40.20	23.81	11.12	-4.18	-20.02	-35.88 APILAT
243.61	241.80	240.31	239.24	238.34	237.34 APILON

DNBP F8 - 01 Aug 1988 - West Pass



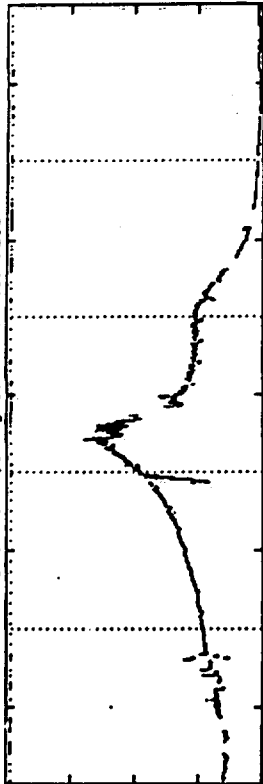
08:30:01	08:34:01	08:38:01	08:42:01	08:46:01	08:50:01 GMT
41.52	26.84	11.80	-3.59	-19.26	-35.05 APILAT
223.03	219.75	216.70	214.14	211.94	209.67 APILON

DNBP F9 - 01 Aug 1988 - East Pass



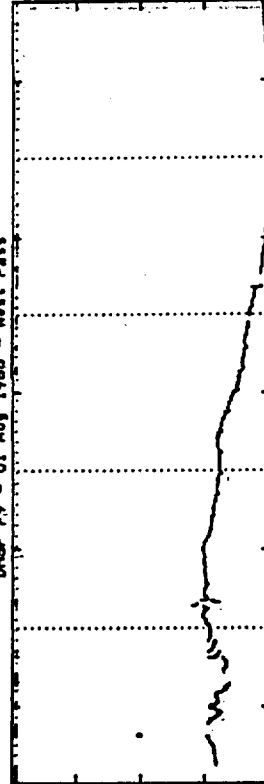
09:12:01	09:16:01	09:20:01	09:24:01	09:28:01	09:32:01 GMT
41.98	27.80	13.41	-1.78	-17.79	-33.88 APILAT
256.00	253.07	254.23	253.57	253.13	253.06 APILON

DNBP F9 - 01 Aug 1988 - Center Pass



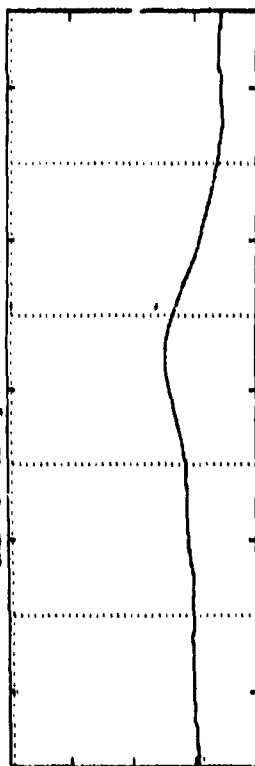
10:53:01	10:57:01	11:01:01	11:05:01	11:09:01	11:13:01 GMT
40.08	23.40	10.42	-4.96	-20.49	-34.45 APILAT
234.63	232.23	230.13	228.30	227.10	225.72 APILON

DNBP F9 - 01 Aug 1988 - West Pass



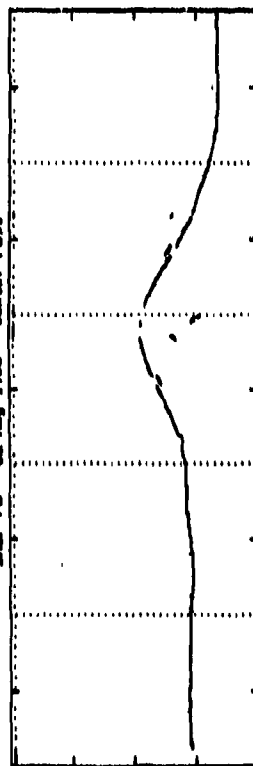
12:34:01	12:38:01	12:42:01	12:46:01	12:50:01	12:54:01 GMT
40.61	23.93	10.78	-4.78	-20.49	-36.67 APILAT
213.64	209.81	206.29	203.32	200.49	197.68 APILON

INSP FB - 02 Aug 1968 - East Pass



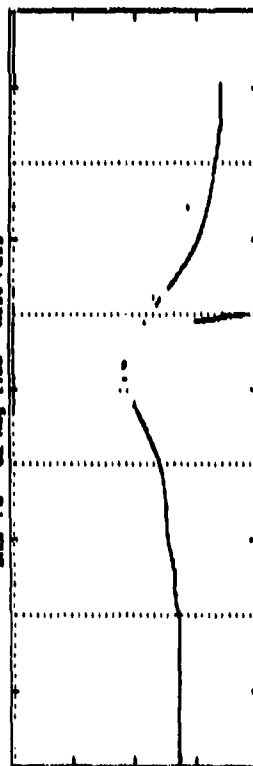
04:34:01 04:40:01 04:44:01 04:48:01 04:52:01 04:56:01 05:00:01 05:04:01 05:08:01 05:12:01 05:16:01 GMT  
258.44 258.34 267.84 267.22 267.99 267.99 267.99 267.99 267.99 267.99 267.99

INSP FB - 02 Aug 1968 - Center Pass



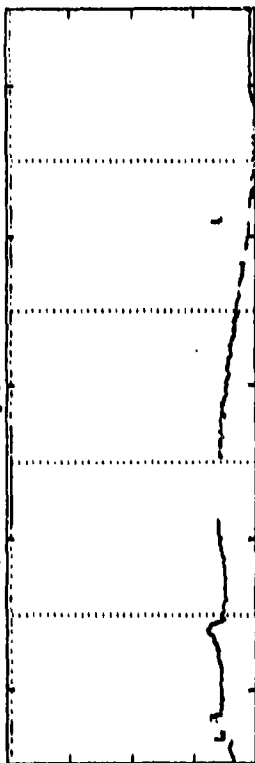
04:34:01 04:40:01 04:44:01 04:48:01 04:52:01 04:56:01 GMT  
244.48 244.85 254.85 254.85 254.85 254.85

INSP FB - 02 Aug 1968 - West Pass



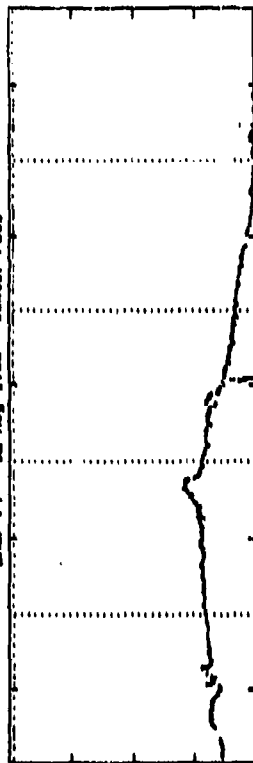
08:18:10 08:22:10 08:26:10 08:30:10 08:34:10 08:38:10 GMT  
233.17 233.67 239.26 244.90 244.90 244.90

INSP FY - 02 Aug 1968 - East Pass



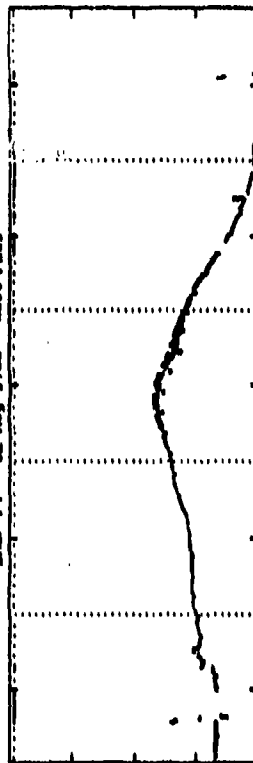
08:52:01 08:56:01 08:57:01 09:01:01 09:05:01 09:09:01 09:12:01 GMT  
238.02 238.34 239.60 239.60 239.60 239.60 239.60

INSP FY - 02 Aug 1968 - Center Pass



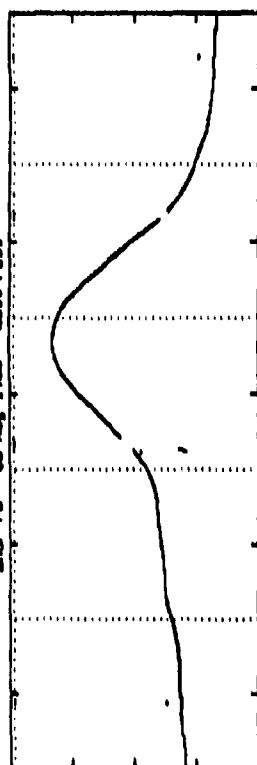
10:32:01 10:36:01 10:37:01 10:41:01 10:45:01 10:47:01 10:52:01 GMT  
231.27 231.27 232.37 232.37 232.37 232.37 232.37

INSP FY - 02 Aug 1968 - West Pass



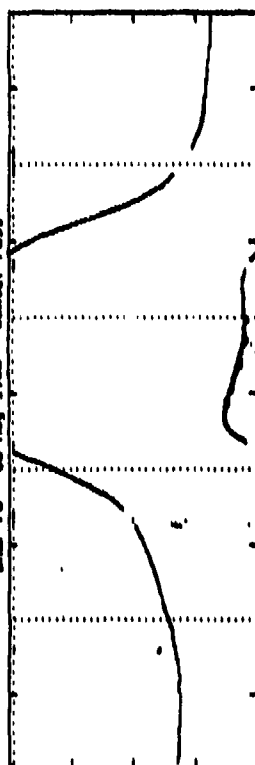
12:14:01 12:18:01 12:22:01 12:26:01 12:30:01 12:34:01 GMT  
203.34 203.34 205.96 205.96 205.96 205.96

SWMP P8 - 03 Aug 1968 - East Pass



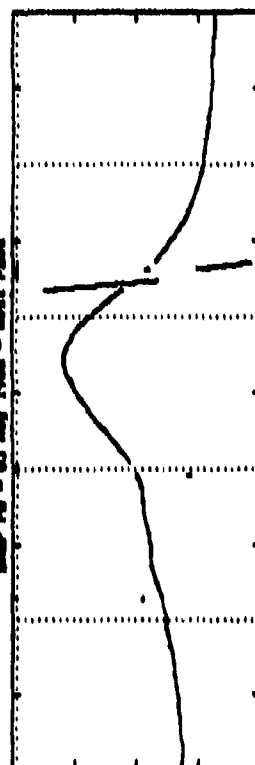
04:43:01	04:47:01	04:51:01	04:55:01	04:59:01	05:03:01 GMT
42.44	32.41	13.90	-1.28	-17.11	-32.95
271.37	271.39	270.99	270.25	270.00	270.44
APRILAT					
APRILON					

SWMP P8 - 03 Aug 1968 - Center Pass



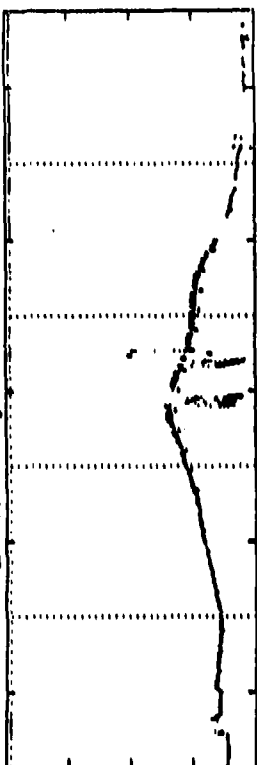
04:43:01	04:47:01	04:51:01	04:55:01	04:59:01	05:03:01 GMT
42.44	32.41	13.90	-1.28	-17.11	-32.95
271.37	271.39	270.99	270.25	270.00	270.44
APRILAT					
APRILON					

SWMP P8 - 03 Aug 1968 - West Pass



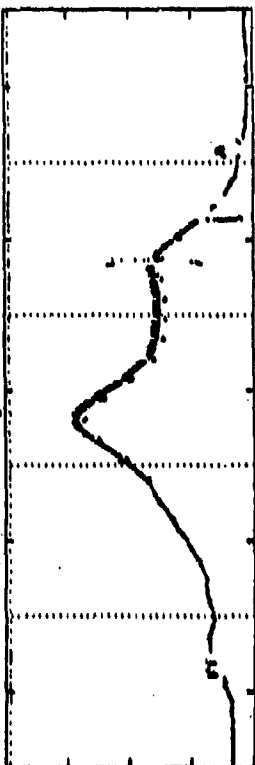
04:43:01	04:47:01	04:51:01	04:55:01	04:59:01	05:03:01 GMT
42.44	32.41	13.90	-1.28	-17.11	-32.95
271.37	271.39	270.99	270.25	270.00	270.44
APRILAT					
APRILON					

SWMP P9 - 03 Aug 1968 - East Pass



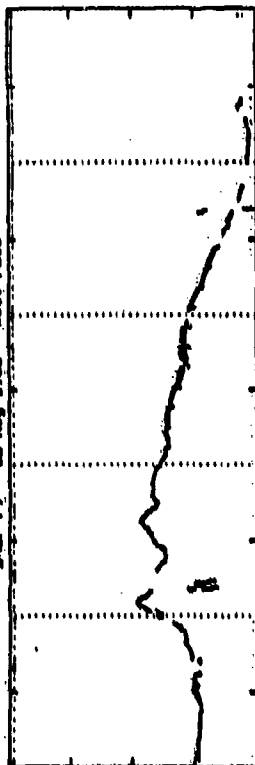
08:32:01	08:37:01	08:41:01	08:45:01	08:49:01	08:53:01 GMT
41.74	27.37	13.14	-2.09	-18.08	-34.06
264.77	264.26	263.82	263.23	262.90	262.23
APRILAT					
APRILON					

SWMP P9 - 03 Aug 1968 - Center Pass



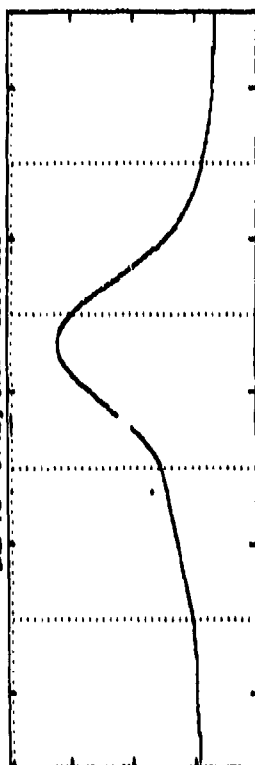
10:12:01	10:17:01	10:21:01	10:25:01	10:29:01	10:33:01 GMT
42.89	28.23	13.46	-1.37	-17.37	-31.27
262.89	261.23	259.44	258.49	257.37	256.73
APRILAT					
APRILON					

SWMP P9 - 03 Aug 1968 - West Pass



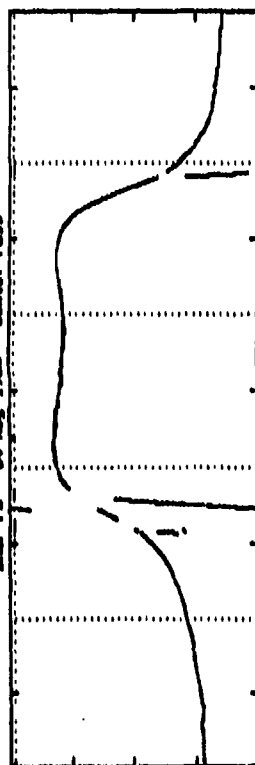
11:54:01	11:59:01	12:02:01	12:06:01	12:10:01	12:14:01 GMT
42.34	27.42	12.34	-2.87	-18.38	-34.42
262.47	259.16	258.07	257.46	256.23	255.49
APRILAT					
APRILON					

INSP F2 - 04 Aug 1968 - East Pass



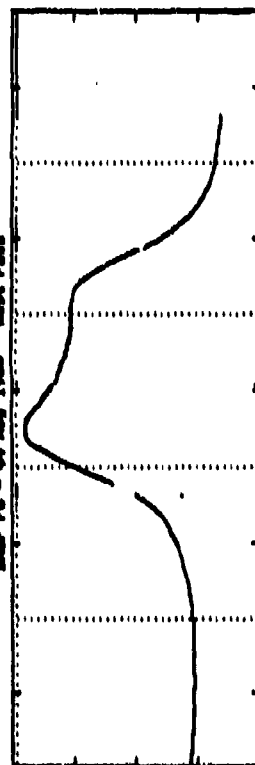
04:31:01	04:39:01	04:43:01	04:47:01	04:51:01	04:54:01	04:57:01
41.32	27.39	12.76	-2.30	-18.29	-34.00	-36.00
274.49	274.38	273.99	273.35	273.05	272.42	272.42
			ONT			
			APRILAT			
			APRILON			

INSP F2 - 04 Aug 1968 - Center Pass



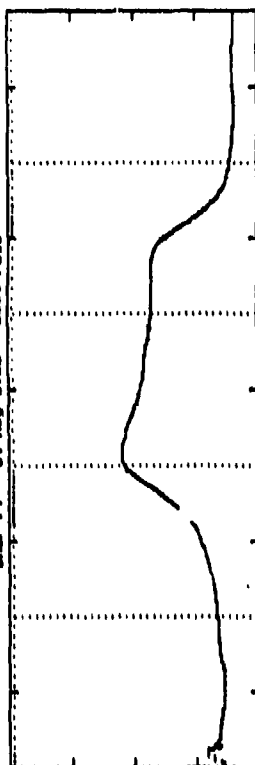
04:12:01	04:14:01	04:20:01	04:24:01	04:28:01	04:32:01	04:36:01
48.59	26.27	11.92	-3.35	-19.33	-35.32	-38.32
254.49	258.24	267.35	268.42	267.06	267.55	267.55
			ONT			
			APRILAT			
			APRILON			

INSP F2 - 04 Aug 1968 - West Pass



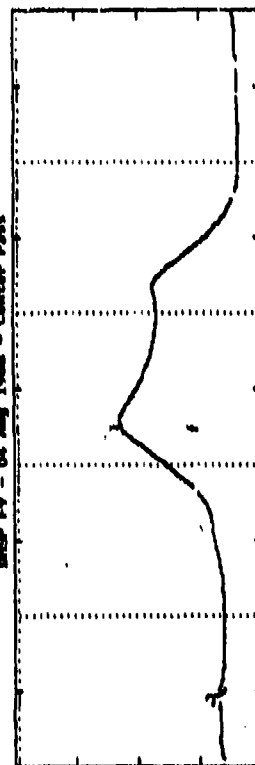
04:12:01	04:14:01	04:20:01	04:24:01	04:28:01	04:32:01	04:36:01
48.59	26.27	11.92	-3.35	-19.33	-35.32	-38.32
254.49	258.24	267.35	268.42	267.06	267.55	267.55
			ONT			
			APRILAT			
			APRILON			

INSP F3 - 04 Aug 1968 - East Pass



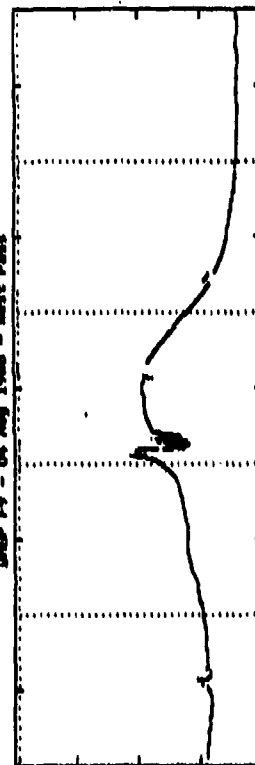
08:14:01	08:18:01	08:22:01	08:26:01	08:30:01	08:34:01
39.87	23.44	11.04	-4.32	-20.29	-36.14
269.29	269.05	268.30	267.98	267.77	268.37
			ONT		
			APRILAT		
			APRILON		

INSP F3 - 04 Aug 1968 - Center Pass



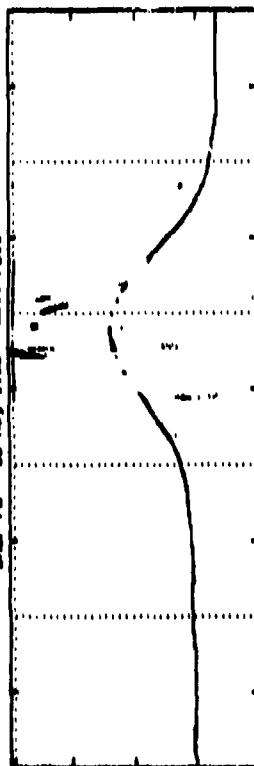
09:54:01	09:58:01	10:02:01	10:06:01	10:10:01	10:14:01
40.43	26.31	11.49	-3.41	-19.34	-35.49
264.93	263.39	264.11	263.22	262.31	261.96
			ONT		
			APRILAT		
			APRILON		

INSP F3 - 04 Aug 1968 - West Pass



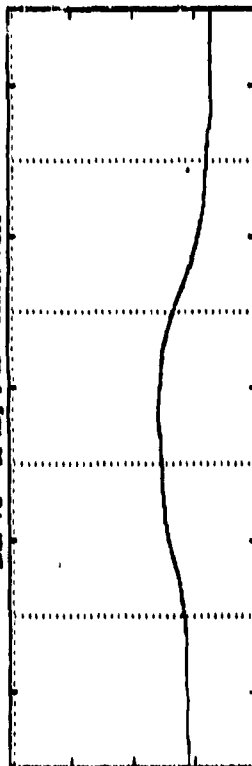
11:39:01	11:43:01	11:47:01	11:51:01	11:55:01	11:59:01
39.48	24.90	9.79	-3.45	-21.30	-37.13
223.98	222.95	220.22	219.02	214.09	214.09
			ONT		
			APRILAT		
			APRILON		

DRIP P8 - 03 Aug 1988 - East Pass



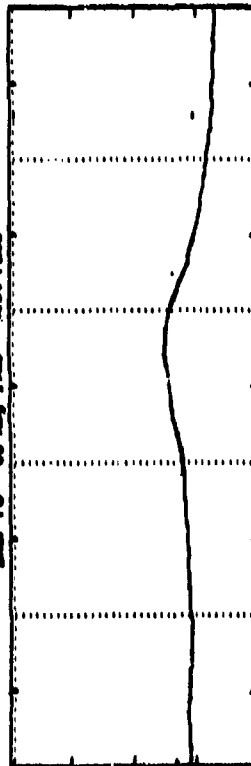
05:59:01	06:02:01	06:07:01	06:11:01	06:15:01	06:19:01	GMT
43.11	28.94	14.61	-8.47	-16.38	-32.45	APRILAT
234.35	232.28	232.31	231.37	231.03	230.61	APRILON

DRIP P8 - 03 Aug 1988 - Center Pass



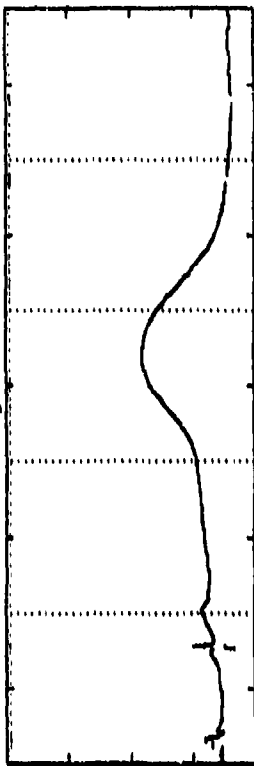
07:41:01	07:45:01	07:49:01	07:52:01	07:57:01	08:01:01	GMT
39.64	24.98	10.09	-3.26	-21.03	-38.75	APRILAT
238.86	238.17	238.02	238.29	238.71	233.16	APRILON

DRIP P8 - 03 Aug 1988 - West Pass



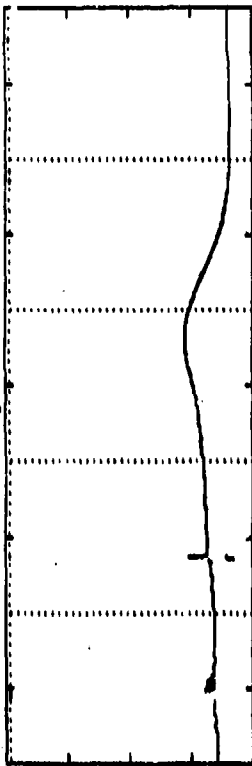
07:41:01	07:45:01	07:49:01	07:52:01	07:56:01	07:59:01	GMT
39.64	24.98	10.09	-3.26	-21.03	-38.75	APRILAT
238.86	238.17	238.02	238.29	238.71	233.16	APRILON

DRIP P7 - 03 Aug 1988 - East Pass



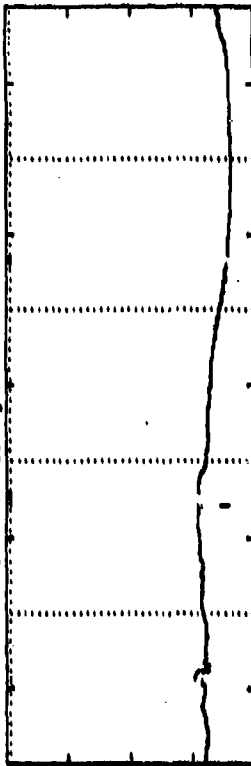
07:56:01	07:58:01	08:02:01	08:06:01	08:10:01	08:14:01	GMT
41.61	27.23	12.39	-2.71	-18.34	-34.27	APRILAT
273.93	273.86	273.49	272.97	272.61	273.23	APRILON

DRIP P7 - 03 Aug 1988 - Center Pass



09:34:01	09:38:01	09:42:01	09:46:01	09:50:01	09:54:01	GMT
42.28	27.93	13.88	-1.88	-17.65	-33.69	APRILAT
251.26	250.88	249.92	248.15	247.38	247.36	APRILON

DRIP P7 - 03 Aug 1988 - West Pass



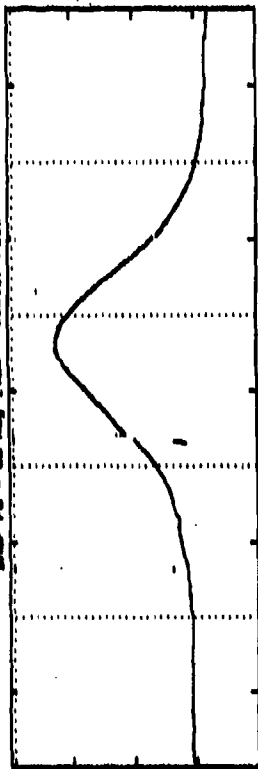
11:13:01	11:17:01	11:21:01	11:25:01	11:29:01	11:33:01	GMT
48.78	38.65	11.01	-4.28	-28.65	-32.01	APRILAT
238.23	237.38	233.63	233.93	231.38	219.64	APRILON

SWMP P8 - 06 Aug 1988 - East Pass



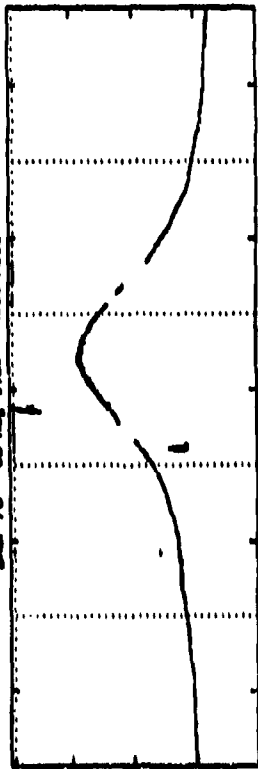
06:47:01	06:58:01	07:09:01	07:20:01	07:31:01	07:42:01	07:53:01	
42.10	27.97	13.64	-1.39	-17.47	-31.53	-31.53	
238.96	238.67	238.24	238.57	238.11	238.04	238.04	
							08:07:01 GMT
							06:47:01 GMT

SWMP P8 - 06 Aug 1988 - Center Pass



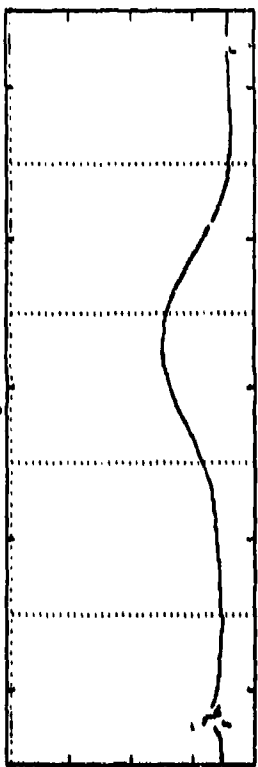
07:28:01	07:39:01	07:50:01	08:01:01	08:12:01	08:23:01	08:34:01	
42.08	27.42	13.39	-2.73	-18.39	-31.14	-31.14	
238.76	238.36	238.23	238.58	238.19	238.03	238.03	
							08:44:01 GMT
							07:42:01 GMT

SWMP P8 - 06 Aug 1988 - West Pass



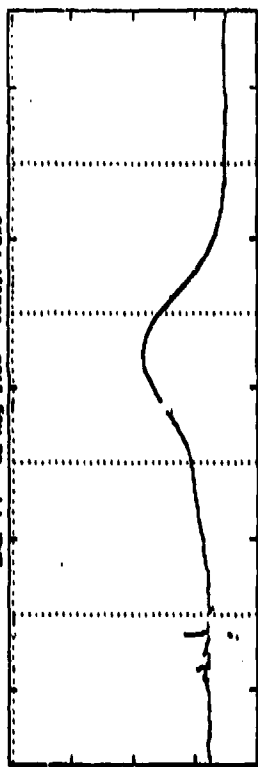
07:58:01	08:09:01	08:20:01	08:31:01	08:42:01	08:53:01	09:04:01	
42.43	28.46	14.99	-4.32	-18.37	-31.29	-31.29	
238.46	238.66	238.09	238.12	238.09	238.52	238.52	
							09:28:01 GMT
							07:58:01 GMT

SWMP P9 - 06 Aug 1988 - East Pass



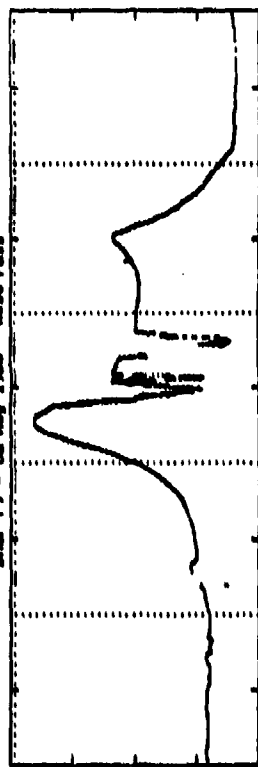
09:15:01	09:26:01	09:37:01	09:48:01	09:59:01	10:10:01	10:21:01	
40.21	26.77	13.07	-1.33	-16.33	-31.84	-31.84	
238.36	238.44	238.62	238.99	238.95	238.41	238.41	
							10:34:01 GMT
							09:15:01 GMT

SWMP P9 - 06 Aug 1988 - Center Pass



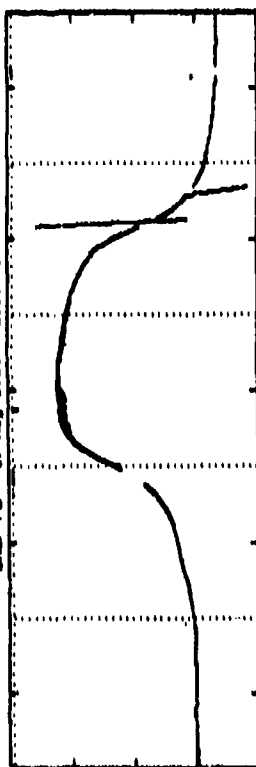
10:55:01	11:06:01	11:17:01	11:28:01	11:39:01	11:50:01	12:01:01	
41.49	27.32	12.39	-2.94	-18.42	-34.39	-34.39	
238.47	238.66	238.80	238.67	238.64	238.23	238.23	
							12:15:01 GMT
							10:55:01 GMT

SWMP P9 - 06 Aug 1988 - West Pass



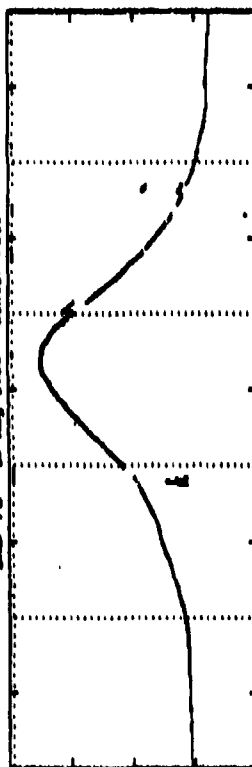
12:36:01	12:47:01	12:58:01	13:09:01	13:20:01	13:31:01	13:42:01	
42.59	27.94	12.86	-2.44	-18.54	-34.54	-34.54	
238.63	238.76	238.13	238.08	238.41	238.47	238.47	
							13:56:01 GMT
							12:36:01 GMT

SWMP PG - 07 Aug 1988 - East Pass



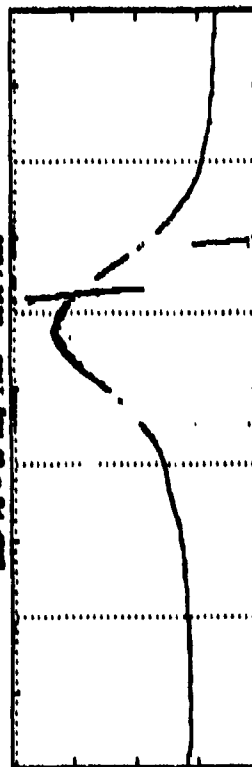
08:30:01	08:42:01	08:47:01	08:51:01	08:55:01 GWT
41.11	12.64	-2.34	-18.97	-34.48
239.64	238.20	237.56	237.17	237.27
				APRILAT
				APRILON

SWMP PG - 07 Aug 1988 - Center Pass



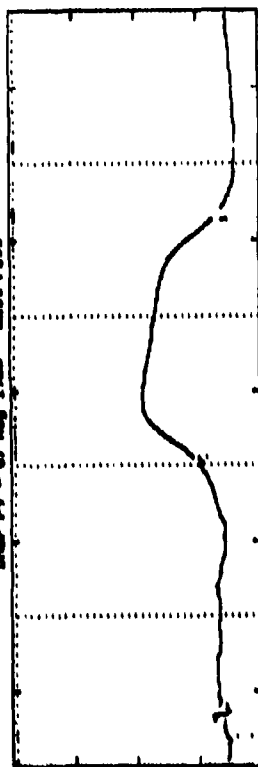
07:14:01	07:20:01	07:25:01	07:30:01	07:35:01 GWT
48.76	11.38	-2.92	-19.44	-38.01
238.07	233.96	232.83	231.31	230.13
				APRILAT
				APRILON

SWMP PG - 07 Aug 1988 - West Pass



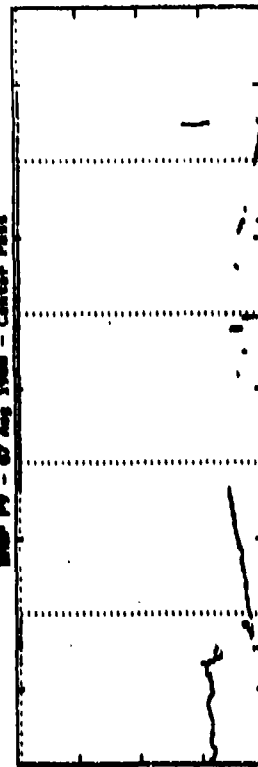
08:07:01	08:08:01	08:09:01	08:10:01	08:11:01 GWT
42.77	12.17	-2.36	-18.01	-34.48
237.05	233.96	232.83	231.31	230.13
				APRILAT
				APRILON

SWMP PG - 07 Aug 1988 - East Pass



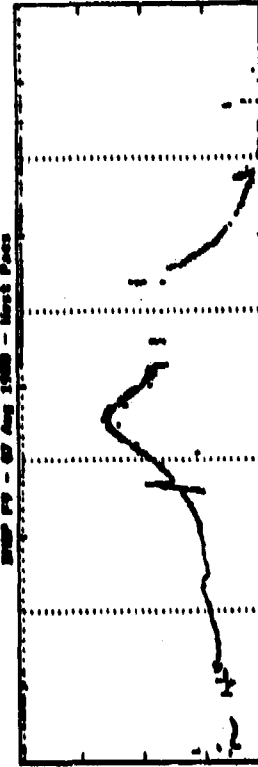
08:32:01	08:39:01	08:42:01	08:47:01	08:51:01 GWT
41.86	27.72	13.20	-1.83	-17.86
239.70	239.10	238.42	237.80	237.42
				APRILAT
				APRILON

SWMP PG - 07 Aug 1988 - Center Pass



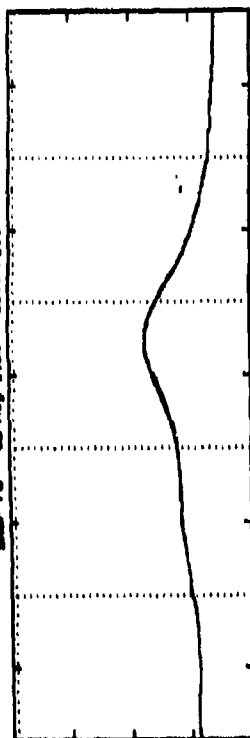
10:30:01	10:39:01	10:42:01	10:47:01	10:51:01 GWT
43.20	28.71	13.91	-1.33	-17.86
238.45	236.40	234.94	233.80	232.80
				APRILAT
				APRILON

SWMP PG - 07 Aug 1988 - West Pass



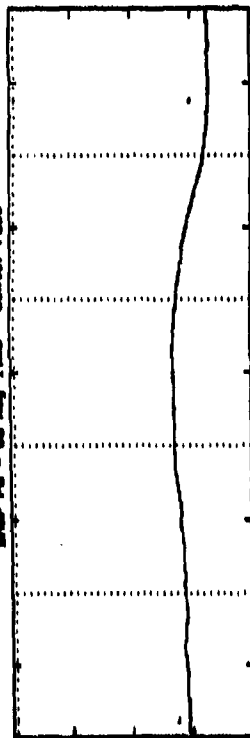
12:17:01	12:21:01	12:25:01	12:29:01	12:33:01 GWT
39.73	24.99	9.60	-8.10	-27.41
217.17	213.56	210.27	208.03	205.30
				APRILAT
				APRILON

INSP P9 - 08 Aug 1968 - East Pass



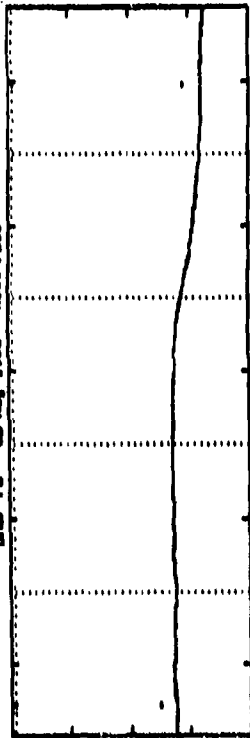
06:22:01	06:27:01	06:31:01	06:35:01	06:39:01	06:43:01	GWT
41.13	28.04	11.44	-3.44	-15.48	-23.44	APFLAT
262.35	261.81	261.18	260.26	260.26	260.31	APFLON

INSP P9 - 08 Aug 1968 - Center Pass



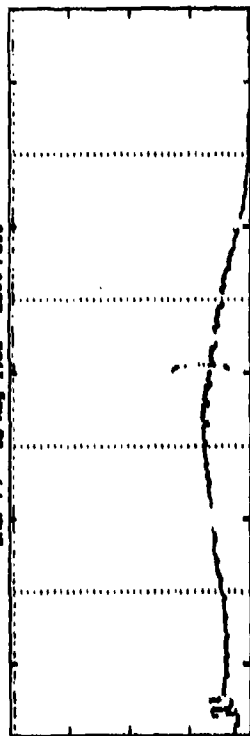
06:02:01	06:07:01	06:11:01	06:15:01	06:19:01	06:23:01	GWT
41.17	28.71	14.02	-1.17	-14.08	-22.70	APFLAT
262.96	258.92	257.12	255.80	254.71	253.69	APFLON

INSP P9 - 08 Aug 1968 - West Pass



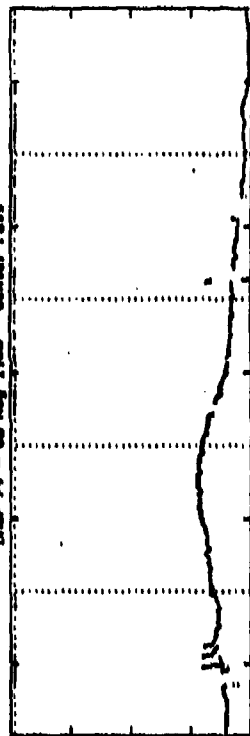
06:02:01	06:07:01	06:11:01	06:15:01	06:19:01	06:23:01	GWT
41.26	28.28	11.50	-3.88	-19.41	-28.44	APFLAT
257.87	254.28	253.14	252.40	252.61	252.52	APFLON

INSP P9 - 08 Aug 1968 - East Pass



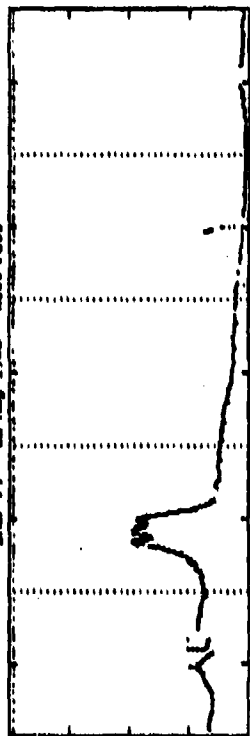
06:26:01	06:30:01	06:34:01	06:38:01	06:42:01	06:46:01	GWT
37.77	23.82	11.33	-4.00	-20.04	-35.00	APFLAT
264.16	263.71	263.15	262.56	262.27	262.70	APFLON

INSP P9 - 08 Aug 1968 - Center Pass



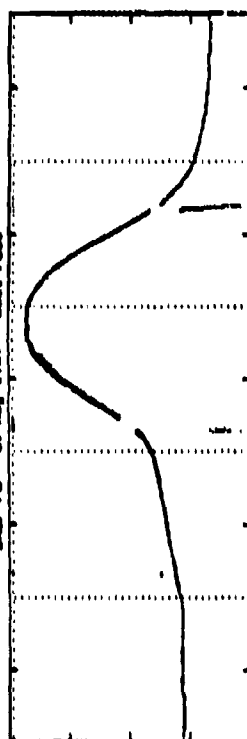
16:14:01	16:18:01	16:22:01	16:26:01	16:30:01	16:34:01	GWT
41.03	26.56	11.82	-3.48	-19.21	-35.18	APFLAT
262.37	260.49	258.90	257.77	256.82	255.96	APFLON

INSP P9 - 08 Aug 1968 - West Pass



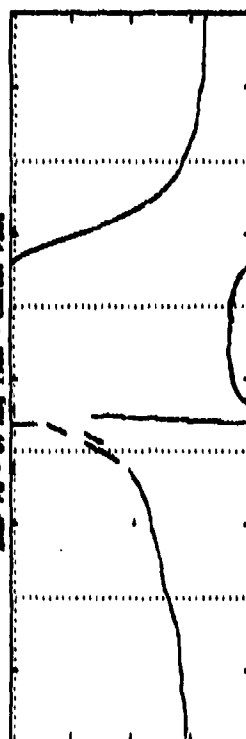
11:57:01	12:01:01	12:05:01	12:09:01	12:13:01	12:17:01	GWT
40.42	25.87	10.76	-4.49	-20.42	-36.26	APFLAT
261.57	258.23	255.15	252.57	250.20	207.97	APFLON

SWP P2 - 07 Aug 1968 - East Pass



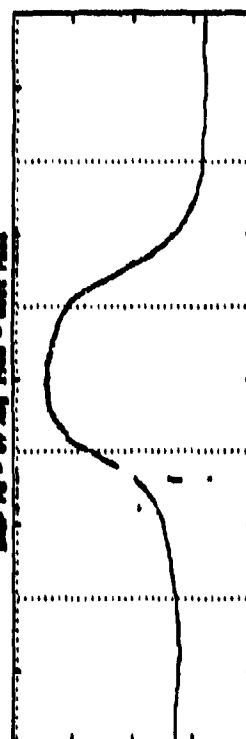
06:10:01	06:14:01	06:18:01	06:22:01	06:26:01	06:30:01
42.74	28.59	14.24	-8.79	-14.79	-22.79
243.28	244.86	244.32	243.69	243.31	243.34
APRILAT					
243.34					

SWP P2 - 07 Aug 1968 - Center Pass



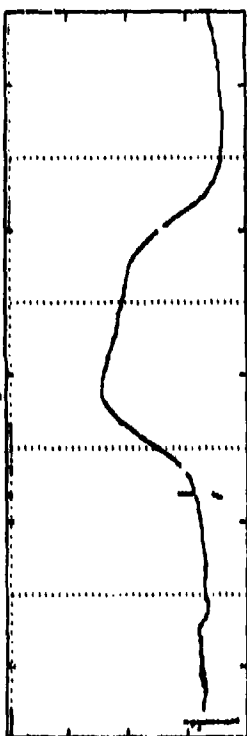
06:31:01	06:35:01	06:39:01	06:43:01	06:47:01	06:51:01
42.62	27.41	12.97	-2.23	-10.03	-22.99
243.34	241.48	239.98	238.76	237.82	236.97
APRILAT					
236.97					

SWP P2 - 07 Aug 1968 - West Pass



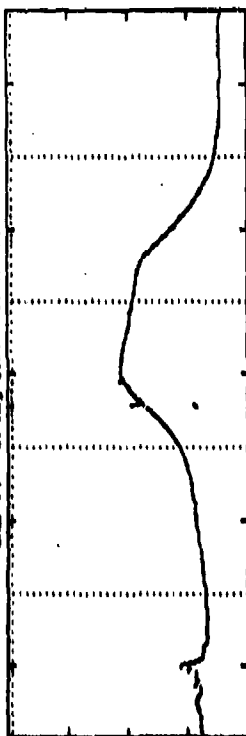
06:32:01	06:36:01	06:40:01	06:44:01	06:48:01	06:52:01
39.77	24.60	9.36	-3.46	-12.13	-24.99
243.13	240.81	240.79	240.20	241.00	240.88
APRILAT					
240.88					

SWP P2 - 07 Aug 1968 - East Pass



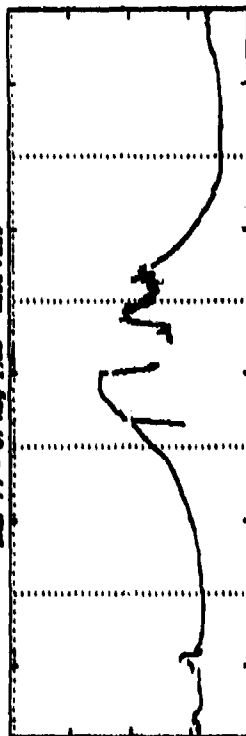
06:14:01	06:18:01	06:22:01	06:26:01	06:30:01	06:34:01
41.48	27.49	12.93	-2.20	-10.23	-23.16
246.74	246.50	246.05	245.45	245.15	245.62
APRILAT					
245.62					

SWP P2 - 07 Aug 1968 - Center Pass



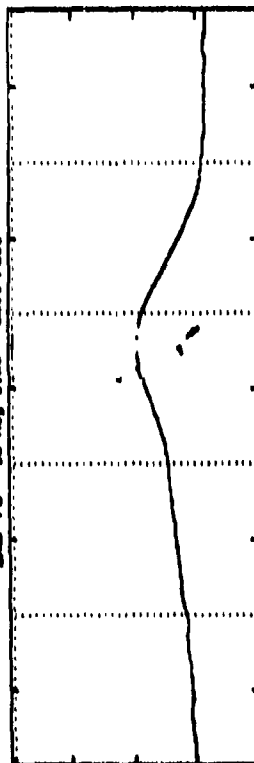
06:34:01	06:38:01	06:42:01	06:46:01	06:50:01	06:54:01
42.39	28.13	13.97	-1.03	-17.47	-33.45
246.63	245.63	243.67	242.72	241.97	241.35
APRILAT					
241.35					

SWP P2 - 07 Aug 1968 - West Pass



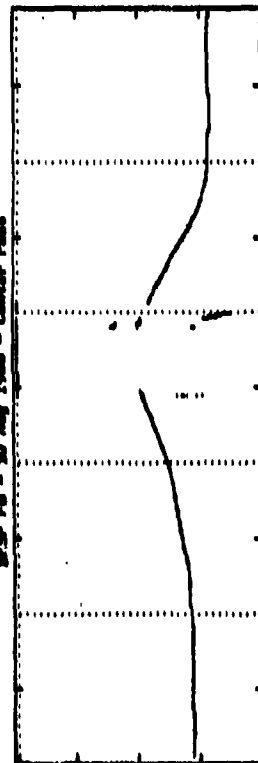
06:37:01	06:41:01	06:45:01	06:49:01	06:53:01	06:57:01
41.41	27.67	11.88	-2.97	-14.27	-30.05
245.87	242.81	240.98	240.00	240.43	241.41
APRILAT					
241.41					

BNBP P9 - 10 Aug 1988 - East Pass



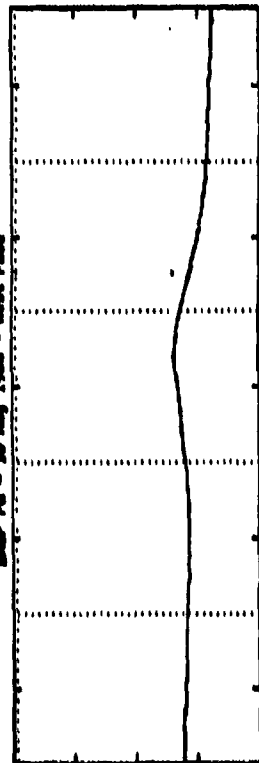
04:38:01	04:52:01	05:06:01	05:20:01	05:34:01	05:48:01	06:02:01
273.36	273.36	267.82	267.82	267.82	267.82	267.82
04:38:01	04:52:01	05:06:01	05:20:01	05:34:01	05:48:01	06:02:01
273.36	273.36	267.82	267.82	267.82	267.82	267.82

BNBP P9 - 10 Aug 1988 - Center Pass



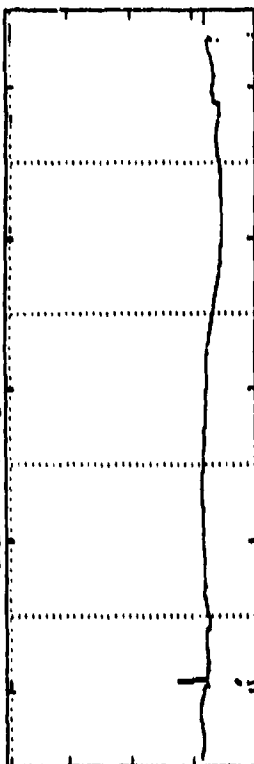
04:38:01	04:52:01	05:06:01	05:20:01	05:34:01	05:48:01	06:02:01
273.36	273.36	267.82	267.82	267.82	267.82	267.82
04:38:01	04:52:01	05:06:01	05:20:01	05:34:01	05:48:01	06:02:01
273.36	273.36	267.82	267.82	267.82	267.82	267.82

BNBP P9 - 10 Aug 1988 - West Pass



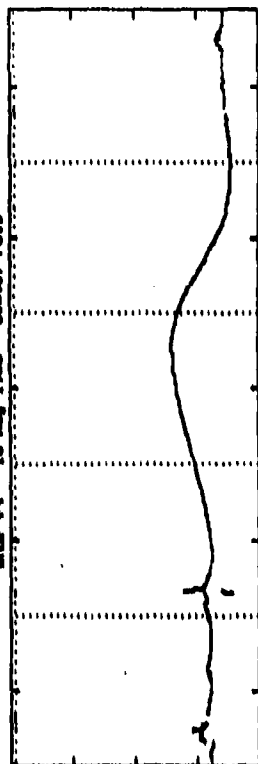
04:38:01	04:52:01	05:06:01	05:20:01	05:34:01	05:48:01	06:02:01
273.36	273.36	267.82	267.82	267.82	267.82	267.82
04:38:01	04:52:01	05:06:01	05:20:01	05:34:01	05:48:01	06:02:01
273.36	273.36	267.82	267.82	267.82	267.82	267.82

BNBP P9 - 10 Aug 1988 - East Pass



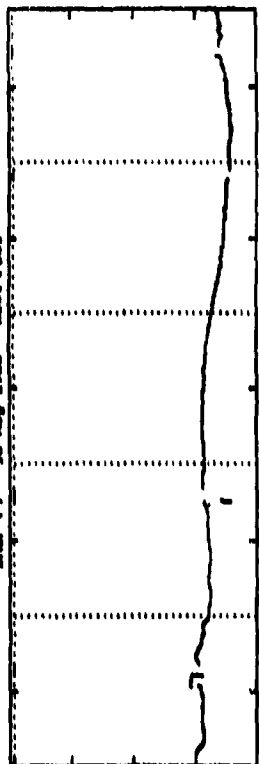
07:37:01	08:04:01	08:09:01	08:14:01	08:19:01	08:24:01	08:29:01
273.36	273.36	272.81	272.81	272.81	272.81	272.81
07:37:01	08:04:01	08:09:01	08:14:01	08:19:01	08:24:01	08:29:01
273.36	273.36	272.81	272.81	272.81	272.81	272.81

BNBP P9 - 10 Aug 1988 - Center Pass



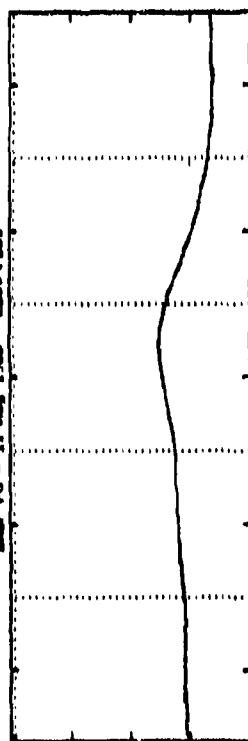
09:37:01	09:41:01	09:45:01	09:49:01	09:53:01	09:57:01	10:01:01
273.36	273.36	272.81	272.81	272.81	272.81	272.81
09:37:01	09:41:01	09:45:01	09:49:01	09:53:01	09:57:01	10:01:01
273.36	273.36	272.81	272.81	272.81	272.81	272.81

BNBP P9 - 10 Aug 1988 - West Pass

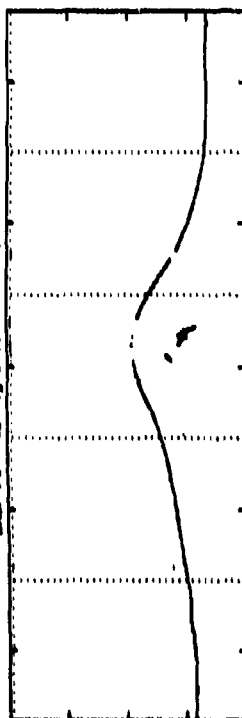


11:17:01	11:21:01	11:25:01	11:29:01	11:33:01	11:37:01	11:41:01
273.36	273.36	272.81	272.81	272.81	272.81	272.81
11:17:01	11:21:01	11:25:01	11:29:01	11:33:01	11:37:01	11:41:01
273.36	273.36	272.81	272.81	272.81	272.81	272.81

SWP 00 - 11 Aug 1968 - East Pass

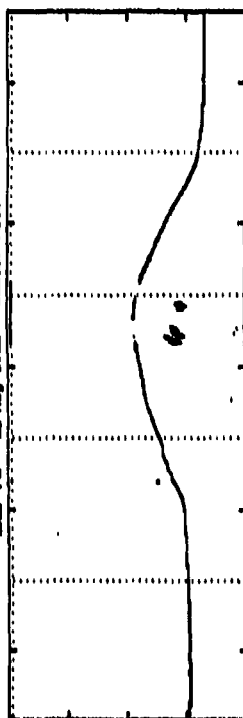


SWMP P8 - 12 Aug 1988 - East Pass



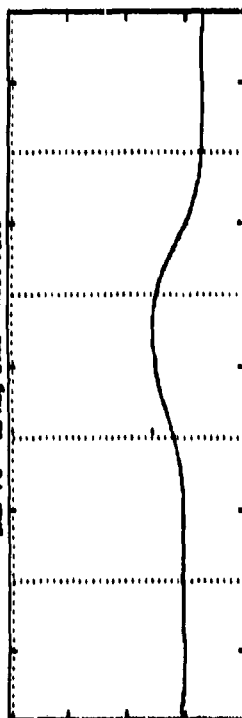
04:38:01	04:38:01	04:44:01	04:50:01	04:54:01	GWT
237.87	237.33	237.36	237.46	237.16	APPLAT
237.98	237.76	237.38	237.46	237.16	APPLIN

SWMP P8 - 12 Aug 1988 - Center Pass



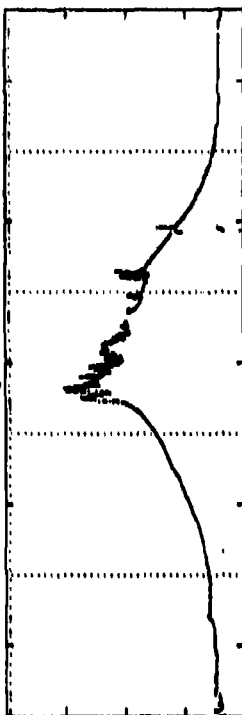
04:54:01	04:54:01	04:54:01	04:54:01	04:54:01	GWT
238.13	238.83	238.71	237.91	237.38	APPLAT
238.13	238.83	238.71	237.91	237.38	APPLIN

SWMP P8 - 12 Aug 1988 - West Pass



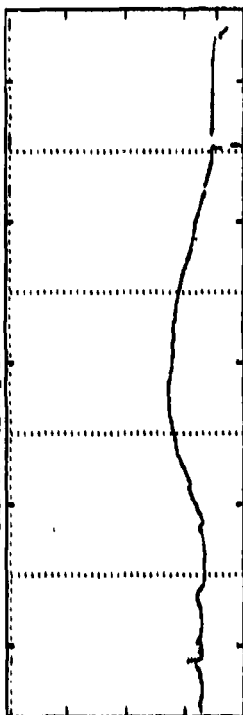
07:38:01	07:38:01	08:02:01	08:07:01	08:12:01	GWT
238.08	237.44	237.04	237.34	237.43	APPLAT
238.08	237.44	237.04	237.34	237.43	APPLIN

SWMP P9 - 12 Aug 1988 - East Pass



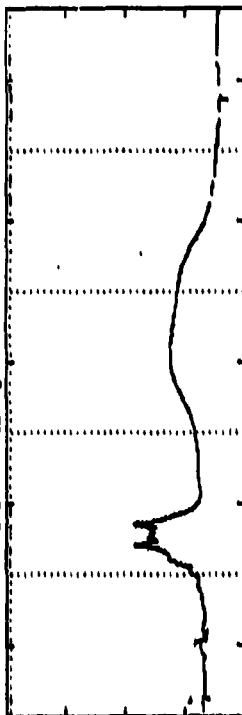
08:38:01	07:02:01	07:04:01	07:10:01	07:14:01	GWT
237.15	238.44	237.34	237.13	236.79	APPLAT
237.15	238.44	237.34	237.13	236.79	APPLIN

SWMP P9 - 12 Aug 1988 - Center Pass



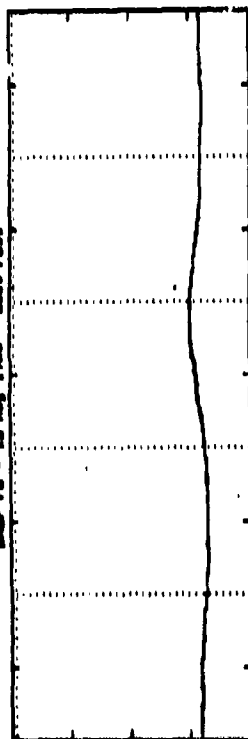
10:38:01	10:02:01	10:04:01	10:30:01	10:34:01	GWT
237.89	238.43	237.76	237.32	236.36	APPLAT
237.89	238.43	237.76	237.32	236.36	APPLIN

SWMP P9 - 12 Aug 1988 - West Pass



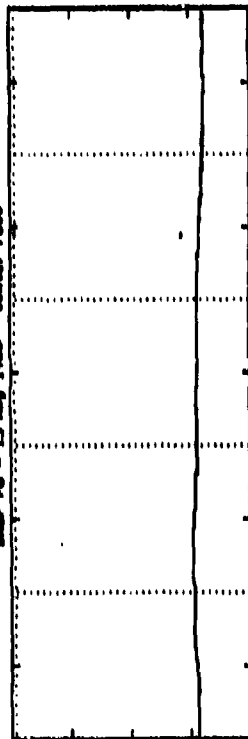
12:19:01	12:02:01	12:27:01	12:31:01	12:35:01	GWT
237.13	237.48	238.09	237.32	236.73	APPLAT
237.13	237.48	238.09	237.32	236.73	APPLIN

SWP P2 - 13 Aug 1968 - East Pass



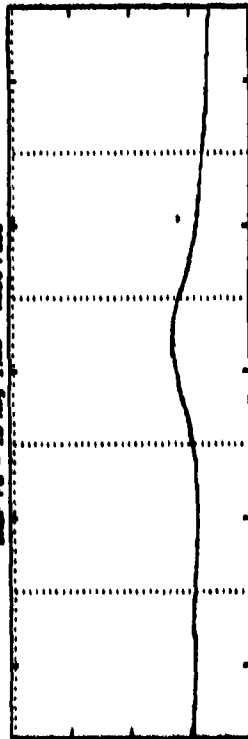
06:02:04	06:06:04	06:10:04	06:14:04	06:18:04	06:22:04	GWT
41.28	27.12	12.72	-2.47	-18.44	-34.49	APRILAT
232.40	232.58	232.62	232.90	232.79	232.17	APRILIN

SWP P3 - 13 Aug 1968 - Center Pass



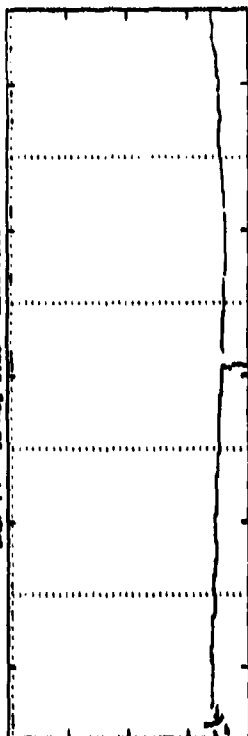
07:42:04	07:47:04	07:51:04	07:56:04	07:59:04	08:03:04	GWT
41.48	26.83	11.89	-0.42	-19.06	-34.77	APRILAT
232.67	232.68	232.71	232.89	234.26	232.69	APRILIN

SWP P4 - 13 Aug 1968 - West Pass



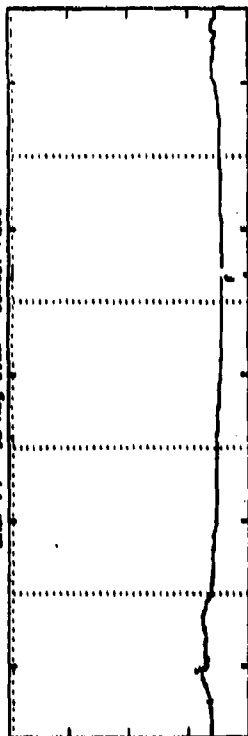
08:20:04	08:25:04	08:30:04	08:35:04	08:41:04	08:46:04	GWT
40.94	26.93	20.11	-4.74	-20.44	-36.42	APRILAT
231.13	232.11	232.45	232.29	232.40	234.26	APRILIN

SWP P5 - 13 Aug 1968 - East Pass



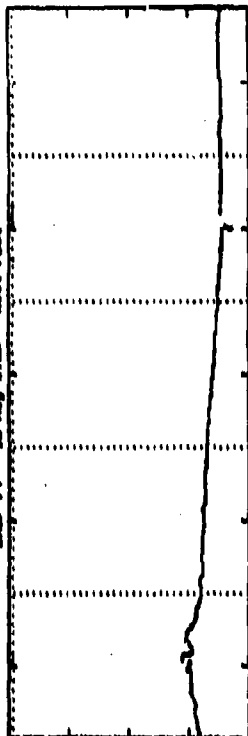
08:28:04	08:32:04	08:36:04	08:40:04	08:44:04	08:48:04	GWT
41.76	27.61	13.21	-1.99	-17.99	-34.01	APRILAT
263.40	263.58	263.62	263.62	261.69	261.97	APRILIN

SWP P6 - 13 Aug 1968 - Center Pass



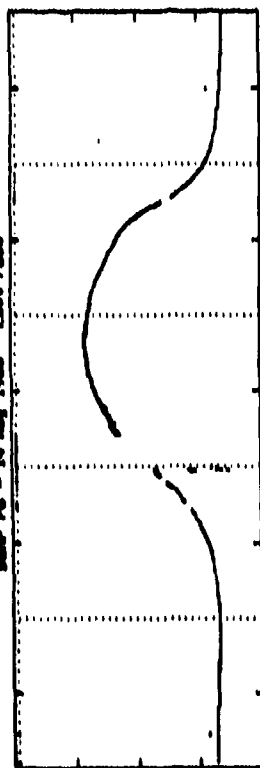
10:10:04	10:14:04	10:18:04	10:22:04	10:26:04	10:30:04	GWT
42.89	28.40	13.71	-1.31	-17.28	-33.15	APRILAT
262.50	262.50	262.50	262.27	262.21	262.49	APRILIN

SWP P7 - 13 Aug 1968 - West Pass



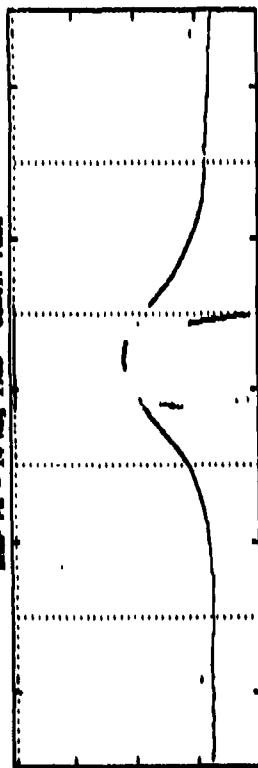
11:39:04	12:03:04	12:07:04	12:11:04	12:15:04	12:19:04	GWT
42.94	27.83	12.79	-0.42	-18.23	-34.17	APRILAT
231.49	232.12	232.46	232.28	232.99	237.44	APRILIN

SWAMP FB - 14 Aug 1968 - East Pass



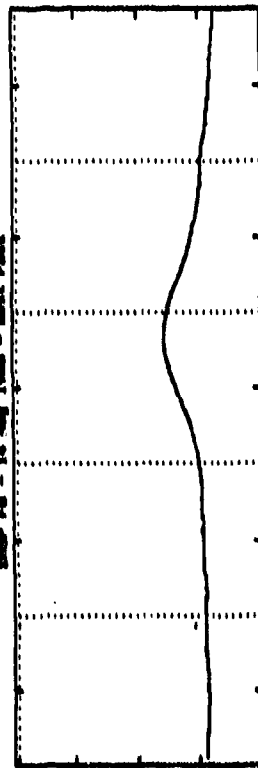
06:28:01	06:34:01	06:38:01	06:42:01	06:46:01	06:50:01
40.26	24.13	11.74	-3.34	-19.33	-33.33
253.31	253.39	254.33	253.90	253.47	253.43
APRIL 01	APRIL 01	APRIL 01	APRIL 01	APRIL 01	APRIL 01

SWAMP FB - 14 Aug 1968 - Center Pass



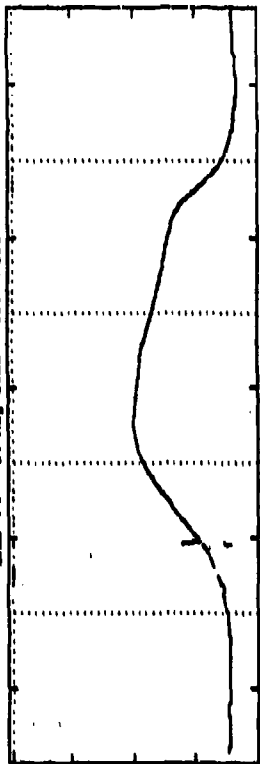
06:28:01	06:34:01	06:38:01	06:42:01	06:46:01	06:50:01
40.26	24.13	11.74	-3.34	-19.33	-33.33
253.31	253.39	254.33	253.90	253.47	253.43
APRIL 01	APRIL 01	APRIL 01	APRIL 01	APRIL 01	APRIL 01

SWAMP FB - 14 Aug 1968 - West Pass



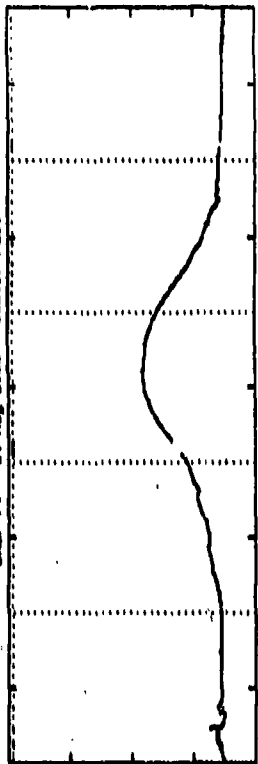
06:28:01	06:34:01	06:38:01	06:42:01	06:46:01	06:50:01
40.26	24.13	11.74	-3.34	-19.33	-33.33
253.31	253.39	254.33	253.90	253.47	253.43
APRIL 01	APRIL 01	APRIL 01	APRIL 01	APRIL 01	APRIL 01

SWAMP FB - 14 Aug 1968 - East Pass



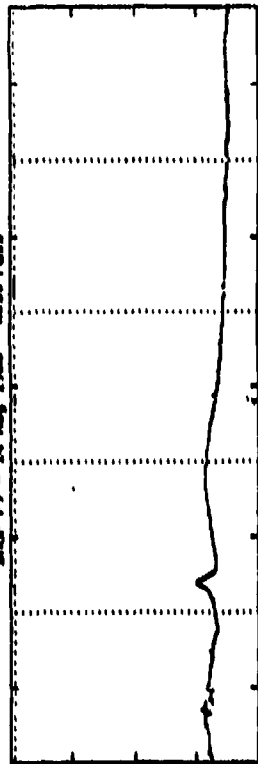
06:28:01	06:34:01	06:38:01	06:42:01	06:46:01	06:50:01
40.26	24.13	11.74	-3.34	-19.33	-33.33
253.31	253.39	254.33	253.90	253.47	253.43
APRIL 01	APRIL 01	APRIL 01	APRIL 01	APRIL 01	APRIL 01

SWAMP FB - 14 Aug 1968 - Center Pass



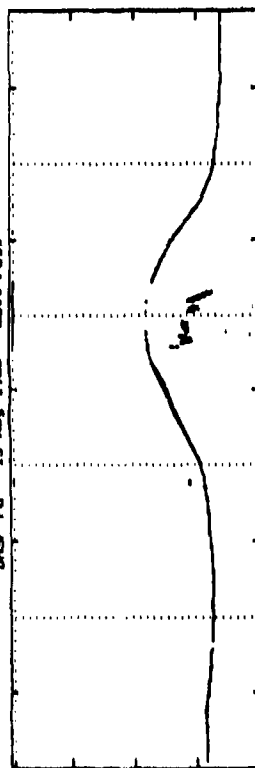
06:28:01	06:34:01	06:38:01	06:42:01	06:46:01	06:50:01
40.26	24.13	11.74	-3.34	-19.33	-33.33
253.31	253.39	254.33	253.90	253.47	253.43
APRIL 01	APRIL 01	APRIL 01	APRIL 01	APRIL 01	APRIL 01

SWAMP FB - 14 Aug 1968 - West Pass



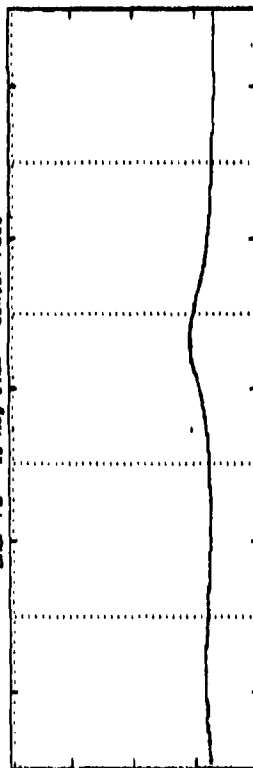
06:28:01	06:34:01	06:38:01	06:42:01	06:46:01	06:50:01
40.26	24.13	11.74	-3.34	-19.33	-33.33
253.31	253.39	254.33	253.90	253.47	253.43
APRIL 01	APRIL 01	APRIL 01	APRIL 01	APRIL 01	APRIL 01

INSP FB - 15 Aug 1968 - East Pass



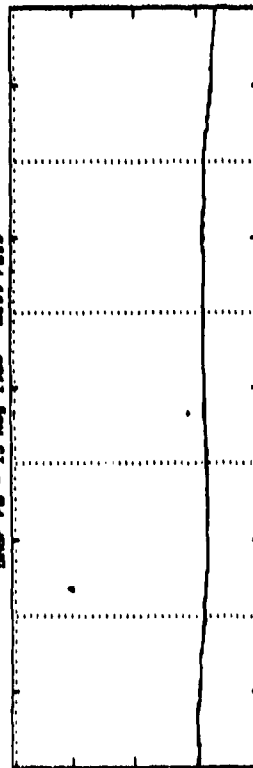
05:37:01	06:41:01	06:45:01	06:49:01	06:53:01	06:57:01 GMT
42.83	28.71	14.41	-0.69	-14.60	-32.65 APRILAT
239.19	238.43	237.67	237.04	236.60	236.60 APRILON

INSP FB - 15 Aug 1968 - Center Pass



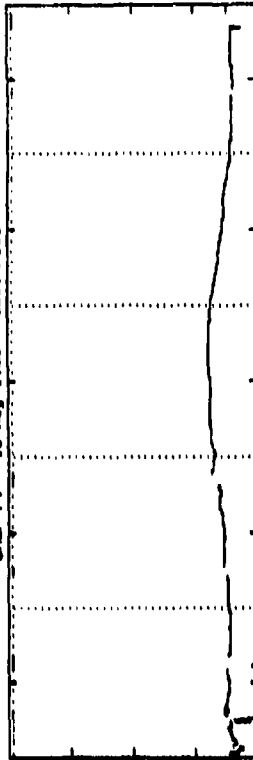
07:18:01	07:22:01	07:26:01	07:30:01	07:34:01	07:38:01 GMT
42.56	28.02	13.22	-2.02	-17.66	-31.44 APRILAT
237.87	233.61	233.61	232.09	230.83	229.61 APRILON

INSP FB - 15 Aug 1968 - West Pass



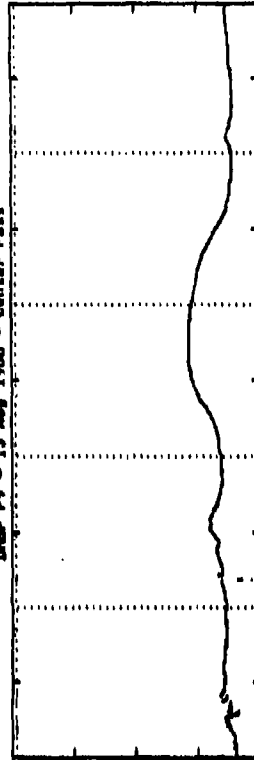
09:00:01	09:04:01	09:08:01	09:12:01	09:16:01	09:20:01 GMT
41.01	24.36	11.29	-4.14	-19.94	-28.82 APRILAT
210.44	212.96	209.33	204.66	204.13	201.36 APRILON

INSP FY - 15 Aug 1968 - East Pass



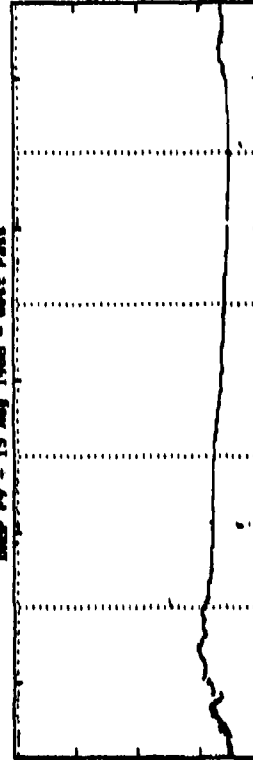
07:39:01	08:03:01	08:07:01	08:11:01	08:15:01	08:19:01 GMT
41.61	27.29	12.69	-2.59	-18.44	-34.22 APRILAT
272.79	272.67	272.28	271.67	271.40	271.98 APRILON

INSP FY - 15 Aug 1968 - Center Pass



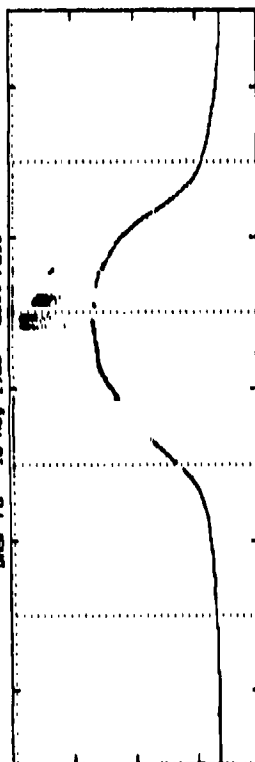
09:39:01	09:43:01	09:47:01	09:51:01	09:55:01	09:59:01 GMT
42.24	27.98	13.32	-1.67	-17.39	-33.42 APRILAT
258.21	248.87	247.73	246.94	246.34	245.94 APRILON

INSP FY - 15 Aug 1968 - West Pass



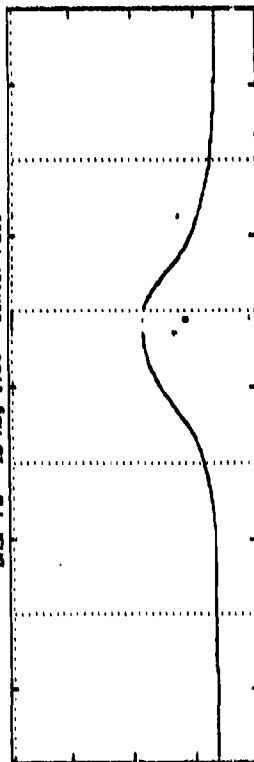
11:20:01	11:24:01	11:28:01	11:32:01	11:36:01	11:40:01 GMT
40.94	26.21	11.17	-4.21	-19.87	-35.62 APRILAT
229.28	226.44	222.91	221.55	220.88	218.38 APRILON

DWSP F8 - 16 Aug 1988 - East Pass



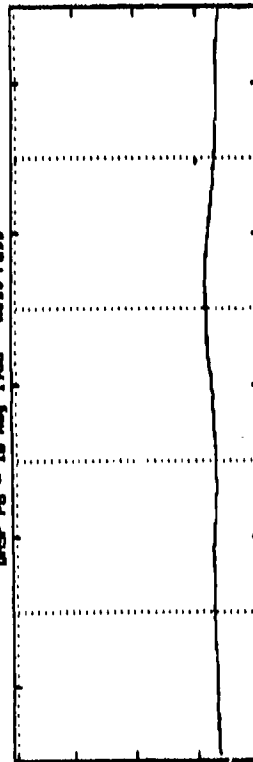
05:25:01	05:29:01	05:33:01	05:37:01	05:41:01	05:45:01 GMT
41.84	27.76	13.40	-1.76	-17.72	-33.72 APILAT
261.90	261.30	260.46	260.03	259.65	259.81 APILON

DWSP F8 - 16 Aug 1988 - Center Pass



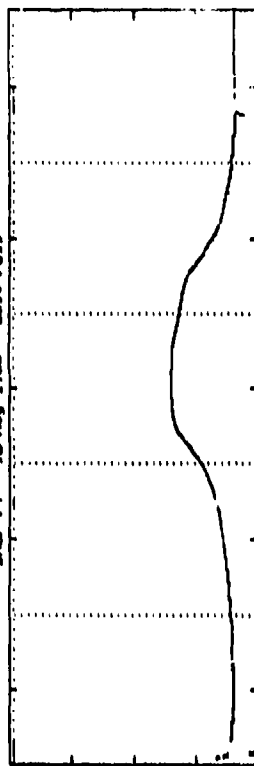
07:04:01	07:10:01	07:14:01	07:18:01	07:22:01	07:26:01 GMT
41.34	26.85	12.10	-3.17	-18.87	-34.68 APILAT
260.21	238.14	236.36	235.05	233.75	232.90 APILON

DWSP F8 - 16 Aug 1988 - West Pass



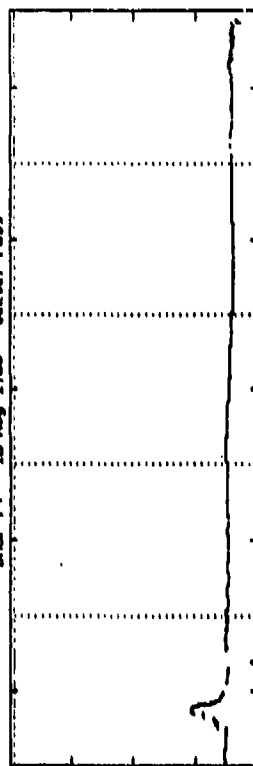
08:47:01	08:51:01	08:55:01	08:59:01	09:03:01	09:07:01 GMT
43.10	28.48	13.07	-1.90	-17.97	-31.42 APILAT
219.80	216.28	212.95	210.12	207.70	205.21 APILON

DWSP F9 - 16 Aug 1988 - East Pass



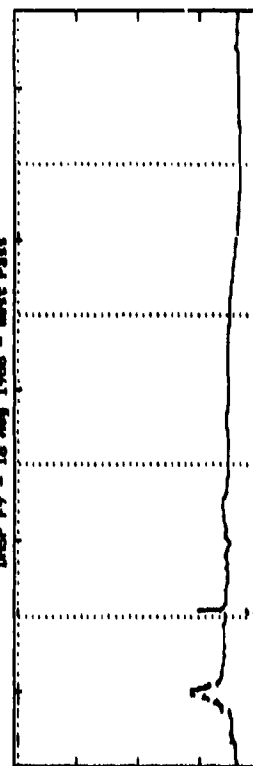
09:20:01	09:24:01	09:28:01	09:32:01	09:36:01	09:40:01 GMT
40.24	26.08	11.62	-3.67	-19.72	-35.74 APILAT
254.28	253.25	252.36	251.70	251.25	251.15 APILON

DWSP F9 - 16 Aug 1988 - Center Pass



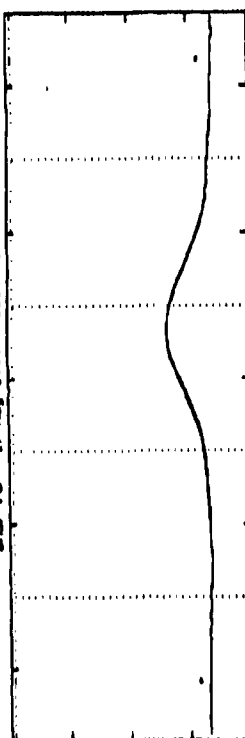
11:00:01	11:04:01	11:08:01	11:12:01	11:16:01	11:20:01 GMT
42.11	27.45	12.50	-2.82	-18.48	-34.24 APILAT
233.49	230.96	228.68	228.89	225.37	223.89 APILON

DWSP F9 - 16 Aug 1988 - West Pass



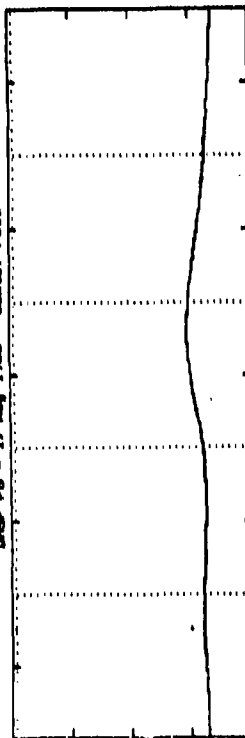
12:41:01	12:45:01	12:49:01	12:53:01	12:57:01	13:01:01 GMT
42.79	28.23	13.14	-2.28	-18.27	-34.28 APILAT
212.65	208.67	205.03	201.91	199.19	196.18 APILON

DROP FB - 17 Aug 1968 - East Pass



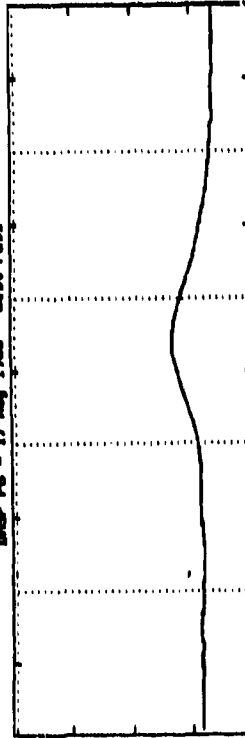
05:13:01	05:17:01	05:21:01	05:25:01	05:29:01	05:33:01 GNT
40.87	26.75	12.34	-2.89	-18.83	-34.79 APPLAT
264.67	264.22	263.65	263.03	262.70	261.02 APRLON

DROP FB - 17 Aug 1968 - Center Pass



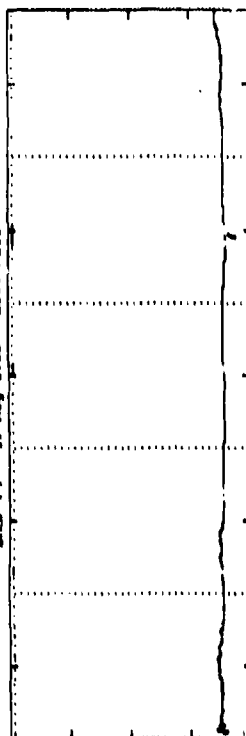
06:34:01	06:38:01	07:02:01	07:06:01	07:10:01	07:14:01 GNT
40.14	23.74	11.03	-4.27	-20.07	-33.88 APPLAT
262.60	260.72	239.15	238.60	237.08	236.21 APRLON

DROP FB - 17 Aug 1968 - West Pass



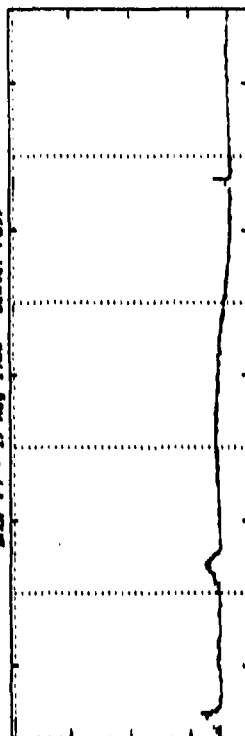
08:32:01	08:37:01	08:43:01	08:47:01	08:51:01	08:55:01 GNT
41.41	26.93	11.67	-2.49	-19.16	-34.94 APPLAT
262.94	238.69	233.37	232.94	230.68	208.34 APRLON

DROP F9 - 17 Aug 1968 - East Pass



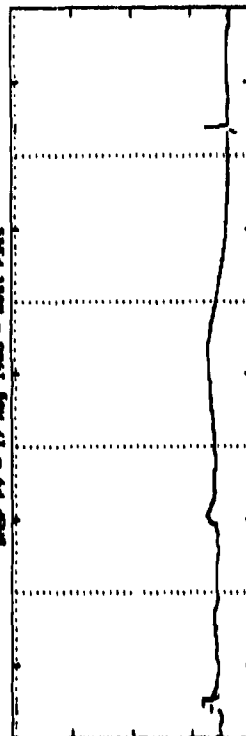
09:00:01	09:04:01	09:08:01	09:12:01	09:16:01	09:20:01 GNT
41.87	27.73	13.37	-1.80	-17.81	-33.88 APPLA
258.70	257.95	257.22	256.60	256.20	254.26 APRLD

DROP F9 - 17 Aug 1968 - Center Pass



10:41:01	10:45:01	10:49:01	10:53:01	10:57:01	11:01:01 GNT
39.73	23.13	10.22	-2.15	-20.90	-36.67 APPLA
257.12	254.88	252.99	251.35	250.32	247.12 APRLD

DROP F9 - 17 Aug 1968 - West Pass



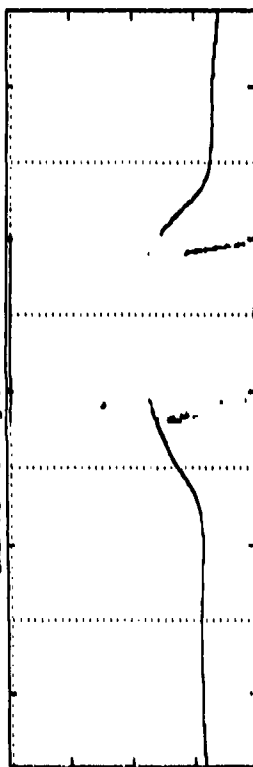
12:22:01	12:26:01	12:30:01	12:34:01	12:38:01	12:42:01 GNT
39.99	23.24	10.10	-3.41	-21.25	-37.17 APPLAT
254.17	252.50	249.14	254.20	253.79	200.98 APRLD

DRSP FB - 18 Aug 1968 - East Pass



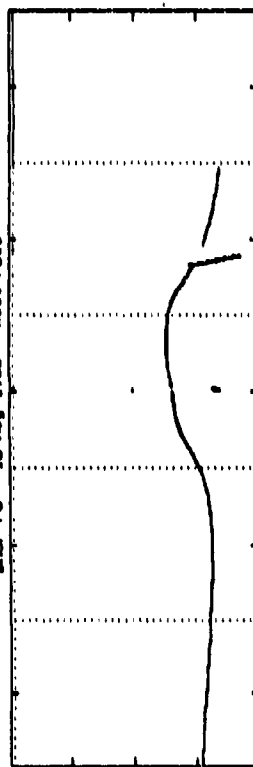
05:01:01	05:03:01	05:09:01	05:13:01	05:17:01	05:21:01 GMT
42.63	23.75	11.24	-4.03	-20.00	-35.84
267.30	267.16	268.64	268.02	265.76	266.24
					APRIL 04

DRSP FB - 18 Aug 1968 - Center Pass



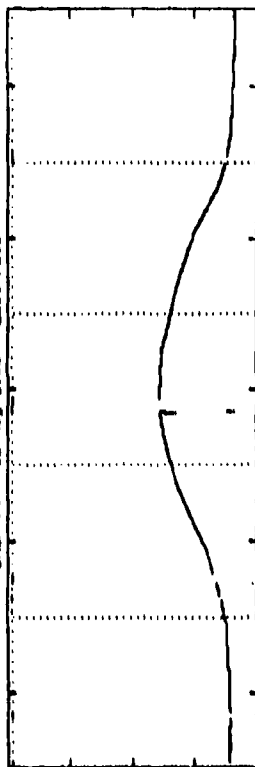
04:41:01	05:35:01	06:49:01	06:53:01	06:57:01	07:01:01 GMT
42.63	28.28	13.72	-1.44	-17.22	-33.12
263.46	263.76	262.27	261.23	260.41	259.68
					APRIL 04

DRSP FB - 18 Aug 1968 - West Pass



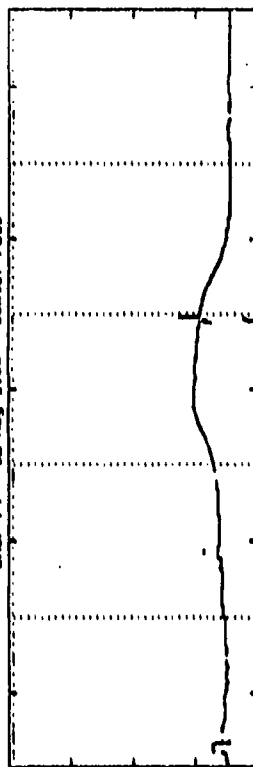
08:23:01	08:27:01	08:31:01	08:35:01	08:39:01	08:43:01 GMT
40.14	23.42	10.24	-3.03	-20.48	-36.43
264.27	267.11	218.22	233.80	213.71	211.33
					APRIL 04

DRSP F9 - 18 Aug 1968 - East Pass



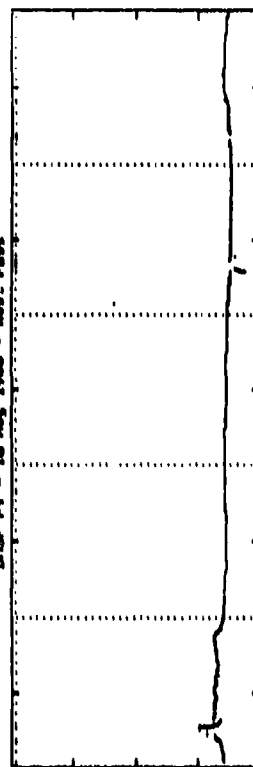
08:41:01	08:45:01	08:49:01	08:53:01	08:57:01	09:01:01 GMT
39.97	23.84	11.28	-3.93	-19.98	-35.94
263.04	262.34	261.95	261.36	261.08	261.43
					APRIL 04

DRSP F9 - 18 Aug 1968 - Center Pass



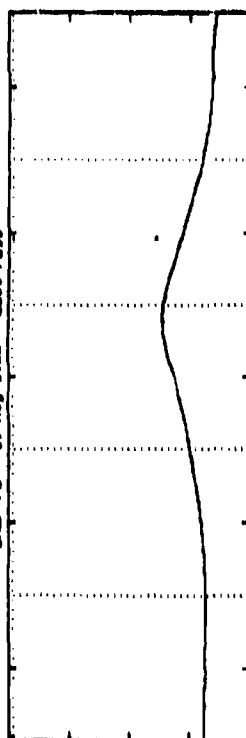
10:21:01	10:25:01	10:29:01	10:33:01	10:37:01	10:41:01 GMT
41.18	24.41	11.83	-3.44	-19.24	-35.08
241.37	239.41	237.76	236.36	235.56	234.63
					APRIL 04

DRSP F9 - 18 Aug 1968 - West Pass



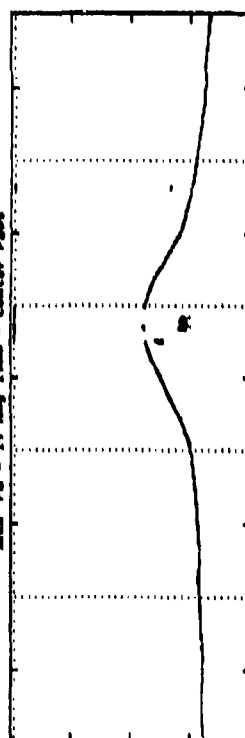
12:02:01	12:06:01	12:10:01	12:14:01	12:18:01	12:22:01 GMT
40.81	24.07	10.99	-4.43	-20.20	-36.04
220.38	217.18	214.03	211.38	209.09	206.63
					APRIL 04

DRIP F9 - 19 Aug 1988 - East Pass



04:48:01	04:52:01	04:56:01	05:00:01	05:04:01	05:08:01 GWT
42.52	28.59	13.83	-1.34	-17.17	-31.60 APRILAT
270.43	270.22	269.79	269.14	268.60	269.22 APRILON

DRIP F9 - 19 Aug 1988 - Center Pass



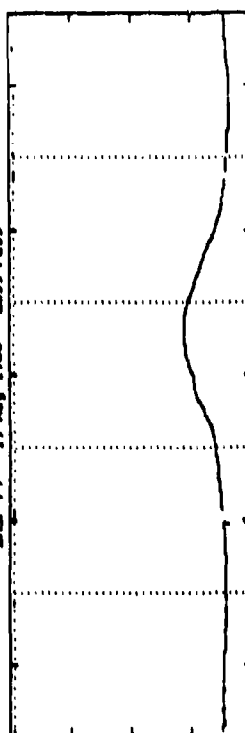
04:29:01	04:33:01	04:37:01	04:41:01	04:45:01	04:49:01 GWT
41.52	27.24	12.73	-2.47	-18.23	-34.26 APRILAT
267.72	268.41	269.13	269.23	269.52	269.96 APRILON

DRIP F9 - 19 Aug 1988 - West Pass



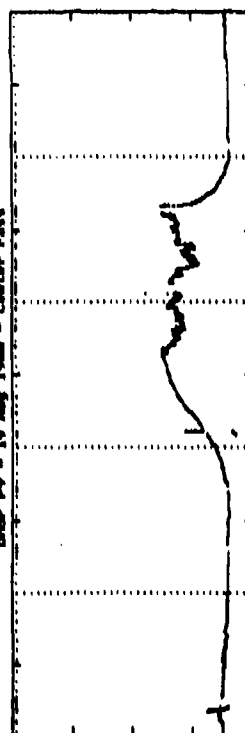
08:16:01	08:20:01	08:24:01	08:28:01	08:32:01 GWT	
42.29	27.48	12.69	-2.63	-18.23	-33.93 APRILAT
269.31	270.52	270.52	269.22	267.29	269.30 APRILON

DRIP F9 - 19 Aug 1988 - East Pass



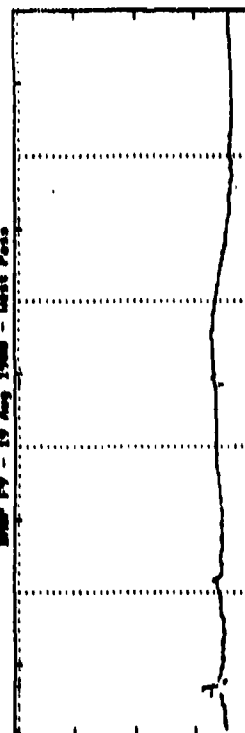
08:21:01	08:25:01	08:29:01	08:33:01	08:37:01	08:41:01 GWT
41.44	27.47	13.01	-2.23	-18.17	-34.10 APRILAT
267.41	267.32	266.83	266.25	265.94	266.37 APRILON

DRIP F9 - 19 Aug 1988 - Center Pass



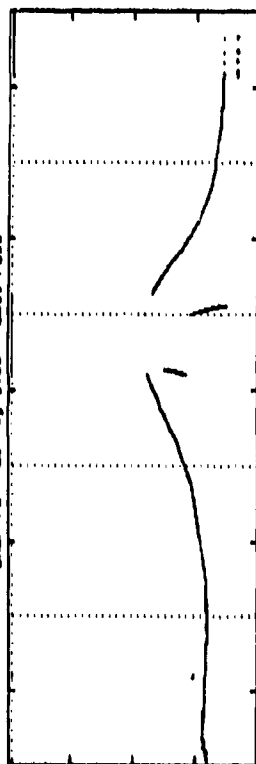
10:01:01	10:05:01	10:09:01	10:13:01	10:17:01	10:21:01 GWT
42.54	28.16	13.08	-1.43	-17.43	-33.39 APRILAT
263.61	263.93	263.92	263.52	263.72	263.04 APRILON

DRIP F9 - 19 Aug 1988 - West Pass



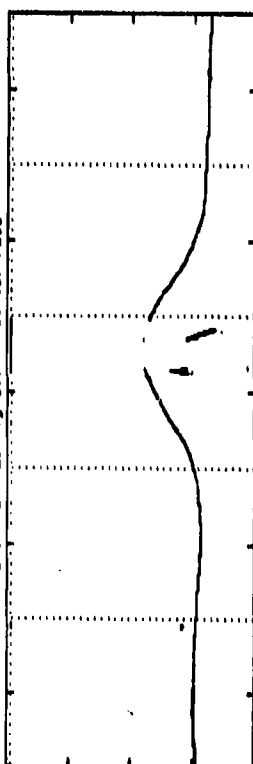
11:42:01	11:46:01	11:50:01	11:54:01	11:58:01	12:02:01 GWT
41.77	27.63	11.95	-3.39	-19.07	-34.83 APRILAT
259.99	261.77	261.87	261.49	261.28	261.28 APRILON

DSP F8 - 20 Aug 1968 - East Pass



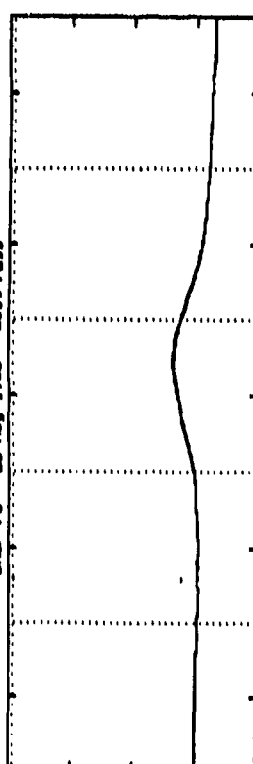
04:28:01	04:40:01	04:44:01	04:48:01	04:52:01	04:56:01 GMT
41.37	27.27	12.48	-2.56	-18.39	-34.06 APRILAT
273.34	273.20	272.79	272.15	271.85	272.40 APRILON

DSP F8 - 20 Aug 1968 - Center Pass



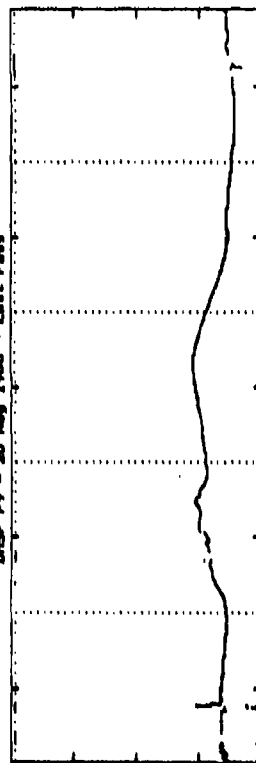
04:17:01	04:21:01	04:25:01	04:29:01	04:33:01	04:37:01 GMT
40.44	26.23	11.79	-3.50	-19.43	-33.38 APRILAT
250.44	249.12	248.01	247.22	246.42	246.25 APRILON

DSP F8 - 20 Aug 1968 - West Pass



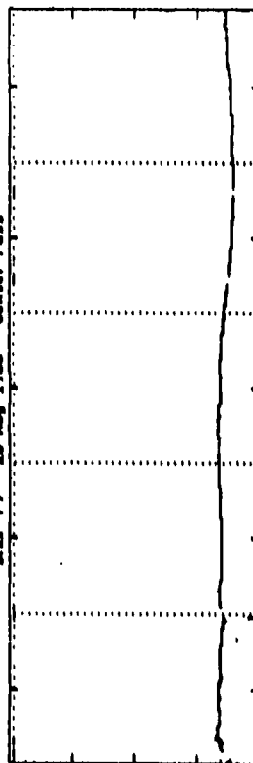
07:36:01	08:02:01	08:06:01	08:10:01	08:14:01	08:18:01 GMT
40.46	26.28	11.29	-4.85	-19.47	-33.36 APRILAT
227.36	226.73	226.18	222.11	220.32	218.53 APRILON

DSP F9 - 20 Aug 1968 - East Pass



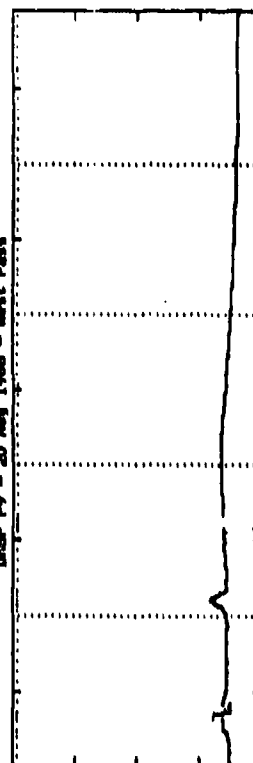
08:02:01	08:06:01	08:10:01	08:14:01	08:18:01	08:22:01 GMT
39.80	25.50	10.85	-4.52	-20.41	-36.15 APRILAT
272.26	272.00	271.61	271.00	270.81	271.51 APRILON

DSP F9 - 20 Aug 1968 - Center Pass



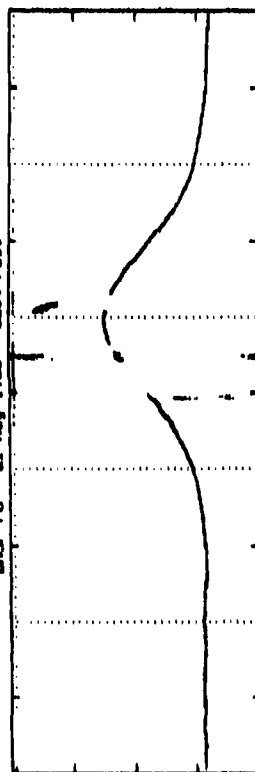
09:42:01	09:46:01	09:50:01	09:54:01	09:58:01	10:02:01 GMT
40.45	26.19	11.66	-3.63	-19.60	-35.58 APRILAT
249.52	248.17	247.04	246.26	245.66	245.27 APRILON

DSP F9 - 20 Aug 1968 - West Pass



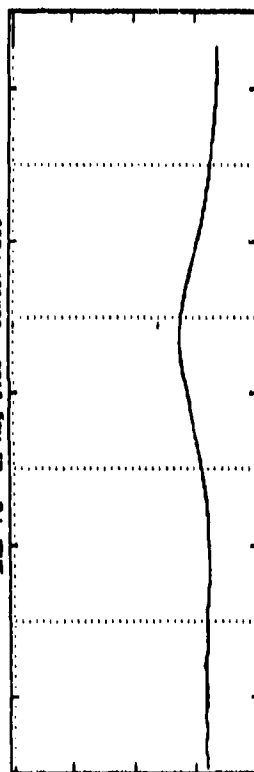
11:22:01	11:26:01	11:30:01	11:34:01	11:38:01	11:42:01 GMT
42.83	28.13	13.13	-2.20	-17.83	-33.58 APRILAT
229.14	226.29	223.45	221.49	219.46	217.87 APRILON

SWSP FB - 21 Aug 1988 - East Pass



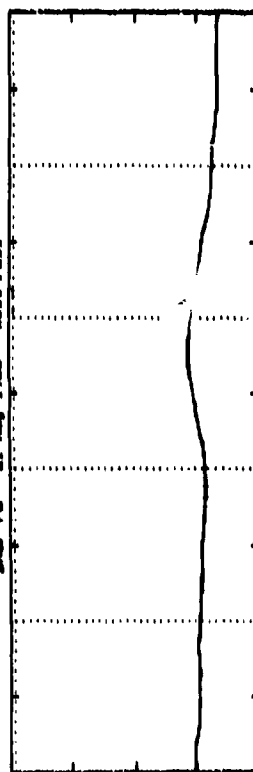
06:34:01	06:08:01	06:12:01	06:16:01	06:20:01	06:24:01	06:28:01
42.97	28.79	14.43	-0.43	-16.30	-32.33	-48.36
253.30	252.15	251.14	250.38	249.83	249.34	248.85

SWSP FB - 21 Aug 1988 - Center Pass



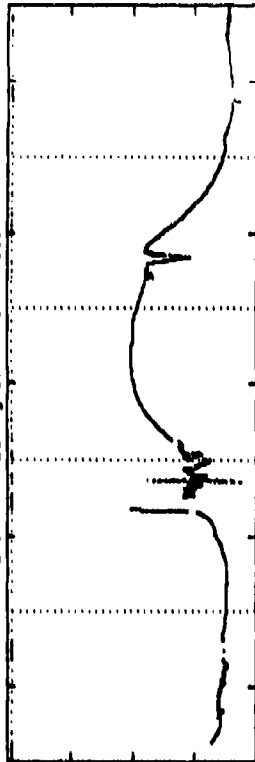
07:43:01	07:49:01	07:52:01	07:57:01	08:01:01	08:06:01	08:10:01
42.97	28.79	14.43	-1.33	-17.12	-32.82	-48.52
253.49	252.85	252.41	252.46	252.82	253.23	253.64

SWSP FB - 21 Aug 1988 - West Pass



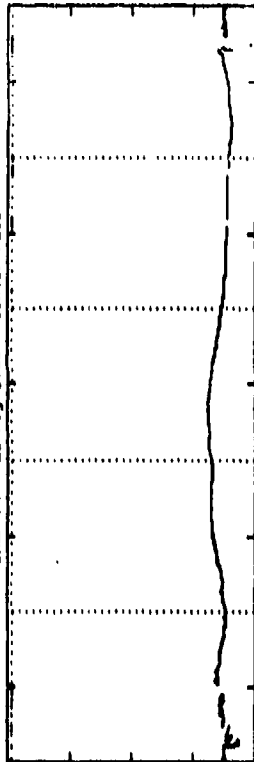
09:37:04	09:38:01	09:39:01	09:40:01	09:41:01	09:42:01	09:43:01
42.97	28.79	14.43	-2.74	-18.43	-34.14	-49.84
253.11	252.84	252.30	252.14	252.34	252.54	252.74

SWSP FY - 21 Aug 1988 - East Pass



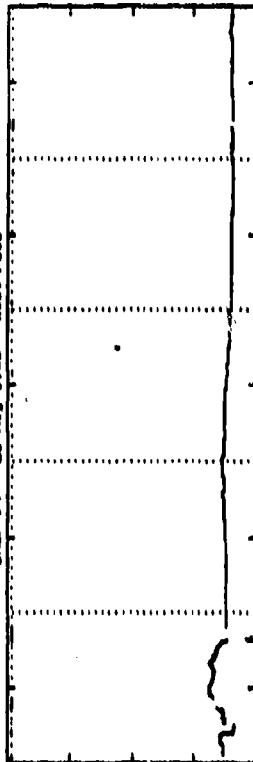
09:22:01	09:24:01	09:26:01	09:28:01	09:30:01	09:32:01	09:34:01
42.97	27.84	13.45	-1.72	-17.49	-32.76	-48.03
253.87	252.81	251.87	251.17	250.68	250.49	250.30

SWSP FY - 21 Aug 1988 - Center Pass



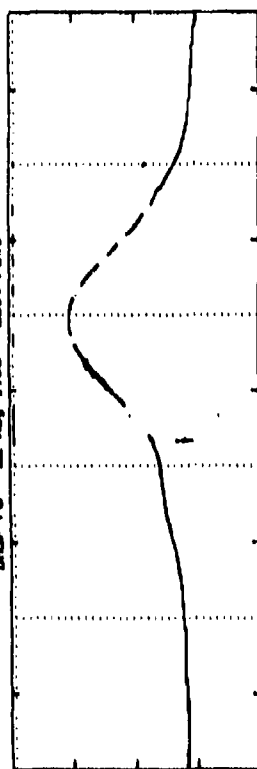
11:02:01	11:07:01	11:11:01	11:15:01	11:19:01	11:23:01	11:27:01
42.97	28.79	14.43	-4.71	-20.40	-36.14	-51.88
253.49	253.12	252.86	252.08	251.55	251.02	250.49

SWSP FY - 21 Aug 1988 - West Pass



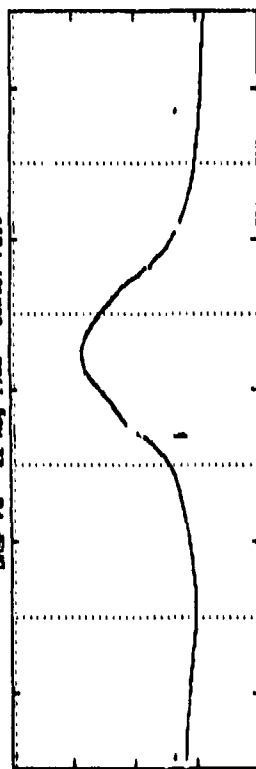
12:44:01	12:46:01	12:48:01	12:50:01	12:52:01	12:54:01	12:56:01
41.09	26.47	11.25	-3.22	-18.43	-34.14	-49.84
251.64	250.46	250.03	250.24	250.44	250.64	250.84

DWSP F8 - 22 Aug 1968 - East Pass



05:32:01	05:34:01	06:00:01	06:04:01	06:08:01	06:12:01 GMT
41.94	27.81	13.48	-1.43	-17.99	-33.62 APILAT
233.90	234.93	234.04	233.37	232.90	232.77 APILON

DWSP F8 - 22 Aug 1968 - Center Pass



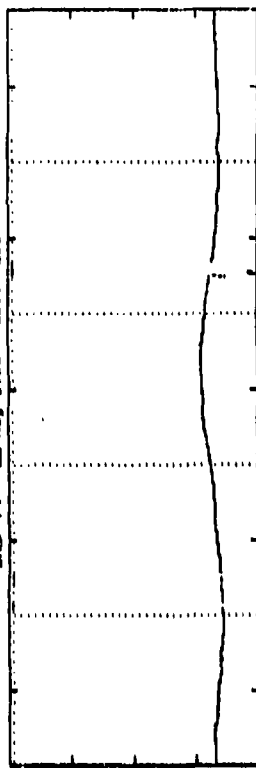
07:32:01	07:37:01	07:41:01	07:45:01	07:49:01	07:53:01 GMT
41.94	27.34	12.46	-2.81	-18.44	-34.13 APILAT
234.77	232.30	230.07	228.38	226.92	223.49 APILON

DWSP F8 - 22 Aug 1968 - West Pass



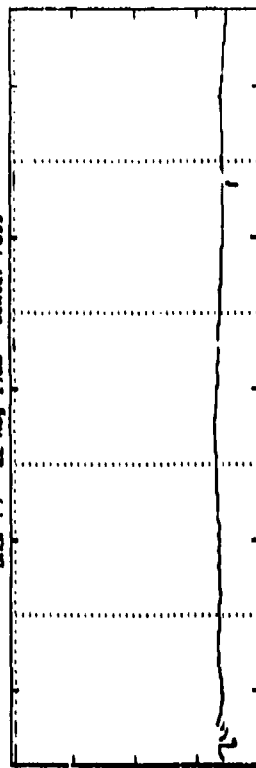
09:15:01	09:19:01	09:23:01	09:27:01	09:31:01	09:35:01 GMT
40.74	26.14	11.04	-4.44	-20.28	-36.20 APILAT
213.39	209.49	203.92	202.92	200.24	197.20 APILON

DWSP F9 - 22 Aug 1968 - East Pass



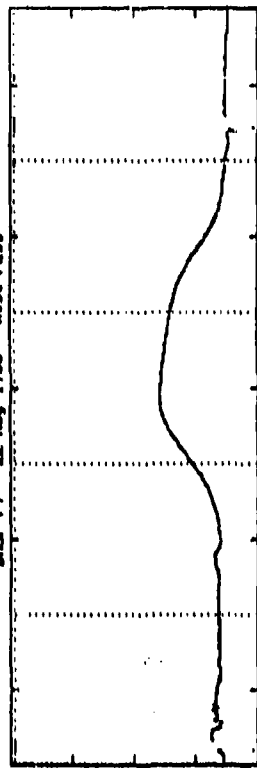
09:03:01	09:07:01	09:11:01	09:15:01	09:19:01	09:23:01 GMT
40.07	23.96	11.32	-3.77	-19.83	-35.86 APILAT
238.04	237.28	234.54	233.93	233.57	233.48 APILON

DWSP F9 - 22 Aug 1968 - Center Pass



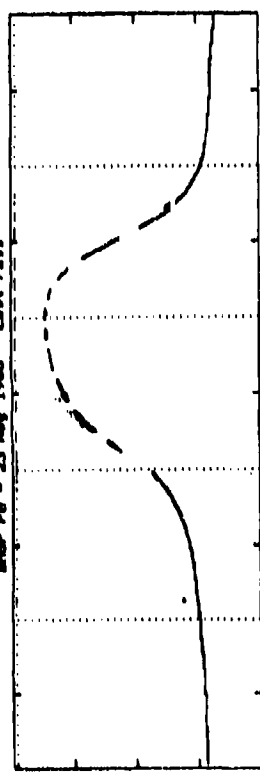
10:43:01	10:47:01	10:51:01	10:55:01	10:59:01	11:03:01 GMT
41.39	26.99	12.12	-3.18	-18.89	-34.67 APILAT
234.91	234.63	232.63	231.11	229.80	228.59 APILON

DWSP F9 - 22 Aug 1968 - West Pass



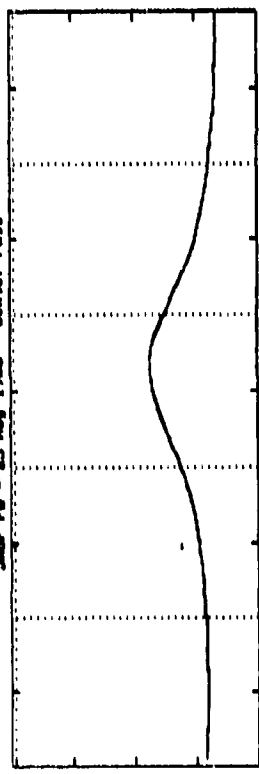
12:24:01	12:28:01	12:32:01	12:36:01	12:40:01	12:44:01 GMT
41.86	27.21	12.13	-3.34	-19.14	-33.09 APILAT
214.13	212.42	208.97	204.04	203.49	200.73 APILON

DRSP F8 - 23 Aug 1988 - East Pass



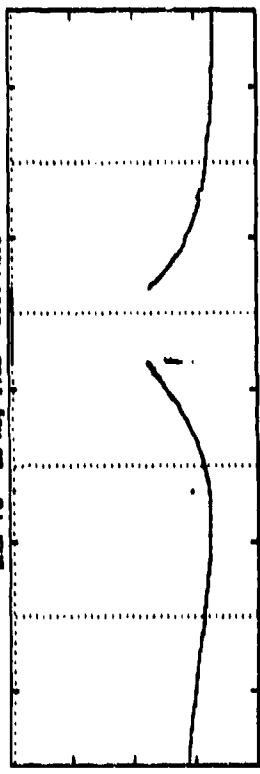
03:40:01	05:44:01	06:48:01	07:52:01	08:56:01	09:00:01
40.51	26.84	12.48	-2.71	-18.70	-34.69
238.56	237.77	237.01	236.37	235.96	236.01
					APRILAT
					APRILON

DRSP F8 - 23 Aug 1988 - Center Pass



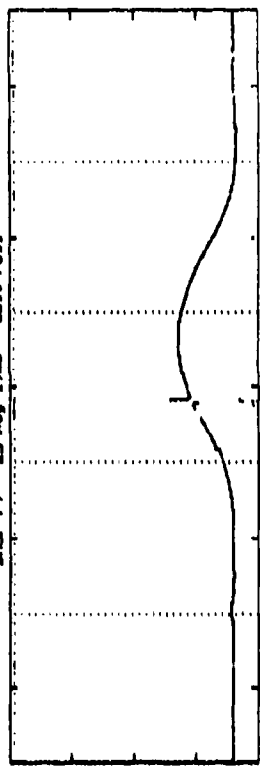
07:21:01	07:25:01	07:29:01	07:33:01	07:37:01	07:41:01
40.67	26.11	11.26	-4.03	-19.71	-35.43
237.08	236.80	232.82	231.32	230.04	228.78
					APRILAT
					APRILON

DRSP F8 - 23 Aug 1988 - West Pass



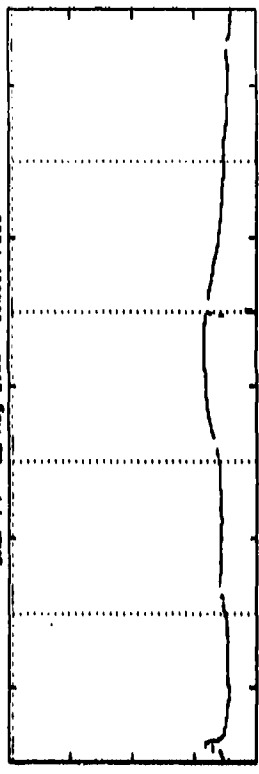
07:02:01	07:06:01	07:10:01	07:14:01	07:18:01	07:22:01
42.89	28.23	13.21	-2.20	-17.94	-32.83
236.48	232.87	230.37	230.48	231.82	231.07
					APRILAT
					APRILON

DRSP F9 - 23 Aug 1988 - East Pass



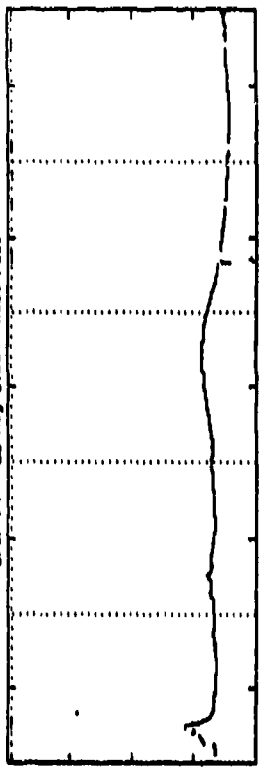
08:43:01	08:47:01	08:51:01	08:55:01	08:59:01	09:03:01
41.74	27.60	13.23	-1.96	-17.96	-34.00
262.55	262.02	261.45	260.82	260.48	260.71
					APRILAT
					APRILON

DRSP F9 - 23 Aug 1988 - Center Pass



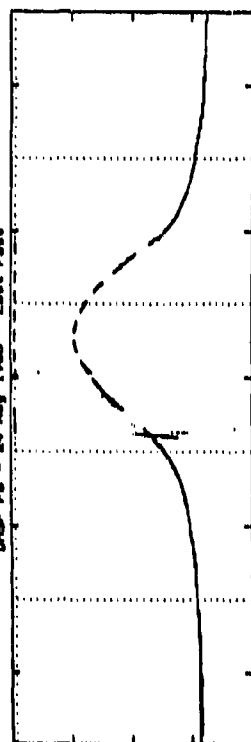
10:22:01	10:26:01	10:30:01	10:34:01	10:38:01	10:42:01
42.93	28.44	13.73	-1.49	-17.23	-33.07
241.11	237.12	237.37	236.07	233.05	234.08
					APRILAT
					APRILON

DRSP F9 - 23 Aug 1988 - West Pass



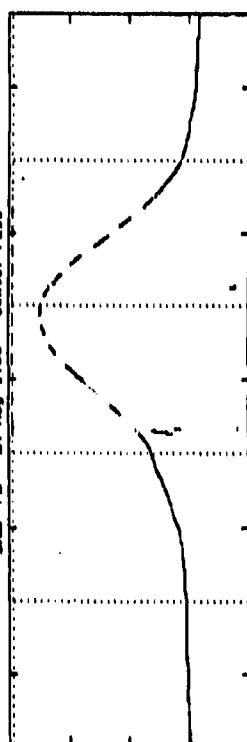
12:04:01	12:08:01	12:12:01	12:16:01	12:20:01	12:24:01
42.71	28.04	13.08	-2.41	-18.12	-33.98
220.51	217.08	213.84	211.10	208.75	206.33
					APRILAT
					APRILON

DWSP FB - 24 Aug 1988 - East Pass



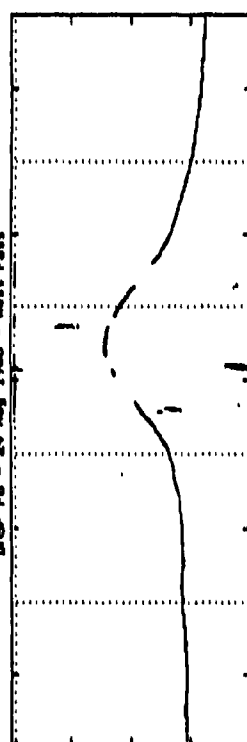
03:28:01	03:32:01	03:36:01	03:40:01	03:44:01	03:48:01
37.94	23.86	11.43	-3.81	-19.81	-35.76
261.28	260.65	259.98	259.37	259.03	259.25
APRILAT					
APRILON					

DWSP FB - 24 Aug 1988 - Center Pass



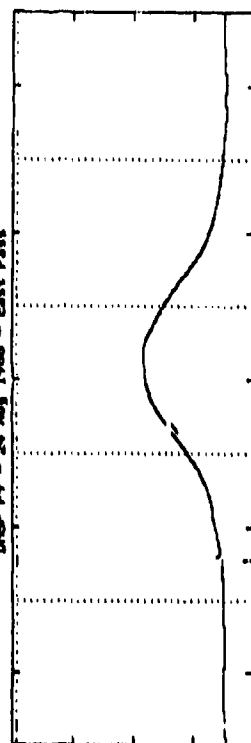
07:08:01	07:12:01	07:16:01	07:20:01	07:24:01	07:28:01
43.07	28.38	13.87	-1.32	-16.99	-32.76
237.96	237.89	233.98	234.60	233.45	232.36
APRILAT					
APRILON					

DWSP FB - 24 Aug 1988 - West Pass



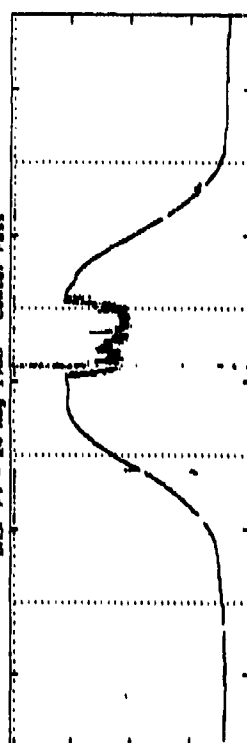
08:30:01	08:34:01	08:38:01	08:42:01	08:46:01	08:50:01
41.26	26.41	11.54	-3.84	-17.56	-33.38
218.89	213.29	211.99	209.20	206.78	204.19
APRILAT					
APRILON					

DWSP FY - 24 Aug 1988 - East Pass



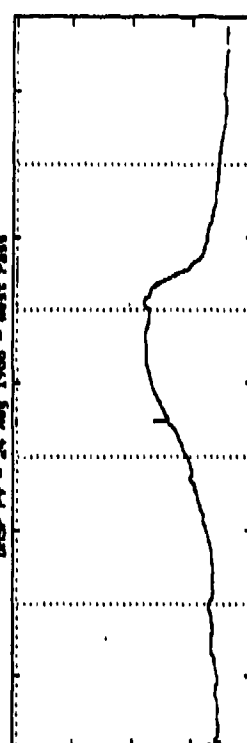
08:24:01	08:28:01	08:32:01	08:36:01	08:40:01	08:44:01
39.86	23.68	11.16	-4.18	-20.17	-36.07
267.00	266.68	266.17	265.38	265.35	265.86
APRILAT					
APRILON					

DWSP FY - 24 Aug 1988 - Center Pass



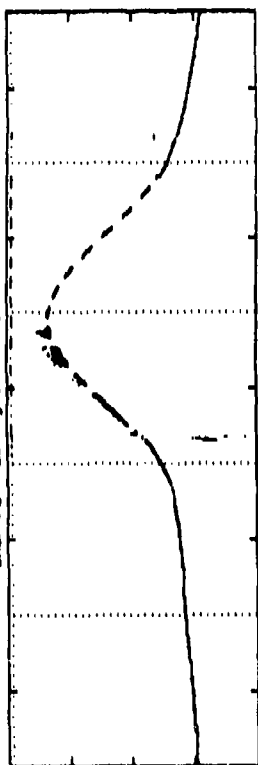
10:04:01	10:08:01	10:12:01	10:16:01	10:20:01	10:24:01
40.74	26.36	11.71	-3.38	-19.49	-35.26
244.89	243.20	241.80	240.81	240.00	239.31
APRILAT					
APRILON					

DWSP FY - 24 Aug 1988 - West Pass



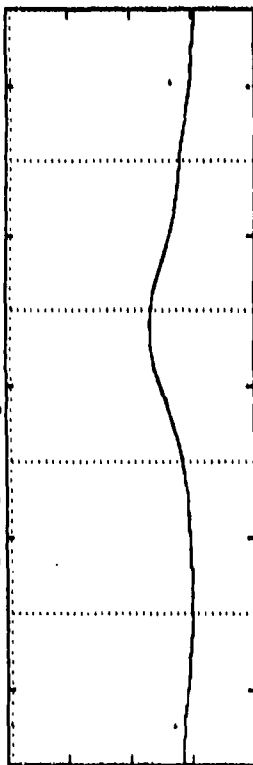
11:45:01	11:49:01	11:53:01	11:57:01	12:01:01	12:05:01
40.01	23.26	10.16	-3.26	-20.78	-36.73
224.02	220.89	217.97	213.38	213.49	211.32
APRILAT					
APRILON					

DRSP F8 - 25 Aug 1988 - East Pass



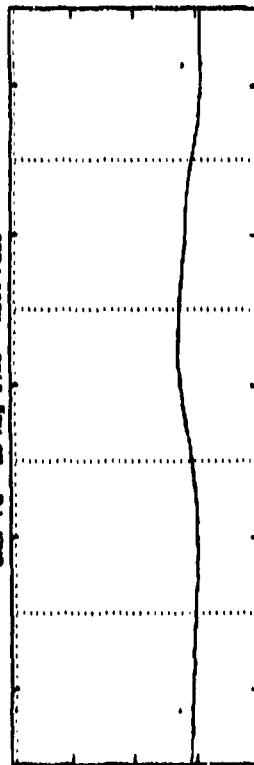
05:13:01	05:19:01	05:22:01	05:31:01	05:35:01 GRT
42.53	28.40	14.08	-1.04	-32.90 APRILAT
264.18	263.70	263.13	262.50	262.32 APRILON

DRSP F8 - 25 Aug 1988 - Center Pass



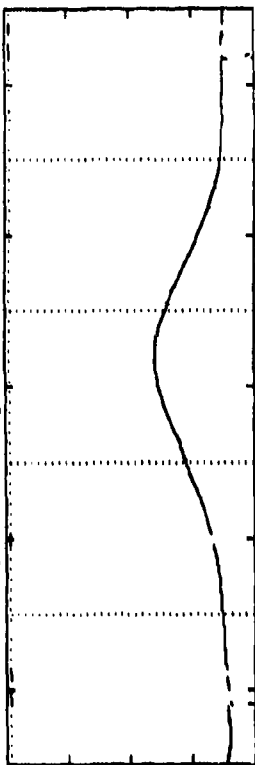
06:26:01	07:00:01	07:04:01	07:08:01	07:14:01 GRT
41.87	37.43	12.78	-2.43	-33.97 APRILAT
262.32	260.40	258.75	257.35	255.65 APRILON

DRSP F8 - 25 Aug 1988 - West Pass



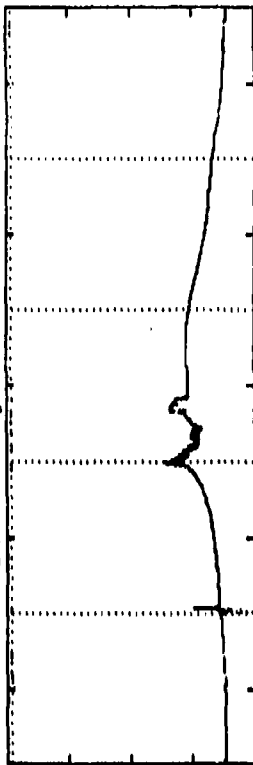
06:38:01	06:42:01	06:46:01	06:50:01	06:58:01 GRT
39.73	23.04	9.94	-3.44	-38.90 APRILAT
257.20	257.72	258.63	259.04	257.34 APRILON

DRSP F9 - 25 Aug 1988 - East Pass



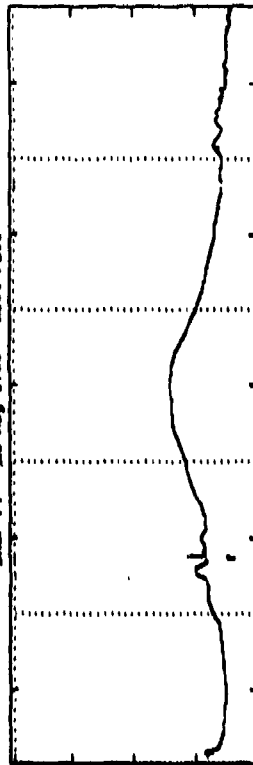
08:04:01	08:08:01	08:12:01	08:14:01	08:20:01	08:24:01 GRT
41.57	27.29	12.73	-2.54	-18.41	-34.22 APRILAT
271.63	271.48	271.08	270.47	270.19	270.73 APRILON

DRSP F9 - 25 Aug 1988 - Center Pass



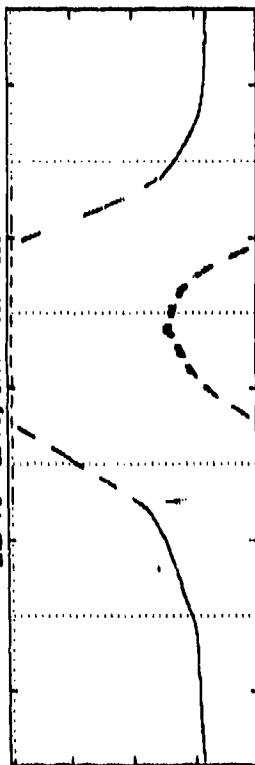
09:44:01	09:48:01	09:52:01	09:54:01	10:00:01	10:04:01 GRT
42.24	27.97	13.47	-1.49	-17.57	-33.60 APRILAT
267.18	267.78	266.38	265.74	265.10	264.64 APRILON

DRSP F9 - 25 Aug 1988 - West Pass



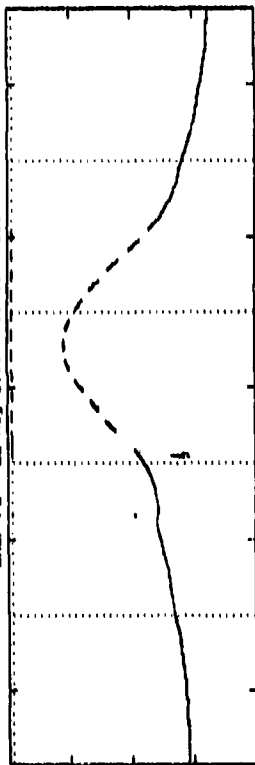
11:22:01	11:26:01	11:30:01	11:32:01	11:38:01	11:42:01 GRT
41.83	26.23	11.27	-4.08	-32.74	-35.47 APRILAT
258.30	258.41	258.79	258.65	258.81	258.96 APRILON

DNRP FB - 26 Aug 1988 - East Pass



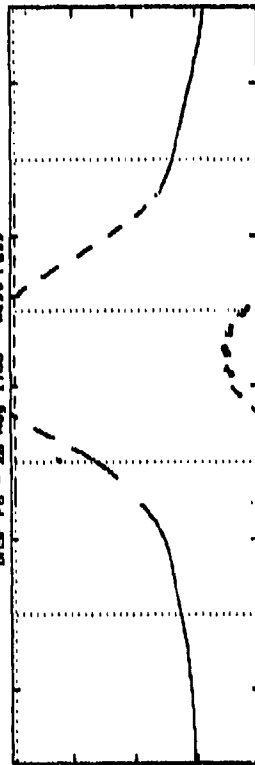
05:02:01	05:07:01	05:11:01	05:15:01	05:19:01	05:23:01 GMT
41.54	27.41	13.00	-2.18	-18.08	-33.97 APRLAT
244.98	244.63	244.12	243.99	243.16	243.52 APRLON

DNRP FB - 26 Aug 1988 - Center Pass



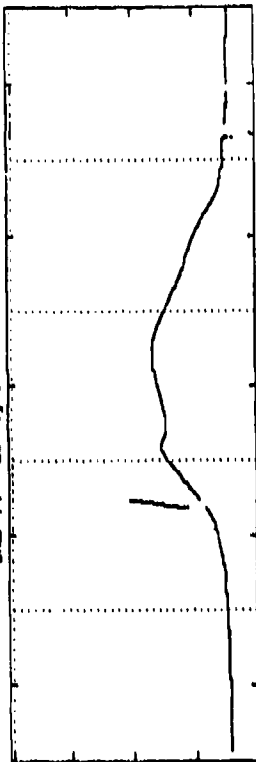
04:44:01	04:48:01	04:52:01	04:56:01	07:00:01	07:04:01 GMT
40.72	26.37	11.73	-3.50	-19.31	-33.15 APRLAT
244.74	243.01	241.56	240.53	239.69	238.95 APRLON

DNRP FB - 26 Aug 1988 - West Pass



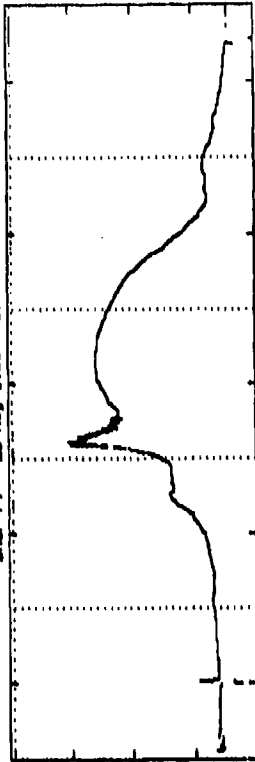
08:23:01	08:27:01	08:30:01	08:37:01	08:41:01	08:45:01 GMT
41.91	27.24	12.22	-3.11	-18.73	-34.47 APRLAT
224.18	220.97	217.98	215.48	213.23	211.15 APRLON

DNRP FY - 26 Aug 1988 - East Pass



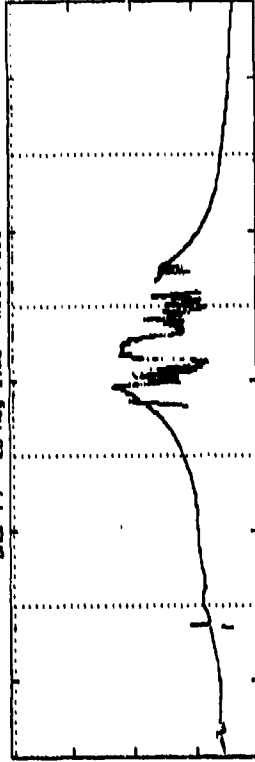
09:25:01	09:29:01	09:33:01	09:37:01	09:41:01	09:45:01 GMT
40.22	26.05	11.58	-3.70	-19.73	-33.75 APRLAT
253.21	252.12	251.18	250.50	250.02	249.86 APRLON

DNRP FY - 26 Aug 1988 - Center Pass



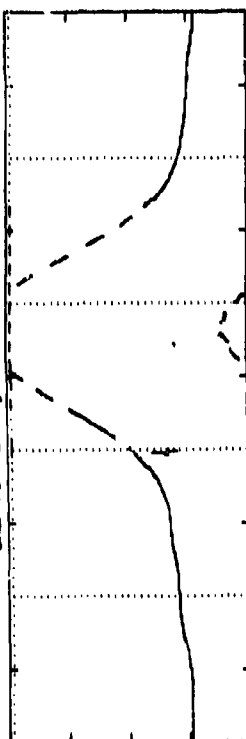
11:09:01	11:09:01	11:12:01	11:17:01	11:21:01	11:25:01 GMT
42.20	27.53	12.58	-2.74	-18.39	-34.14 APRLAT
232.52	229.92	227.56	225.69	224.10	222.55 APRLON

DNRP FY - 26 Aug 1988 - West Pass



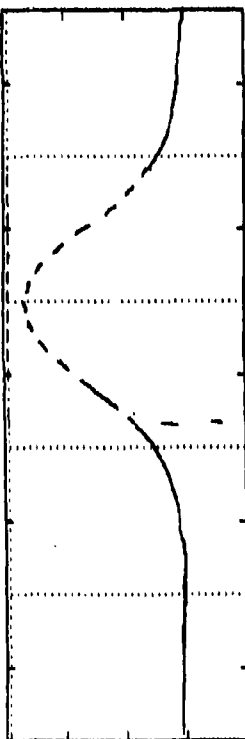
12:46:01	12:50:01	12:54:01	12:58:01	13:02:01	13:06:01 GMT
42.98	28.43	13.38	-2.14	-18.04	-34.08 APRLAT
211.64	207.61	203.65	200.74	197.97	194.89 APRLON

DRSP F8 - 27 Aug 1968 - East Pass



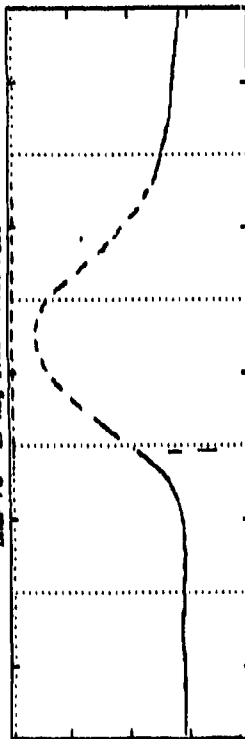
04:51:01	04:55:01	04:59:01	05:03:01	05:07:01	05:11:01 GMT
43.20	26.39	11.89	-3.37	-19.24	-35.03 APILAT
269.04	269.39	269.12	268.99	268.21	268.73 APILON

DRSP F8 - 27 Aug 1968 - Center Pass



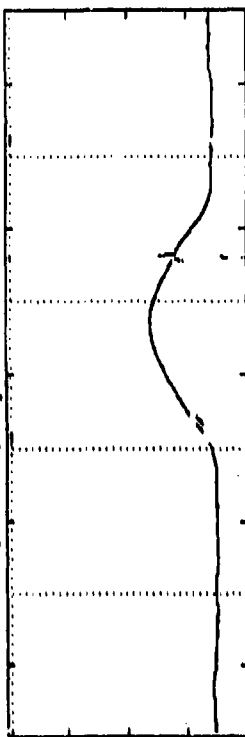
04:51:01	04:55:01	04:59:01	05:03:01	05:07:01	05:11:01 GMT
43.20	26.39	14.46	-0.66	-14.44	-32.36 APILAT
267.39	268.04	268.07	268.73	268.98	268.37 APILON

DRSP F8 - 27 Aug 1968 - West Pass



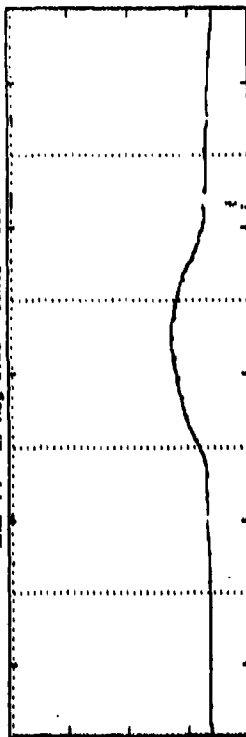
05:13:01	05:17:01	05:21:01	05:25:01	05:29:01	05:33:01 GMT
46.47	23.77	10.74	-4.41	-20.23	-33.93 APILAT
268.43	268.39	268.63	268.39	268.38	268.36 APILON

DRSP F9 - 27 Aug 1968 - East Pass



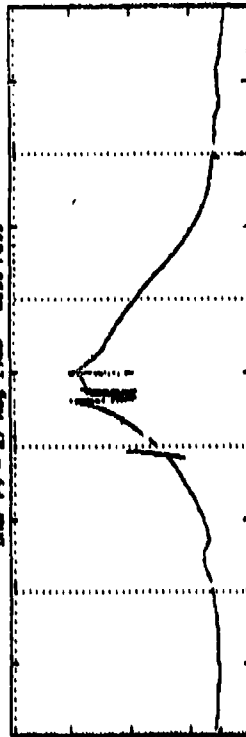
09:05:01	09:09:01	09:13:01	09:17:01	09:21:01	09:25:01 GMT
41.84	27.70	13.35	-1.82	-12.82	-33.90 APILAT
257.62	258.60	258.04	258.40	258.99	259.00 APILON

DRSP F9 - 27 Aug 1968 - Center Pass



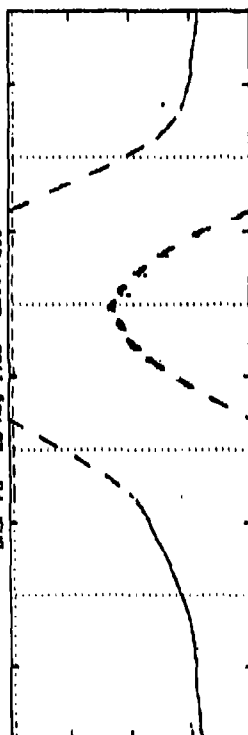
10:44:01	10:50:01	10:56:01	10:58:01	11:02:01	11:04:01 GMT
39.78	25.17	10.24	-3.12	-30.55	-36.61 APILAT
258.13	258.82	258.89	258.36	259.04	257.77 APILON

DRSP F9 - 27 Aug 1968 - West Pass



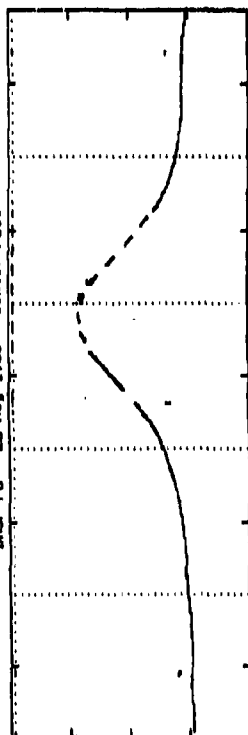
12:27:01	12:31:01	12:35:01	12:39:01	12:43:01	12:47:01 GMT
40.13	27.42	16.32	-2.20	-31.86	-37.00 APILAT
259.14	259.42	258.09	258.11	258.59	259.64 APILON

DWSP FB - 28 Aug 1988 - East Pass



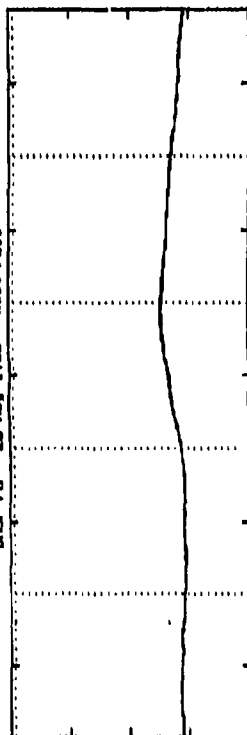
Time	Altitude (ft)	Latitude (N)	Longitude (W)
04:28:01	272.76	27.84	271.67
04:42:01	272.84	27.84	271.63
04:44:01	272.26	27.84	271.23
04:56:01	277.84	27.84	271.67

DWSP FB - 28 Aug 1988 - Center Pass



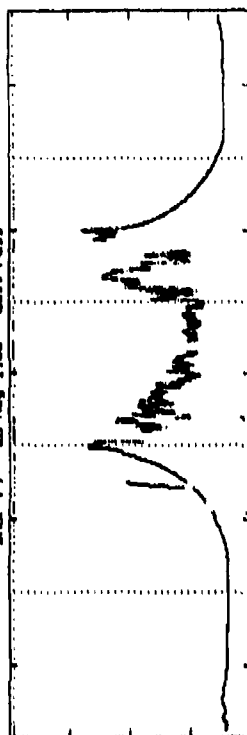
Time	Altitude (ft)	Latitude (N)	Longitude (W)
04:19:01	270.05	27.84	271.67
04:23:01	270.72	27.84	271.63
04:27:01	270.55	27.84	271.23
04:39:01	277.84	27.84	271.67

DWSP FB - 28 Aug 1988 - West Pass



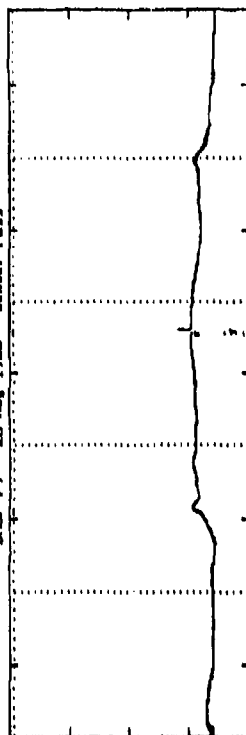
Time	Altitude (ft)	Latitude (N)	Longitude (W)
08:00:01	279.40	28.06	271.67
08:04:01	279.53	28.06	271.63
08:08:01	279.90	28.06	271.23
08:20:01	277.84	28.06	271.67

DWSP FY - 28 Aug 1988 - East Pass



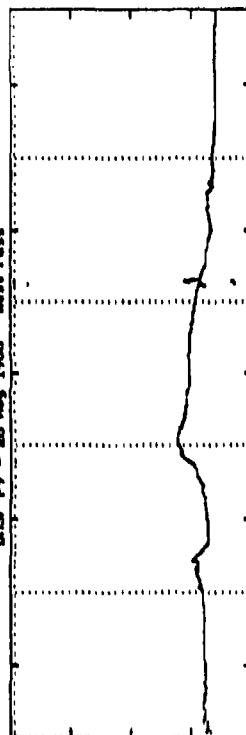
Time	Altitude (ft)	Latitude (N)	Longitude (W)
08:44:01	261.93	26.92	260.17
08:50:01	261.37	26.92	260.16
08:54:01	260.75	26.92	260.16
09:04:01	269.86	26.92	260.17

DWSP FY - 28 Aug 1988 - Center Pass



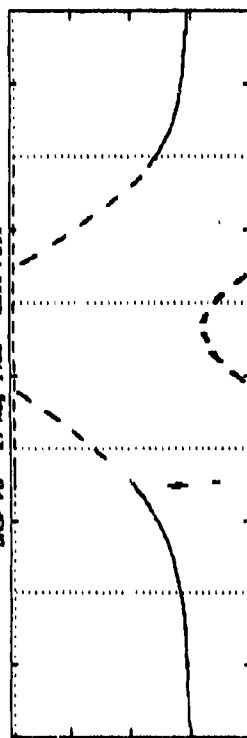
Time	Altitude (ft)	Latitude (N)	Longitude (W)
10:24:01	260.37	41.12	260.17
10:30:01	260.62	41.12	260.16
10:34:01	260.61	41.12	260.16
10:44:01	269.86	41.12	260.17

DWSP FY - 28 Aug 1988 - West Pass



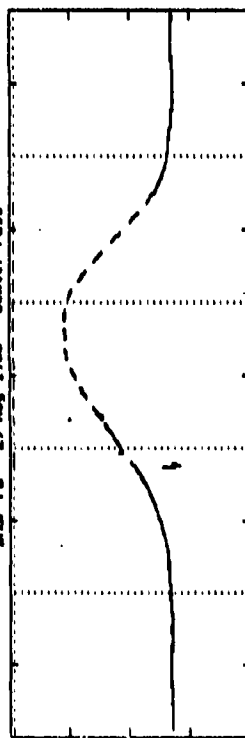
Time	Altitude (ft)	Latitude (N)	Longitude (W)
12:07:01	217.37	40.96	217.67
12:11:01	216.11	40.96	217.63
12:15:01	212.90	40.96	217.23
12:27:01	219.84	40.96	217.67

DRIP F8 - 29 Aug 1988 - East Pass



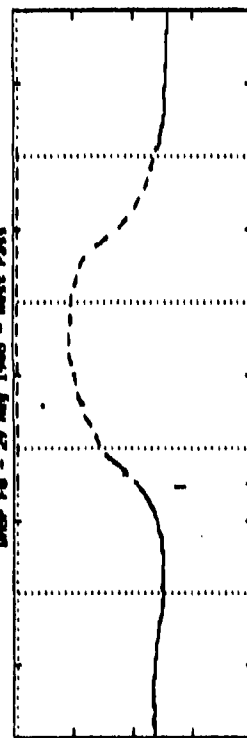
04:07:01	04:11:01	04:15:01	04:19:01	04:23:01	04:27:01
41.04	24.87	12.48	-2.70	-18.43	-34.59
252.63	251.45	250.44	249.70	249.16	248.89
APRILAT					
APRILON					

DRIP F8 - 29 Aug 1988 - Center Pass



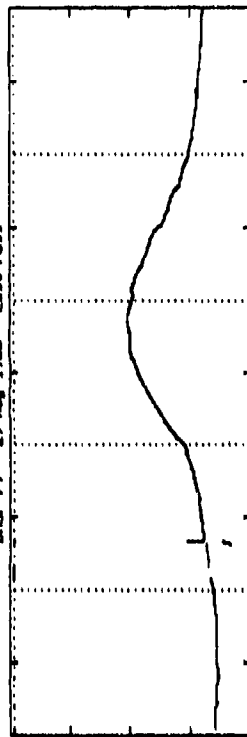
07:48:01	07:52:01	07:56:01	08:00:01	08:04:01	08:08:01
41.34	28.70	11.75	-3.54	-17.14	-34.82
231.67	228.96	228.57	224.44	222.98	221.35
APRILAT					
APRILON					

DRIP F8 - 29 Aug 1988 - West Pass



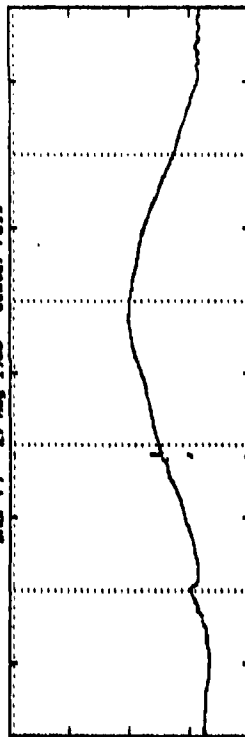
09:28:01	09:32:01	09:36:01	09:40:01	09:44:01	09:48:01
42.32	23.94	10.84	-0.43	-10.43	-26.38
250.00	250.97	250.28	197.17	196.36	193.02
APRILAT					
APRILON					

DRIP F9 - 29 Aug 1988 - East Pass



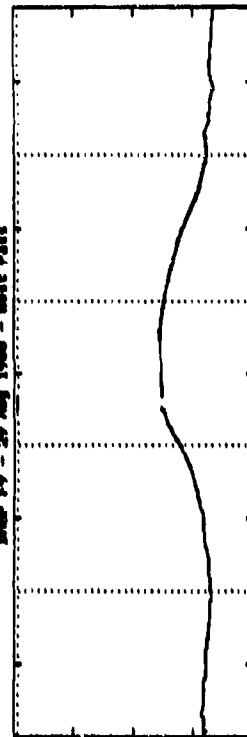
08:24:01	08:28:01	08:32:01	08:36:01	08:40:01	08:44:01
41.41	27.44	12.00	-2.22	-18.17	-34.13
264.48	264.14	263.45	263.05	262.74	262.13
APRILAT					
APRILON					

DRIP F9 - 29 Aug 1988 - Center Pass



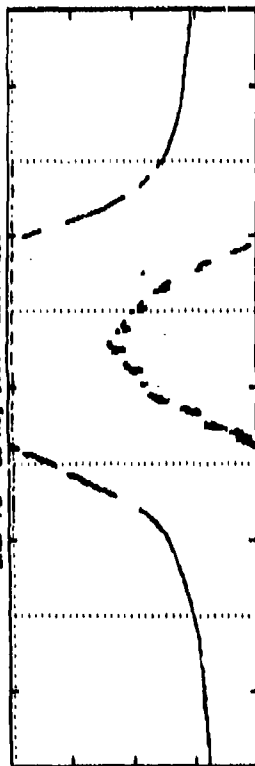
10:04:01	10:08:01	10:12:01	10:16:01	10:20:01	10:24:01
42.33	28.15	13.30	-1.66	-17.47	-33.39
242.67	241.37	240.32	239.47	238.73	238.01
APRILAT					
APRILON					

DRIP F9 - 29 Aug 1988 - West Pass



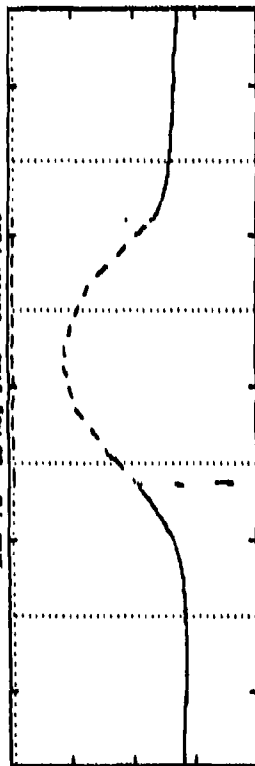
11:47:01	11:51:01	11:55:01	11:59:01	12:03:01	12:07:01
41.87	27.19	12.14	-2.23	-18.93	-34.73
222.52	220.72	217.76	213.25	213.12	210.95
APRILAT					
APRILON					

INSP FB - 30 Aug 1968 - East Pass



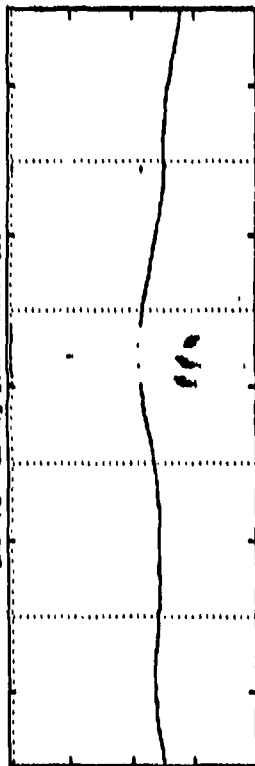
06:30:01	06:39:01	06:03:01	06:07:01	06:15:01	06:19:01	GWT
40.01	23.91	11.50	-3.76	-19.73	-23.48	APRILAT
250.24	254.24	253.77	252.70	252.25	252.16	APRILON

INSP FB - 30 Aug 1968 - Center Pass



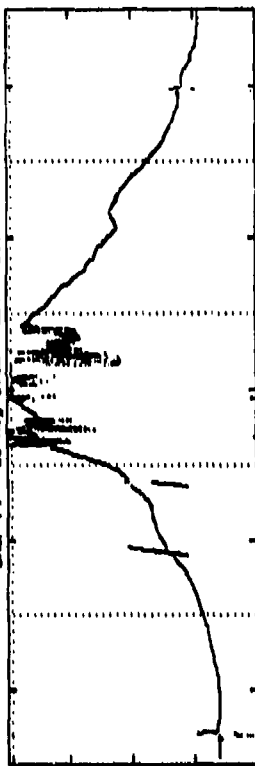
07:36:01	07:40:01	07:44:01	07:48:01	07:52:01	07:56:01	GWT
40.02	23.39	10.47	-4.84	-28.48	-26.15	APRILAT
221.45	221.45	227.28	227.28	228.10	228.43	APRILON

INSP FB - 30 Aug 1968 - West Pass



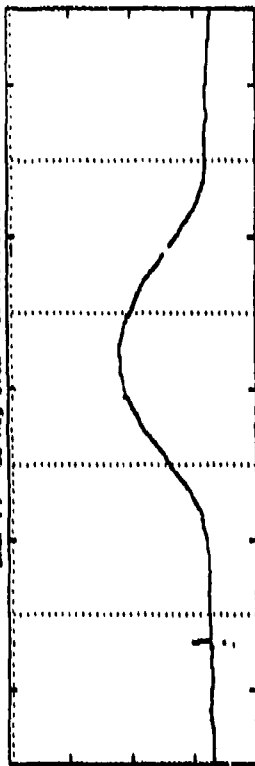
09:17:01	09:21:01	09:25:01	09:29:01	09:33:01	09:37:01	GWT
42.51	27.97	12.96	-2.89	-18.30	-24.23	APRILAT
213.24	209.41	205.76	202.14	197.96	196.98	APRILON

INSP FY - 30 Aug 1968 - East Pass



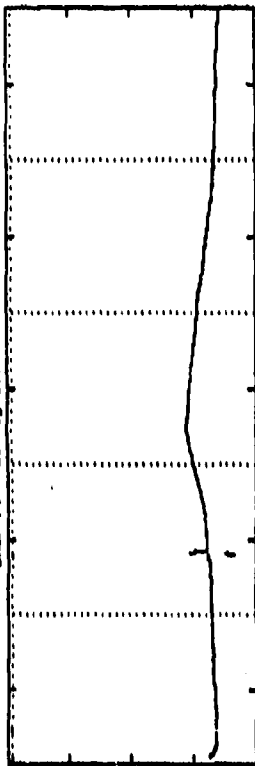
08:07:01	08:11:01	08:15:01	08:19:01	08:23:01	08:27:01	GWT
39.74	23.48	18.86	-4.30	-20.41	-26.20	APRILAT
271.04	279.80	279.80	289.41	289.41	270.27	APRILON

INSP FY - 30 Aug 1968 - Center Pass



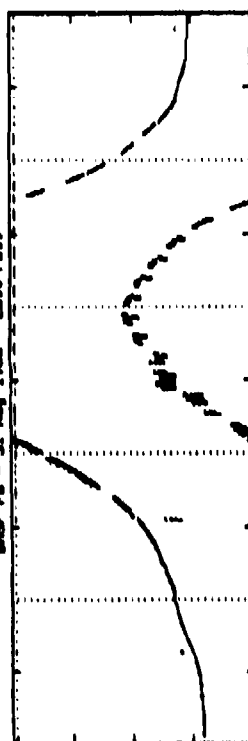
09:47:01	09:51:01	09:55:01	09:59:01	10:03:01	10:07:01	GWT
40.43	24.14	11.40	-3.48	-19.43	-25.40	APRILAT
248.49	247.06	243.03	243.03	244.41	243.96	APRILON

INSP FY - 30 Aug 1968 - West Pass



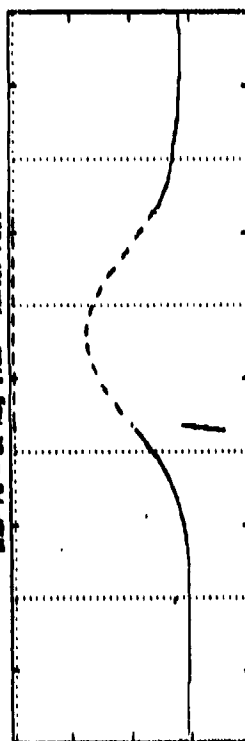
11:27:01	11:30:01	11:33:01	11:36:01	11:39:01	11:42:01	GWT
42.52	28.23	13.23	-2.10	-17.73	-23.49	APRILAT
228.14	222.53	222.53	220.30	218.48	216.54	APRILON

SWP F8 - 21 Aug 1988 - East Pass



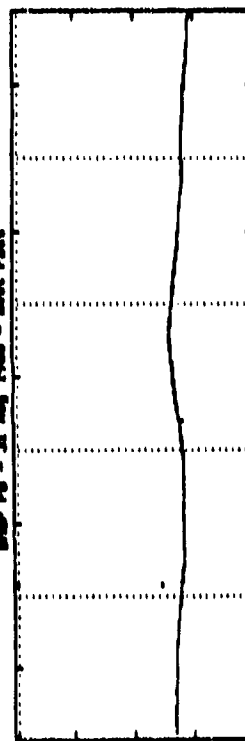
05:42:01	05:50:01	05:58:01	06:02:01	GMT
238.12	257.29	255.37	255.35	APRIL 88
238.43	256.51	255.84	255.35	APRIL 88
238.43	256.51	255.84	255.35	APRIL 88

SWP F8 - 21 Aug 1988 - Center Pass



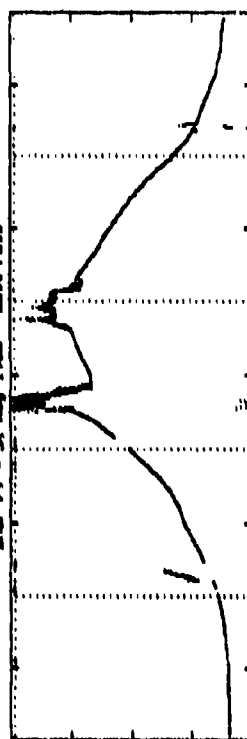
07:22:01	07:28:01	07:32:01	07:32:01	GMT
238.86	252.47	252.09	252.27	APRIL 88
238.86	252.47	252.09	252.27	APRIL 88
238.86	252.47	252.09	252.27	APRIL 88

SWP F8 - 21 Aug 1988 - West Pass



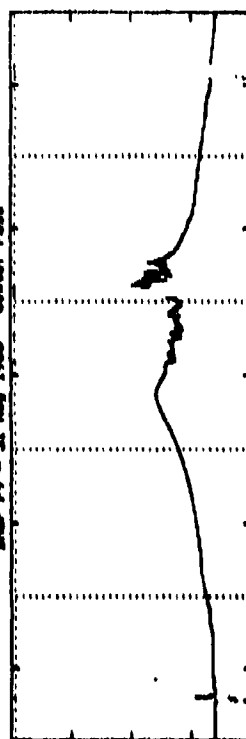
07:00:01	07:08:01	07:16:01	07:20:01	GMT
238.86	251.00	250.20	250.00	APRIL 88
238.86	251.00	250.20	250.00	APRIL 88
238.86	251.00	250.20	250.00	APRIL 88

SWP F9 - 21 Aug 1988 - East Pass



09:27:01	09:35:01	09:39:01	09:47:01	GMT
252.02	256.49	249.97	249.21	APRIL 88
252.02	256.49	249.97	249.21	APRIL 88
252.02	256.49	249.97	249.21	APRIL 88

SWP F9 - 21 Aug 1988 - Center Pass



11:00:01	11:10:01	11:20:01	11:20:01	GMT
251.71	257.07	257.07	257.07	APRIL 88
251.71	257.07	257.07	257.07	APRIL 88
251.71	257.07	257.07	257.07	APRIL 88

SWP F9 - 21 Aug 1988 - West Pass



12:00:01	12:10:01	12:20:01	12:20:01	GMT
251.00	257.07	257.07	257.07	APRIL 88
251.00	257.07	257.07	257.07	APRIL 88
251.00	257.07	257.07	257.07	APRIL 88